Production of CO₂-reduced Eco-cements using bauxite-mining overburden Belterra Clay and bauxite washing residue from Brazilian Amazon

Dissertation
to obtain the
Doctoral degree in natural sciences (Dr. rer. nat.)

from the
Naturwissenschaftliche Fakultät III
Agrar- und Ernährungswissenschaften,
Geowissenschaften und Informatik

of the Martin-Luther-Universität Halle-Wittenberg,

Presented by
Leonardo Boiadeiro Ayres Negrão
born 04 February 1992 in Campinas, São Paulo, Brazil

Examiners:
1. Prof. Dr. Dr. Herbert Pöllmann
2. Prof. Dr. Bastian Raab

Date of Defense: 3 March 2022

Table of contents

Table of contents

Abstract

The increasing CO_2 emissions of the cement industry due to the rising cement production, and the efforts to prevent global warming, have challenged the cement sector for solutions to reduce emissions. Among them is the use of less carbon-intensive clinkers to replace the most world-used ordinary Portland cement (OPC). Calcium sulfoaluminate cement (CSA), or CSA-based that have ye'elimite as the principal hydraulic phase, has been quoted as an interesting alternative to OPC thanks to its lower CO_2 emissions. However, CSA requires high amounts of alumina, which increases costs, and has limited CSA production to larger scales. In this work, residues of the bauxite mining were tested as alumina sources to produce CSA-based eco-cements. These residues are the clays that cover the bauxite deposits in the Amazon region (Belterra Clays), and the clay from the beneficiation process of bauxite washing. Both clays have similar mineralogy composed of kaolinite, gibbsite, goethite, hematite and anatase, and similar chemical composition with high contents of alumina (35-41%) and silica (25-35%), besides iron oxide (approx. 10%) and titanium oxide (2%). Diverse clinker raw meals composed of calcium carbonate (calcite), calcium sulfate (gypsum), and the bauxite residues (Belterra Clay and bauxite washing clay) were tested using design of experiments and stoichiometric calculations to define optimal raw meal design and clinkering temperature to produce clinkers with maximised ye'elimite contents using as much as possible of the residues. Up to 38 or 34.4% of Belterra Clay (depending on its composition), and up to 37.6% of bauxite washing clay can be used to produce CSA clinkers at 1250 °C with 34 to 45% of ye'elimite. The clinkers have high amounts of belite and ternesite depending on the gypsum contents used in the raw meal. Brownmillerite and Fe-rich perovskite are the main iron-carrying phases and form a discontinuous solid solution in the clinkers, with the decomposition of brownmillerite and consequent increased formation of Fe-perovskite at 1300 °C. At this temperature, ternesite is also unstable, releasing sulfate that can be partially lost or that combines with Al from brownmillerite to form additional ye'elimite. The clinkers generate at least 30% less CO_2 than OPC clinkers. The CSA-based clinkers can be mixed with different amounts of gypsum to form cements for special purposes. Upon hydration, the main phases were ettringite and monosulfoaluminate, besides straetlingite, aluminium hydroxide (amorphous and as gibbsite) and hemicarboaluminate. The produced mortars developed similar and higher compressive strength than a commercial OPC at 7 and 28 days. The results show that both residual clay are suitable raw materials to produce CSA-based eco-cements in the Amazon region.

Keywords: bauxite, mining residues, eco-cement, calcium sulfoaluminate, CO_2-reduction

Zusammenfassung

Die zunehmenden CO_2-Emissionen der Zementindustrie aufgrund der steigenden Zementproduktion und die Bemühungen, die globale Erwärmung zu verhindern, haben den Zementsektor vor die Herausforderung gestellt, Lösungen zur Reduzierung der Emissionen zu finden. Dazu gehört die Verwendung von weniger kohlenstoffintensiven Klinkern als Ersatz für den weltweit am häufigsten verwendeten gewöhnlichen Portlandzement. Calciumsulfoaluminatzement (CSA) oder CSA-basierte Zemente, die Ye'elimit als wichtigste hydraulische Phase enthalten, werden aufgrund ihrer niedrigeren Klinkertemperaturen und geringeren CO_2-Emissionen als interessante Alternative zu Portlandzement genannt. CSA erfordert jedoch große Mengen an Aluminiumoxid, was die Kosten erhöht und die CSA-Produktion auf größere Maßstäbe beschränkt hat. In dieser Arbeit wurden Abfälle aus dem Bauxitabbau als Aluminiumoxidquellen für die Herstellung von Ökozementen auf CSA-Basis getestet. Bei diesen Abfällen handelt es sich um die Tone, die die Bauxitlagerstätten im Amazonasgebiet bedecken (Belterra-Tone), und um den Ton aus dem Aufbereitungsprozess der Bauxitwäsche. Beide Tone haben eine ähnliche Mineralogie bestehend aus Kaolinit, Gibbsit, Goethit, Hämatit und Anatas und eine ähnliche chemische Zusammensetzung mit hohen Gehalten an Aluminiumoxid (35-41%) und Siliziumdioxid (25-35%), außerdem Eisenoxid (ca. 10%) und Titanoxid (2%). Verschiedene Klinkerrohmehle, die aus Kalziumkarbonat (Kalzit), Kalziumsulfat (Gips) und Bauxitabfällen (Belterra-Ton und Bauxit-Waschton) bestehen, wurden mit Hilfe von statistischen Versuchsplänen und stöchiometrischen Berechnungen getestet, um ein optimales Rohmehldesign und eine optimale Klinkertemperatur für die Herstellung von Klinkern mit maximalem Ye'elimit-Gehalt unter Verwendung eines möglichst hohen Anteils der Abfälle zu bestimmen. Bis zu 38 bzw. 34,4% Belterra-Ton (je nach Zusammensetzung) und bis zu 37,6% Bauxit-Waschton können zur Herstellung von CSA-Klinkern bei 1250°C mit 34 bis 45% Ye'elimit verwendet werden. Die Klinker weisen je nach dem im Rohmehl verwendeten Gipsgehalt hohe Anteile an Belit und Ternesit auf. Braunmillerit und eisenreicher Perowskit sind die wichtigsten eisenhaltigen Phasen und bilden in den Klinkern einen diskontinuierlichen Mischkristall, wobei sich Brownmillerit bei 1300°C zersetzt und infolgedessen verstärkt Fe-Perowskit gebildet wird. Bei dieser Temperatur ist auch Ternesit instabil und setzt Sulfat frei, das teilweise verloren gehen kann oder sich mit Al aus Brownmillerit zu zusätzlichem Ye'elimit verbindet. Die Klinker erzeugen mindestens 30% weniger CO_2 als Portlandklinker. Die Klinker auf CSA-Basis können mit unterschiedlichen Mengen an Gips gemischt werden, um Zemente für spezielle Zwecke herzustellen. Nach der Hydratation waren die Hauptphasen Ettringit und Monosulfoaluminat, daneben Straetlingit,

Aluminiumhydroxid (amorph und als Gibbsit) und Hemicarboaluminat. Die hergestellten Mörtel entwickelten nach 7 und 28 Tagen eine ähnliche und höhere Druckfestigkeit als ein kommerzieller Portlandzement. Die Ergebnisse zeigen, dass sowohl Belterra-Ton als auch Bauxit-Waschton geeignete Rohstoffe für die Herstellung von Ökozementen auf CSA-Basis in der Amazonasregion sind.

Keywords: Bauxit, Bergbaureststoffe, Öko-Zement, Calciumsulfoaluminat, CO_2-Reduktion

Acknowledgements

Nomenclature and list of abbreviations

Cement nomenclature

$C = CaO$ $S = SiO_2$ $A = Al_2O_3$ $F = Fe_2O_3$ $s = SO_3$ $c = CO_2$

$H = H_2O$ $T = TiO_2$

Anhydrous phases

Cement Notation – chemical name – related mineral

C_4A_3s – Calcium sulfoaluminate – ye'elimite

C_2S (belite) – Dicalcium silicate – larnite (β-C_2S) and flamite (α_H-C_2S)

C_5S_2s – Calcium sulfosilicate – ternesite

C_4AF – Tetracalcium aluminate ferrite – brownmillerite

C_2AS – Dicalcium aluminosilicate – gehlenite

CT – Calcium titanate – perovskite

C_3A – Tricalcium aluminate

CA – Monocalcium aluminate – krotite

CA_2 – Monocalcium dialuminate – grossite

Cc – Calcium carbonate – calcite

Cs – Calcium sulfate – anhydrite

Hydrated phases

$C–S–H$ – Calcium silicate hydrate

CH – Calcium hydrate – portlandite

$C_3A \cdot 3Cs \cdot H_{32}$ – Tricalcium aluminate trisulfate hydrate – ettringite

$C_3A \cdot Cs \cdot H_{12}$ – Tricalcium monosulfoaluminate hydrate – kuzelite

$C_3A \cdot Cc_{0.5} \cdot H_{12}$ – Hemicarboaluminate

C_2ASH_8 – Straetlingite

$C_3(A,F)H_6$ – Hydrogarnet

Techniques of investigation

EDS = Energy dispersive X-Ray spectroscopy

DTG = Differential thermogravimetry

SEM = Scanning electron microscopy

TGA = Thermogravimetric analysis

XRF = X-ray Fluorescence spectroscopy

XRPD = X-ray powder diffraction

Others

BSE = Backscattered electrons

CSA = Calcium Sulfoaluminate

CSA-based = CSA cement that has ye'elimite as the main hydraulic clinker phase, but still might contain other phases such as belite, ferrite and/or ternesite as a major component(s)

DIN = Deutsches Institut für Normung e.V.

ICDD = International Centre for Diffraction Data

ICSD = Inorganic Crystal Structure Database

LOI = Loss on ignition

OPC = ordinary Portland cement

w/c = water to cement ratio

RM-CO_2 = raw material-related CO_2 emissions

Definitions

Clinker: is the intermediary product in cement manufacturing and the major component of the cement. Clinker is produced by the calcination of limestone in a kiln (clinkerization process) with other raw materials. Portland types of cement are usually produced with a mixture of limestone, clay, sand, and minor additives.

Cement: is the binding agent in concrete, which is produced by mixing cement, sand, and crushed stones (or gravel) with water. Cement is produced after grinding and homogenising the clinker with other mineral components, including but not restricted to limestone, blast furnace slags, gypsum, fly ashes and calcined clays.

1   Introduction

1.1   **General introduction**

Cements, the primary material of concrete, are unquestionably a needful building material in the construction industry. The rising world population and urbanisation indicates that cement demand will increase continuously in the future (IEA, 2018) (Figure 1). Meanwhile, the reduction of CO_2 emissions has been one of the key challenges of the cement industry, considering that the sector is responsible for approximately 8% of the global CO_2 emissions (Andrew, 2019). Consequently, the cement sector plays an important role in the Paris Agreement negotiated in 2015 to limit global warming below 2 ºC.

Diverse new approaches have been discussed to mitigate CO_2 in the cement sector, including the optimisation of industrial processes, the use of alternative (and less carbon-intensive) fuels in the cement kilns, the lowering of the clinker to cement ratio, and the use of alternative binders to replace the world-used ordinary Portland cement (OPC) (IEA, 2018; Naqi and Jang, 2019). The research on new alternative clinkers has a particular advantage, considering that only the clinkerization process accounts for up to 70% of the CO_2 emitted during OPC production.
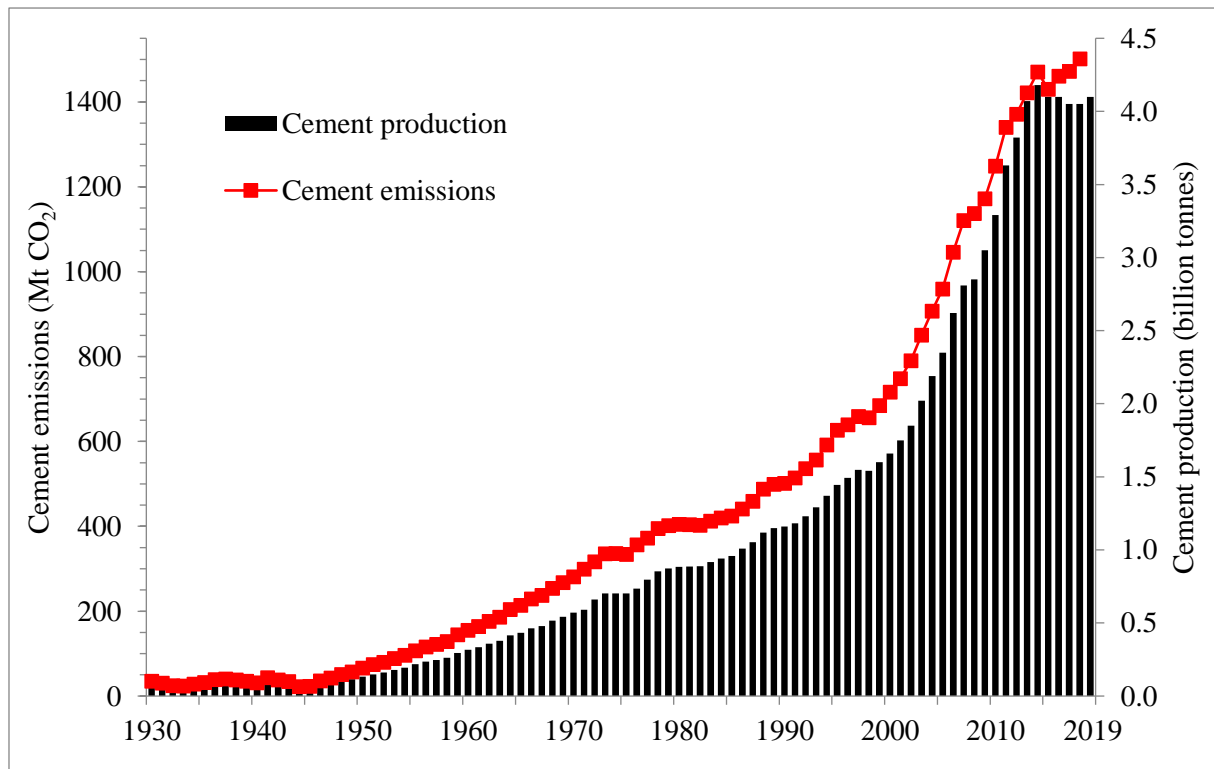
Figure 1 Global cement production and its CO_2 emissions from 1930 to 2019 (Kelly and Matos, 2014; Andrew, 2019; U.S Geological Survey, 2020).

During the clinkerization, the cement raw meal, basically composed of limestone and clay, is calcined at high temperatures. Calcination of limestone releases CO_2 from the burning of its major component $CaCO_3$. Therefore, alternative binders that demand lower $CaCO_3$ amounts than OPC are desirable. Calcium sulfoaluminate cements (CSA) are interesting alternative clinkers that require less $CaCO_3$ in the kiln mix, can be produced using lower temperatures, are softer and easier to grind (Mehta, 1980; Beretka et al., 1996; Martín-Sedeño et al., 2010; Álvarez-Pinazo et al., 2013). CSA cements are further known for their faster hardening, higher strength development, slight expansion and lower alkalinity (Pöllmann and Stöber, 2014), and have been considered for different special applications, including high performance high early strength concrete, self-levelling screed, self-levelling topping mortars and glass-fibber-reinforced composites (Péra and Ambroise, 2004).

These features stand CSA as a promissory alternative binder with lower CO_2 emissions when compared to OPCs. Nevertheless, CSA cements require, besides limestone and calcium sulfates, much higher contents of alumina in the clinker raw mixture to form their main reactive phase ye'elimite (C_4A_3s). Bauxite has been the traditional alumina source used to produce CSA. However, bauxite is also used in the aluminium industry, which turns it into a comparatively expensive raw material for application in the cement industry. Therefore, the high costs to produce CSA cements using bauxite have limited CSA production to a larger scale, which was only observed in China during the seventies (Zhang et al., 1999).

In order to overcome the bauxite-price limitation, several works reported the use of alumina-rich industrial residues and by-products to produce CSA-based cements (Arjunan et al., 1999; Ukrainczyk et al., 2013; Pöllmann and Stöber, 2014; Pöllmann et al., 2015; Galluccio et al., 2019), which still have ye'elimite as the main hydraulic phase. The compositions of the used residues and by-products differ from that of (Al-richer) bauxite, and their frequent iron and silica impurities result in clinkers with ye'elimite but also moderate to high contents of belite (C_2S), ferrite (C_4AF) and diverse others minor phases. The appearance of such CSA-based cements, which are still comparable to OPCs, has encouraged extensive research on these binders and, automatically, on suitable alumina-rich raw materials for their production.

Belterra Clay (Figure 2) is a thick alumina-rich clay covering most of the bauxite deposits of the Brazilian Amazon region (Truckenbrodt et al., 1991; Horbe and Costa, 2005; Negrão et al., 2018a). The high alumina content, close to 40 wt.%, simple mineralogical composition, and widespread distribution of Belterra Clay, sets it a promissory raw material for the production of CSA-based cements. The material lies widespread on the top of plateaus held by bauxitic

profiles in the Amazon region and is removed during bauxite mining. These clay packets can be 20 m thick, but generally are 10 m thick in bauxite mines. The Belterra Clay thickness can therefore be decisive for bauxite mining, as the increase of this clay removal is proportional to higher mining-operation costs to get into the ore. For example, if in the surface mining of a considerably thick bauxite layer of 3 m, 10 m of Belterra Clay needs to be relocated, roughly two-thirds of the excavated material comprises Belterra Clay – considering other 2 m of lateritic material occurring between Belterra Clay and bauxite.

Figure 2 Relocation of Belterra Clay (yellowish material) in the strip mining of bauxite in Porto Trombetas, lower Amazon region in Brazil. Photo from Carlos Penteado. Source: Documentária Fotographia (http://carlospenteadofotographia.blogspot.com/).

The mining of bauxite in Amazon results not only in Belterra Clay relocation but also in the production of a clay residue from the washing of bauxite in the bauxite beneficiation plant, which is performed to increase the quality of the ore before transporting it to the alumina refineries (Racanelli et al., 2020). This material is deposited in large tailing ponds for drying and differs from the "red mud" produced during the Bayer Process in the alumina refineries. As for Belterra Clay, bauxite washing clay with high alumina amounts makes it another interesting material to produce CSA cements.

1.2 **Motivation and goals**

The large and uniform distribution of Belterra Clay and bauxite washing clay, their easy availability, high alumina contents and simple mineral assemblage rise them as a possible raw material to produce CO_2-reduced calcium sulfoaluminate cements. The conversion of Belterra Clay and bauxite washing clay from mining residues to raw material for CSA-based cements can simultaneously:

a. Promote a more sustainable and cost-efficient bauxite mining.

b. Produce CO_2-reduced calcium sulfoaluminate-based cements.

c. Raise the competitiveness of the cement industry in the Brazilian Amazon region with the input of new environmental-friendly binders in the market.

d. Extend the lifespan of limestone reserves, and consequently of many cement factories.

e. Reduce environmental impacts of local cement manufacturing.

f. Create opportunities to earn carbon credits by savings of carbon dioxide in the future.

g. Promote a sustainable environmentally friendly initiative in the region.

Therefore, the primary goal of this work was to produce CO_2-reduced cements using Belterra Clay as raw material, and to test bauxite washing clay residue for the same purpose. The experiments were performed based on the production of clinkers using Belterra Clay and common raw materials used in the cement industry: limestone (here represented as $CaCO_3$) and gypsum. The technical aspects, commercial viability, and sustainability of the produced clinkers are reported and compared to Portland cement.

Additionally, this work aimed at the optimisation of the phase composition of the produced CSA-based clinkers, the understanding of their phase stability and the investigation of the hydrated cements.

1.3   **Bauxite mining residues**

The European Commission defines mining residues (i.e. wastes) as hazardous and non-hazardous materials coming from extracting and processing mineral resources, such as topsoil overburdens, waste rock and any materials deposited in tailings (Commission, 2006). The mining of bauxite and the production of aluminium ingots include a sequence of processes that generate diverse types of residues (Figure 3).

Before mining bauxite, any vegetation covering it must be removed. The vegetation removal is usually combined with the removal of a shallow fertilised portion of the topsoil, which is stored for further rehabilitation processes of the mined areas. Any material between the topsoil and the bauxite ore needs to be excavated during the strip mining of bauxite to get into the ore. In Northern Brazil, this material is basically composed of Belterra Clay and lateritic materials, such as iron crusts and bauxitic nodules (Truckenbrodt et al., 1991; Costa et al., 2014). The finally reached bauxite ore is transported to the beneficiation plant, usually very close to the mine, where it is crushed and washed, and the resulting clayey residue (i.e., bauxite washing clay) from the washing process is deposited into tailing ponds.
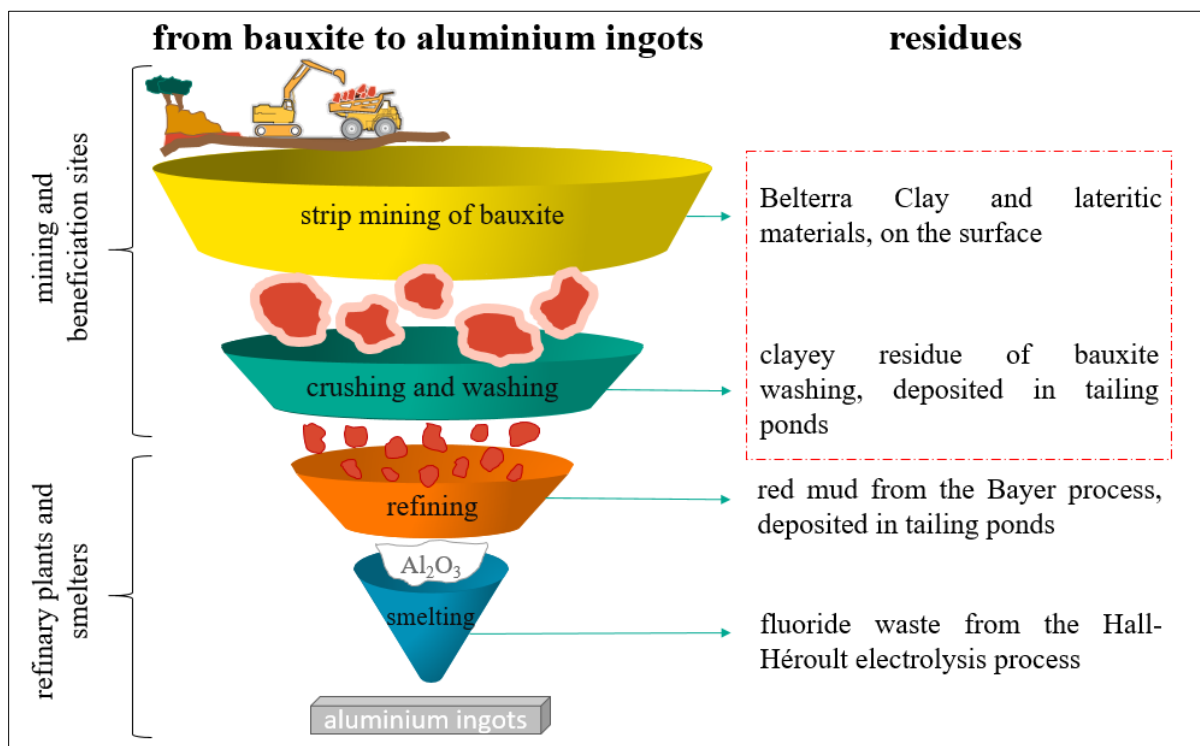
Figure 3 Residues from the bauxite mining and aluminium production. In the red box are the bauxite residues addressed in this work.

The following residues that are part of the aluminium production chain include the red mud produced by the Bayer process that extracts alumina from bauxite using caustic soda (Archambo and Kawatra, 2020), and diverse fluoride waste from the Hall-Héroult electrolysis process that reduces aluminium to later form the metal ingots in the smelters (Kvande and Drabløs, 2014). These two lasts are related to the residues of refining bauxite in the refinery plant and wastes from the smelters and are not discussed or tested for cement production in this work.

1.3.1 Belterra Clay bauxitic overburden

The Belterra Clays covering the bauxite deposits in the Amazon region can reach up to 25 m depth. This material was firstly named by Sombroek (1966) after he observed similar clays but not related to bauxites near the city Belterra, in the Brazilian lower Amazon. The material has yellowish to reddish colours and can be generally related to latosols, oxisols in the USDA soil taxonomy, or ferrosols in the World Reference Base for Soil Resources. These soils, including the Belterra Clay outside of the bauxite-mining areas, have been ground to the agricultural (mostly soya bean) and cattle pasture expansion in the Eastern Brazilian Amazon. Similar clays are also found covering the bauxites of Central Africa (Tardy, 1997).

Belterra Clay is widespread on the top of extensive plateaus in Amazonia, mainly covering bauxite reserves (Figure 4). Some of these reserves are currently large bauxite mines in operation within the Brazilian federal state Pará, including those in Porto Trombetas operated by Mineração Rio do Norte (MRN), in Juruti by Alcoa, and in Paragominas by Hydro, while others are still in the research phase as in Rondon do Pará.
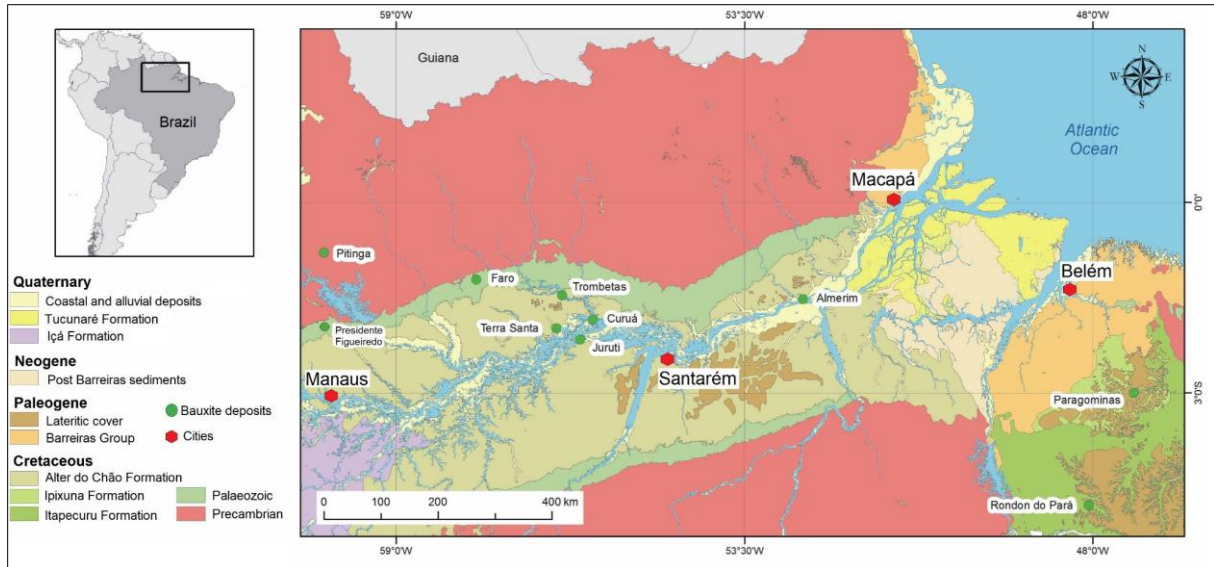
Figure 4 Simplified geological map of the eastern Amazon region with the main bauxite deposits, all of them covered with Belterra Clay (Negrão et al., 2018a). Licensed under CC BY 4.0 https://creativecommons.org/licenses/by/4.0/

Belterra Clay is excavated and relocated during bauxite mining. The strip-mining of bauxite includes the removal of all material that covers the bauxite ore: the Amazon Forest, the fertilised topsoil, the Belterra Clay and part of the lateritic profile (Figure 5). After the bauxite mining, the disturbed Belterra Clay lies on the surface until the rehabilitation of the mined areas.
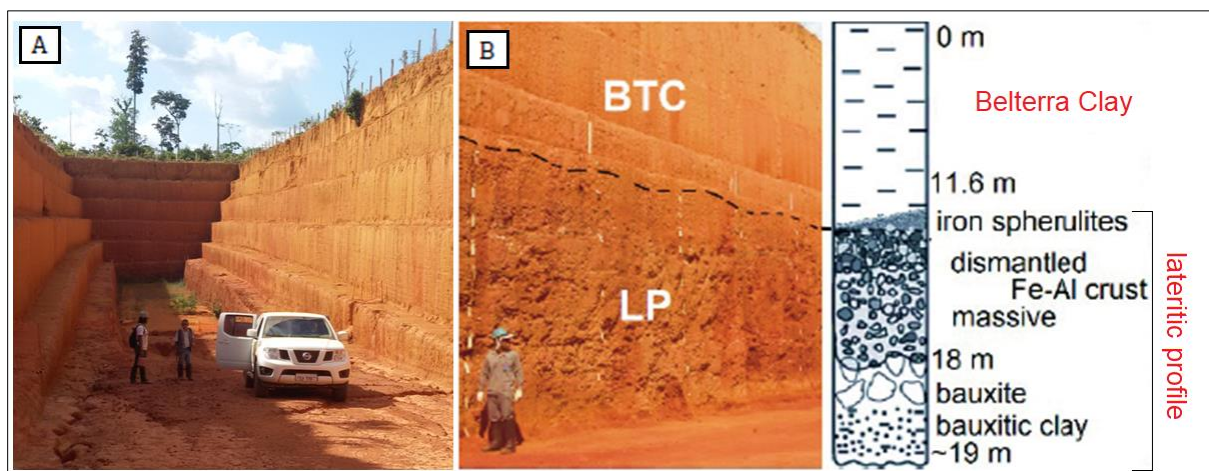
Figure 5 A: Belterra Clay expositions at an open pit in Rondon do Pará, Brazil. B: underlying lateritic bauxite profile and its summarised description (left) in the Críaco pilot-mine. Source: modified from Negrão et al. (2018), licensed under CC BY 4.0 https://creativecommons.org/licenses/by/4.0/

Except for the works of Barreto and Costa, which investigated the use of Belterra Clay to produce red ceramics (Barreto and Costa, 2018a, 2018b) and geopolymers (Barreto and da

Costa, 2021), most of the publications about this material are focused on its geological aspects and (still) controversial genesis (Sombroek, 1966; Grubb, 1979; Truckenbrodt and Kotschoubey, 1981; Kronberg et al., 1982; Kobilsek and Lucas, 1988; Truckenbrodt et al., 1991; Tardy, 1993; Horbe and Costa, 2005; Abouchami et al., 2013; Negrão et al., 2018a). The mineralogical and chemical composition of Belterra Clay and the underneath laterite-bauxitic profile is notably very similar. Therefore, it has been suggested that Belterra Clay was formed under a tropical environment by intense weathering processes of the underneath laterite-bauxitic profile, followed by local transport and deposition (Horbe and Costa, 2005; Costa et al., 2014; Negrão et al., 2018a).
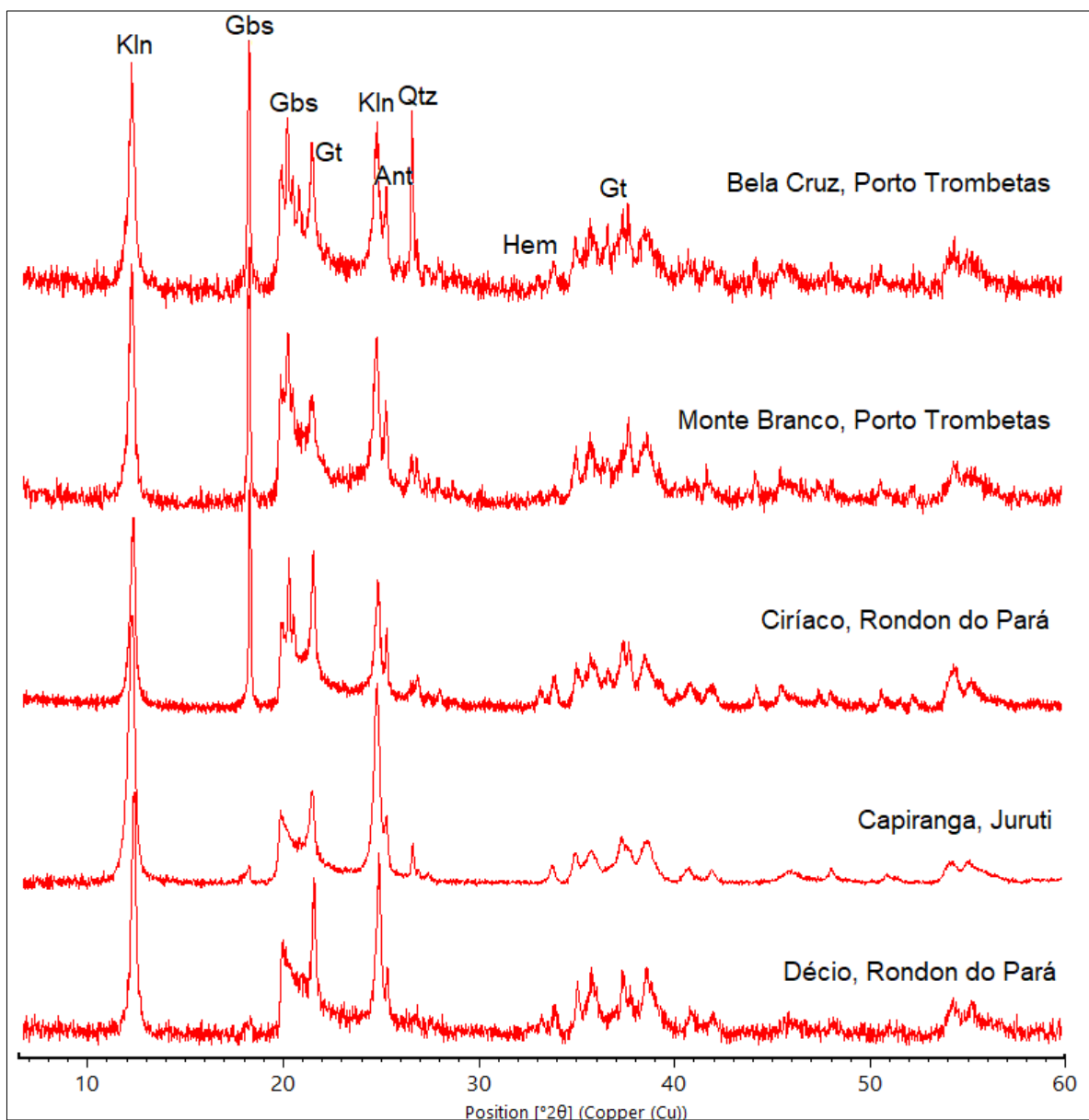
Figure 6 Comparison of X-ray diffractograms of Belterra Clay samples from different sites in the Brazilian Amazon region. Kln: kaolinite; Gbs: gibbsite, Gt: goethite; Ant: anatase; Hem: hematite; Qtz: quartz (Negrão et al., 2021b).

The mineral composition of Belterra Clay is quite uniform throughout the Amazon region and formed by kaolinite, gibbsite, hematite, goethite, quartz and anatase (Figure 6). Accordingly, the major chemistry of the material is dominated by SiO_2, Al_2O_3, Fe_2O_3 and TiO_2. Consequently, its chemical composition is similar from place to place (Figure 7).
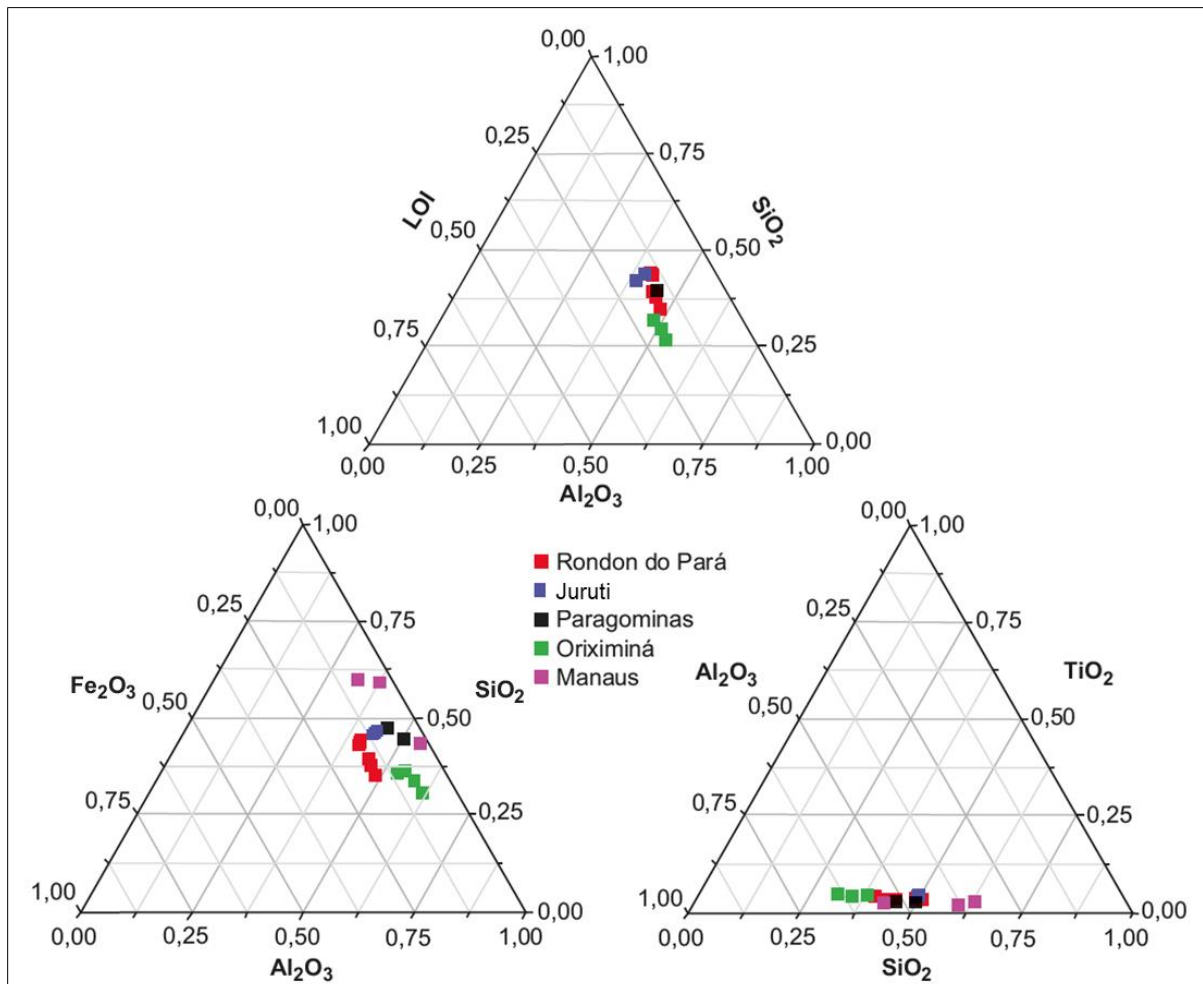
Figure 7 Chemistry composition of Belterra Clay from different locations within the Amazon region (Negrão et al., 2018a). Licensed under CC BY 4.0 https://creativecommons.org/licenses/by/4.0/.

1.3.1.1 The Belterra Clay in Rondon do Pará

Rondon do Pará is a county in the eastern part of the State of Pará, in the Brazilian Amazon region. The place has bauxite reserves that are part of the large Paragominas Bauxitic District, which currently has a bauxite mine operated by the company Hydro in the municipality of Paragominas. Exploration studies in the last decade in Rondon do Pará have found at least 642 Mt of world-class bauxites grading 42.7% available alumina (De Oliveira et al., 2016). Three large pilot-mines (i.e., trenches) were performed for the ore evaluation during the exploration

campaigns (Figure 8), as part of the "Alumina Rondon project" of the mining company Votorantim Metais.
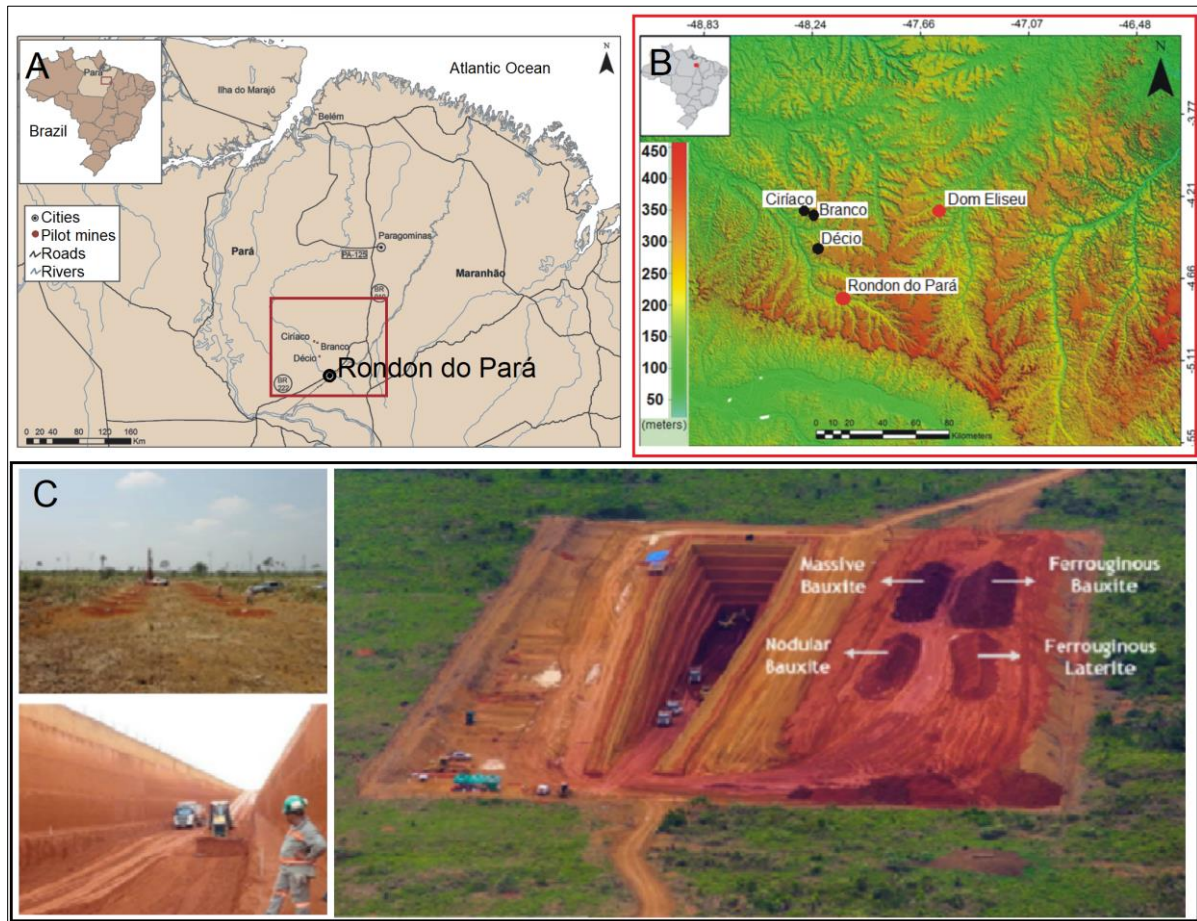
Figure 8 A: Location of Rondon do Pará and open pit in the pilot-mines conducted for bauxite ore evaluation. B: SRTM image of the area showing the bauxitic plateaus with Belterra Clay on the top. C: Aerial and in situ photographs of the pilot-mine excavations. Source: Negrão et al. (2021b) and Prazeres Filho et al. (2015).

The pilot-mines exposed up to 14 m of Belterra Clay (Figure 8), which were studied by Negrão et al. (2018a). The drilling program, part of the Alumina Rondon exploration campaigns, attested that Belterra Clay has an average thickness of close to 10 m in Rondon do Pará, with a uniform lateral distribution for several kilometres (Figure 9).
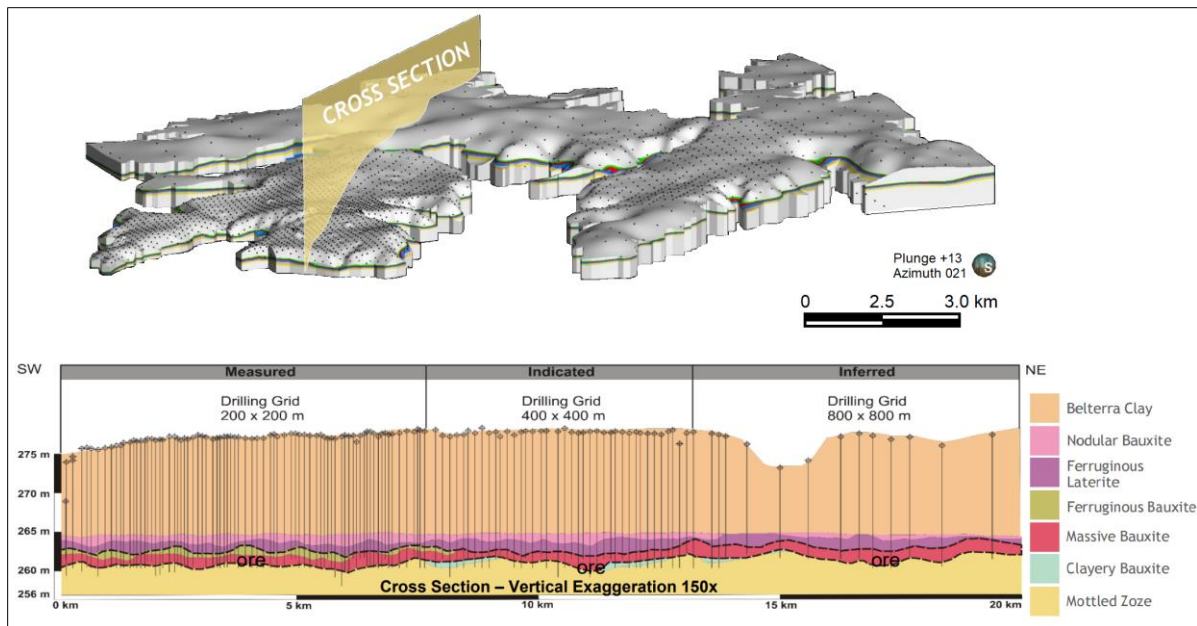
Figure 9 Cross-section of a plateau in Rondon do Pará showing the continuous thickness of Belterra Clay on the lateritic profile and bauxite ore. The vertical scale is the altitude. Source: Gatti (2016).

1.3.2 Bauxite washing clayey residue

After mining the bauxite, one of the first steps in the ore processing is the disaggregation of the ore by crushing and washing. The washing comprises a combination of processes including elutriation and cyclone classification to remove the clayey fraction of the bauxite ore, which is considered a residue rich in aluminosilicates.

The final beneficiated bauxite ore has higher available alumina (alumina of bauxite that is effectively converted into powder alumina in the Bayern process) and lower reactive silica contents (bauxite's silica that reacts with caustic soda in the Bayern process). Diverse bauxite mines use the bauxite washing processes to obtain a beneficiated ore with higher available alumina to reactive silica ratios, including the mines in Juruti, Trombetas and Paragominas (in Brazil), in Awaso (Ghana), in Weipa (Australia), and in Coermotibo (Suriname) (Buntenbach, 2008).

The washed ore is then sent to the alumina refineries, whereas the resulting washing clay residue is deposited into large tailings ponds (Figure 10) close to the mining facilities. The bauxite washing clayey residue is not the "red mud", a well-known insoluble alkali-rich residue formed during the industrial Bayer process used to produce alumina powder.

Figure 10 Tailing ponds with bauxite washing clay residue in Porto Trombetas, Lower Amazon, Brazil. Photo from Carlos Penteado, Documentária Fotographia (http://carlospenteadofotographia.blogspot.com/).

Some bauxite beneficiation plants have changed the process to reduce the amount of tailing ponds with bauxite washing clay. Hydro Paragominas, for example, has implemented a new method, called Dry Backfill, where the mud is dried in a temporary deposit for approximately 60 days (Figure 11). The dried solid residues are deposited in the previously mined sites following the mining sites rehabilitation (Hydro, 2021).

Figure 11 Bauxite washing clay in the tailing pond located in the facilities of the bauxite mine of Mineração Paragominas SA (Hydro), in Paragominas, Brazil. The material in the photo is dried and being removed. Source: Hydro Paragominas.

To date, the bauxite washing clayey residue has no industrial application, but it was tested for the production of red ceramics (Santos et al., 2013), geopolymers (Racanelli et al., 2020) and to produce a mortar with Portland cement (Santiago et al., 2018).

1.4   Calcium sulfoaluminate (CSA) -based clinkers

CSA was produced on large scale during the seventies in China, where it is known as the third cement series (Zhang et al., 1999), but the knowledge on CSA cements dates back to the works of Professor Alexander Klein (Klein, 1963). Klein's salt, or ye'elimite (C_4A_3s), is the major phase of CSA clinkers and the main hydraulic phase of CSA cements, controlling with calcium sulfates the setting time of CSA cements by the formation of the hydrated phase ettringite ($C_3A \cdot 3Cs \cdot H_{32}$). Besides ye'elimite, other common phases occurring in CSA clinkers include, but are not restricted to, belite (C_2S), ferrite (C_4AF, i.e., brownmillerite), ternesite (C_5S_2s), calcium aluminates (C_3A, CA, $C_{12}A_7$), and calcium silicoaluminates (C_2AS - gehlenite, and CAS_2).

CSA-based cements are defined here as cements that have ye'elimite as the main hydraulic clinker phase but still might contain other phases such as belite, ferrite and/or ternesite as major components. CSA-based cements are usually named according to the abundancy of their main phases: CSAB (ye'elimite>belite); BCSA (belite>ye'elimite); BCSAF (belite>ye'elimite >ferrite); BCSAT (belite>ye'elimite>ternesite), etc. Analogous to BCSAF, the well-known "BYF" nomenclature stands for belite-ye'elimite-ferrite cements. This extensive family of CSA cements can be produced in standard OPC plants, which is a key factor to consider these binders as an alternative to OPC without high investments costs in the cement manufacturing process (Gartner and Sui, 2018).

Except for the expressive production of ye'elimite-rich CSA in China during the seventies, this cement is currently limited to special applications. In North America, over 2 million metric tons of BCSA cement have been produced in the last 30 years and were mainly used for rapid paving of roads, including airstrips (Bescher and Kim, 2019). In Europe, diverse initiatives have tested some CSA-based compositions. The Aether® BCSA cement of Lafarge Holcim was tested in a trial industrial production during the European Union "Aether" Life + project with the production of over 10 thousand tons of clinker (Gartner et al., 2011), and Heidelberg Cement

patented the BCT-cement (Ternocem®), which has a BCSAT composition (Dienemann et al., 2013).

The raw meal of CSA-based binders must essentially have calcium, sulfate, and alumina to form C_4A_3s. The sources for calcium and sulfate are usually limestone (mainly composed of $CaCO_3$) and gyps, and both are common raw materials used in the production of OPCs. The aluminium source for the CSA meal is usually bauxite, which is also used in the production of OPC, but in minor proportions only to adjust the clinker raw meal compositions.

Since CSA-based cements require much less $CaCO_3$ in their raw meal formulation, the CO_2 emissions from the calcination of the raw material (RM-CO_2) to produce them will be lower than compared to those of OPC (Figure 12). Gartner and Sui (2018) estimated that 541 kg of CO_2 per tonne of produced clinker is emitted in the production of OPC, whereas 289 kg of CO_2 is released to produce ye'elimite, representing a reduction of 47% in the CO_2 emissions. A BCSA cement with high amounts of C_2S (High BCSA, composed of 46% of C_2S, 35% C_4A_3s and 17% C_4AF), has an RM-CO_2 emission of 409 Kg per tonne of clinker, whereas a Low BCSA (60% C_2S, 20% C_4A_3s and 17% C_4AF) generates 404 Kg of RM-CO_2 per tonne of clinker (Gartner and Sui, 2018).
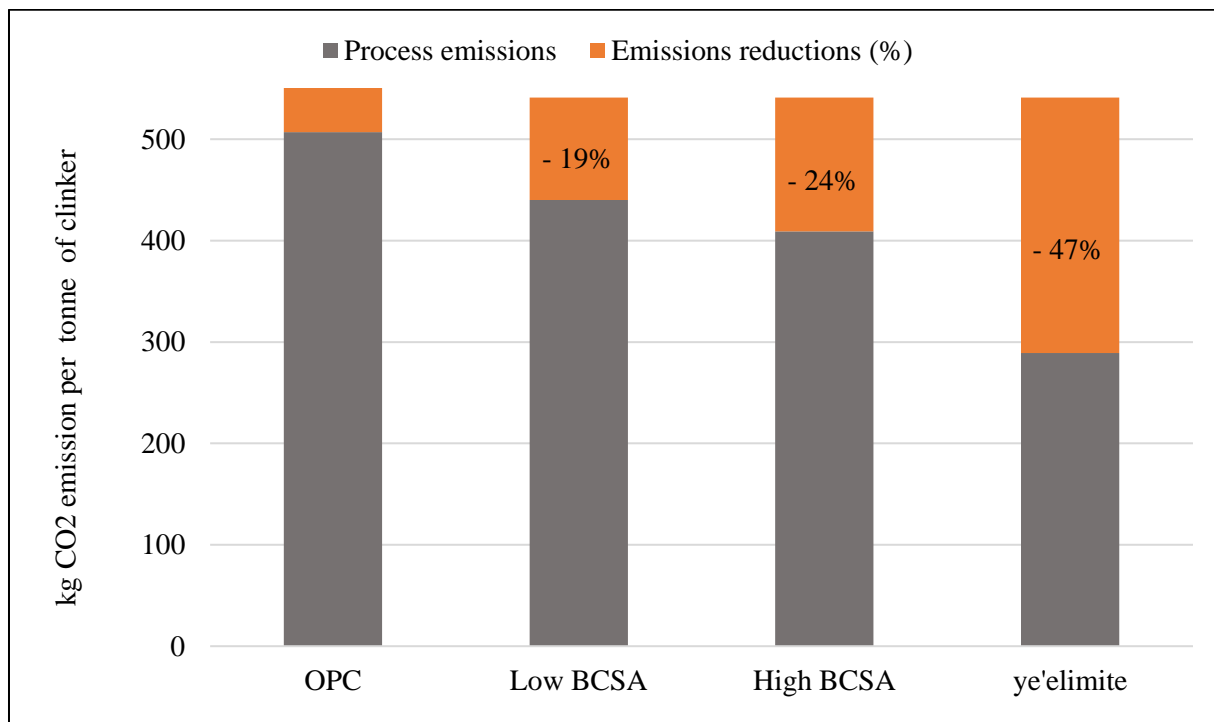
Figure 12 CO_2 emissions per binding material of OPC, Low BCSA, High BCSA and ye'elimite. Source: Gartner and Sui (2018).

The much higher amounts of Al needed to produce CSA result in more bauxite consumption compared to the production of OPC, and consequently elevated costs, which has been the major factor restricting CSA production at larger scales (Ben Haha et al., 2019). Diverse secondary sources of silica and alumina have been tested for CSA production, including coal fly ashes (Arjunan et al., 1999; Schmidt and Pöllmann, 2000), steelmaking slags (Adolfsson et al., 2007), kaolin and low-grade bauxites (Galluccio et al., 2019), and red mud and alumina powders (Pace et al., 2011). Using alumina-rich wastes and by-products are of particular interest as partial or total substitutes for the expensive bauxite in the CSA raw meal.

1.4.1   Production of CSA-based clinkers using bauxite mining residues

CSA-based clinkers produced using limestone, gypsum and Belterra Clay or bauxite washing clay residue should have besides ye'elimite, other phases due to the contents of SiO_2, Fe_2O_3 and TiO_2 in the bauxite residues. The $CaO-SiO_2-Al_2O_3-SO_3-Fe_2O_3$ system studied by Galan et al. (2017) permits the prediction of some phases in CSA-based clinkers. According to the authors, C, C_2S, C_3S_2, CS, C_3A, $C_{12}A_7$, CA, CA_2, CA_6, CAS_2, C_2AS, C_4A_3s C_5S_2s, Cs, C_4AF are among the possible phases for this system at 1250 °C.

Limestone, represented as $CaCO_3$, is the primary source of CaO, whereas gypsum ($CaSO_4 \cdot 2H_2O$) gives CaO and SO_3. When bauxites are used as Al source, their high alumina/silica ratios promote the formation of ye'elimite (C_4A_3s) in the restriction of calcium silicoaluminates (i.e. CAS_2) undesirable in CSA clinkers due to their low or no hydraulic activity. Berrio et al. (2018) studied the influence of different alumina/silica ratios in the production of CSA cements. According to the authors, clinkers produced at 1250 °C with $Al_2O_3/SiO_2 \geq 2$ resulted in compositions with an excess of CAS_2 over ye'elimite. Nevertheless, the 2-ratio limit should not be strict, as complex chemical phase interactions when using secondary raw materials might promote the formation of C_2S.

The high Al_2O_3 contents of bauxite mining residues should be primarily addressed to form ye'elimite. Belite is also expected due to the SiO_2 coming mostly from kaolinite. The high iron contents in the residues, from hematite and goethite, can form C_4AF. Perovskites (CT) are expected after the few TiO_2 amounts in these materials. Solid solutions are common in clinker systems and can change the phase composition considerably.

2   Materials and methods

2.1 **Materials**

2.1.1 Belterra Clay samples

Belterra Clay samples from Rondon do Pará in Brazil were used in the experimental trials. The samples were collected by the author during an exploration campaign carried by the company Votorantim Metais. Prior characterisation of the Belterra Clay samples was described by Negrão et al. (2021a) as part of this thesis and is presented here. This characterisation let to choose two samples with distinct alumina/silica ratios to produce the CSA-based cements presented in this work. One sample is from the Círiaco bauxite pilot-mine and was collected at approximately 14 m depth from the surface, and the other was from the Branco pilot-mine, from 13 m depth.

2.1.2 Bauxite washing clay sample

A sample of bauxite washing clay from Paragominas, Brazil, was also tested for CSA clinkers' raw material. The sample was collected from the tailing pond where these residues are disposed, in the facilities of the Hydro Paragominas bauxite mine.

2.1.3 Calcium Carbonate

Commercial $CaCO_3$ ($\geq$99.5% purity) from Applichem Panreac was used as a CaO source to produce the experimental clinkers.

2.1.4 Calcium sulfate

Commercial $CaSO_4 \cdot 2H_2O$ ($\geq$98%) from Carl Roth GmbH was used as sulfate source.

2.1.5 Raw materials used to synthesise pure phases

To synthesise the pure phases (perovskites and brownmillerites), the following reagents were used: CaO, produced by firing $CaCO_3$ at 1000°C for 2 hours; Fe_2O_3 ($\geq$ 99%, from Fluka); Al_2O_3 ($\geq$ 99 %, from Roth); and TiO_2 ($\geq$ 99%, from Kronos).

2.2 Analytical methods

2.2.1 X-ray powder diffraction analysis

X-ray powder diffraction (XRPD) was used for the mineralogical characterisation and quantification of the raw materials, of the obtained clinkers and hydrated cements, and of the synthesised pure phases. The samples were carefully ground by hand with agate mortar and pestle and prepared by back-loading. 27 mm-diameter sample holders were used for the clinkers and synthesised phases, and 16 mm-diameter sample holders for the hydration products.

The samples were measured with a PANalytical X'Pert[3] Pro MPD X-ray diffractometer (Figure 13) located at the University of Halle and equipped with a Cu anode (Cu Kα1 λ = 1.5418 Å). The diffractometer was operated with 45 kV and 40 mA and set in the θ-θ Bragg-Brentano-Geometry with a PIXcel[1D] detector.
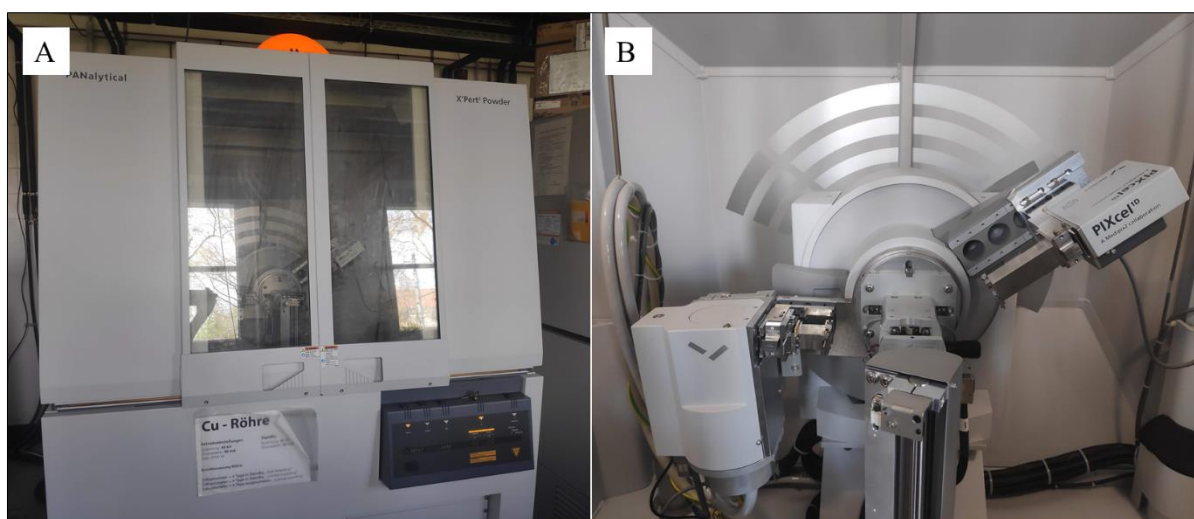
Figure 13 Photography of the used PANalytical X'Pert[3] Pro MPD X-ray diffractometer (A), set in the θ-θ Bragg-Brentano-Geometry with a PIXcel[1D] detector (B).

The measuring conditions, including the used divergence slits, beam masks and the anti-scatter slits were adjusted to each of the used sample holders (Table 1). Due to the longer measurement times, the 5-100 °2θ range resulted in XRPD patterns with higher resolution and was used to measure the synthesised pure phases.

Table 1 XRPD measurement conditions used in this work.

Samples	2θ range	Step size	Time per step	Beam mask	Divergent slit	Anti-scatter slit	Soller slits	β-filter
clinker and cements	5-70°	0.013°	38 s	15 or 10 mm	¼ ° or ⅛°	½° or ¼°	0.04 rad	Ni
synthesised phases	5-100°	0.007°	118 s	15 mm	¼ °	½°	0.04 rad	Ni

2.2.1.1 High-Temperature X-Ray Powder Diffraction (HTXRPD)

HTXRPD was used to investigate possible phase transitions in a synthesised Fe-perovskite, from 25 °C to 900 °C in an air atmosphere. The measurements were performed in a PANalytical Empyrean diffractometer set in transmission geometry with Mo radiation operated with 45 kV and 40 mA. The diffractometer was equipped with an Anton Paar HTK 1200 high-temperature oven chamber and a GeliPIX^{3D} detector.

The Fe-perovskite fine sample powder was filled into a 0.6 mm Ø glass silica capillary, heated to 900 °C and measured at each 10 °C with a hold time of 15 minutes. The measurement occurred in the 4.5 to 86 °2θ (Mo) range, with 0.007 °2θ step size and a measurement time of 120 seconds per step, totalling 49 minutes for each measurement.

2.2.1.2 Phase characterisation and Principal Component Analysis

The mineral characterisation and the Rietveld quantification of the phases were performed with the software HighScore Plus 4.5. The Powder Diffraction Files (PDF) from the International Center for Diffraction Data (ICDD) were used in the mineral characterisation.

Principal component analysis (PCA) was used to find systematic variances (eigenvalues) in the set of XRPD patterns of different Belterra Clay samples. PCA is based on a correlation matrix that displays the most relevant eigenvalues (or Principal Component) in a 3D plot. Similar diffractograms were clustered according to their similarity of pattern profiles and peaks by using Euclidian average linkage with a user-defined cut-off of 9.5. The most representative sample of each group was chosen with the centroid method, i.e., admitting that the closest sample of each sphere centroid group is the most representative one.

2.2.1.3 Rietveld phase quantification

The Rietveld method (Rietveld, 1969) was performed by refining the following parameters and variables: background, as polynomial or manually determined (when complex); scale factor; 2θ zero shift correction; unit cell parameters; profile variable W; and profile asymmetry. Additionally, the profile variables U or V were systematically refined after observing their influence on the XRDP-Rietveld calculated patterns. The Rietveld refinements were evaluated by monitoring the fitting of the calculated profile to the observed one and its resulting difference curve, and by checking the Rietveld agreement indices GOF (Goodness of fit) and Rwp (R-weighted profile). The crystal information files (.cif data) used in the refinements were obtained from the Inorganic Crystal Structure Database (ICSD) and are listed in Table 2.

For comparison purposes, a Rietveld refinement of a Belterra Clay sample (CIR14m) was performed with the software Profex (Doebelin and Kleeberg, 2015). In the refinement, a model of disordered kaolinite was used. The model was downloaded from the BGMN database (Kaolinitedis.str file, in http://www.bgmn.de/download-structures.html, accessed on: 04/02/2021). In the model, the stacking faults related to b/3 shifts and layers rotations in the crystal structure of kaolinite were refined. For that, the disordered kaolinite was refined using the sub-phase approach, where sub-phases that share the same lattice parameter have their hkl-dependent broadening described by individual models in a phenomenological way (Bergmann and Kleeberg, 1998).

Amorphous quantification

Two methods based on XRPD-Rietveld were used to quantify the amorphous fractions in the samples: the internal standard method (Westphal et al., 2009), and the external standard method (Snellings et al., 2014). In both cases, the amorphous fraction is here related as possible amorphous, refinement miss-fittings due to low-ordered crystalline phases and/or any minor unknown crystalline phases possibly not determined within the background.

Table 2 Phases and their respective ICSD codes used for the Rietveld refinements.

Phase	Chemical Formula	Space group	ICSD code	Authors
Anatase	TiO_2	$I4_1/amd$	92363	(Weirich et al., 2000)
Anhydrite	$CaSO_4$	Cmcm	16382	(Kirfel and Will, 1980)
Brownmillerite	$Ca_2(Al,Fe)_2O_5$	Ima2	9197	(Colville and Geller, 1971)
Calcium aluminate	$CaAl_2O_4$	$P12_1/c1$	260	(Hörkner and Müller-Buschbaum, 1976)
Ettringite	$Ca_6Al_2(SO_4)_3(OH)_{12}\cdot 26(H_2O)$	P31c	16045	(Moore and Taylor, 1970)
Flamite (α_H-C$_2$S)	$Ca_2(SiO_4)$	Pnma	81097	(Mumme et al., 1995)
Fluorite	CaF_2	Fm-3m	60368	(Batchelder and Simmons, 1964)
Gehlenite	$Ca_2Al(Al,Si)O_7$	P-421m	87144	(Louisnathan, 1971)
Gibbsite	$Al(OH)_3$	$P2_1$	6162	(Saalfeld and Wedde, 1974)
Goethite	$(Fe_{0.83}Al_{0.17})O(OH)$	Pnma	109411	(Li et al., 2006)
Hematite	Fe_2O_3	R-3c	82137	(Sadykov et al., 1996)
Hemicarboaluminate	$Ca_4Al_2(OH)_{12})OH(CO_3)_{0.5}\cdot 4(H_2O)$	R-3c	263124	(Runčevski et al., 2012)
Kaolinite	$Al_2Si_2O_5(OH)_4$	P1	63192	(Bish and Von Dreele, 1989)
Kuzelite	$Ca_4Al_2(OH)_{12}(SO_4)\cdot 6(H_2O)$	R-3	100138	(Allmann, 1977)
Larnite (β-C$_2$S)	$Ca_2(SiO_4)$	$P2_1/c$	39006	(Udagawa and Urabe, 1978)
Lime	CaO	Fm-3m	60704	(Jay and Andrews, 1946)
Fe-perovskite	$Ca(Ti_{0.75}Fe_{0.25})O_{2.88}$	Pnma	96683	(Dunyushkina and Gorbunov, 2002)
Quartz	SiO_2	$P3_121$	16331	(d'Amour et al., 1979)
Rutile	TiO_2	$P4_2nmn$	88626	(Gesenhues and Rentschler, 1999)
RP-Perovskite	$Ca_4(Ti_3O_{10})$	Pbca	86242	(Elcombe et al., 1991)
Shulamitite	$Ca_3Ti(Fe_{1.18}Al_{0.82})O_8$	Pmma	187749	(Sharygin et al., 2013)
Straetlingite	$Ca_2Al_2(SiO_2)(OH)_{10}\cdot 2.5(H_2O)$	R-3m	431951	(Santacruz et al., 2016)
Perovskite	$CaTiO_3$	Pm-3m	31865	(Barth, 1925)
Ternesite	$Ca_5(SiO_4)_2(SO_4)$	Pnma	85123	(Irran et al., 1997)
Ye'elimite	$Ca_4Al_6(SO_4)O_{12}$	Pcc2	237892	(Cuesta et al., 2013)
Ye'elimite	$Ca_4Al_6(SO_4)O_{12}$	I4-3m	9560	(Saalfeld and Depmeier, 1972)

RP-perovskite: Ruddlesden-Popper series perovskite.

In the internal standard method, a high-crystalline phase was mixed to the sample of interest and the difference of the added crystalline amount of the phase to the quantified by XRPD-Rietveld is normalised and accounted as the amorphous fraction. To minimise peak overlapping of the standard and the minerals present in the sample, fluorite was chosen as the internal standard for the amorphous quantification of the Belterra Clay samples, and rutile as the internal standard for the clinkers produced using the Belterra Clay from Círiaco pilot-mine.

The external standard method was later tested and chosen to quantify the amorphous contents in the hydrated cements and in the clinkers produced using the Belterra Clay sample from Branco pilot-mine and the bauxite washing clay sample. For the external standard method, rutile (Kronos 3025) was used as a high-crystalline standard and measured on the same day and under the same conditions and equipment setting of the studied samples. The crystallinity of rutile was measured as 94.4% ($\pm$0.9%) using high crystalline quartz (NIST 1878b) as a standard. The refined unit-cell parameters obtained for NIST 1878b quartz were: $a = 4.91388(5)$ Å; and $b = 5.405371(1)$ Å; values in agreement with the obtained by (Black et al., 2016).

The quantification of the amorphous contents using both independent methods was tested in the refinement of the clinker SD3-OP with low amorphous, and of the clinker SD3-OP-B with high amorphous contents. The quantified amorphous contents had a good agreement when using both internal and external methods, but with slightly higher amorphous contents quantified by the internal standard approach.

Table 3 Comparison of phase and amorphous Rietveld-quantification of the clinkers SD3-OP and the clinker SD3-OP-B obtained using the internal and external standard approaches. Std.: standard

Approach Phase / Sample	Internal Std. SD3-OP	External Std. SD3-OP	Internal Std. SD3-OP-B	External Std. SD3-OP-B
larnite	46.3	47.4	-	-
flamite	-	-	40.3	40.6
ye'elimite ort.	19.7	20.2	18.2	18.4
ye'elimite cub.	9.5	9.7	11.7	11.8
gehlenite	0.9	0.9	4.9	4.9
Fe-perovskite	2.4	2.4	4.1	3.1
ternesite	3.8	4.0	-	-
brownmillerite	12.4	12.7	2.4	2.4
anhydrite	2.4	2.4	2.1	2.1
amorphous	**2.6**	**0.3**	**16.4**	**16.2**

Accuracy of the Rietveld results

The verification of the Rietveld quantification was made with aid of the addition method (Figure 14) by adding successive amounts of 1%, 5%, and 10% of synthesised pure ettringite, larnite, ternesite and ye'elimite to the hydrated cement samples (Negrão and Pöllmann, 2020).
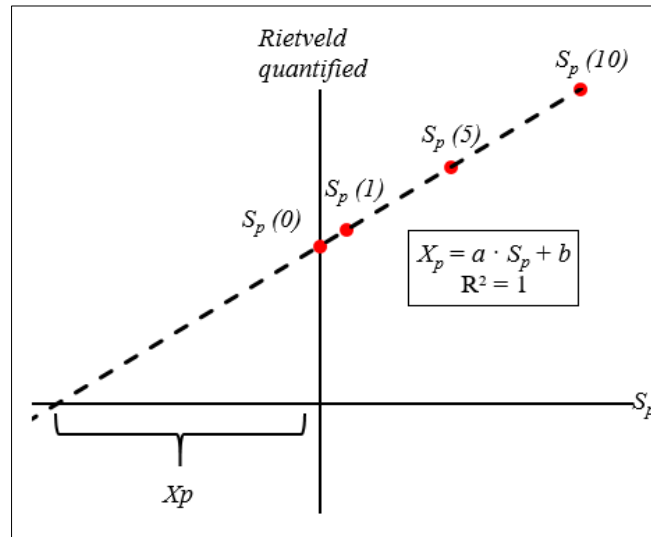
Figure 14 Graphical explanation of the addition method using the Rietveld quantification. The plot presents the Rietveld quantified results as a function of the known amount (Sp) of the added phase p (in this example 1, 5, and 10%). Sp = 0 corresponds to the original amount of the phase in the sample without addition. The calibration curve represents a linear function Xp = a * Sp + b, where Xp is the calibrated amount of the phase p in the original sample. In a perfect agreement ($R^2 = 1$), the amount of the phase in the original sample without addition (Sp = 0) is given as Xp = b. Source: Negrão and Pöllmann (2020).

The mixture additions were carefully homogenised using agate mortar and pestle, then measured and quantified using the Rietveld method in triplicate. The plot of the amount of added mineral phases *vs* its quantified contents by Rietveld resulted in regression lines that presented R>0.99%. The resulting linear equations of these plots permitted the calculation of the following confidence intervals of the Rietveld quantification for the tested phases: ±0.2% for ye'elimite; ±0.1% for larnite; ±1.1% for ternesite; and ±1.1% for ettringite (Negrão and Pöllmann, 2020). Considering the obtained accuracy of the method of roughly ±1%, no decimal places are given when reporting the phase contents in this work.

The Rietveld-derived chemistry of the Belterra Clay samples was calculated by stoichiometry from the quantified mineral contents, as in Figure 15. These results were later compared with the chemistry obtained by XRF to prove the Rietveld analysis and are presented in the results section.
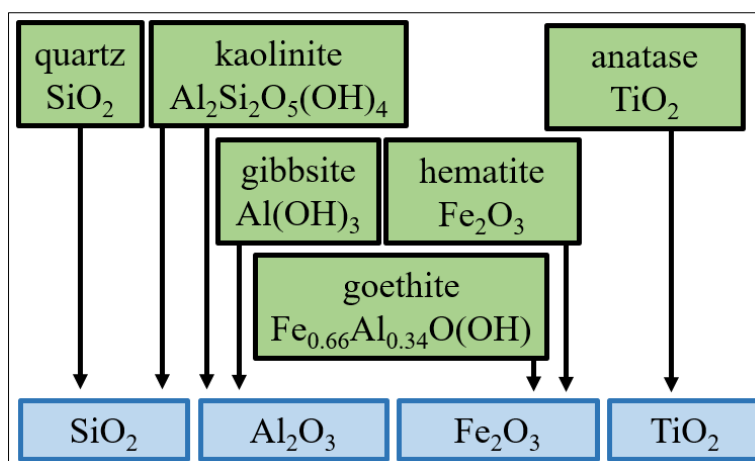
Figure 15 Flowchart showing the stoichiometric composition of the minerals in the Belterra Clay, used to calculate its chemical composition derived by the XRPD-Rietveld quantification.

2.2.2 X-ray Fluorescence spectroscopy

XRF was used to determine the chemical composition of the samples of Belterra Clay and bauxite washing clay. For the Belterra Clay samples, fused pearls were prepared by mixing 1 g of sample and 8 g of fusion agent ($Li_2B_4O_7$). The samples were measured in a Bruker SRS 3000 sequential spectrometer, calibrated with the SQ1-3 (SQ1, SQ2 and SQ3) standard kit and STG2 certified standard materials provided by Bruker. The loss on ignition (LOI) of the samples was determined after calcination at 1000 °C for one hour.

A sample of the bauxite washing clay was analogously prepared but measured in a Bruker S8 Tiger sequential spectrometer, calibrated with the Bruker GEO-QUANT Advanced reference kit.

Finally, to avoid SO_3 loss during fusion of the sample, approximately 8 g of the clinker BWC-3 was mixed with wax, pressed into a pellet, and measured in the Bruker S8 Tiger spectrometer. Both XRF spectrometers are located at the University of Halle.

2.2.3 Infrared spectroscopy

Fourier-transformed infrared (FTIR) spectroscopy was additionally used to probe the OH stretching bands of the minerals occurring in the Belterra Clay and assist their characterisation. Approximately 1 mg of dried sample and 160 mg of KBr were ground for homogenisation and

pressed into a disk shape. The transmission IR spectra were recorded between 370 and 4000 cm^{-1} at room temperature, with 4 cm^{-1} resolution, using a Bruker Tensor II TGA-IR spectrometer (Figure 16) at the University of Halle.

Figure 16 Bruker Tensor II TGA-IR spectrometer.

2.2.4 Scanning electron microscopy

The micromorphology of the clinkers and of their hydration products were investigated using a Jeol 640 Scanning Electron Microscope (SEM) in the University of Halle (Figure 17), and a Zeiss Gemini 300 field emission electron microscope equipped with a coupled energy dispersive X-ray spectrometer (EDS) located at the Zentrum für Werkstoffanalytik Lauf. Prior to analysis, the samples were heated to 35 °C for 24 hours and metallised with gold for the Jeol 640, and with carbon for the Gemini 300.

Figure 17 Jeol 640 Scan Electron microscope (A), and TM4000 Plus Hitachi Tabletop Scan Electron Microscope.

Backscattered electron and elemental mapping images from carbon-coated polished sections of clinker fragments were acquired at the University of Halle using a Hitachi Tabletop Scanning Electron Microscope model TM4000 Plus (Figure 17). The SEM is equipped with a High-Sensitivity 4-segment Backscatter detector and a Bruker Quantax75 EEDX detector.

2.2.5 Thermal analysis

2.2.5.1 Thermogravimetry and differential scanning calorimetry

The thermal characterisation of the bauxite residues, selected clinkers and hydrated cements were performed by thermogravimetric analysis (TGA) and differential scanning calorimetry (DSC) in a Netzsch STA 449 F3 Jupiter Thermo-analyser (Figure 18). Approximately 20 mg of sample was heated from 35 ℃ to 1000 ℃ in alumina crucibles under Ar-atmosphere with a heating rate of 10 K per minute.

Figure 18 Netzsch STA 449 F3 Jupiter thermo-analyser.

2.2.5.2 Isoperibolic calorimetry

Isoperibolic heat flow calorimetry was used to measure the enthalpies changes during the hydration of the clinkers, following the methodology of Kuzel and Pöllmann (1989). A calorimeter with a quadruplet arrangement composed of one reference and three measurement cells was used (Figure 19). The measurement cells were calibrated by placing a high-precision resistor of 10 kΩ and applying a voltage of 10 V.
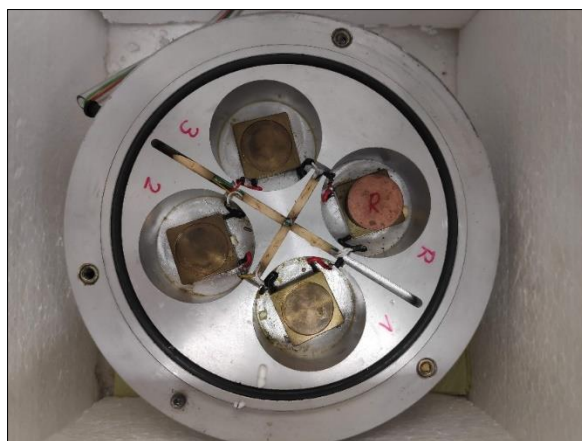
Figure 19 Isoperibolic calorimeter used in the analysis, composed by one reference cell (R) and three other measurements cells (1, 2 and 3).

Before the water injection and start of the analysis, the clinkers were placed in polythene pots and the distilled water was kept separately inside the calorimeter for 24 hours to adjust their temperature to the room temperature (23 ºC).

Initially, water was injected into the pots using water to cement ratio (w/c) of 1, to ensure the complete hydration of the phases and promote a general comparison of the hydration behaviour among the cements. The analysis was further conducted using a w/c ratio of 0.5, which showed no relevant differences in the hydration of the cement pastes when compared to that using a w/c = 1 within the investigated 72 hours.

After 72 hours, the hardened cement pastes were removed from the calorimeter and soaked in ethanol (99.9% grade) to stop the hydration. The hardened fragments were then disaggregated with an agate mortar and dried at 35 °C for approximately 8 hours. The dried powders were measured by XRPD, and the fragments were analysed by SEM-EDS.

The remained fragments were heated from 35 to 1000 °C and remained at this temperature for one extra hour. The resulting loss on ignition of the dried samples is attributed to the bonded water in the structure of the hydrated phases of the cement (Li et al., 2019), which permitted to determine the non-reacted (or free) water from the known water content added to the cement. The initial and known amount of water added to the cement minus the bonded water lost by LOI gives the non-reacted water.

2.2.6 ^{57}Fe Mössbauer spectroscopy

Mössbauer analyses of a pure Fe-perovskite were conducted in the Institute of Solid State Physics of the Technische Universität Wien by Professor Dr. Michael Reissner. The ^{57}Fe Mössbauer spectra were recorded at room temperature in transmission mode with constant acceleration with a 32 mCi ^{57}CoRh source, relative to which all centre shift (CS) data are given in Table 4. The velocity was calibrated by α-Fe foil, and the spectra were analysed by solving the full Hamiltonian, taking into account the thickness of the sample by using the Mørup-Both equations (Mørup and Both, 1975).

The Mössbauer fits were also performed by Professor Reissner. The measured spectra were fitted by three and four sub-spectra, according to Fe in tetrahedral (CN4), octahedral (CN6) and penta-coordinated (CN5) positions, as well as for possible Fe^{4+} atoms. Hyperfine parameters were hold in the range reported in the literature for the different Fe-sites obtained from $Ca(Fe,Ti)O_3$ perovskites and a Ruddlesden-Popper perovskite (n=2) (McCammon et al., 2000; Waerenborgh et al., 2001; Figueiredo et al., 2003) (Table 4).

Table 4 Expected range of centre shift (CS relative to CoRh) and quadrupole splitting (QS = eQVzz/4) according to McCammon et al. (2000), Waerenborgh et al. (2001) and Figueiredo et al. (2003).

	CN4 Fe^{3+}		CN5 Fe^{3+}		CN6 Fe^{3+}		Fe^{4+}	
	min	max	min	Max	min	max	min	max
CS (mm/s)	0.05	0.09	0.12	0.20	0.21	0.25	-0.13	-0.15
QS (mm/s)	0.70	0.80	0.47	0.53	0.17	0.28	~0.25	

2.3 Experimental methods

2.3.1 Clinker production using design of experiments

Design of Experiments (DoE) was used to reduce the number of experimental trials to produce the CSA-based clinkers using Belterra Clay. The main advantage of using DoE in the formulation of new clinker raw meals, made using a non-traditional raw material, is that the statistical designs deal with variable parameters by calculating all observations (outputs) and trends with minimal experimental work (Antony, 2003).

The traditional stoichiometric Bogue calculations (Taylor, 1989), mainly used to predict clinker phases in OPC, is tricky when applied to CSA as it considers the phase assemblage C-C_2S-C_2A,F-C_4A_3s-Cs (Majling et al., 1999). The other possible phases common in CSA (i.e., ternesite, gehlenite and perovskite) are neglected. Moreover, the calculations do not account for solid solutions (Stutzman et al., 2014).

In the DoE calculations, the influence of individual and combined factors is computed to predict a maximum or a minimum performance of a target result. Here, the factors used in the DoE were the raw materials used in the meal, the different tested firing temperatures, and the time of synthesis. The response variable (target) was the clinker phases ye'elimite set to be maximised (Figure 20).
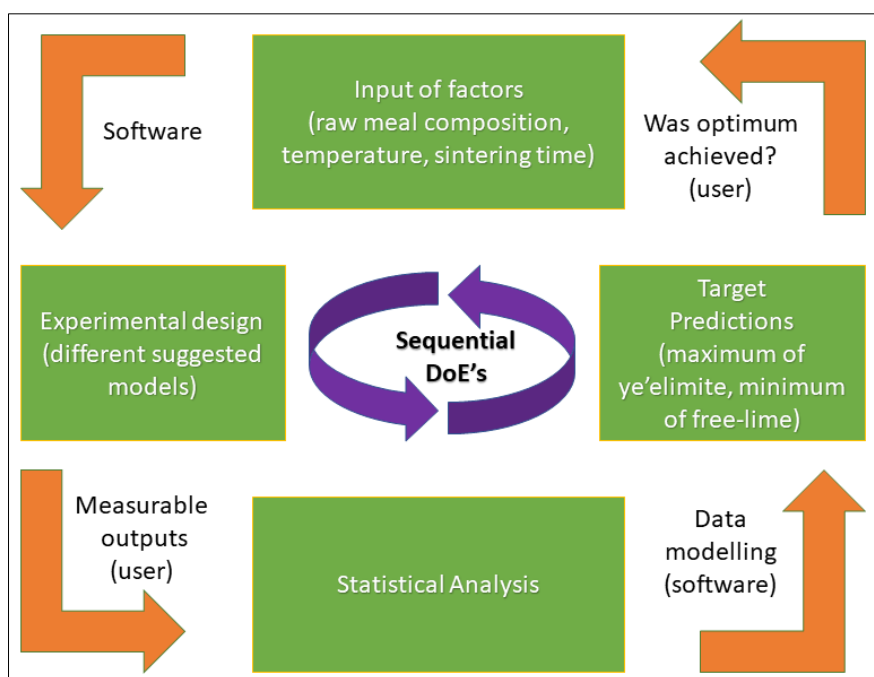
Figure 20 Flow chart showing the steps of the used sequential Design of Experiments.

The software STAVEX, from AICOS Technologies, works with three successive design stages: screening; modelling (linear model) and optimisation (quadratic model) (Seewald and Grize, 1997). The successive stages claim to reduce the number of factors that influence the response variable, identifying an optimum after the last step.

Three Statistical designs of experiments (SD1, SD2, and SD3) were performed using different Belterra Clay samples. SD1 and SD2 were performed using the Belterra Clay sample from the Críaco pilot-mine, whereas SD3 was using Belterra Clay from Branco pilot-mine.

SD1 was set using a linear Vertex-Centroid Design with interactions. The raw material components (i.e., factors) were mixed in the following varying proportions: 30 to 60% of Belterra Clay; 30 to 60% of $CaCO_3$; and 6.5 to 13% of $CaSO_4 \cdot 2H_2O$, at 1100 °C and 1250 °C firing temperatures, and 1 or 2 hours of synthesis. The first statistical design was composed of 16 experiments. After the evaluation of SD1, the second design (SD2) was created by reducing the mixture range of the components to 35 – 45% of Belterra Clay, 40 – 50% of $CaCO_3$, and 8 – 15% of $CaSO_4 \cdot 2H_2O$, at 1200 °C, 1250 °C and 1300 °C, and fixed 1-hour clinkering time. The second statistical design (SD2) resulted in 14 experiments and a software-suggested optimum (SD2-OP).

SD3 was also defined using a Vertex-Centroid Design, with the following variation in the raw materials mixture: 30 to 60% of Belterra Clay, 30 to 60% of $CaCO_3$, and 6.5 to 13% of $CaSO_4 \cdot 2H_2O$. The software-suggested mixtures were produced at 1200 °C and 1250 °C for 1 hour according to the experimental plan SD3, and then the clinkering temperature of 1300 °C was tested for selected compositions. A total of thirteen clinkers were produced using the SD3 DoE, and were named as SD3-1, -2, -3, (…), -13. After the clinkers were evaluated, a user-defined optimal composition (SD3-OP) was defined and synthesised at 1250 °C and 1300 °C. SD1, SD2, and SD3 raw mixtures and clinkering conditions are displayed with their related phase contents, in tables 7 (SD1), 8 (SD2) and 9 (SD3) in the Results section.

2.3.2 Clinker production after stoichiometric calculations

The stoichiometric computation on the flowchart of Figure 21 was used to define the raw meal composition of stoichiometric modelled (SM) clinkers. The solid solutions that commonly occur in ye'elimite (with Fe), belite (Fe), ferrite (Al) and perovskite (Fe, Al) were not considered in these calculations. Before the computations, the chemical composition of the raw materials

(calcium carbonate, gypsum and Belterra Clay or bauxite washing clay), were normalised after discounting their LOI. The stoichiometric modelled clinker produced out of Belterra Clay from the Branco pilot-mine was named BRA-SM, and the one produced with the bauxite washing clay was named BWC-SM.

To produce a clinker using as much as possible of bauxite residue (Belterra Clay or bauxite washing clay) with a maximum of ye'elimite, all Al_2O_3 was addressed to form ye'elimite in the calculations. After that, the required amount of sulfate to form ye'elimite was calculated as calcium sulfate and added as gypsum. All Fe_2O_3 from Belterra Clay was computed to form ferrite (C_2F), all SiO_2 to belite (C_2S) and all the TiO_2 to perovskite (CT). The required amount CaO to stoichiometric balance the compositions were added as $CaCO_3$. The adapted Bogue calculations do not provide true contents of the four considered phases (ye'elimite, belite, ferrite and perovskite), as these contents are expected to diverge from the calculated phase proportions due to the compositional variations of each phase caused by possible solid solutions.
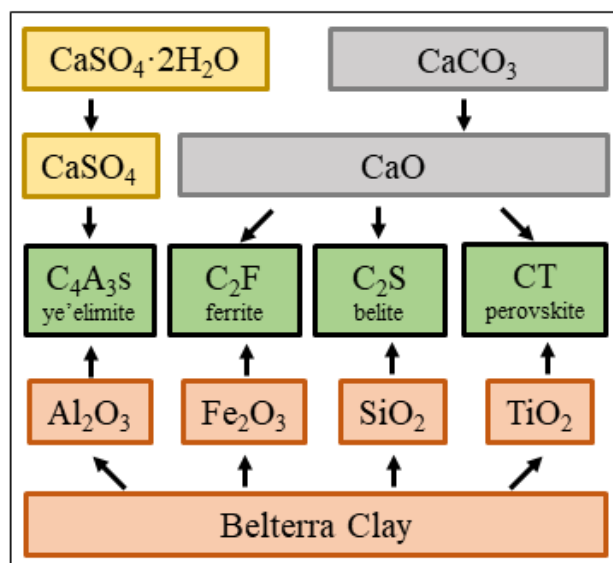
Figure 21 Flowchart of the stoichiometric calculations to produce the clinkers BRA-SM and BWC-SM.

2.3.3   Clinker preparation

The raw mixtures were weighted according to the experimental plans defined by DoE, or the stoichiometry modelling, and manually homogenised using agate mortar and pestle. Approximately 7 g of the mixed raw materials were placed in alumina crucibles and calcined in a programmable electric muffle furnace (Carbolite RHF 15/3). The firing started under

atmospheric conditions and room temperature (approximately 23 °C), until the furnace meets the experiment-planed temperature of 1100 °C, 1200 °C, 1250 °C, or 1300 °C for an extra 1 or 2 hours, depending on the defined experimental conditions. A heating rate of 10 °C per minute was used.

After firing, the alumina crucibles with the clinkers were removed from the furnace and air-cooled at room temperature (Figure 22). The clinkers were then carefully crushed and ground with an agate mortar for their characterisation. Crushed fragments were used for SEM analysis. Additionally, selected clinkers were prepared as pressed pellets, using 2.5 kN in 1 cm-diameter pellets, to obtain polished sections for SEM studies.

Figure 22 Clinkers in alumina crucibles during the cooling process after firing at 1250 °C for 1 hour.

The preparation of some selected clinkers was 10 times up scaled, to produce approximately 60 g of clinker. For that, the raw mixtures of selected clinkers were weighted, homogenised by hand, and using a RETSCH R100 vibrating disc (agate) mill for 2 minutes. The produced clinkers were then milled in a vibrating disc mill for approximately 5 minutes until they have similar fineness.

2.3.4   Stabilisation of $\alpha_{H'}$-belite polymorph

β-C_2S (e.g., larnite) is often described to have a slow hydraulic reactiveness in cements. To stabilise the more reactive $\alpha_{H'}$-C_2S (e.g. flamite mineral analogue), boron is used as a dopant. (Martín-Sedeño et al., 2010; Li et al., 2019) reported molar ratios of 0.1 – 0.2 of B to 1 of belite used in clinkers with similar composition, with 0.1 B considered enough to stabilise larnite into

flamite. Similarly, Cuberos et al. (2010) used 0.35 to 0.61 % of B to stabilise such phase in similar clinkers, attesting that only the higher B concentration converted all larnite into flamite. To ensure the stabilisation of all belite into its $\alpha_{H'}$ polymorph flamite a ratio of 0.2 mol B to 1 mol of belite was used in the clinker SD3-OP, which corresponded to an addition of 0.56% of B (as H_3BO_3) in the raw mixtures. The B-doped clinker was named SD3-OP-B, and its mineralogical composition, hydration behaviour and early strength development were further compared to its equivalent non-doped clinker SD3-OP synthesised without boron.

2.3.5 Synthesis of pure phases

Brownmillerite [$Ca_4Al_2Fe_2O_{10}$], perovskite [$CaTiO_3$], and Fe-perovskite [$Ca(Ti_{0.5},Fe_{0.25})O_{2.37}$] were synthesised as pure phases for special investigations. Brownmillerite and perovskite were used to test the stability of ternary mixtures with other main CSA-based clinker phases. The synthesised Fe-perovskite corresponds to the average compositions of this phase obtained in the produced clinkers by SEM-EDS.

For the synthesis of these pure phases, the chemical reagents were calcined and weighted according to the stoichiometric composition of each phase to obtain 3 g of sample. The powders were homogenised by hand in an agate mortar and then in a RETSCH R100 vibrating agate disc mill for extra 5 minutes. The homogenised powders were pressed (2.5 kN) to 1 cm-diameter pellets.

The pressed pellets of brownmillerite and perovskite were then synthesised at 1250 °C for 24 h and quenched in water. Two samples of Fe-perovskite were synthesised with different cooling methodologies. The first one, named sample P-AQ, was synthesised at 1300 °C for 24 h and air-cooled at room temperature to reproduce the same cooling conditions used in the production of the clinkers, and the second one was rapidly quenched in water and named P-WQ-500.

2.3.6 Ternary mixtures of synthesised pure phases

To better understand the stability of the main clinker-phases in the presence of perovskite and brownmillerite, pure clinker-phases were manually mixed and fired at 1250 ºC and 1300 ºC. For that, the following ternary mixtures were prepared using 1:1:1 ratios of ye'elimite-brownmillerite-perovskite (YBP sample), ternesite-brownmillerite-perovskite (TBP sample),

and larnite-brownmillerite-perovskite (LBP sample). The preparation of the mixtures consisted of the homogenisation of the pure synthesised phases in a RETSCH R100 vibrating agate disc mill for 6 minutes and pressing (2.5 kN) the homogenised powders into 1 cm-diameter pellets. The pellets were quenched in water after firing at 1250 and 1300 ºC for one hour. The resulting materials were partially crushed into small fragments for SEM studies and ground to powder for XRPD analysis.

2.3.7 Properties of the produced cements

2.3.7.1 Calculation of process-related CO_2 emissions

According to Shen et al. (2014), CO_2 emissions from the cement industry are usually divided into raw-material related (RM, also called process-related) CO_2 emissions that accounts for the CO_2 produced from the calcination of the raw materials (mainly limestone), combustion-related emissions that are the emissions from the burning of the fossil fuels used to heat the kilns (coal, petroleum coke, natural gas, etc.), and electricity-related emissions that arises from the production of the electric energy used for motors, fans and blowers for whirling a kiln, drying, heating and grinding of the clinkers and materials.

The RM-CO_2 emissions are the amount of CO_2 arising from the raw meal calcination to produce one ton of clinker. In the clinkers produced in this work, all the CO_2 is generated by the calcination of $CaCO_3$, according to Equation 2.1:

$$CaCO_3 \rightarrow CaO + CO_2 \uparrow \text{ (Equation 2.1)}$$

Each mole of CaO derived from calcium carbonate (CaO_{Cc}) in the clinker emits one mole of CO_2. Consequently, RM-CO_2 can be obtained as in Equation 2.2:

$$RM\text{-}CO_2 = CaO_{Cc} * (44.01 \text{ g/mole } CO_2 / 56.08 \text{ g/mole CaO}) \text{ (Equation 2.2)}$$

$$RM\text{-}CO_2 = CaO_{Cc} * 0.785 \text{ (Equation 2.2)}$$

To compare the RM-CO_2 emissions of the clinkers produced in this work to the RM-CO_2 of OPC, the Intergovernmental Panel on Climate Change (IPCC) default value of 64.4% of CaO in OPC is used (Gibbs et al., 2002). The OPC RM-CO_2 correspond to 507 Kg of CO_2 released per tonne of produced OPC clinker. The energy-related emissions (combustion- and electricity-related) are not addressed in this work, as they depend on complex technical aspects of the cement plant and the source of the energy (e.g., fossil fuel or hydro-electrical).

2.3.7.2 Density determination

The densities of the clinker powders were calculated and determined with a pycnometer. Firstly, the calculation after XRPD-Rietveld results was made considering the theoretical density of the quantified phases and normalising their compositions to 100% when amorphous was present. The density was further determined using a pycnometer (5 ml) with alcohol ethyl. The average of these results, which were very similar, were used to calculate the fineness of the clinkers and the water demand of the cements as described ahead.

2.3.7.3 Fineness after Blaine

The cement fineness is normally expressed as its specific surface, or the total surface area of all the cement in a determined mass of cement. The Blaine fineness, after DIN EN 196-6, is an indirect determination of the specific surface area of the cement, by comparison with the reference material. The method is based on the principle of air permeability, by measuring the time a fixed quantity of air takes to flow through a compacted cement bed of known density and volume.

The Blaine method was conducted in triplicate for selected clinkers, using a Blaine apparatus Toni Technik at 23 °C room temperature. The previously mentioned average density of the powders was used in the calculations. Because the method is comparative rather than absolute, a reference sample of quartz sand with known specific surface area was used to calibrate the Blaine apparatus.

2.3.7.4 Water demand determination

The water demand of cement is the amount of water necessary to produce a cement paste of standard consistency (Popovics, 1980). To avoid bleeding of the cement paste caused by excess of water, the water demand, and consequent the water/cement ratio, were calculated for the cement powders to produce the cement mortars used in the compressive strength tests.

According to Puntke (2002), the necessary mass of water (m_w) to fill all the voids and saturate a cement powder can be calculated by the total used volume of water, considering the water density = 1.0 g/cm^3. The water demand, or the necessary water to fill all the pores (n_{water} in Equation 2.3), is computed using the density (d_{cement}) and the mass (m_{cement}) of the cement powder as follows:

$$n_w = m_w / (m_{cement} + d_{cement}) + m_w \text{ (Equation 2.3)}$$

To calculate the water demand of the cements, the Puntke method (Puntke, 2002) was adapted to use 5 g of sample instead of 50 g. A 20 ml beaker was filled with 5 g of cement weighted with ±0.0002 precision. Distilled water was slowly and carefully pipetted into the beaker with successive gently knocking the bottom of the beaker on a flat surface from approximately 5 cm height to homogenise the mixture and ensure the water enters all powder voids. The pipetting was stopped after the surface of the powder appeared shining. The measurements were performed in triplicate.

2.3.7.5 Compressive strength tests of mortars

To produce the cement mortars, selected clinkers were mixed with gypsum using a mass ratio of 95:5 and with distilled water (w/c = 0.3). The 0.3 w/c ratios were chosen after the water demand determination using the Puntke method. This amount of water was calculated as sufficient to convert all ye'elimite into ettringite when only 5% of gypsum was used as cement additive.

Later, four mortars were produced using a finer clinker (BWC-3) made with the bauxite washing clay. This clinker was mixed with different gypsum amounts (5%, 10%, 15% and 25%) to produce the BWC-3 cement mortars 95:5, 90:10, 85:15 and 75:25, following their clinker to gypsum ratios. The added higher ye'elimite amount in these compositions combined with the higher gypsum contents should react to produce more ettringite, consuming more water than in

the previous experiments. Therefore, to avoid a lack of water on the surface of the mortars and compensate for the higher fineness of this cement, an increased w/c = 0.45 was used in these tests.

Considering the limited amount of material, all the compressive strength tests were performed adapted to a lab-scale, similar to Li et al. (2019). The cement pastes were filled into 20 x 20 x 20 mm^3 casts, wrapped with plastic film to keep the relative humidity close to 99% and cured at 23 °C for 24 h. After that, the cubic specimens (Figure 23) were removed from the casts and kept in distilled water baths until testing. The compressive strength of the mortars was measured at 7 and 28 days using a STRASSENTEST (Baustoff-Prüfsysteme) testing machine, with a loading speed of 2.5 kN/s. The presented values are an average of two tests. For the sake of comparison, the same procedure was done using a commercial Portland cement class CEM I 42.5 R (DIN EN 197).
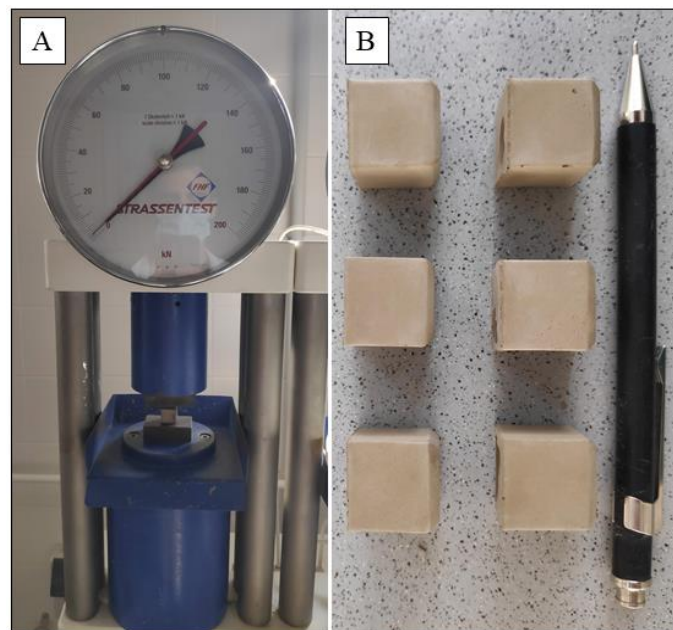
Figure 23 Compressive strength testing machine (A), and cement mortars (B).

After testing, the outer surfaces of the specimens were discarded, and the remaining pieces were soaked into alcohol ethyl (99% pure) to replace water and stop the hydration. The pieces were then dried at 35 °C for 24 h. Part of the pieces were kept for SEM analysis, and parts were manually ground with agate mortar to powder for XRPD analysis, for the non-evaporable water determination, and thermal analysis.

3 Results - Characterisation of the raw materials

3.1   **Belterra Clay characterisation**

The main results of the Belterra Clay samples characterization were published in (Negrão et al., 2021a). The material have a very fine particle size with clay aggregates showing the predominance of the silt grain size (Negrão et al., 2018a). The clay has yellowish-brown (ochreous) colours in the first meters of the sequences, and reddish-brown colours towards its base (close to 10 m depth). No sedimentary structures are observed in the geological profile where Belterra Clay is exposed, except for some abrupt changes in the contact of Belterra Clay and the underneath part of the lateritic bauxitic profile. At this portion, Belterra Clay is in contact with either some nodules of bauxite (also known as "popcorn bauxite") and with ferruginous nodules. Both the bauxitic and the ferruginous nodules also occur within the bottom-most portion of Belterra Clay (Figure 24), turning it richer in Fe_2O_3 and Al_2O_3.

Figure 24 Belterra Clay exposed in Rondon do Pará with the general view of the Círiaco pilot-mine sampling site (A), showing the abrupt contact of the Belterra Clay with ferruginous nodules (B) and with bauxitic nodules (C).

3.1.1 Mineralogy by XRPD

Statistical Principal Component Analysis (PCA) of the XRPD patterns of Belterra Clay samples from Rondon do Pará (Brazil) was carried out to classify similar samples and to choose which samples were going to be used in the experimental plans to produce clinkers. For that, the samples from three different pilot-mines were sorted into three groups using the PCA analysis (Figure 25).

In the first group (green sphere) are the samples BRA0.5m, BRA5.0m and BRA13m from the Branco (BRA) pilot-mine, and the samples DEC0.8m, DEC7.2m and DEC10m from the Décio (DEC) pilot-mine. The samples CIR0.5m, CIR5.0m and CIR7.5m from the Círiaco pilot-mine are in group 2 (blue sphere). Finally, the samples CIR10m and CIR14m form group 3 (grey sphere) (Negrão et al., 2021a).
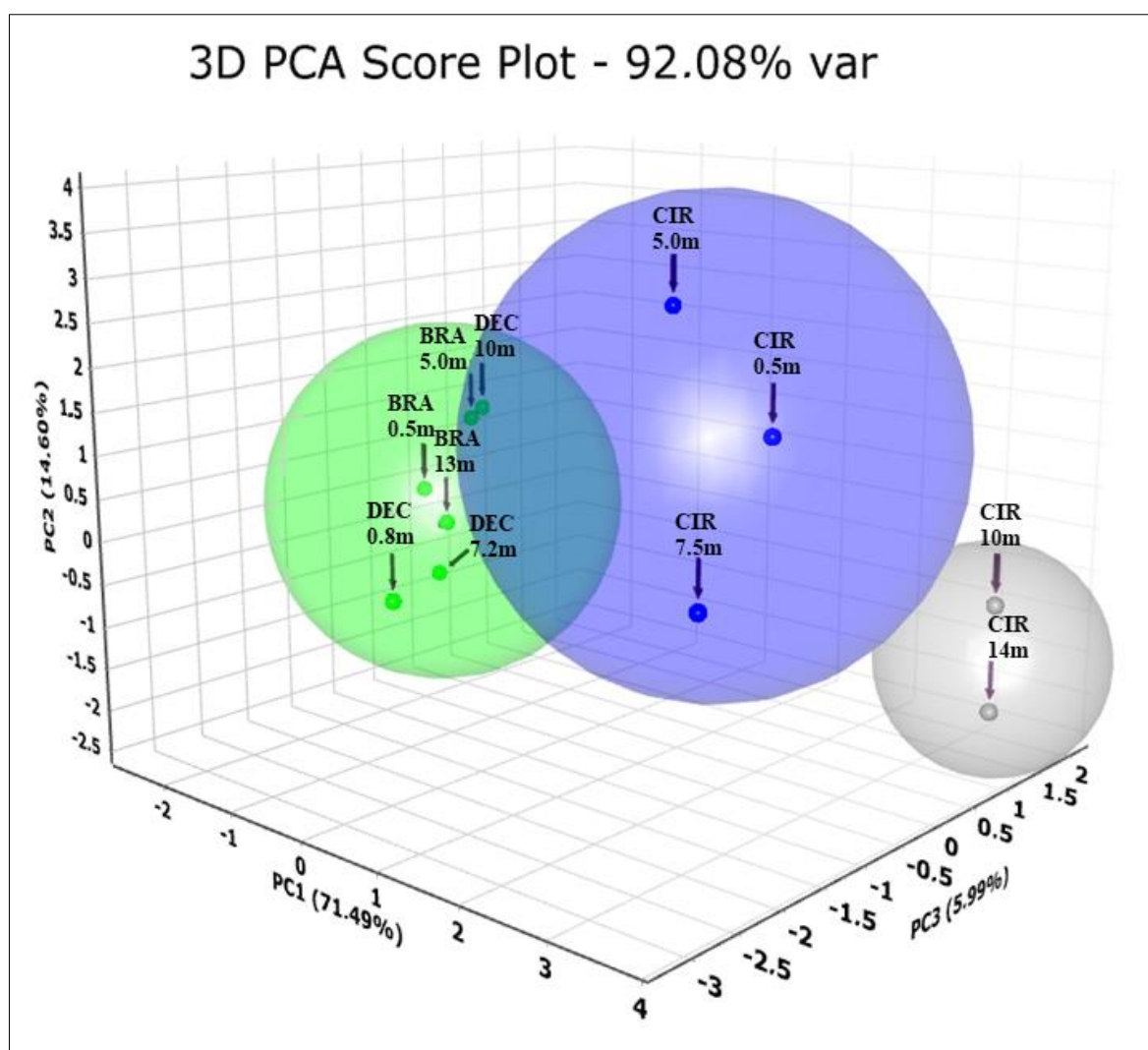
Figure 25 Principal Component Analysis (PCA) of the Belterra Clay samples from Rondon do Para. Source: Negrão et al. (2021a), licensed under CC BY 4.0 https://creativecommons.org/licenses/by/4.0/.

Kaolinite, gibbsite, goethite, hematite, anatase and quartz (Figure 26) compose the mineralogical assemblage of the samples. Quartz occurs occasionally in some samples, and hematite is restricted to the Belterra Clay samples of the bottom of the sequence. The distinctiveness of their XRPD patterns permitted sorting them into three different groups. For group 1, the samples BRA0.5m and BRA13m were chosen as representative, whereas the sample CIR 0.5m was selected for group 2, and sample CIR 14m for group 3.
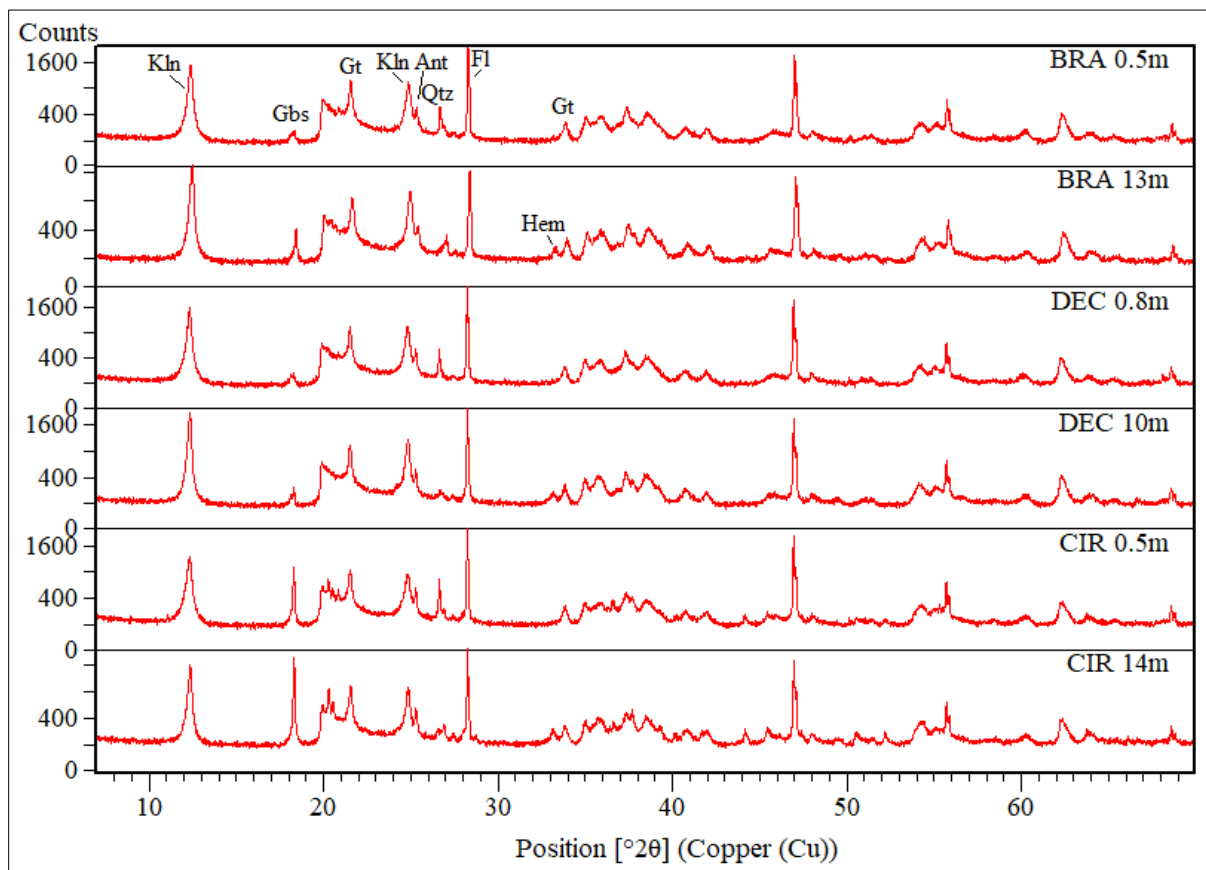
Figure 26 XRPD patterns of the Belterra Clay samples from the top and bottom of the Belterra Clay packages in the pilot-mines Branco (BRA), Décio (DEC) and Círiaco (CIR).

The selected representative samples were used for the Rietveld refinements. The phase quantification shows that kaolinite is the main mineral (Figure 27), representing at least 60% (sample CIR 14m) and up to 77% (BRA0.5m) of the samples. Goethite has only a slight variation from 15 to 16% in the samples. Gibbsite, on the other hand, varies from 3% (BRA 0.5m) to up to 19% (CIR 14m), with higher contents in the samples of the Círiaco pilot-mine. Up to 2% of hematite is present, but this mineral is restricted to the deepest samples, whereas those close to the surface (0.5 m) have no hematite. Anatase varies slightly around 2% in all samples. Quartz occurs as sparse grains in some of the samples, representing up to 3%.
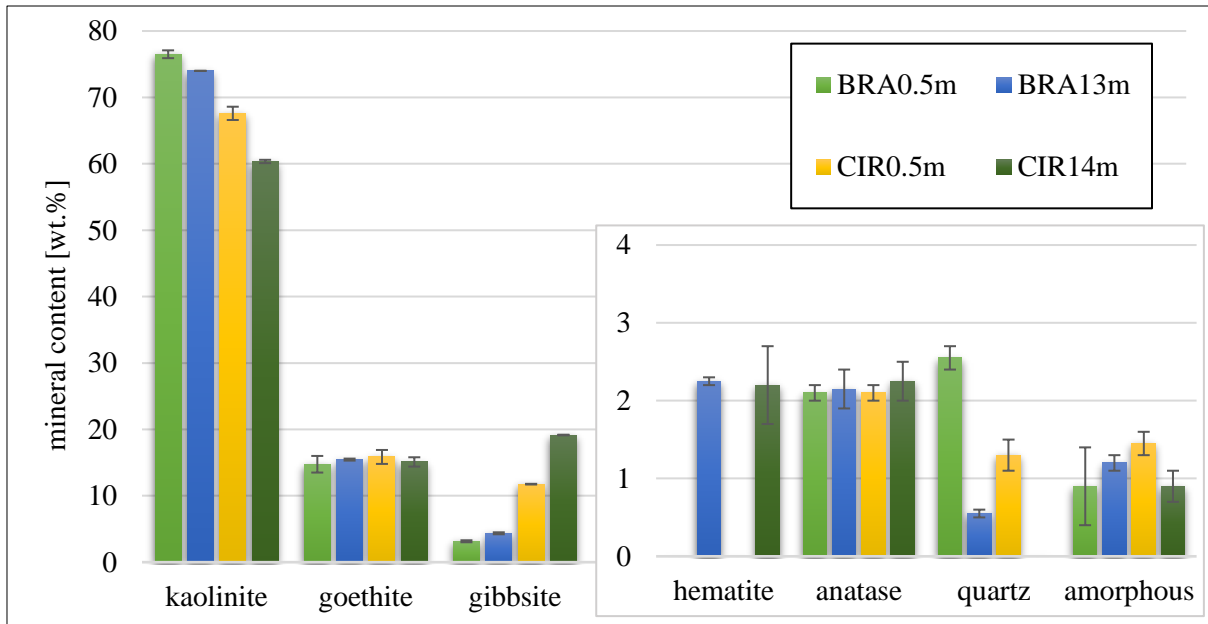
Figure 27 Mineral and amorphous contents of the Belterra Clay samples, after the XRPD-Rietveld quantification. Source: Negrão et al. (2021a).

The Rietveld refinements have obvious miss-fittings in the 19.6 – 26° 2θ (4.5 – 3.4 Å) and 34.5 – 37° 2θ (2.6 – 2.4 Å) regions (Figure 28), that are related to the calculated profile of kaolinite. Similar anomalous XRPD patterns of kaolinites have been observed for this mineral occurring not only in Belterra Clays, but also in lateritic materials including bauxites, and are attributed to disorder in the structure of kaolinite (Paz et al., 2017; Negrão et al., 2018b).
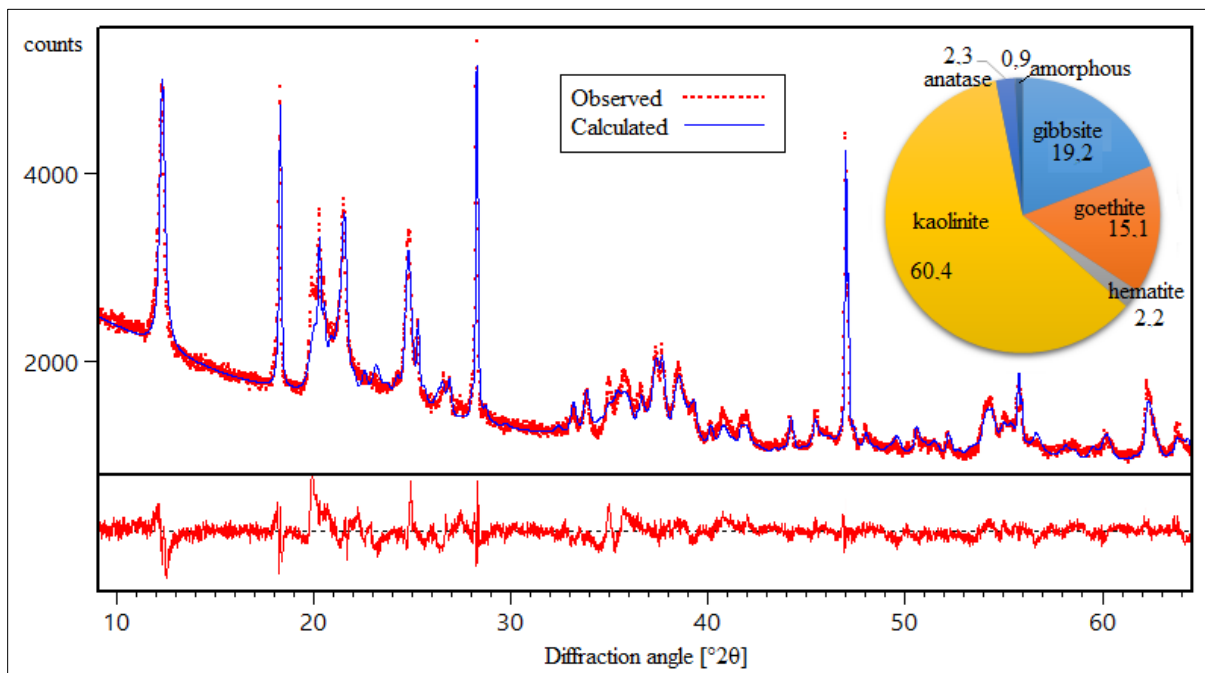
Figure 28 Rietveld-refined XRPD and its difference plot of the sample CIR 14m. GOF = 1.6 and Rwp = 5.5. Source: Negrão et al. (2021a), licensed under CC BY 4.0 https://creativecommons.org/licenses/by/4.0/.

According to Ufer et al. (2015), the structural disorder in kaolinite is mainly caused by faults in the stacking of its layers. The crystal structure of kaolinite consists of a silica tetrahedral layer and an alumina octahedral layer. The octahedral layer has three possible octahedral sites, and one of them (i.e., B or C) is unoccupied (Figure 29). Ordered kaolinites have successive B octahedral layer stacking, whereas disordered kaolinites contain not only the regular B stacking but also alternating B and C stacking due to vacancy displacements (Ufer et al., 2015). Regular B-C stacking is characteristic of dickite, also an $Al_2SiO_5(OH)_4$ polymorph.
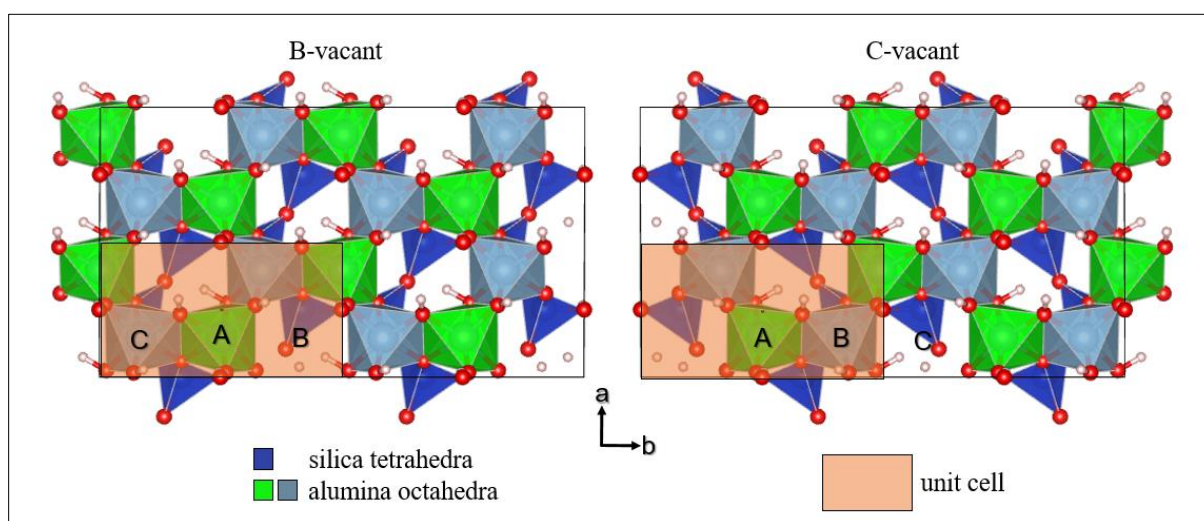
Figure 29 Layer types of kaolinite. B-vacant octahedra layer (left), and C-vacant octahedra layer (right). The alumina octahedra have different colours for better visualisation.

For comparison, the XRPD of sample CIR 14m was additionally refined with the software PROFEX (Figure 30) using a model of disordered kaolinite, which accounts for some of the stacking defects in the structure of kaolinite. The resulting calculated pattern has a much better fitting when using the disordered kaolinite, whereas the results of the phase quantification are in general similar to the refinement made using ordered kaolinite. The exception is for the slightly different amorphous amounts in both refinements. Nevertheless, refining using the model was much more time consuming and unstable.

In the attempt to better understand the nature of defects in natural kaolinites and their influence on the XRPD pattern, Leonardi and Bish (2020) simulated diverse XRPD patterns of kaolinites with different layer-stacking defects. According to the authors, the $00l$ reflections of kaolinite are affected by the amount of layers in the crystal structure, whereas the hkl reflections are mainly influenced by the quantity and nature of stacking defects, including the stacking distance, the lateral identitation, the structure misorientation and shifts in the structure. The

work brings a much better understanding on stacking defects of low ordered kaolinites. Nevertheless, such complex profile simulations still require the use of supercomputers.
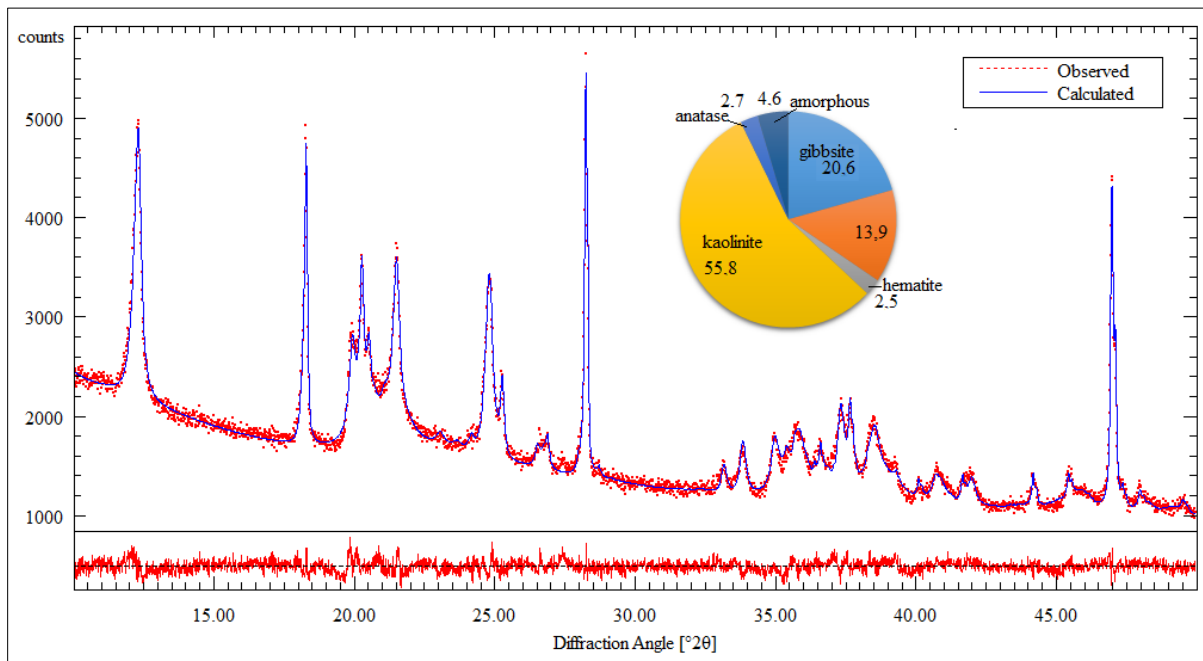
Figure 30 Rietveld-refined XRPD, and its difference plot, of the sample CIR 14m using a model of disordered kaolinite with the software PROFEX-BGMN. GOF = 1.3 and Rwp = 3.2. Source: Negrão et al. (2021a), licensed under CC BY 4.0 https://creativecommons.org/licenses/by/4.0/.

The quality of the Rietveld refinements was proved using the addition method. For that, successive amounts (of 1%, 5% and 10%) of hematite and gibbsite were added, respectively, to the samples BRA13m and BRA0.5m. The plotted results show a good correlation line (R^2>0.99) for both samples, and the obtained linear functions allow to calculate the calibrated amount of these phases in the samples when x=0 (Figure 31).
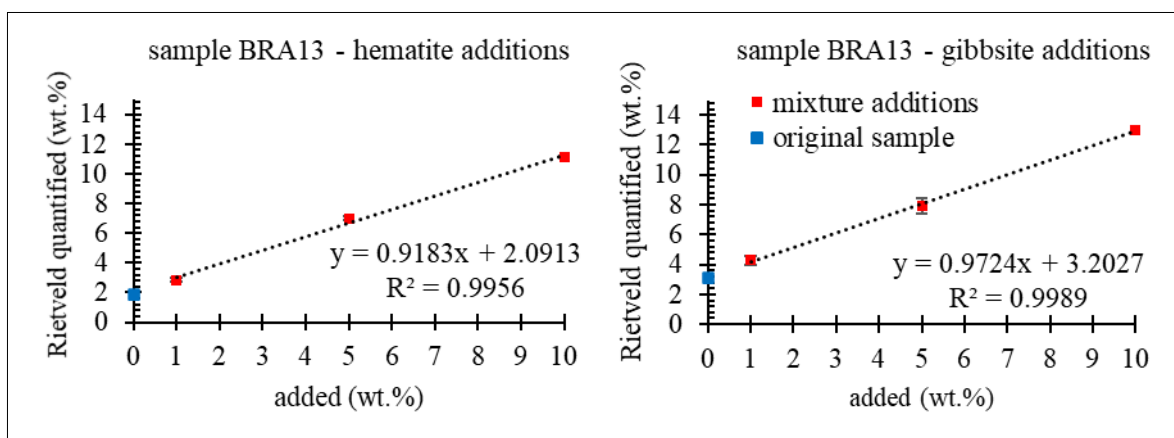
Figure 31 Results of the Rietveld-quantifications of the mixture additions plotted against the added values and the derived linear functions. Source: Negrão et al. (2021a).

According to the equations (Figure 31), 3.15% of gibbsite is present in the sample BRA05m, and 1.99% of hematite is in the sample BRA13m. These values are very close to the 3.10% (gibbsite) and 2.20% (hematite) quantified in the samples without additions (Figure 27). Nevertheless, the quantification results of the sample with the addition of 5% of gibbsite showed a larger standard deviation. This is attributed to the preferred orientation of the (*00l*) planes of gibbsite, which often result in very intense peaks that cannot be completely solved with the March-Dollase function for preferred orientation used in the Rietveld refinements.

3.1.2   Chemical composition

The chemical composition of the Belterra Clay samples, as determined by XRF, is dominated by silica, alumina, iron oxide and titanium oxide, with minor amounts of MnO, CaO and K_2O (Table 5). The loss on ignition varies from 14.86% in the sample from the Branco pilot-mine to 17.64% in the sample of the Círiaco pilot-mine.

The chemistry by XRF confirms the mineralogical composition of the samples. The higher alumina contents in the samples from the Círiaco pilot-mine are associated with the higher amounts of gibbsite, whereas the lower silica contents are due to the lesser kaolinite amounts in this sample. That is, kaolinite and gibbsite contents of the samples control the main differences in their chemical compositions in respect to silica, alumina, and the loss on ignition.

Table 5 Chemical composition (by XRF) of the Belterra Clay samples.

Sample	BRA0.5m	BRA13m	CIR0.5m	CIR14m
SiO_2	36.81	35.66	32.49	28.88
Al_2O_3	34.97	35.58	37.6	39.76
Fe_2O_3	10.58	11.27	10.47	11.12
TiO_2	1.78	2.17	1.9	2.17
MnO	0.03	0.03	-	0.03
CaO	0.03	-	0.04	-
K_2O	0.04	0.03	0.04	-
LOI	15.39	14.86	17.13	17.64
Total	99.63	99.6	99.67	99.6

The iron oxide and titanium oxide contents are slightly higher in the deeper samples (BRA13m and CIR14m). The higher iron amounts are related to hematite, which is absent in the samples close to the surface after the mineralogical analysis. The higher TiO_2 contents might correspond to some traces of zircon in the deepest samples (Truckenbrodt et al., 1991; Kotschoubey et al., 2005). However, if present, this mineral is in very low amounts, which could not be reached by the XRPD analysis.

The chemical composition determined by XRF and the LOI of the samples is compared with their chemical data obtained stoichiometric after the Rietveld quantification (Figure 32). The plotted data resulted in linear regression lines with a very good correlation ($R^2 > 0.9$) for Al_2O_3, SiO_2, Fe_2O_3 and LOI. For visualisation, if Al-free goethite were used for the stoichiometric calculations, the correlation would be much poorer, with an $R^2 = 0.8334$. The worst correlation is observed for TiO_2 ($R^2 = 0.6297$), which is influenced by the quantified anatase contents by the Rietveld refinement and is within the expected errors inherent to the Rietveld refinement (Bish and Howard, 1988). Moreover, TiO_2 present the lowest values, wherein even slight variations of it affect the correlation line more intensely.
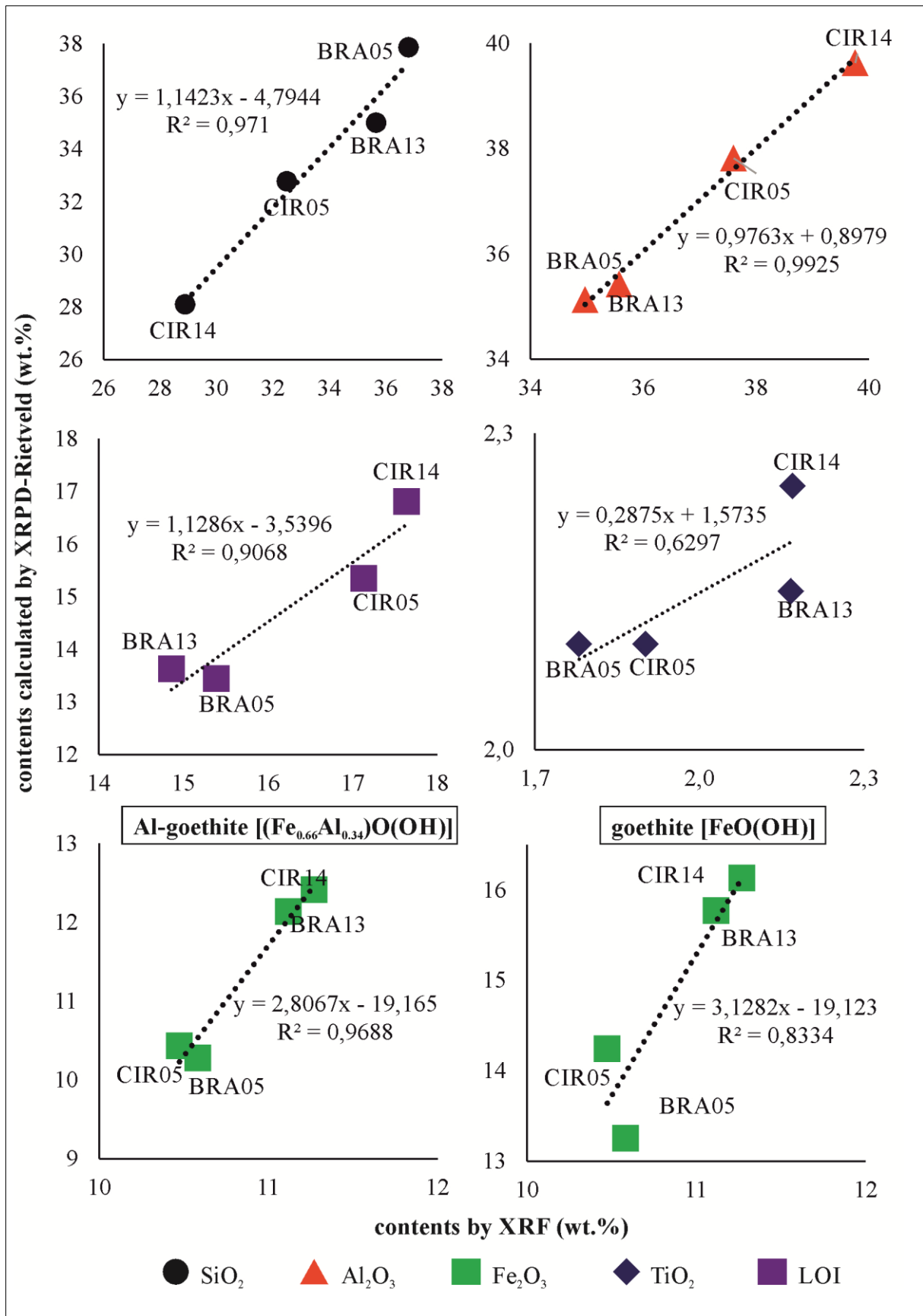
Figure 32 Chemical composition of the samples measured by XRF and calculated after the Rietveld analysis. Source: Negrão et al. (2021a), licensed under CC BY 4.0 https://creativecommons.org/licenses/by/4.0/.

3.1.3   FTIR spectroscopy

The samples BRA13m and CIR14m have very similar FTIR spectra, that present the same bands but with different intensities (Figure 33). The bands at 3697, 3652 and 3620 cm^{-1} are the OH stretching bands of ordered kaolinite (Balan et al., 2001; Chukanov and Chervonnyi, 2016). The 3652 kaolinite band, usually weak, is strong in the Belterra Clay samples. Well defined OH stretching bands of modelled and well-ordered kaolinite are usually observed at 3697 (strong), 3669 (weak), 3652 (weak) and 3620 cm^{-1} (Balan et al., 2001; Chukanov and Chervonnyi, 2016).
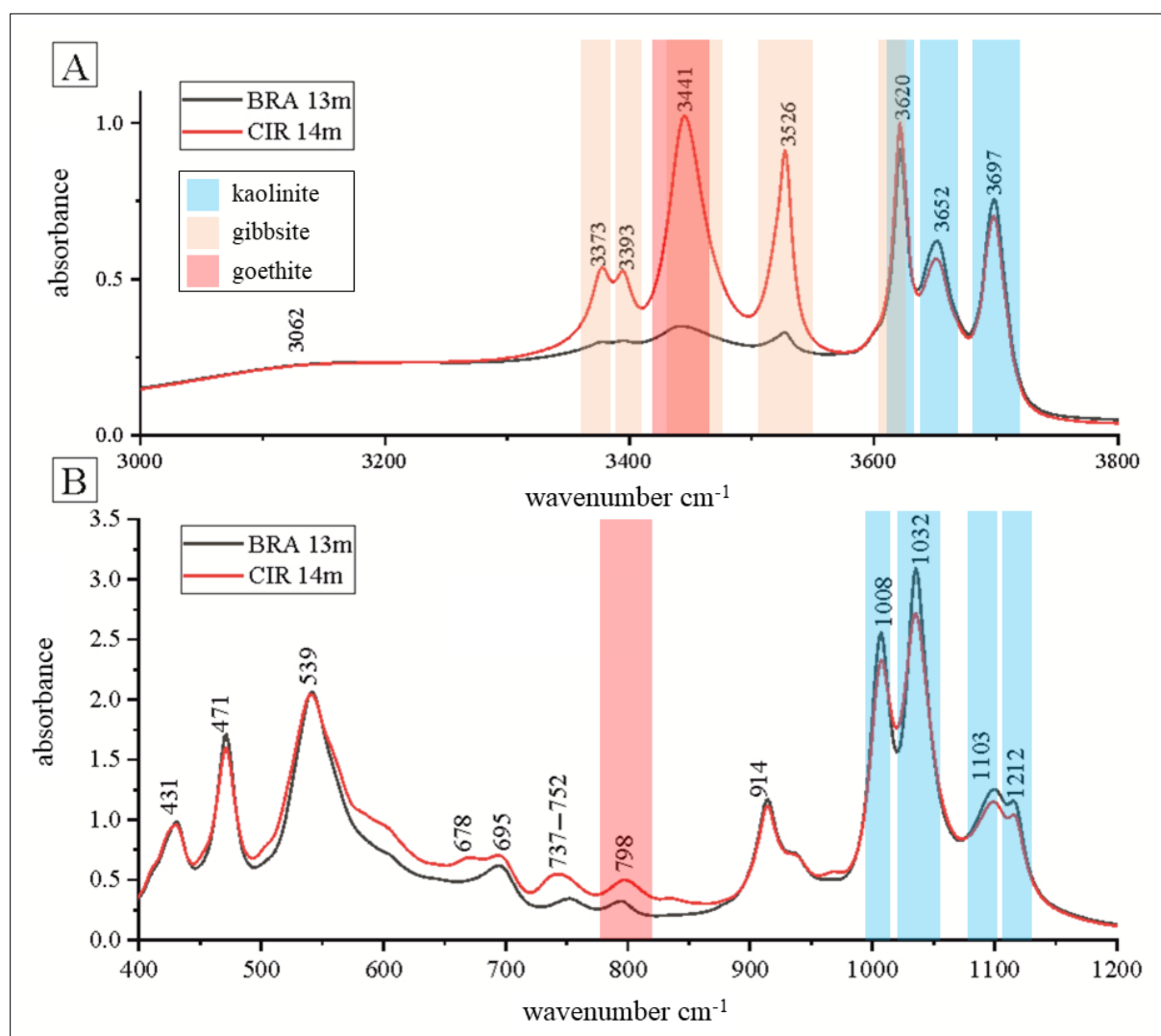
Figure 33 FTIR spectra, in the OH-stretching region (A) and middle range (B) of the Belterra Clay samples. The colour-marked bands are to facilitate the visualisation of which bands were attributed to each minerals.

However, the band 3669 cm^{-1}, which is common for ordered kaolinites, is not present in the FTIR spectra of the studied samples. The band at 3652 cm^{-1} is characteristic of the $Al_2Si_2O_5(OH)_4$ polymorph dickite, and its presence is a consequence of a disorder in kaolinite due to the displacement of octahedral sites vacancies and consequent formation of dickite-like layers within the structure of kaolinite (Brindley et al., 1986).

Gibbsite can be characterised in the IR spectra by the bands at 3620 cm^{-1}, 3526 cm^{-1} and 3373 cm^{-1} (Balan et al., 2006), which are much more intense in the spectra of the CIR14m sample due to this sample higher gibbsite contents.

The broader bands with maximum intensity around 3441 cm^{-1} and the less obvious around 3034 cm^{-1} are attributed, respectively, to non-stoichiometric and stoichiometric OH stretching of goethite. Non-stoichiometric hydroxyl units are incorporated in the structure of goethites and found to increase with higher Al/Fe ratios in Al-rich goethites (Schulze and Schwertmann, 1984; Ruan et al., 2002). In Al-free goethites, the intensity of the band ~3034 cm^{-1} is higher than of the band at 3441 cm^{-1}, whereas the opposite was observed for Al-rich goethites. The goethite of Belterra Clay has a much more similar infrared spectrum to the Al-richest goethites (30 mol% of Al) studied by Ruan et al. (2002), attesting the Al-rich character of the Belterra Clay goethites.

In the 400 cm^{-1} to 1200 cm^{-1} range of the spectra, the bands at 1112, 1103, 1032 and 1008 cm^{-1} are attributed to the Si-O stretching modes of kaolinite. The band at 798 cm^{-1} is due to the OH bend of goethite, and the other less intense bands mostly represent the Si, Al, and H displacement.

3.1.4   Thermal characterisation

The heating of the samples results in at least four main mass losses observed in the TG analysis and in the DSC curves (Figure 34). These losses have their maximums at 50 °C, 270 °C, 375 °C and 535 °C. The first one is due to the loss of some residual water absorbed onto the grains of the Belterra Clay.

The second loss, with a maximum close to 270 °C, represents the dehydroxylation of gibbsite, which is usually from 240 to 380 °C forming ρ-Al_2O_3 (Colombo and Violante, 1996). This corresponds to a mass loss of 5.49% for the sample CIR14m, and a mass loss of 1.8% for BRA13m.

The third mass loss, close to 375 °C, is from the dehydroxylation of goethite, which is common from 340 to 410 °C (Schulze and Schwertmann, 1984; Ruan et al., 2002). This mass release accounts for approximately 1.8% of the sample and is similar for both the CIR14m and BRA13m samples.
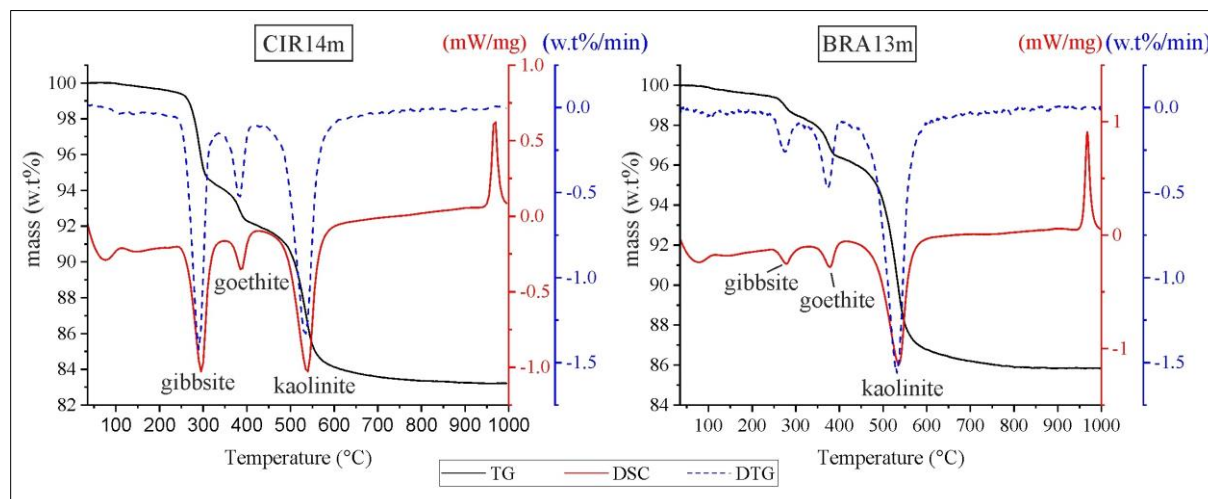
Figure 34 Thermal analysis (TGA and DSC) of the Belterra Clay samples CIR14m and BRA13m. Heating rate 10 K/min. Source: Negrão et al. (2021a), licensed under CC BY 4.0 https://creativecommons.org/licenses/by/4.0/.

The fourth and last mass loss, close to 535 °C, is due to the decomposition of kaolinite, which forms metakaolinite (Yeskis et al., 1985), and later mullite at 980 °C (Chen et al., 2004) as observed in the DSC curve.

Stoichiometric calculations, using the mass losses, resulted in 59.5% of kaolinite, 15.8% of gibbsite, and 16.2% of goethite in the sample CIR14m. For the sample BRA13m, the computations resulted in 71.9% of kaolinite, 3.8% of gibbsite, and 16.2% of goethite. These values are very close to the obtained by the XRPD-Rietveld quantifications.

3.1.5 Micromorphology

The Belterra Clay is composed mostly of nanometric crystals of kaolinite as agglomerates (Figure 35). Larger crystallites with pseudohexagonal morphology are also visible. The size of the crystallites is in general smaller than 1 µm, which do not permit an accurate distinction of them using EDS points analysis. Therefore, it was not possible to distinguish the present phases, as they probably share a similar morphology.
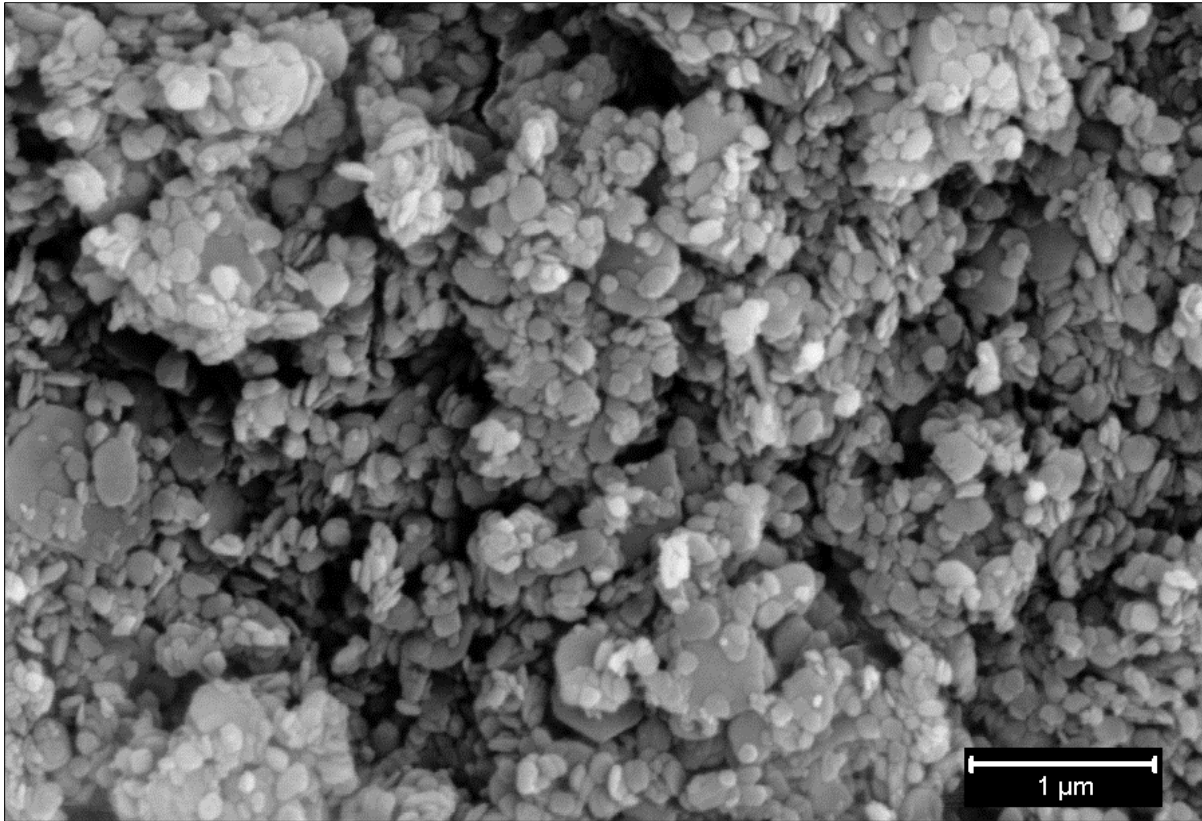
Figure 35 SEM image of the Belterra Clay sample CIR14m from the Círiaco pilot-mine.

3.2   **Bauxite washing clay characterisation**

The bauxite washing clay sample has a very fine and humid (plastic) aspect (Figure 36). After drying the sample in a muffle, it is composed of soft clayey aggregates. The material has a reddish-brown colour and is very homogeneous.
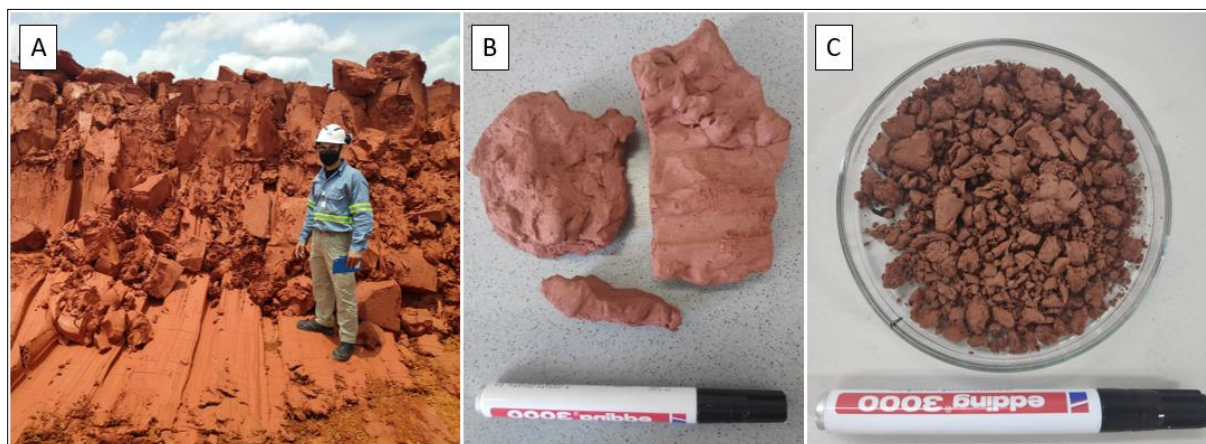
Figure 36 A: Photography of the bauxite washing clay inside of the tailing's ponds of the bauxite mine in Paragominas, Brazil; B: dried mud aggregate; C: the same sample dried and crushed into smaller clay aggregates.

3.2.1   Mineralogy by XRPD

Kaolinite and gibbsite are the most abundant minerals of the bauxite washing clay, comprising respectively 54% and 29% of it. Al-goethite (10%), hematite (5%), and anatase (2%) are the other minerals identified by XRPD and quantified using the Rietveld method (Figure 37). No amorphous was quantified in the samples. The anomalous XRPD pattern of kaolinite is very similar to the low-ordered kaolinite found in the Belterra Clay samples, showing the same typical anomalous XRPD pattern of Belterra Clay's kaolinite, that also results in non-accurate fittings in the Rietveld refinement.
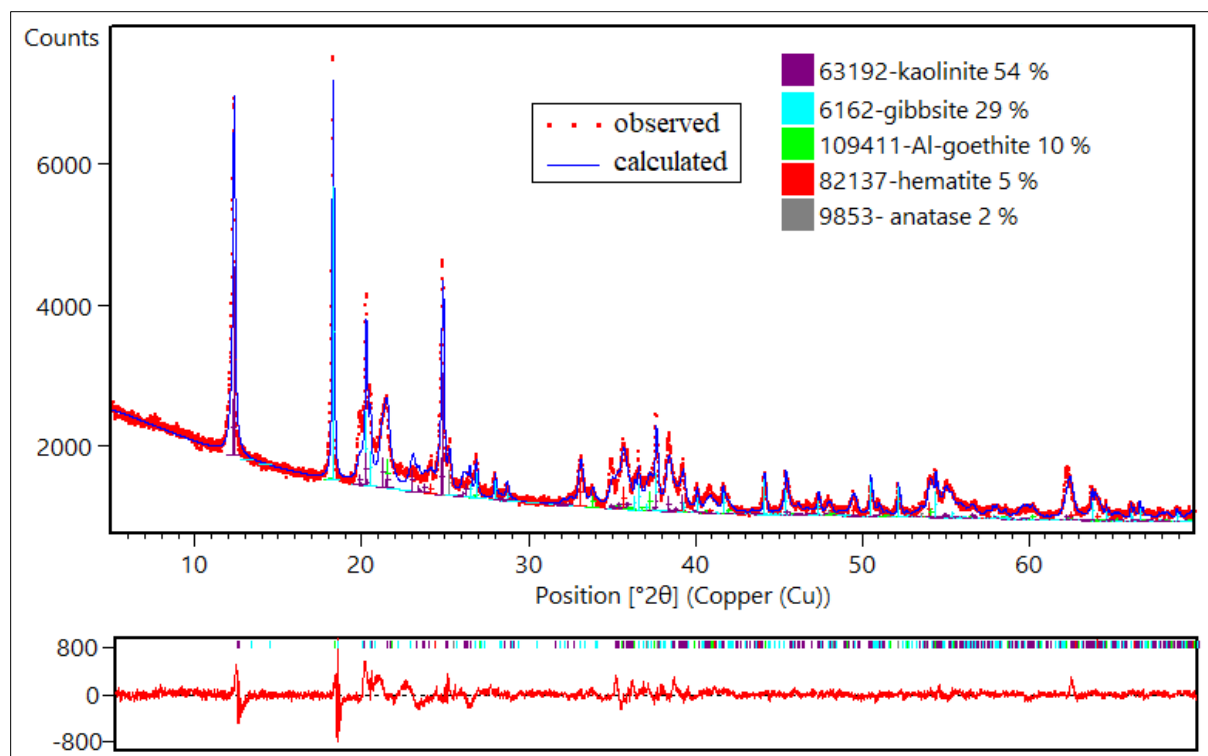
Figure 37 Rietveld-refined XRPD pattern and difference plot of the bauxite washing clay sample. GOF = 1.88, Rwp = 4.87.

3.2.2 Chemical composition

The chemical composition of the bauxite washing clay sample, determined by XRF, is very similar to that of the Belterra Clay samples. Silica, alumina, iron oxide, and titanium oxide are the principal oxides (Table 6). The main difference between the bauxite washing clay and the Belterra Clay is the higher alumina and iron oxide amounts of the first, which are mainly because of the higher gibbsite and hematite contents in the bauxite washing clay compared to the Belterra Clay. The XRF results are also very close to the chemical composition calculated using the mineralogical contents from the Rietveld quantification.

Table 6 Chemical composition, by XRF and calculated from mineralogical quantification, of the Bauxite washing clay sample.

Method	SiO_2	Al_2O_3	Fe_2O_3	TiO_2	MgO	CaO	K_2O	Na_2O	ZrO_2	LOI	Total
XRF	25.35	41.12	12.40	2.04	0.12	0.02	0.02	0.03	0.1	18.73	99.93
XRPD*	25.16	41.28	12.67	2.27	-	-	-	-	-	18.61	100.0

XRPD* = chemical composition calculated from XRPD-Rietveld mineralogical quantification.

3.2.3   Thermal characterisation

The heating of the bauxite washing clay sample to up to 1000 °C resulted in four mass losses seen in the thermogravimetric curve, which are coincident with four endothermic peaks in the DSC curve (Figure 38). The first loss is attributed to some residual absorbed water in the first 50°C, whereas the following ones represent the dehydroxylation of gibbsite (at 310 °C), goethite (380 °C) and kaolinite (530 °C). Close to 970 °C, an exothermic peak is seen in the DSC curve as a consequence of mullite formation. The thermal behaviour of the bauxite washing clay confirms its main mineralogy and is very similar to the thermal behaviour of the Belterra Clay samples.
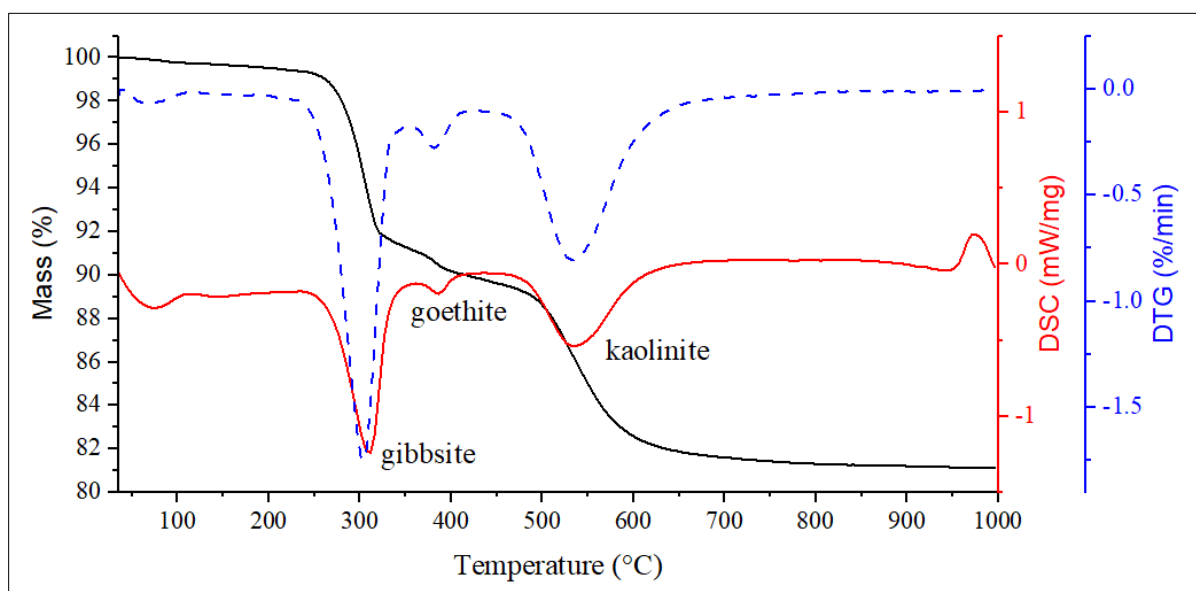
Figure 38 Thermal analysis (TGA and DSC) of the bauxite washing clay sample. Heating rate 10 K/min.

3.2.4   Micromorphology

The bauxite washing clay sample has a very similar micromorphology (Figure 39) compared to the Belterra Clay. The very fine material is formed by aggregates of nanometric size crystals of kaolinite, gibbsite, goethite and anatase. Due to the very thin and small crystallites, the minerals could not be distinguished by EDS.
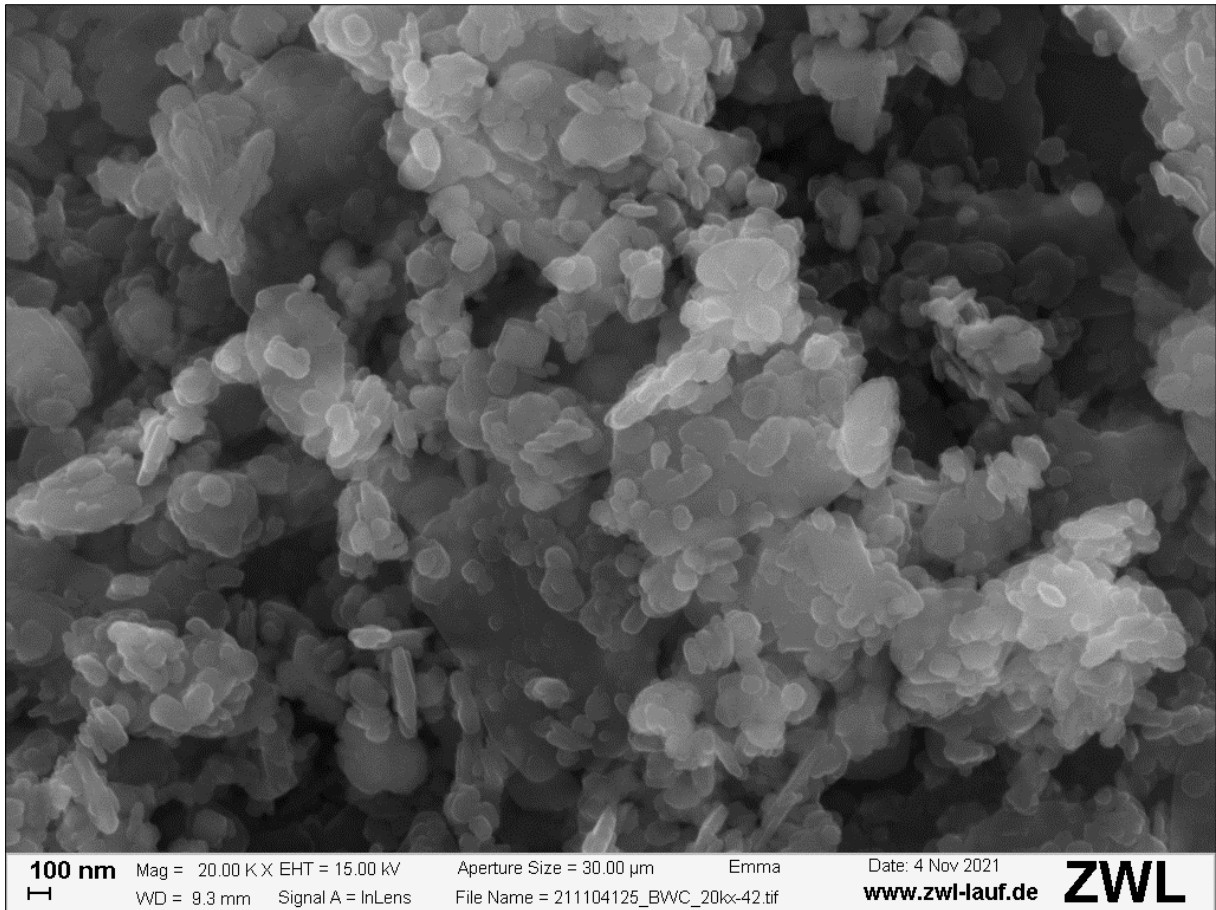
Figure 39 SEM image of bauxite washing clay sample.

3.3 Commercial reagents characterisation

3.3.1 Calcium carbonate and calcium oxide

Calcite ($CaCO_3$, ICDD code 01-072-1937) was the only mineral identified in the XRPD pattern of the used commercial $CaCO_3$ (Figure 40). The measured LOI of the material was 43.70%, which is close to the theoretical amount of CO_2 (43.97%) in calcite. The resulting sample after LOI had only calcium oxide after the XRPD analysis.
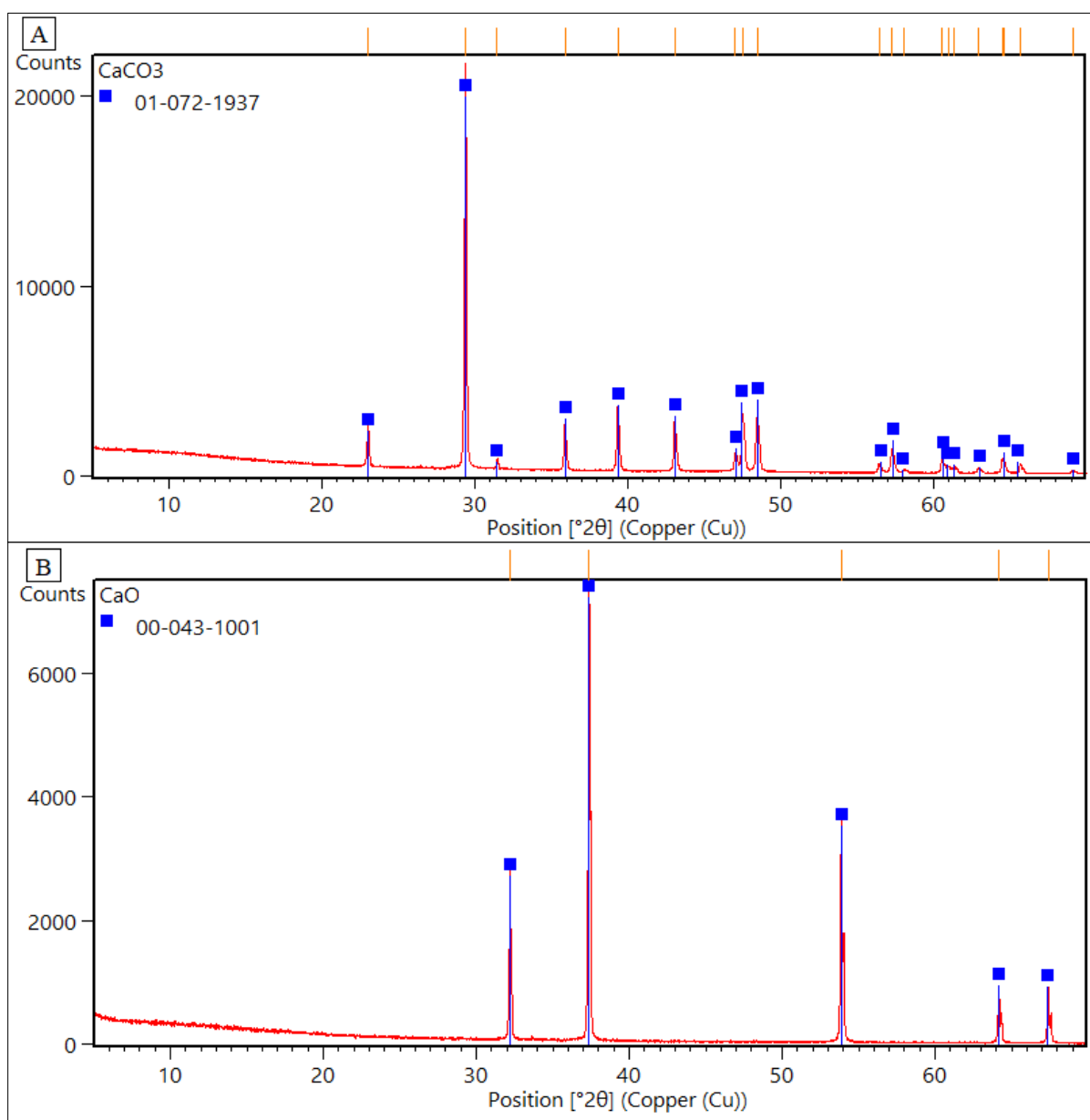
Figure 40 A: XRPD pattern of the commercial $CaCO_3$ reagent (Applichem Panreac) showing calcite (ICDD code 01-072-1937) as the unique mineral phase. B: XRPD pattern of the same sample after LOI showing cubic CaO (ICDD code 01-072-1937).

3.3.2 Calcium sulfate di-hydrate

Gypsum (CaSO$_4$·2H$_2$O, ICDD code 01-074-1433) was the main phase characterised in the XRPD pattern of the CaSO$_4$·2H$_2$O commercial reagent (Figure 41). Besides gypsum, bassanite (CaSO$_4$·½H$_2$O, ICDD code 01-081-1848), and anhydrite (CaSO$_4$, ICDD code 01-072-0503) were also identified in the XRPD diffractograms. The measured LOI of the sample was 20.50%, which is close to the theoretical amount of H$_2$O (20.94%) in gypsum.
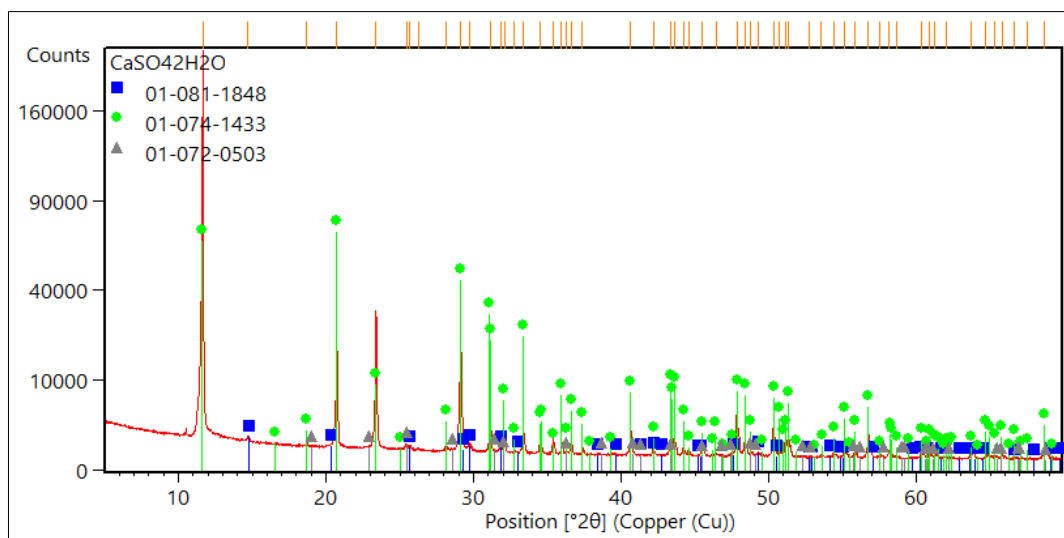
Figure 41 XRPD pattern of the commercial CaSO$_4$·2H$_2$O reagent with gypsum (ICDD code 01-074-1433), bassanite (ICDD code 01-081-1848), and anhydrite (ICDD code 01-072-0503).

3.3.3 Iron oxide

The Fe$_2$O$_3$ commercial sample (from Fluka) is composed of only hematite (Fe$_2$O$_3$, ICDD code 01-084-0306) after the XRPD characterisation (Figure 42).
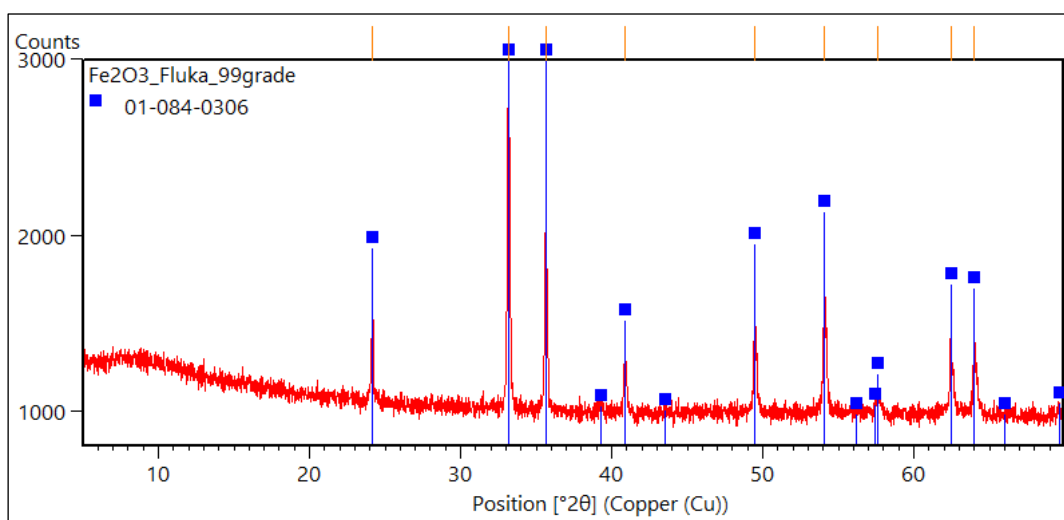
Figure 42 XRPD pattern of the commercial Fe$_2$O$_3$ (Fluka) composed of hematite (ICDD code 01-084-0306).

3.3.4   Aluminium oxide

Corundum (Al$_2$O$_3$, ICDD code 01-089-7717) and minor amounts of hydrated alumina (Al$_{22}$H$_{3.58}$O$_{34.79}$, ICDD code 01-070-0384) was characterised in the sample of commercial alumina (Figure 42).
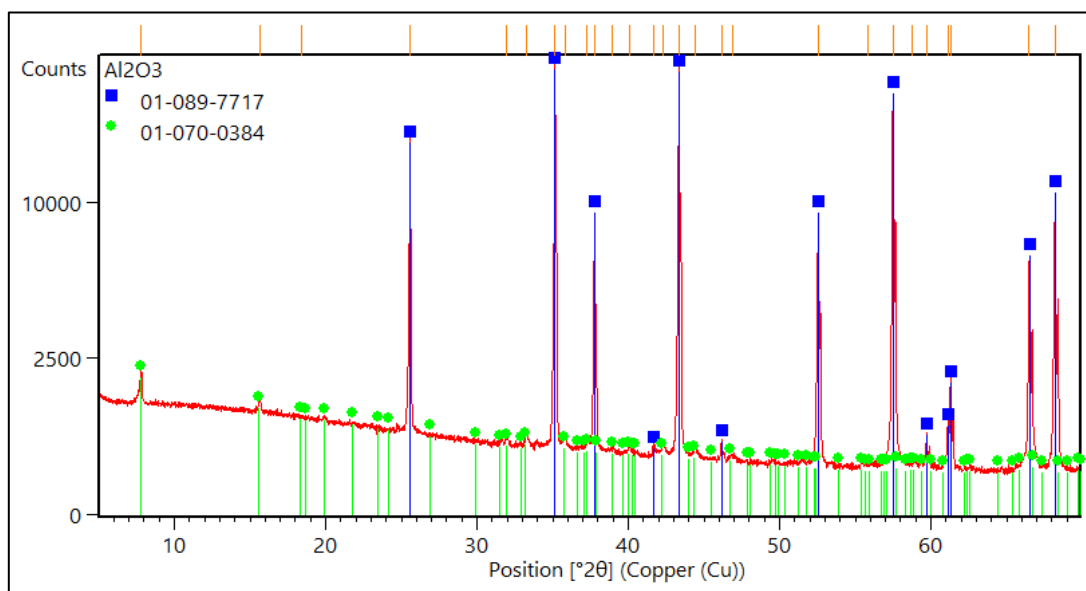
Figure 43 XRPD pattern of the commercial Al$_2$O$_3$ with corundum (ICDD code 01-089-7717) and hydrated alumina (ICDD code 01-070-0384).

3.3.5   Titanium oxide

The titanium oxide (from Kronos) used for the synthesis of pure phases is composed of only rutile (TiO$_2$, ICDD code 01-089-8303) after the XRPD characterisation.
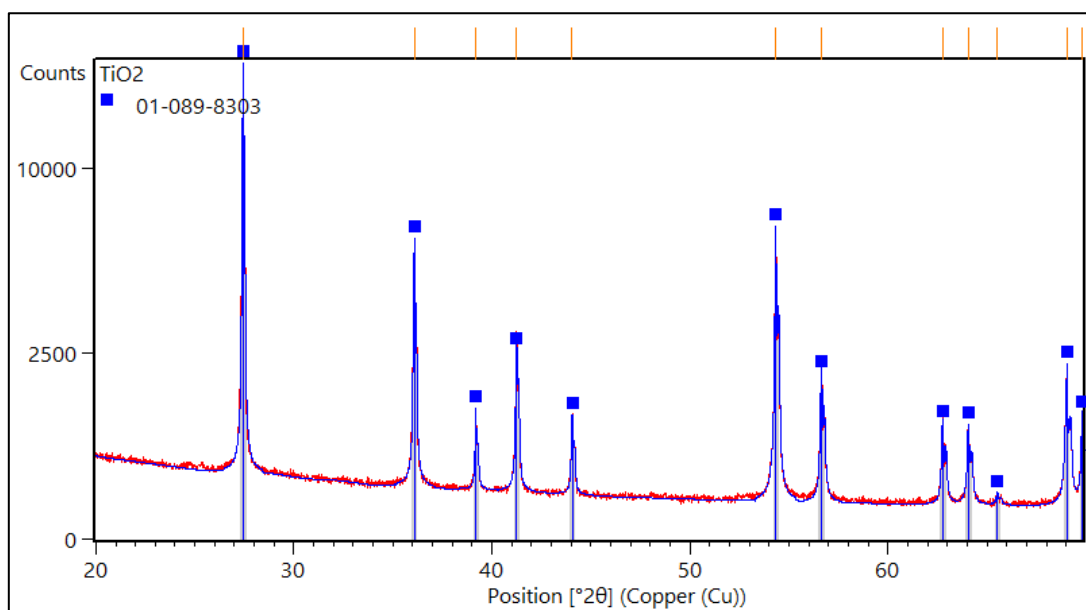
Figure 44 XRPD pattern of the commercial TiO$_2$ (Kronos) with rutile (ICDD code 01-089-8303).

4 Results – Produced clinkers

4.1 SD1 and SD2 clinkers produced with Al-richer Belterra Clay of Círiaco pilot-mine

The clinkers produced using the Belterra Clay samples from the Círiaco mine are referred to as SD1 and SD2, following their sequential statistical design of experiments (SD) 1 and 2, and published in Negrão et al. (2021c). Rietveld-quantified phase assemblage of these clinkers and the raw meal composition of each of them are displayed in Table 7 and Table 8.

4.1.1 Phase composition

The SD1 experiments started with a broader mixture range of the raw materials, with $30 - 60\%$ of Belterra Clay, $30 - 60\%$ of $CaCO_3$, and $6.5 - 13\%$ of $CaSO_4 \cdot 2H_2O$, using the clinkering temperatures of 1100 and 1250 °C (Table 7). The resulted clinkers are composed of diverse phases including ye'elimite, larnite, ternesite, brownmillerite, Fe-perovskite, gehlenite, free-lime, anhydrite, cristobalite and anorthite.

Ideally, ye'elimite and larnite were expected in the CSA-based clinkers and should be the most abundant phases because of the high amounts of Al_2O_3 and SiO_2 in Belterra Clay. When excesses of free-lime and anhydrite are identified in the clinkers, it means that too much $CaCO_3$ or $CaSO_4 \cdot 2H_2O$ was used in the raw meal. In most of the SD1 clinkers, the ye'elimite contents were very low, and high amounts of free-lime and anhydrite were quantified.

Raw meal compositions with Belterra Clay / $CaCO_3$ ratios lower than 0.7 resulted in clinkers with increased free-lime contents. On the other hand, when Belterra Clay was used in excess, high amounts of gehlenite formed. The presence of this phase is not desirable, considering that it captures part of the Al to form ye'elimite.

Only the orthorhombic modification of ye'elimite was identified in the clinkers produced at 1100 °C, whereas cubic ye'elimite was present in the clinkers produced at 1250 °C and 1300 °C. The cubic and the orthorhombic polymorphs have a similar XRPD pattern (Figure 45), with the main reflex at 3.75 Å (close to 23°2θ, Cu) that correspond to the (121) reflex of the cubic form, or to the band formed by the (131) and (202) reflexes of the orthorhombic modification. The peak close to 4.92 Å (18°2θ, Cu) corresponds to the (121) and (211) reflexes of the orthorhombic ye'elimite.
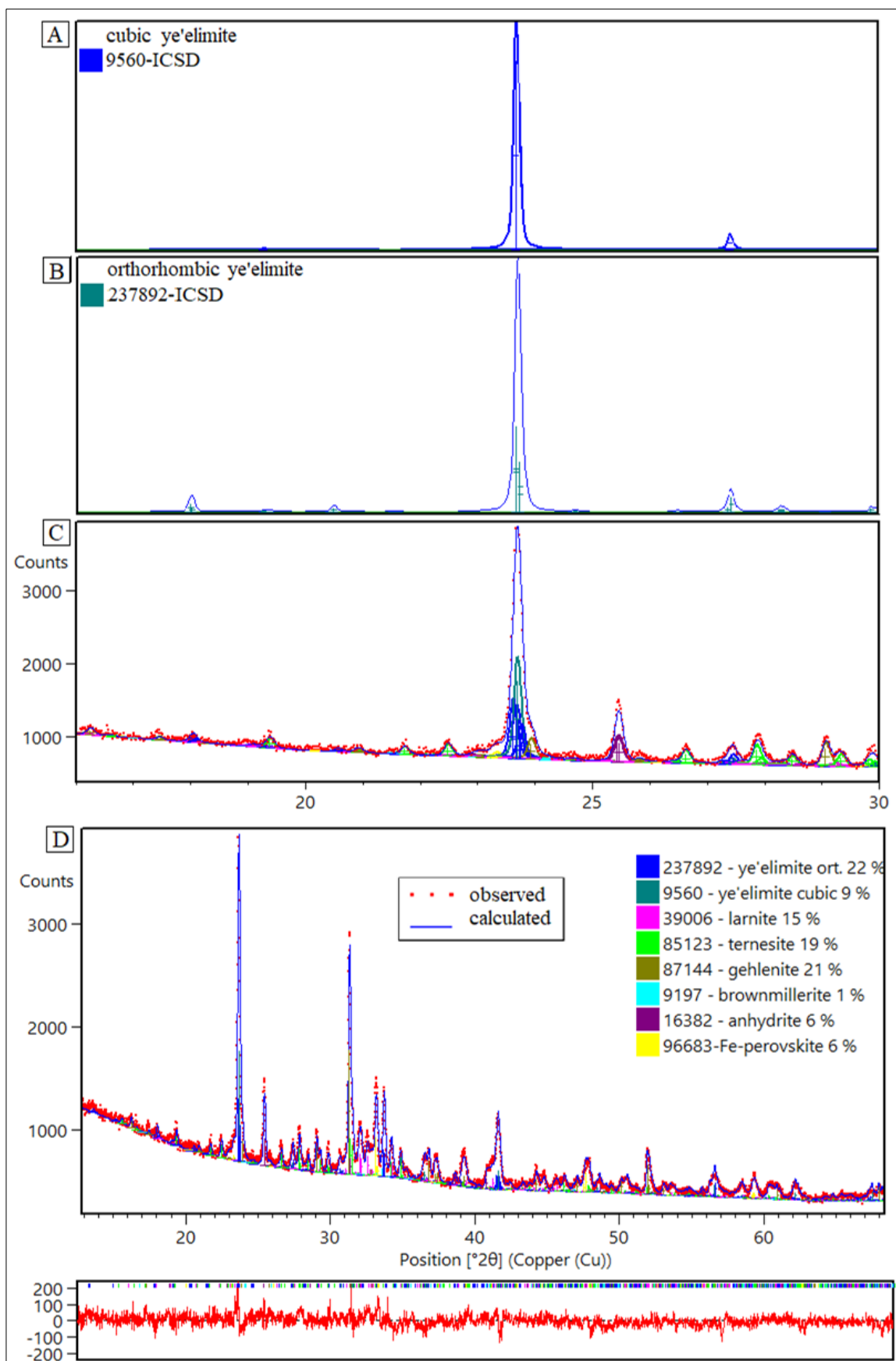
Figure 45 XRPD pattern simulations (16-30°2θ Cu range) of A - cubic ye'elimite (Cuesta et al., 2013); B - orthorhombic ye'elimite (Saalfeld and Depmeier, 1972); C – zoomed Rietveld-refined XRPD pattern of clinker SD1-13 showing the contribution of both ye'elimite modifications. D - Complete Rietveld-refined XRPD pattern of the clinker SD1-13. GOF = 1.3, Rwp = 4.60.

The careful observation of the intensity ratio of these two peaks (at 3.75 and 4.92 Å) was crucial in the characterisation of the two polymorphs. But, in practice, it was more effectively done by looking at the refined XRPD patterns, where a misfitting in one of these peaks is evident in the resulting difference plot, meaning that the contribution of the two polymorphs should be considered in the refinement. In all clinkers, orthorhombic ye'elimite was the predominant form, while the cubic form was more abundant in the clinkers produced at higher temperatures.

Clinkering at 1200 °C was not sufficient to maximise ye'elimite in the clinkers. This can be specially observed for the clinkers SD1-12 and SD13, produced using the same raw meal composition but at different temperatures. SD1-12, produced at 1100 °C, is composed of 11% of ye'elimite and 20% of free-lime, whereas SD1-13 (fired at 1250 °C) has up to 31% of ye'elimite and no free-lime. Moreover, the occurrence of cristobalite and anorthite, which are not usual in clinkers, is a good indication that 1100 °C was not the ideal clinkering temperature.

After the input of the responses (ye'elimite contents) in the interface of the software, the design of experiments suggested an optimum raw meal composition of 30% of Belterra Clay, 60% of $CaCO_3$, and 10% of $CaSO_4 \cdot 2H_2O$ to obtain a clinker with 36% of ye'elimite (Figure 46-A). This first software-suggested composition was not tested, because this amount of $CaCO_3$ was observed too high, as proved for the clinker SD1-9 (37% of ye'elimite) formed out of similar raw meal composition but with high free-lime contents (15%).
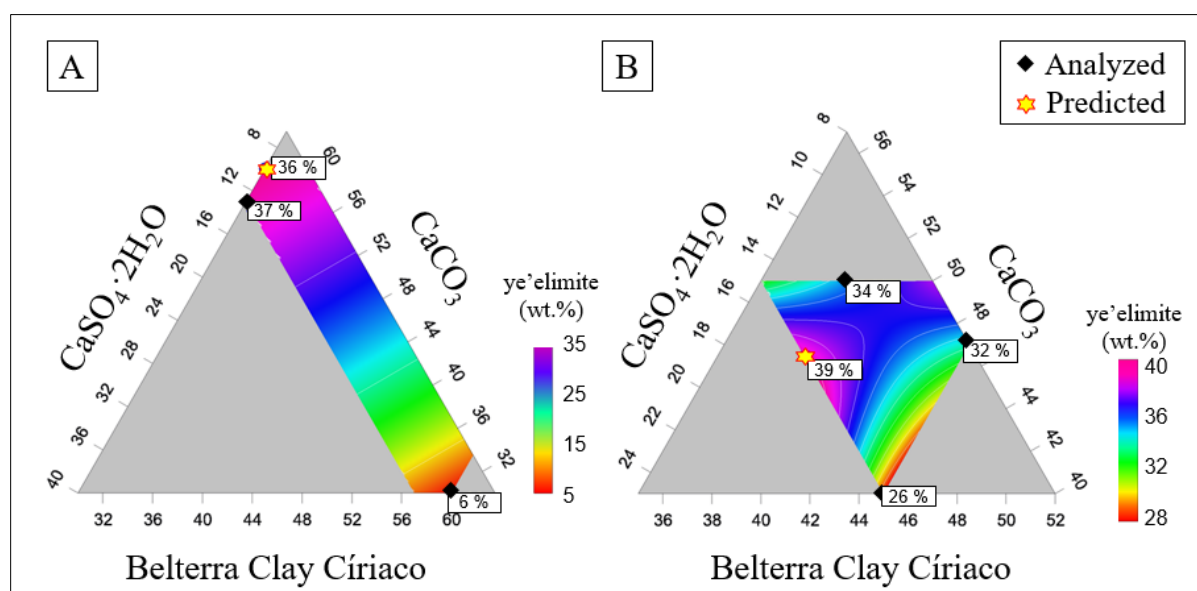
Figure 46 Predicted ye'elimite contents and measured ye'elimite contents in the clinkers using the design of experiments SD1 (A) and SD2 (B) for the experiments conducted at 1250 °C.

Table 7 Phase and raw composition (wt.%) of the produced clinkers according to the Statistical Design of experiments SD1, using Belterra Clay from the Círiaco pilot-mine.

Clinker	ye'elimite o.	c.	tot.	larnite	brownm.	gehlenite	ternesite	anhydrite	lime	Fe-perov.	cristob.	anorthite	GOF	Rwp	BTC	CaCO$_3$	Gyps	Temp. (°C)	Time (h)
SD1-1	10	-	10	7	9	34	17	10	8	3	2	-	1.4	5.2	60	33.5	6.5	1100	1
SD1-2	9	-	9	9	7	15	10	11	39	0	-	-	1.5	6.2	30	60	10	1100	1
SD1-3	12	-	12	9	6	32	16	19	4	1	2	-	1.5	5.3	57	30	13	1100	1
SD1-4	8	-	8	9	9	19	4	11	39	0	-	-	1.3	5.3	33.5	60	6.5	1100	2
SD1-5	10	-	10	8	8	36	13	19	3	3	2	-	1.5	5.3	57	30	13	1100	2
SD1-6	8	-	8	8	5	16	8	17	37	1	-	-	1.4	5.8	30	57	13	1100	2
SD1-7	6	-	6	-	-	63	5	11	-	4	-	11	1.4	2.0	60	30	10	1250	1
SD1-8	26	5	31	23	15	5	1	-	22	4	-	-	1.3	5.4	33.5	60	6.5	1250	1
SD1-9	32	5	37	18	15	5	1	5	15	5	-	-	1.4	5.7	30	57	13	1250	1
SD1-10	9	-	9	-	-	69	5	3	-	5	-	10	1.5	5.4	60	33.5	6.5	1250	2
SD1-11	10	-	10	10	9	27	13	12	17	2	1	-	1.3	5.1	45.1	45.1	9.8	1100	2
SD1-12	11	-	11	7	7	24	11	16	20	3	1	-	1.4	5.3	43.5	43.5	13	1100	1
SD1-13	22	9	31	15	1	21	19	6	-	6	-	-	1.3	4.6	43.5	43.5	13	1250	2
SD1-14	15	-	15	9	8	40	16	6	3	1	2	-	1.4	5.1	60	33.5	6.5	1100	2
SD1-15	34	3	37	16	13	3	-	5	19	8	-	-	1.5	6.1	30	60	10	1250	2
SD1-16	2	-	2	-	-	72	3	12	-	3	-	9	1.4	5.1	57	30	13	1250	2

Ye'elimite: o = orthorhombic, c = cubic modifications; brownm. = brownmillerite; Fe-perov. = Fe-perovskite; lime = free-lime (CaO); cristob. = cristobalite. R-indicators are the Rietveld refinement indicators, GOF = goodness of fit and Rwp = R weighted profile; Gyps = gypsum; BTC = Belterra Clay; Temp. = firing temperature in Celsius grade.

To produce the sequentially planned SD2 clinkers, the mixture range compositions in this design of experiments were varied more restrictedly from 35 to 45% of Belterra Clay, 40 to 50% of $CaCO_3$, and 8 to 15% of $CaSO_4 \cdot 2H_2O$ (Table 8). Additionally, the clinkering temperature of 1100 °C was abandoned, and the clinkering time of only one hour was adopted because no significant differences were found between one- and two-hour clinkering times. Seeking the ideal temperature range, the temperatures of 1200 ℃, 1250 ℃ and 1300 ℃ were tested in the SD2 experiments.

The SD2 clinkers have higher ye'elimite contents than the SD1 ones and considerably fewer free-lime. The 1200 °C clinker temperature was, however, not optimal to maximise ye'elimite, as observed for the clinkers SD2-01 (1200 ℃) and SD2-13 (1250 ℃) produced from the same raw meal formulation. Much more ye'elimite and less free-lime were formed in SD2-13, proving that clinkering at 1250 °C increased the ye'elimite contents in the clinkers.

The evaluation of the optimal clinkering temperature was made by reproducing at 1250 °C the clinkers SD2-5, SD2-6 (Figure 47), and SD2-12 (initially produced at 1300 °C). The ye'elimite contents in these clinkers slightly decreased after clinkering at 1250 °C. However, the 1300 °C temperature promoted the destabilisation of brownmillerite to form hydraulic non-reactive Fe-perovskites.
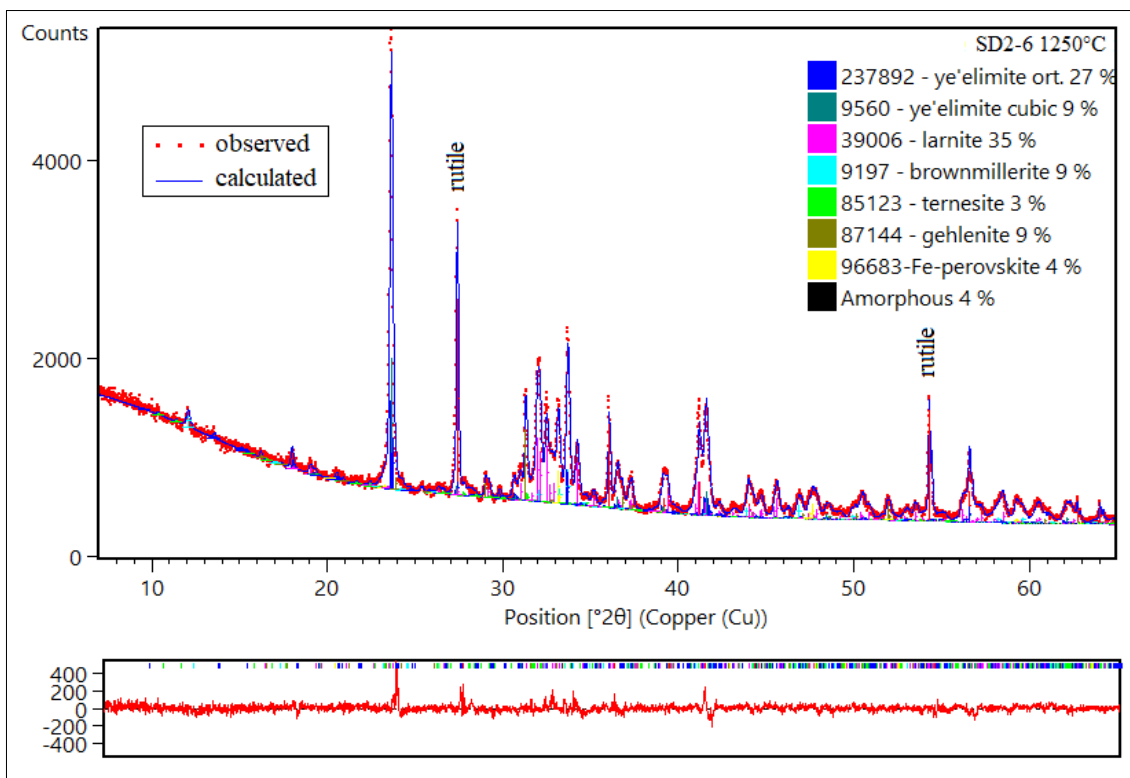
Figure 47 XRPD Rietveld-refined pattern and difference plot of the clinker SD2-6 synthesised at 1250 °C. Rutile was used as the internal standard for amorphous quantification. GOF = 1.24, Rwp = 4.4.

Table 8 Phase and raw composition (wt.%) of the produced clinkers according to the Statistical Design of experiments SD2, using Belterra Clay from the Círiaco pilot-mine.

Clinker	ye'elimite			larnite	brownm.	gehlenite	ternesite	anhydrite	lime	Fe-perov.	amorphous	R-indicators		raw composition			Temp. (° C)
	o.	c.	tot.									GOF	Rwp	BTC	CaCO$_3$	Gyps	
SD2-1	25	-	25	15	12	18	25	1	3	2	n.d.	1.4	3.7	45	47	8	1200
SD2-2	21	-	21	5	10	9	29	12	13	1	n.d.	1.5	4.1	35	50	15	1200
SD2-3	22	-	22	16	13	14	26	>1	7	2	n.d.	1.5	3.8	42	50	8	1200
SD2-4	22	-	22	10	9	19	21	15	1	3	n.d.	1.5	4	45	40	15	1200
SD2-5	32	5	37	43	11	-	-	8	-	1	n.d.	1.8	4.9	35	50	15	1300
SD2-5 [LT]	27	6	33	34	12	3	6	9	-	3	n.d.	1.4	5.3	35	50	15	1250
SD2-6	36	5	42	38	3	9	-	-	-	8	n.d.	1.83	5.3	42	50	8	1300
SD2-6 [LT]	27	9	36	35	9	9	3	-	-	4	4	1.24	4.4	42	50	8	1250
SD2-7	19	10	29	24	-	41	-	-	-	7	n.d.	1.68	4.7	45	40	15	1300
SD2-8	25	10	34	19	13	3	29	-	-	1	n.d.	1.66	4.8	38.5	50	11.5	1250
SD2-9	22	-	22	11	11	19	27	7	1	2	n.d.	1.8	5	45	43.5	11.5	1200
SD2-10	21	-	21	7	9	14	28	13	7	1	n.d.	1.7	4.8	40	45	15	1200
SD2-11	20	10	31	25	-	37	-	-	-	7	n.d.	1.66	4.7	45	43.5	11.5	1300
SD2-12	23	23	46	41	-	3	-	1	-	10	n.d.	1.74	5.2	40	45	15	1300
SD2-12[LT]	26	9	35	16	3	10	24	6	-	7	n.d.	1.19	4.23	40	45	15	1250
SD2-13	20	12	32	23	9	17	14	0	-	5	n.d.	1.78	5	45	47	8	1250
SD2-14	18	9	26	9	-	28	21	10	-	6	n.d.	1.71	4.8	45	40	15	1250
SD2-OP	24	12	36	13	9	3	35	3	-	3	-	1.29	4.5	38	47	15	1250

SD2-X [LT] = raw material compositional analogous clinker produced again at a lower temperature of 1250 °C. ye'elimite: o = orthorhombic, c = cubic modifications; brownm. = brownmillerite; Fe-perov. = Fe- perovskite; lime = free-lime (CaO). R-indicators are the Rietveld refinement indicators, GOF = goodness of fit and Rwp = R weighted profile; BTC = Belterra Clay; Gyps = gypsum; Temp. = firing temperature in Celsius degrees. n.d.= not determined.

Additionally, the clinkers produced at 1300 °C have no ternesite because this phase decomposes after 1250 °C (Liu et al., 2021), and is unstable at temperatures close to 1290 °C (Hanein et al., 2017). That could explain the absence of ternesite and the consequent increase in larnite in clinker produced at 1300 °C. The stability of ternesite depends, however, on the fugacity of the volatiles in the firing atmosphere (Hanein et al., 2017).

The 1250 °C clinkering temperature was therefore considered the best one to optimise ye'elimite, minimise energy consumption, and maintain ternesite and brownmillerite stability in the clinkers. The design of experiments suggested a raw mixture composition of 38% of Belterra Clay, 47% of $CaCO_3$, and 15% of $CaSO_4 \cdot 2H_2O$ to obtain a clinker with 39% of ye'elimite at this temperature. The suggested optimised composition was tested, and the clinker SD2-OP was finally produced and composed of 36% of ye'elimite (Figure 48).
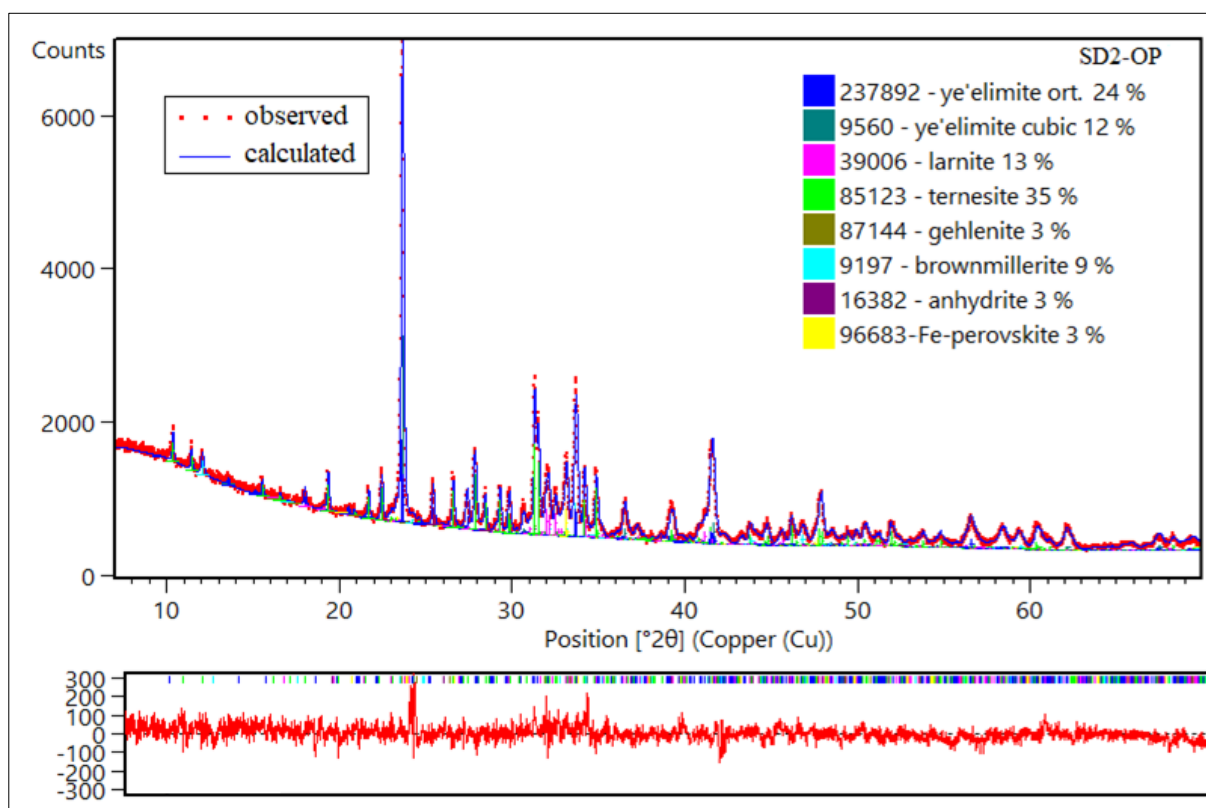
Figure 48 XRPD Rietveld-refined pattern and difference plot of the clinker SD2-OP. GOF = 1.29, Rwp = 4.5.

The clinkers SD2-6 and SD2-OP produced at 1250 ºC have high ye'elimite contents and no free-lime. To evaluate if amorphous was present, they were mixed with the internal standard rutile and quantified by the XRPD-Rietveld method. SD2-6 has a low amorphous content of

4%, and no amorphous was quantified in the clinker SD2-OP. SD2-OP was produced again in triplicate to test the reproducibility of the experimental setup used in this work (Figure 49), and no differences were observed among the XRPD pattern of the reproduced clinkers.
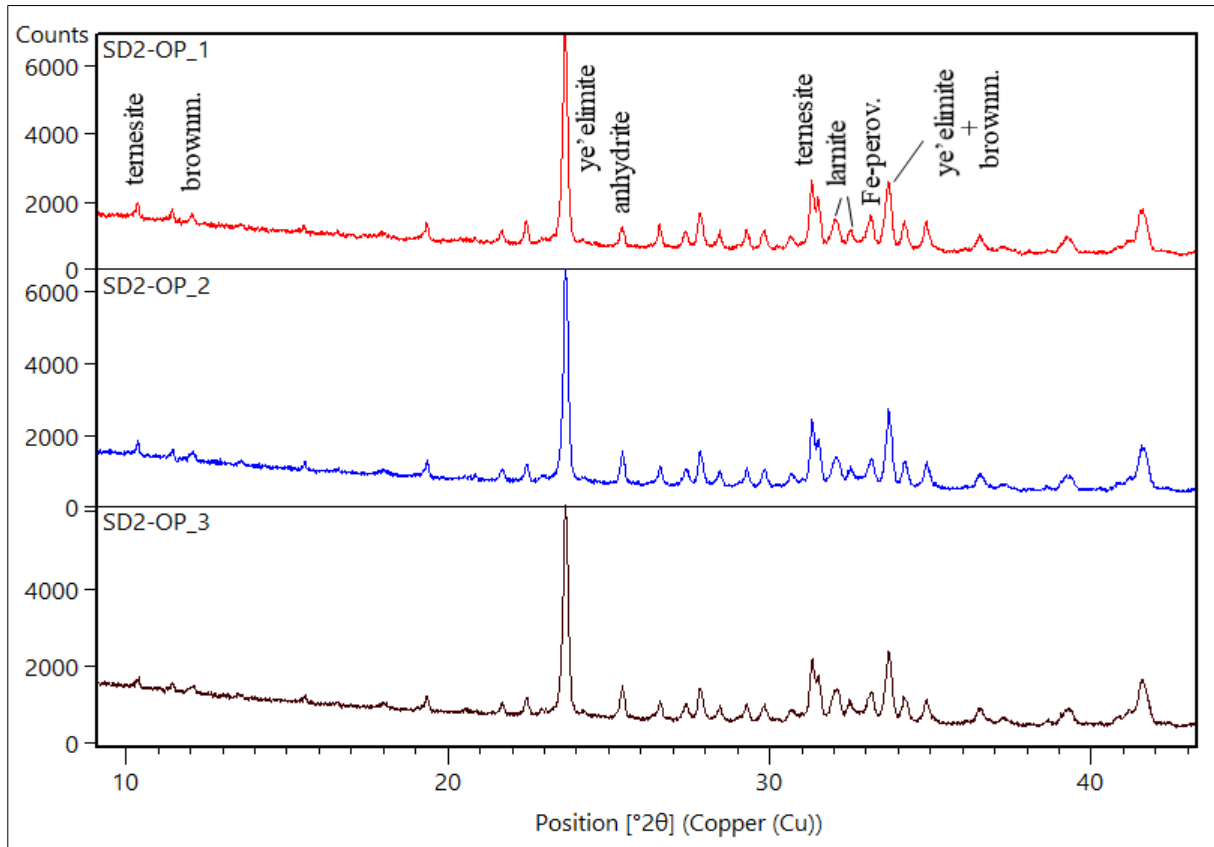
Figure 49 XRPD Rietveld-refined patterns of the clinker SD2-OP reproduced in triplicate. Fe-perov. = Fe-perovskite; brownm. = brownmillerite.

SD2-6 produced at 1250 °C has 36% of ye'elimite, which is close to the maximum of 37.5% predicted by stoichiometry if ye'elimite is considered the only sulfate. The minor deviation to this value is explained by low contents of ternesite accommodating part of the sulfate. The high belite contents of SD2-6, but still slightly lower than ye'elimite, allow classifying this clinker as a CSA-belite (CSAB) clinker.

SD2-OP has high contents of ternesite and therefore might be named a CSAT clinker. Approximately half of the gypsum fired in its raw meal was used to form ye'elimite, whereas the rest of it formed ternesite and some anhydrite.

4.1.2 Microstructure

The clinkers are formed by mosaic multiphase aggregates. Ye'elimite and larnite, the main phases, can be identified by their different grey tones in the BSE images (Figure 50). The lighter-coloured (whitish) phase is brownmillerite and/or Fe-perovskite and could not be distinguished in the BSE images due to the close electronic configuration of Fe and Ti, which result in a very similar amount of backscattered electrons emitted by these elements.
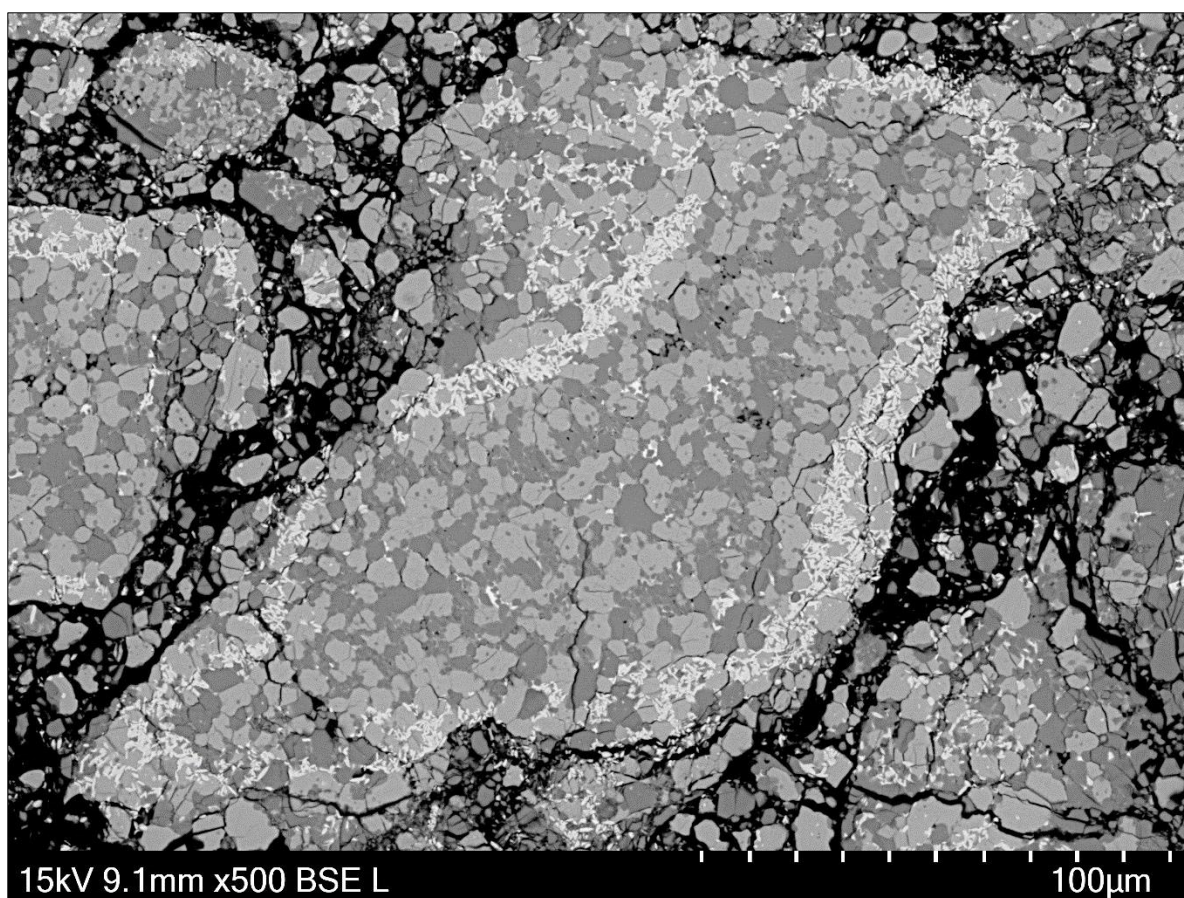
Figure 50 BSE image of the clinker SD2-5 produced at 1300 °C. The dark-grey crystals are ye'elimite, middle-grey are larnite and the light-grey are Fe-perovskite and brownmillerite. The black portions are filled with epoxy resin. Image acquired at the University of Halle.

The clinkers developed different crystallite sizes after clinkering at 1250 °C and 1300 °C. Ye'elimite and larnite developed larger crystallites in the higher temperature (Figures 51 and 52). Brownmillerite / Fe-perovskite maintained a similar size but seem to have formed shorter crystals. Most of the crystallites of larnite have few microns and form cobblestone-like aggregates (Figure 53). Ye'elimite has a similar size, but bigger and edge crystals are also common (Figure 52). Ternesite formed large prismatic crystals easily distinguished in the SD2-OP clinker (Figure 54).
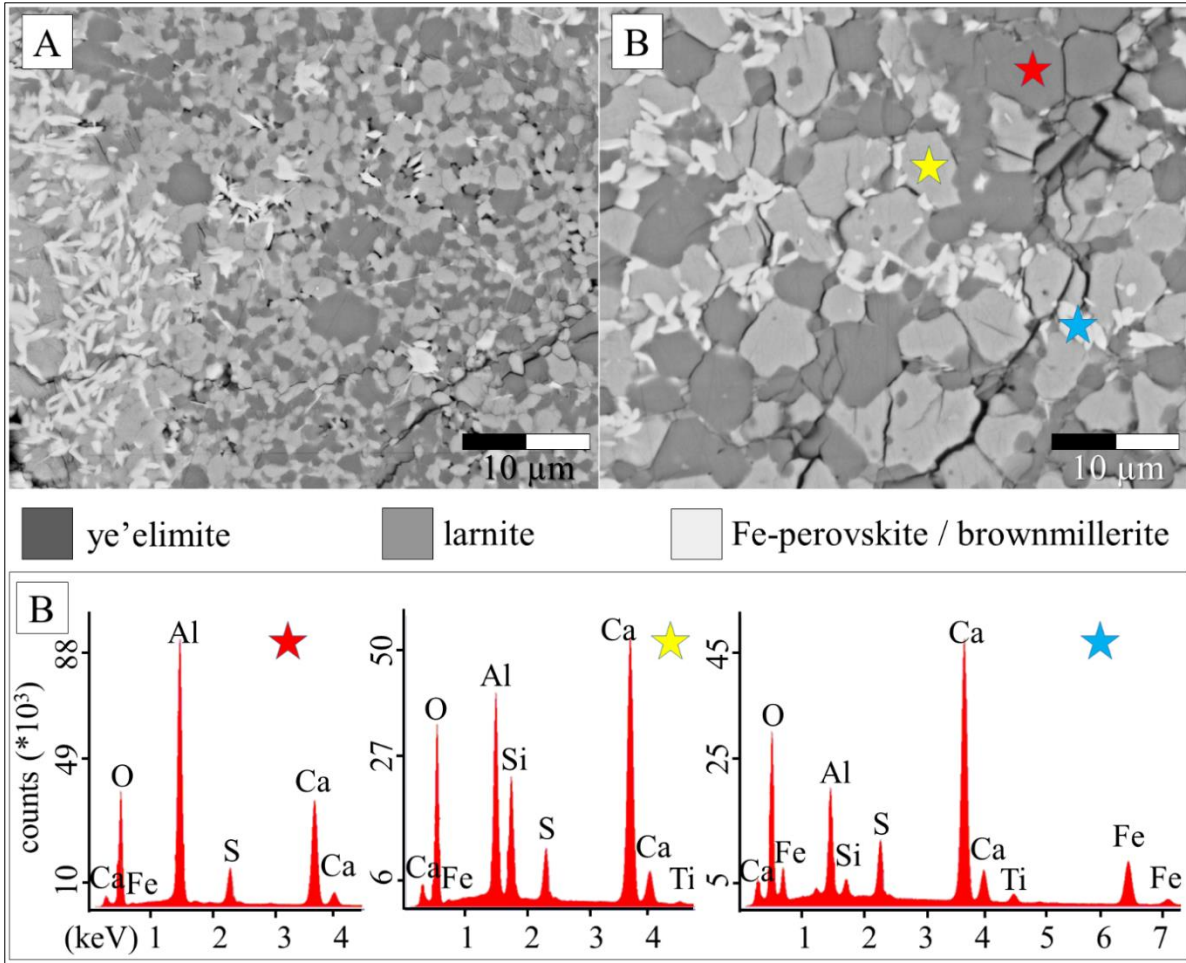
Figure 51 BSE images of polished sections of the clinker SD2-5. A: produced at 1250 ℃. B: produced at 1300 ℃. C: EDS measurements of the phases. The black portions are porous/cracks filled with epoxy resin. Images acquired at Zentrum für Werkstoffanalytik in Lauf, Germany.
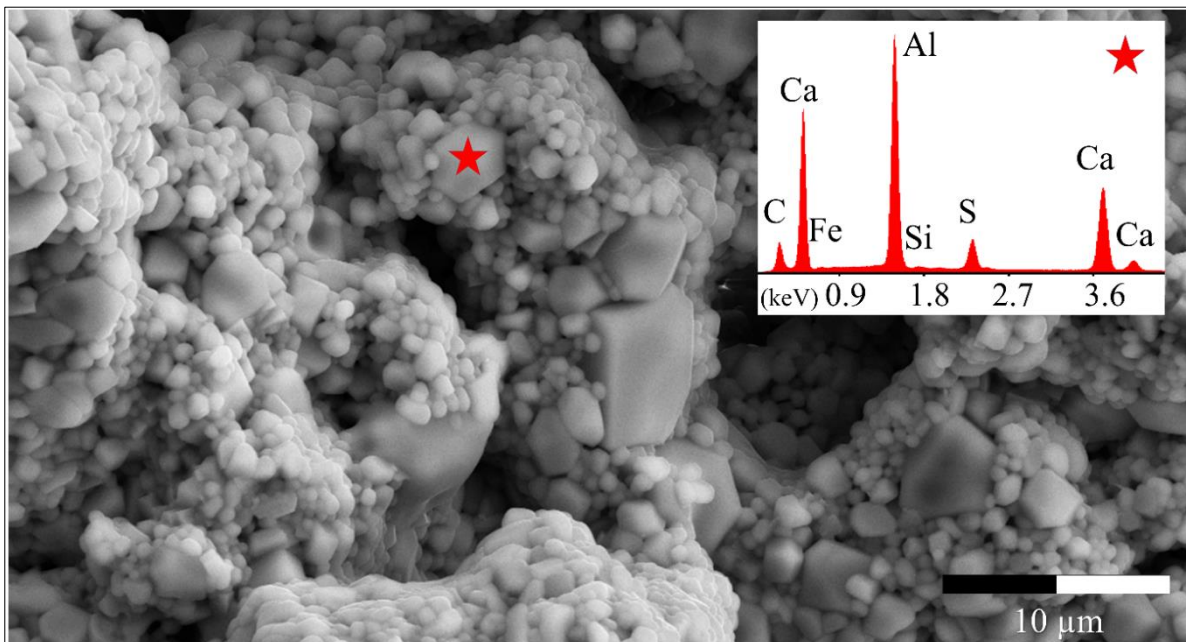
Figure 52 SEM image of the clinker SD2-6 with larger ye'elimite crystallites and EDS spectrum. Image acquired at Zentrum für Werkstoffanalytik in Lauf, Germany.
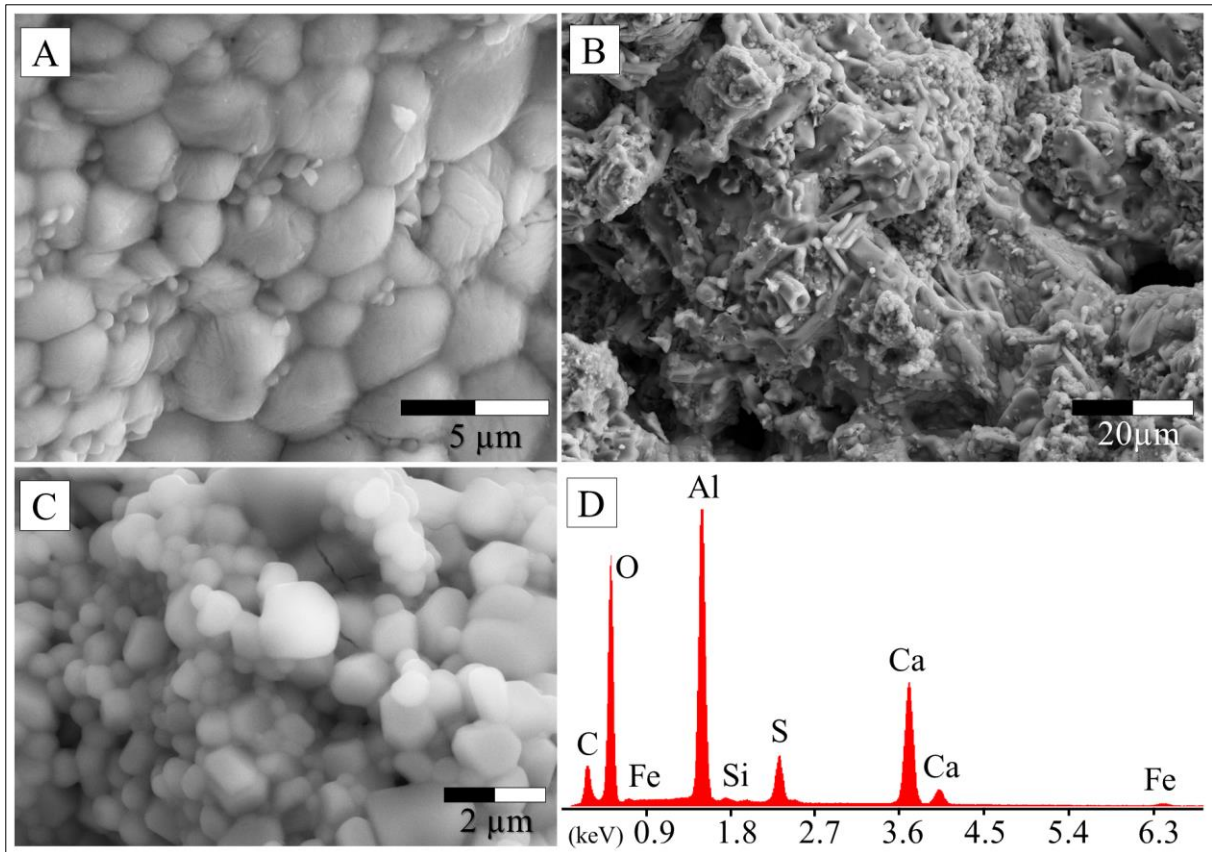
Figure 53 A: cobblestone larnite aggregates in the clinker SD2-6; B: morphology of the clinker SD2-OP with ye'elimite and prismatic ternesite crystals; C: ye'elimite crystallites in clinker SD2-OP and EDS measurement of the whole area (D). Images acquired at Zentrum für Werkstoffanalytik in Lauf, Germany.
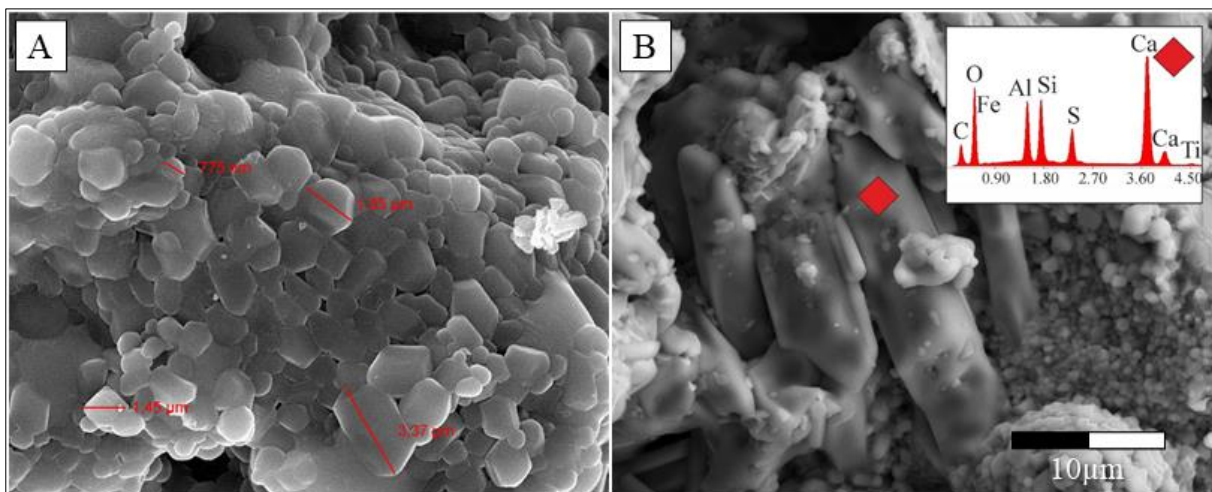
Figure 54 A: SEM image of the clinker SD2-6 with crystallites of ye'elimite. B: Micromorphology of the clinker SD2-OP and EDS analysis of a ternesite crystal. Image A acquired at University of Halle, and image B at Zentrum für Werkstoffanalytik in Lauf, Germany.

4.2 SD3 clinkers produced with Al-poorer Belterra Clay of Branco pilot-mine

The clinkers made with Belterra Clay from the Branco pilot-mine were produced following the mixture compositions of the statistical design of experiments SD3 (Table 9), which the main results were published in Negrão et al. (2022) . In general, the produced clinkers have yellowish colourations when synthesised at 1200 °C, whereas the same raw meal compositions originate in yellowish-grey and grey clinkers when clinkered at 1250 °C and 1300 °C (Figure 55).
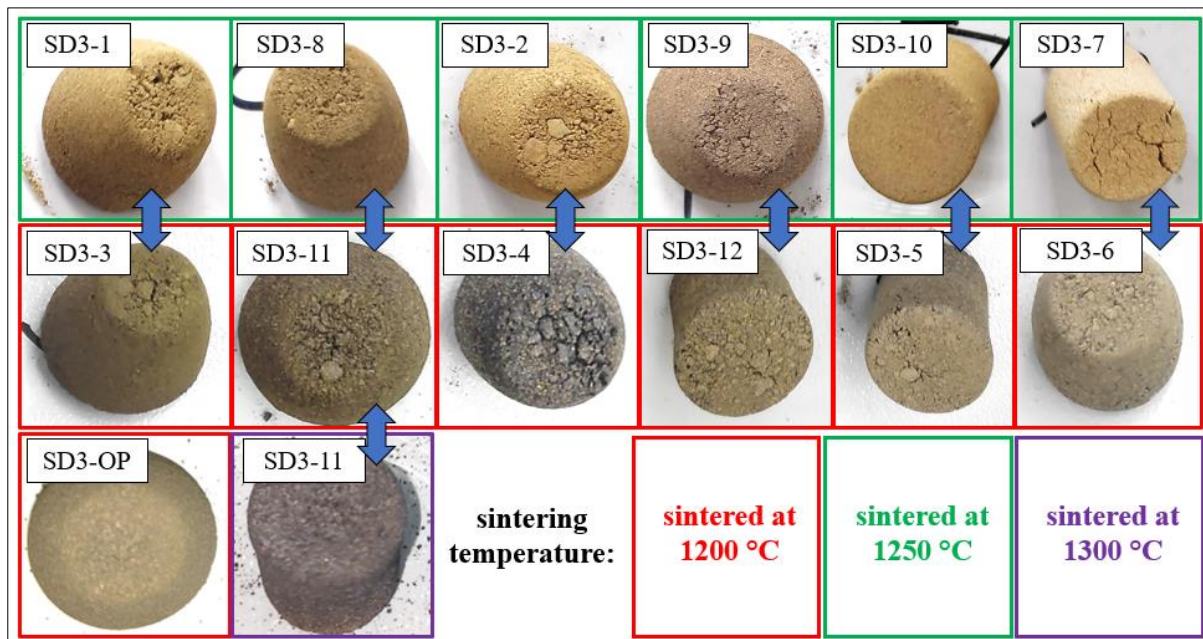
Figure 55 Photos of the produced clinkers using the statistical design of experiments SD3. The blue arrows indicate clinkers produced out of the same raw meal composition (Table 9), and the coloured frames of each clinker indicated their synthesised temperature. Note the darker colours of clinkers produced with higher temperatures of 1250°C and 1300 °C.

After the evaluation of the results obtained using the design of experiments, a clinker with optimised ye'elimite contents (clinker SD3-OP) was produced. Another clinker, with analogous raw meal composition of SD3-OP, was produced with boron doping (clinker SD3-OP-B).

Finally, a clinker was produced using this same Belterra Clay sample from the Branco pilot-mine. But instead of using DoE, the raw meal composition of this clinker was formulated after stoichiometric calculations (as described in 2.3.2) to obtain as much as possible of ye'elimite. This clinker is hereinafter named BRA-SM and was synthesised at 1250 °C and 1300 °C. Because the clinkers SD3-OP-B and BRA-SM were not produced in the view of the DoE, they are described separately in the sections 4.2.2 and 4.2.3.

4.2.1 Phase composition

The phase composition of the clinkers produced out of the Branco Belterra Clay is similar to those produced using Belterra Clay from the Círiaco pilot-mine (SD1 and SD2). Ye'elimite, larnite, ternesite, brownmillerite, Fe-perovskite, gehlenite, free-lime, and anhydrite were identified by XRPD. After the XRPD-Rietveld quantification, no amorphous was quantified in the clinkers using the external standard approach, except for the clinker doped with boron SD3-OP-B. The phase contents of these clinkers, as well as their raw mixture composition and clinkering temperatures, are displayed in Table 9.

The contents of ye'elimite predicted by DoE are close to the quantified by Rietveld-XRPD in the produced clinkers (Figure 56). As for the SD1 and SD2 clinkers, the firing temperature of 1250 °C resulted in clinkers with higher ye'elimite contents (Table 9), and both the cubic and the orthorhombic modifications of this mineral were identified. The maximum predicted amount of ye'elimite by the design of experiments was 30%, whereas a close value of 32% was obtained in the clinker SD3-11. The optimised clinker SD3-OP had 34% of ye'elimite.
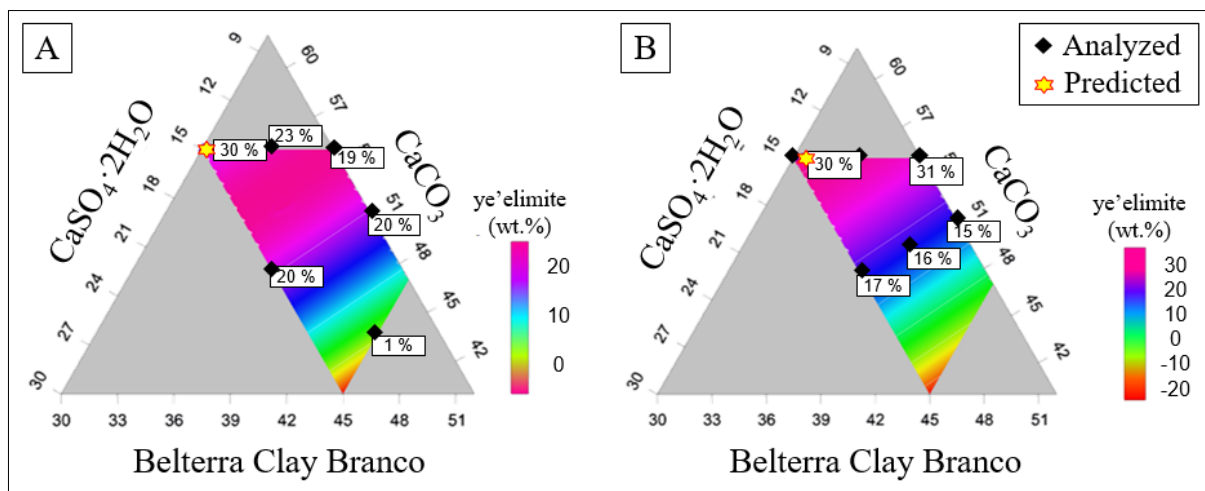
Figure 56 Predicted ye'elimite contents and measured ye'elimite contents in the clinkers using the design of experiments SD3 at the 1200 °C (A) and 1250 °C (B) clinkering temperature.

Table 9 Phase composition and raw composition (wt.%) of the produced clinkers according to the Statistical Design SD3, using Belterra Clay from the Branco pilot-mine.

clinker	ye'elimite			belite		brownm.	gehlenite	ternesite	anhydrite	Fe-perov.	lime	amorphous	R-indicators		raw composition			Temp. (°C)
	o.	c.	total	β	$\alpha_{H'}$								GOF	Rwp	BTC	$CaCO_3$	Gyps	
SD3-1	22	-	22	11	-	11	7	43	2	1	4	-	1.1	3.8	30	55	15	1200
SD3-2	19	-	19	25	-	12	20	21	-	2	1	-	1.1	3.9	37	55	8	1200
SD3-3	27	-	27	35	-	14	-	16	6	1	1	-	1	3.6	30	55	15	1250
SD3-4	20	9	30	37	-	4	19	4	-	8	-	-	1.2	4.0	37	55	8	1250
SD3-5	12	5	17	12	-	-	39	21	6	6	-	-	1.2	3.7	37.5	47.5	15	1250
SD3-6	12	5	17	15	-	-	45	15	4	6	-	-	1.2	3.8	39.3	49.3	11.5	1250
SD3-7	1	-	1	3	-	-	73	10	9	5	-	-	1.6	5.3	45	43.5	11.5	1200
SD3-8	23	-	23	20	-	12	10	33	0	1	1	-	1.1	3.8	33.5	55	11.5	1200
SD3-9	14	6	20	23	-	-	35	13	2	7	-	-	1.2	4.1	41	51	8	1200
SD3-10	15	5	20	15	-	4	24	23	8	6	-	-	1.2	4.0	37.5	47.5	15	1200
SD3-11	20	12	32	30	-	8	7	18	1	4	-	-	1.1	3.7	33.5	55	11.5	1250
SD3-11[HT]	23	17	40	47	-	-	-	-	2	11	-	-	1.4	4.9	33.5	55	11.5	1300
SD3-12	15	-	15	18	-	-	51	10	1	6	-	-	1.3	4.0	41	51	8	1250
SD3-OP	21	13	34	44	-	12	-	6	2	3	-	-	1.1	4.1	33	57	10	1250
SD3-OP-B	17	13	30	-	41	2	5	-	2	4	-	16	1.1	7.0	33	57	10	1250
BRA-SM	22	12	**34**	49	-	9	2	-	-	5	-	-	1.2	4.4	34.4	58.7	6.9	1250
BRA-SM[HT]	19	16	**35**	51	-	6	-	-	-	8	-	-	1.1	4.3	34.4	58.7	6.9	1300

SD3-X [HT] = raw material compositionally analogous clinker produced again at a higher temperature. Ye'elimite: o = orthorhombic and c = cubic modifications; brownm. = brownmillerite; belite: β (larnite) and $\alpha_{H'}$ (flamite) modifications; Fe-perov. = Fe- perovskite; Lime = free-lime (CaO); R-indicators are the Rietveld refinement indicators, GOF = goodness of fit and Rwp = R weighted profile; BTC = Belterra Clay; Gyps = gypsum; Temp. = firing temperature in Celsius grade.

The clinkers with the highest ye'elimite contents were produced out of raw mixtures with Belterra Clay/$CaCO_3$ ratios close to 0.6. These clinkers also had the lowest gehlenite contents and no free-lime (i.e., clinkers SD3-8 and SD3-11). Belterra Clay/$CaCO_3$ ratios close to 0.8, or higher resulted in clinkers (i.e., SD3-5, -6, -7, -9 and -12) with much more gehlenite. Moreover, clinkers formed from raw mixtures with Belterra Clay/$CaCO_3 \geq 0.8$ have lower brownmillerite contents and higher amounts of Fe-perovskite (Table 9).

Larnite was, as in the clinkers SD1 and SD2, the only C_2S polymorph present in the SD3 clinkers. Up to 44% of larnite was quantified in the clinker SD3-OP, and this is the main phase capturing Belterra Clay' silica. High amounts of ternesite were formed by the excess of calcium sulfate, to that necessary to form ye'elimite. This excess further resulted in clinkers with some left unreacted anhydrite.

In general, brownmillerite contents are opposite to that of Fe-perovskite. The lower Ca input (when Belterra Clay/$CaCO_3 \geq 0.8$) favoured the formation of Fe-perovskite [$Ca(Ti_{0.75}Fe_{0.25})O_{2.88}$] over brownmillerite [$Ca_2(Al,Fe)_2O_5$], which is more enriched in Ca. Similarly, Yao et al. (2020) observed that lower amounts of CaO in the raw meal of similar clinkers resulted in decreased amounts of brownmillerite. Not only the higher Belterra Clay/$CaCO_3$ ratios were observed to influence the predominance of Fe-perovskite over brownmillerite, but also the higher clinkering temperatures as observed in SD2 clinkers and described below.

SD3-11 was clinkered again at 1300 ℃ to check if the increase in temperature causes any changes in its phase assemblage. The clinker presented higher amounts of ye'elimite and larnite at 1300 ℃. The content of Fe-perovskite increased, whereas brownmillerite disappeared (Figure 57). Ternesite was absent, confirming that it is unstable at 1300 ℃ (Hanein et al., 2017; Liu et al., 2021) and under the experimental setup of the present work. Besides the slightly increased ye'elimite contents, the clinkers produced at 1300 ℃ were much harder to grind.
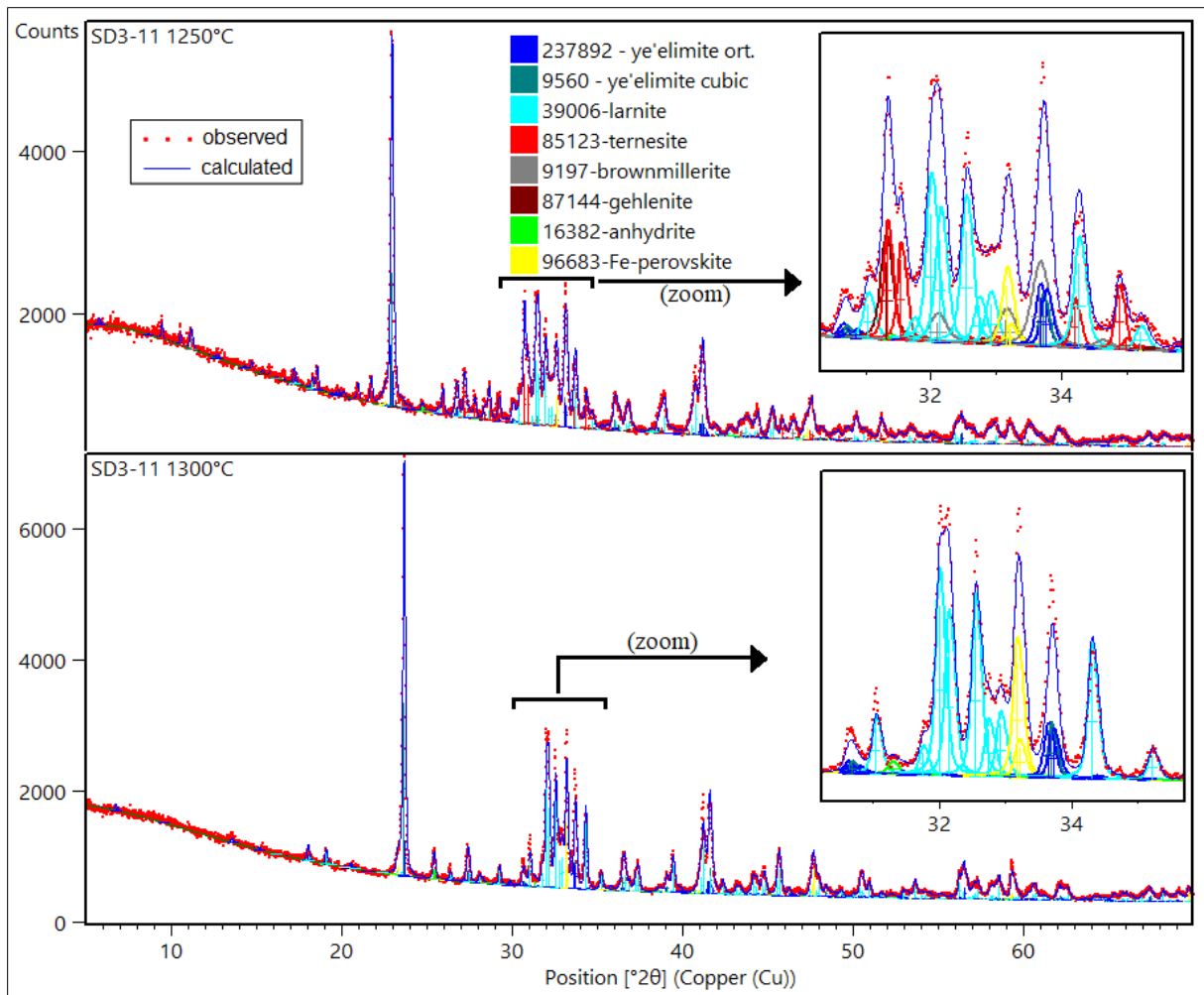
Figure 57 Rietveld –refined XRPD patterns of clinker SD3-11 produced at 1250 °C and 1300 °C. Note the decrease in brownmillerite and the increase in Fe-perovskite (yellow) at 1300 °C. The quantified phase contents are displayed in Table 9.

4.2.2   Stabilisation of $\alpha_{H'}$-belite in a boron-doped clinker

The clinker SD3-OP was doped with 0.56% of boron to stabilise the $\alpha_{H'}$-C_2S modification (flamite). This chosen amount corresponds to a ratio of 0.2 mol of B to 1 mol of belite, considering the belite contents in the clinker SD3-OP without B addition. This amount of B is considered enough to convert all the larnite into flamite (Martín-Sedeño et al., 2010; Li et al., 2019).

The resulting boron-doped clinker, referred to as SD3-OP-B, had a reddish-brown colour (Figure 58) different from the colourations observed in the other clinkers and was much harder to grind. After removing the clinker from the alumina crucible, it showed a molten morphology at its base and some residual impregnation of it in the inner bottom of the crucible, which was not observed in the other produced clinkers.
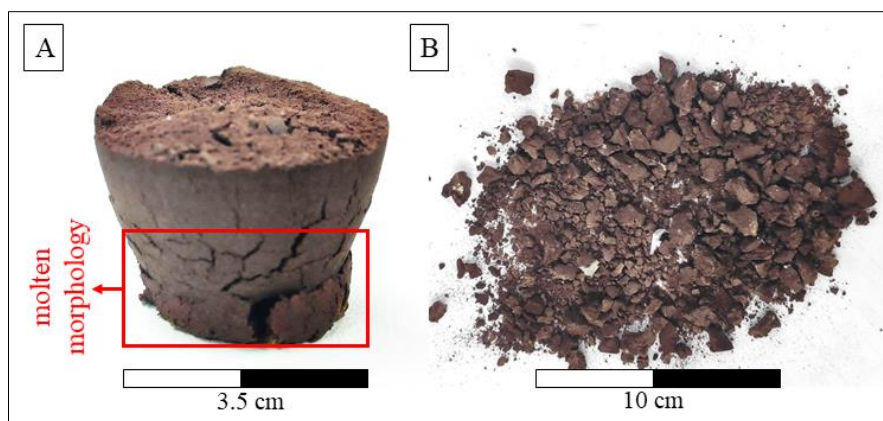
Figure 58 Boron-doped clinker SD3-OP-B (produced at 1250 °C) with molten morphology after its removal from the alumina crucible (A), and after crushing (B).

All belite in SD3-OP-B was successfully stabilised into the flamite polymorph ($\alpha_{H'}$-C2S) (Figure 59). The clinker SD3-OP-B has 30% of ye'elimite, with a predominance of the cubic (17%) over the orthorhombic modification (13%) (Figure 59). Compared to its analogous and non-doped composition (SD3-OP), the brownmillerite contents sharply decreased from 12 to 3% in the doped one, while Fe-perovskite contents increased from 3 to 5%. Ternesite was not identified in the doped clinker, and 6% of gehlenite was formed.
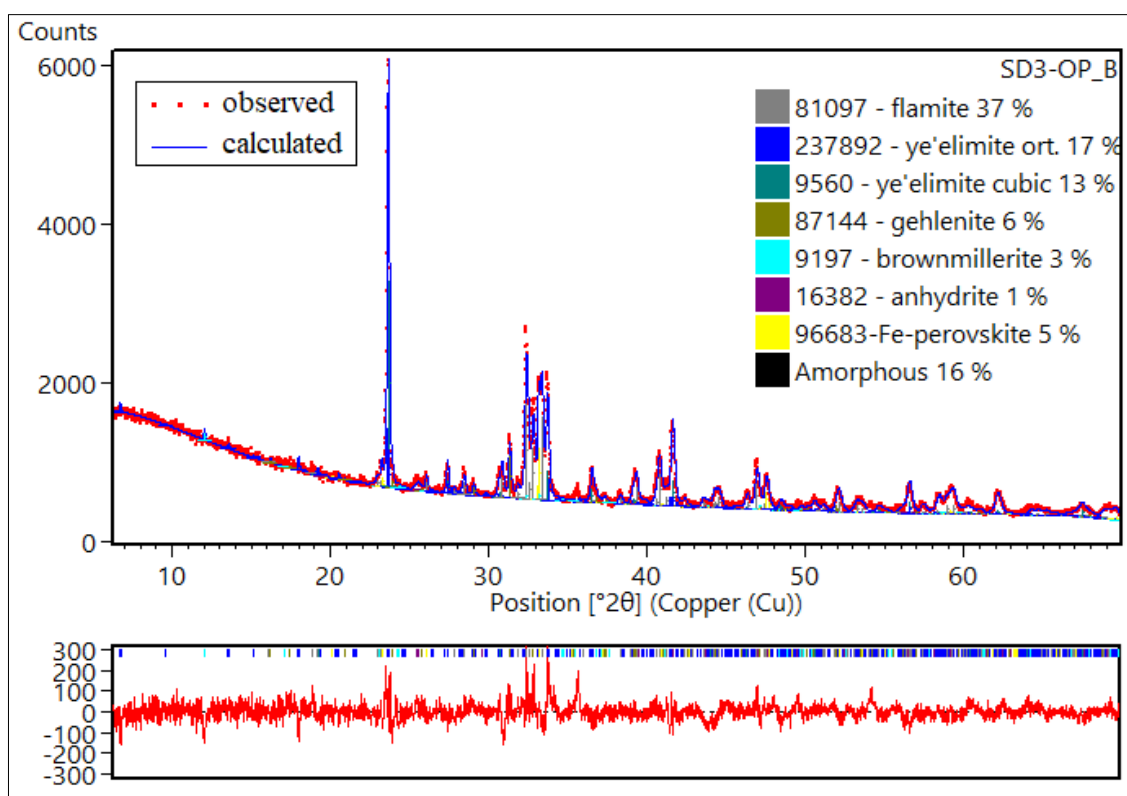
Figure 59 XRPD-Rietveld refined pattern of clinker SD3-OP-B. GOF = 1.1, Rwp = 7.0.

The major differences between the doped and non-doped composition are their amorphous contents. SD3-OP-B has 16% of amorphous, whereas no amorphous was quantified in the non-doped one. The indications of melting and the high amorphous content can be explained by boron, which is known as a strong fluxing agent that stabilises the liquid phase and increases clinker viscosity (El Hayek et al., 2017; Ben Haha et al., 2019), consequently forming higher amorphous amounts after rapid air-cooling.

4.2.3   Stoichiometric modelled clinker BRA-SM

The clinker BRA-SM has a yellowish-grey colouration (Figure 60). Its ye'elimite and larnite contents are close to the stoichiometric calculated amounts of these phases, for the same composition produced at 1250 °C and 1300 °C (Table 10).
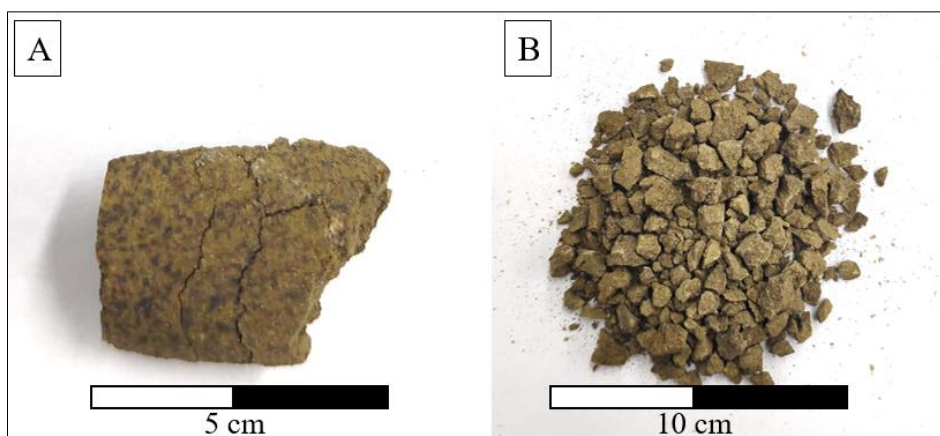
Figure 60 Clinker BRA-SM produced at 1250 °C after removal from the alumina crucible (A) and crushed (B).

Differences from the goal composition were expected because no solid solution in the phases was considered for the stoichiometric calculations. The most obvious difference is for ferrite, for which Al-free C_2F was computed and C_4AF (brownmillerite) was formed, which is much more common in CSA and OPC.

Likewise, the Fe-free perovskite (CT) was considered for the stoichiometric calculations, but Fe-rich perovskite was formed. Fe-perovskite contents were also higher and seemed to increase by the expenses of brownmillerite in the clinker produced at 1300 °C (Table 10), confirming again the higher stability of Fe-perovskite at this higher temperature.

Table 10 Raw meal composition to produce BRA-SM clinker, and its phase compositions calculated stoichiometrically, and quantified by XRPD-Rietveld after clinkering at 1250 °C and 1300 °C.

		BRA-SM Goal*			BRA-SM 1250 °C	BRA-SM 1300 °C
phase	ye'elimite	36	ye'elimite	ort.	22	19
				cub.	12	16
				total	34	35
	larnite	52	larnite		49	51
	ferrite (C_2F)	10	brownmillerite		9	6
	perovskite (CT)	2	Fe-perovskite		5	8
			gehlenite		2	-
	Rietveld indicators		GOF		1.44	1.63
			Rwp		4.53	4.69
raw meal	bauxite washing clay	34.4	-		34.4	34.4
	$CaCO_3$	58.7	-		58.7	58.7
	$CaSO_4 \cdot 2H_2O$	6.9	-		6.9	6.9

Ye'elimite: ort. = orthorhombic and cub. = cubic modifications; R-indicators are the Rietveld refinement indicators, GOF = goodness of fit and Rwp = R weighted profile. Goal*= stoichiometric modelled goal composition calculated for the BRA-SM clinker.

The raw meal composition of BRA-SM was defined after the stoichiometric calculations to maximise ye'elimite in this clinker. This composition is very close to the raw meal compositions defined by DoE for the clinkers with the highest ye'elimite contents (clinkers SD3-11 and SD3-OP, Table 9). The fundamental difference is related to the $CaSO_4 \cdot 2H_2O$ contents in the raw mixtures, which were higher for SD3-11 and SD3-OP (Table 9). Consequently, these clinkers formed extra ternesite and have some left anhydrite, which was not observed in the clinker BRA-SM.

4.2.4 Microstructure

The clinkers SD3-11, SD3-OP, and SD3-OP-B have the composition with the highest ye'elimite contents compared to all the other clinkers produced from Belterra Clay of Branco pilot-mine (SD3). Therefore, they were selected for SEM-EDS studies.

The main phases ye'elimite and larnite are easily distinguished by their grey contrasts in the BSE images, which can be further assisted with EDS-elemental mappings (Figure 61). After adjusting the brightness and contrast of the images, ye'elimite is dark-grey, larnite is middle-grey and the iron-rich phases brownmillerite and/or Fe-perovskite are light-grey (whitish). These last phases cannot be distinguished in the BSE images. Nevertheless, the elemental

mapping (Figure 61) indicates that the light-grey phase is mostly Fe-perovskite, confirming the previously Rietveld-quantification for this phase in sample SD3 produced at 1300ºC (Table 9).
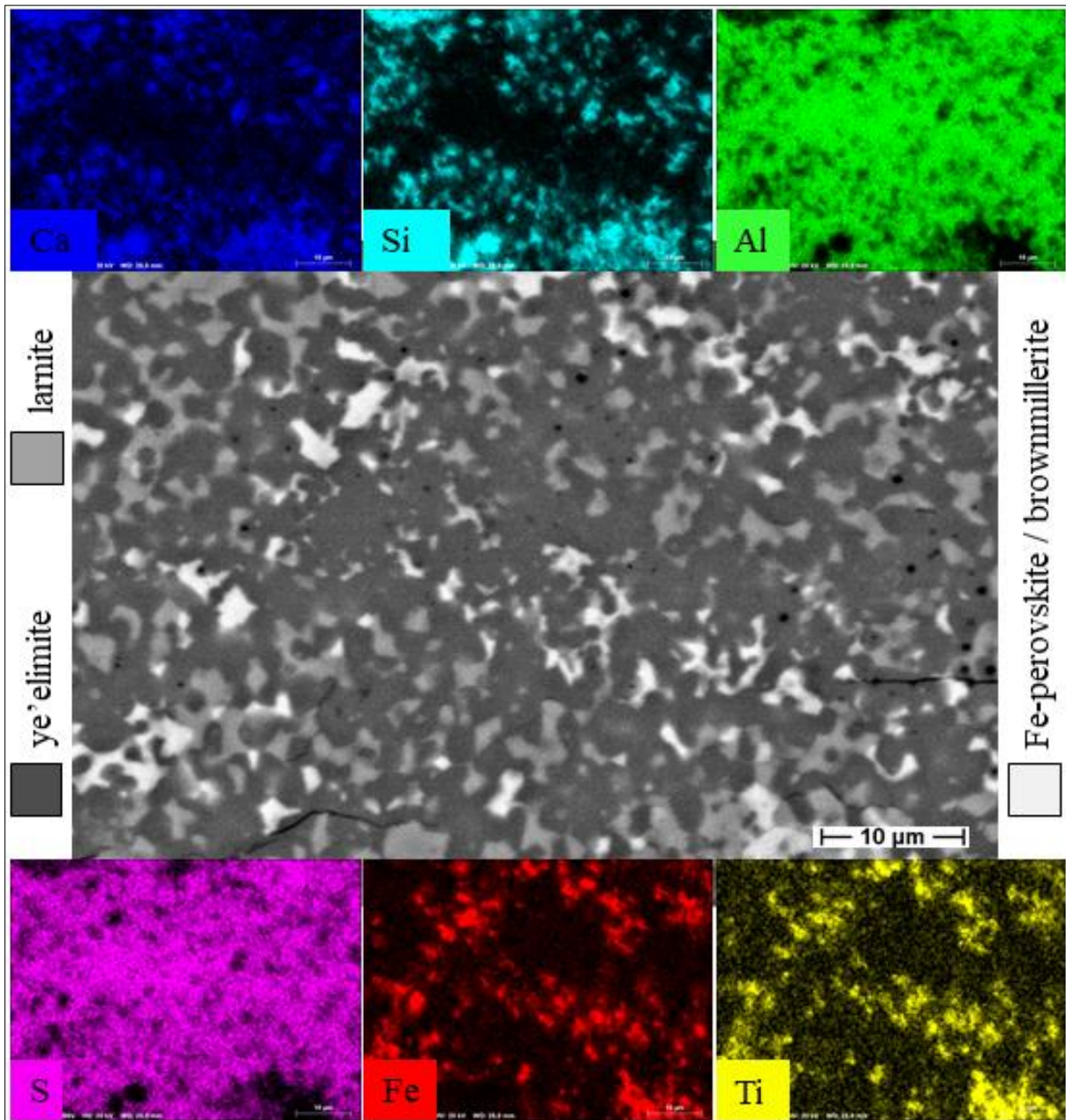
Figure 61 Back-scattered electron (BSE) image and EDS-elemental mappings of a polished section of clinker SD3-11 produced at 1300 ºC. Image and mapping acquired at the University of Halle.

The clinkers have a porous matrix with multiphase aggregates measuring hundreds to some few millimetres (Figure 62). The increase in the firing temperature to 1300 °C resulted in larger crystallites and in a higher complexation and densification of the aggregates, which showed a more closed structure. The more closed structure might cause a reduced porosity that explains the harder-to-grind clinkers produced at 1300 °C.
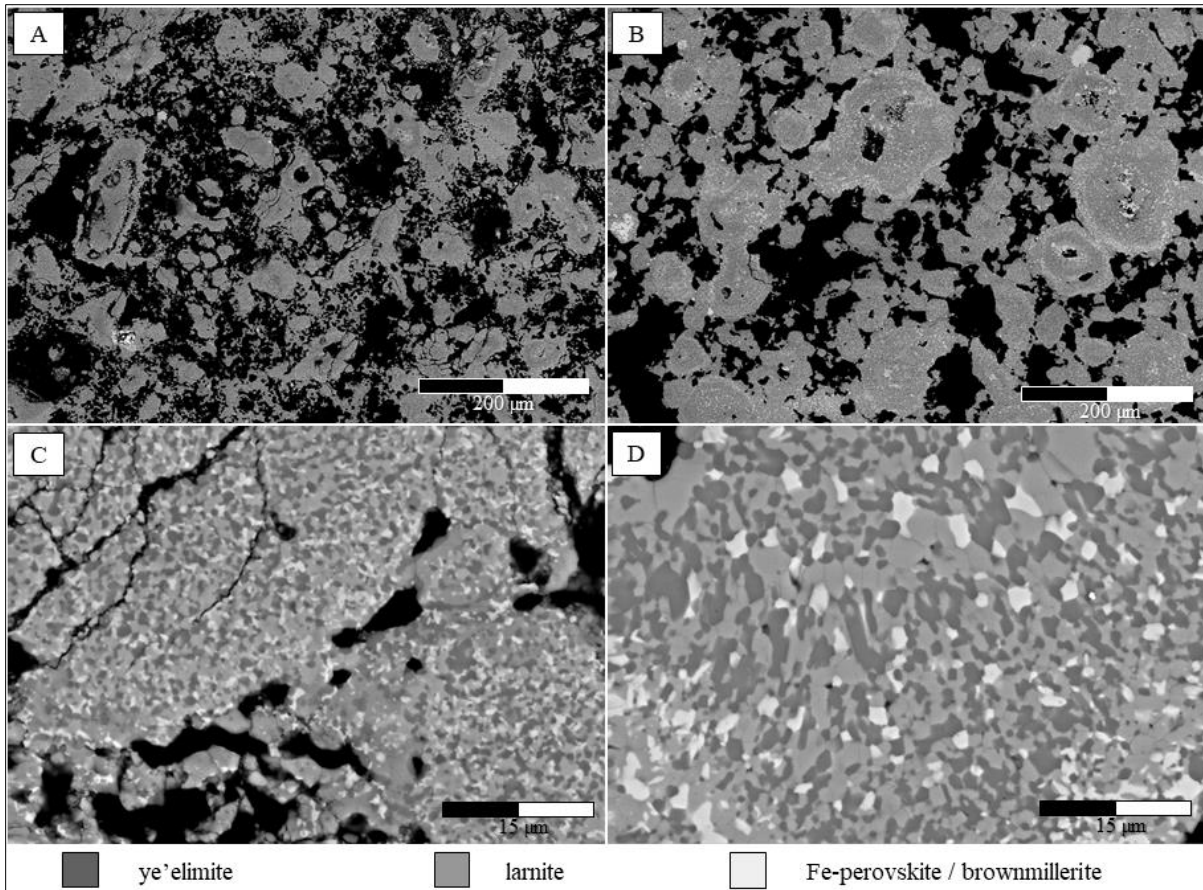
Figure 62 BSE images of the clinker SD3-11 produced at 1250 ℃ (A and C) and at 1300 ℃ (B and D). Note the increased crystallite sizes from C to D. Images acquired at Zentrum für Werkstoffanalytik in Lauf, Germany.

The boron addition in the clinker SD3-OP-B also resulted in similar changes in the microstructure of the clinker (Figure 63) when compared to the effects of the increased clinkering temperature. The non-doped clinker SD3-OP is much more porous and softer than the doped one. The size of the crystallites also increased with the boron additions and the phases became more edge in the SD3-OP-B.
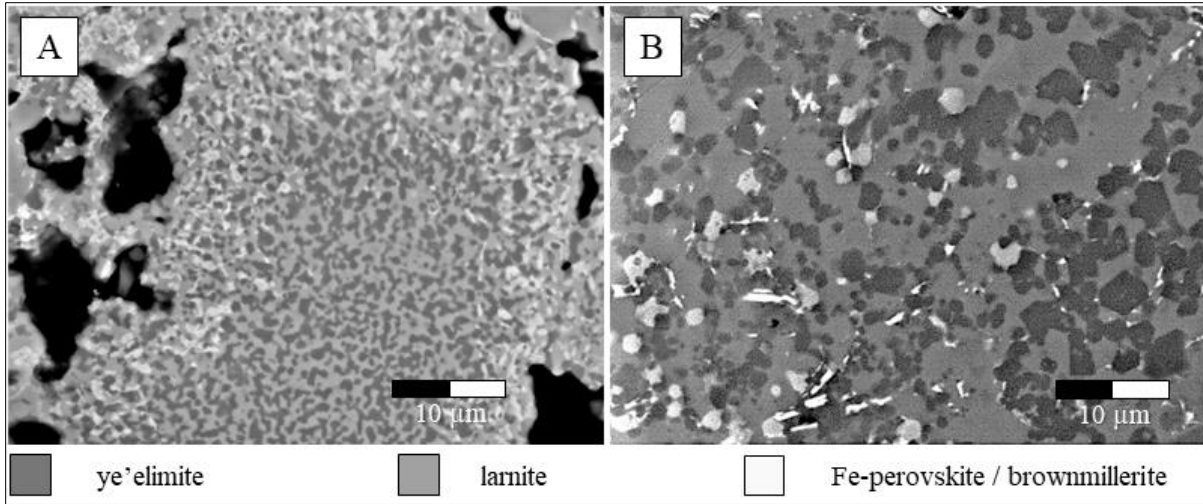
Figure 63 BSE images showing the effects of boron doping. A: clinker SD3-OP without boron doping; B: clinker SD3-OP-B doped with 0.56% of boron. The black portions are porous filled the epoxy resin. Note de different sizes and shapes of the phases. Image acquired at the University of Halle.

Whereas the EDS mappings helped to distinguish the phases in the clinker, EDS semi-quantitative analyses of the crystallites were used to determine the average chemical composition of the phases. However, EDS point analyses of the very small crystallites often resulted in EDS spectra influenced by the composition of the surrounded phases. That was especially the case for brownmillerite, which usually formed elongated crystallites in the clinkers (Figure 64).
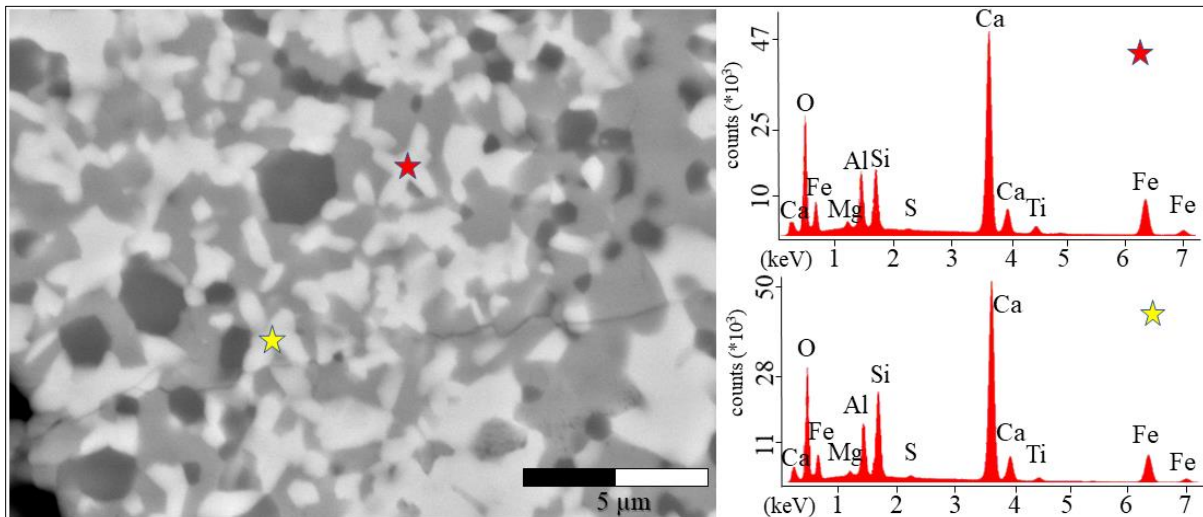
Figure 64 Polished section of the clinker SD3-11 produced at 1300 °C showing light-grey elongated brownmillerite crystallites in the clinker matrix. The point EDS analyses show the main compositions with Ca, Fe, Al and some Ti, but apparently affected by the neighbouring phases with Si (larnite, middle-grey), and with Al and S (ye'elimite, dark-grey). Image acquired at Zentrum für Werkstoffanalytik in Lauf, Germany.

When larger crystals were found (i.e., Figure 65), their chemical composition was semi-quantitatively determined as follows:

- ye'elimite has few amounts of iron in all the SD3 clinkers. The S-normalised chemical composition after measuring 6 larger ye'elimite crystallites is $Ca_{4,64}Al_{5,08}Fe_{0,21}S_{1,00}O_{15,46}$;

- larnite, after measuring 14 crystals, has the average Si-normalised composition $Ca_{2,36}Si_{1,00}Al_{0,05}O_{3,44}$.

- gehlenite, has the Si-normalised composition $Ca_{2,41}Al_{1,81}Fe_{0,18}Si_{1,00}O_{7,32}$, after the measurement of 20 crystals.

- Fe-perovskites have distinct compositions with varying Fe and Ti contents. Its Ca-normalised average composition, after analysing 4 crystallites, is $Ca_{1,00}Al_{0,04}Fe_{0,27}Ti_{0,41}Si_{0,13}O_{2,76}$.

- The Ca-normalised average composition of five crystallites of brownmillerite is $Ca_{2,00}Al_{0,47}Fe_{0,87}Ti_{0,09}Si_{0,23}O_{4,68}$
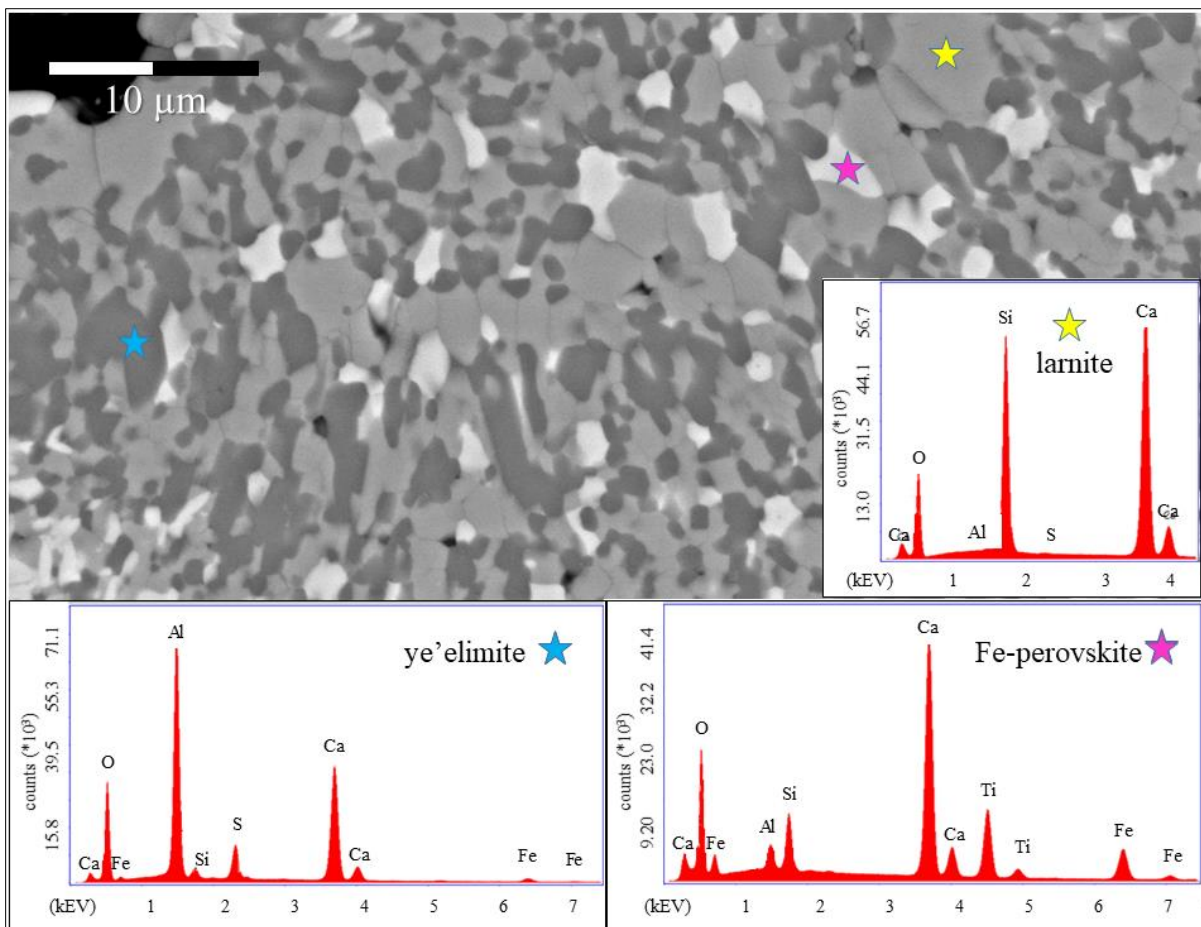
Figure 65 BSE image of clinker SD3-11 produced at 1300°C and EDS spectra of ye'elimite, Fe-perovskite and larnite. Image acquired at Zentrum für Werkstoffanalytik in Lauf, Germany.

All the SD3 clinkers studied under SEM have similar micromorphology, which is also similar to the SD2 clinkers produced using Belterra Clay from the Círiaco pilot-mine. Ye'elimite and larnite have rounded crystallite shapes, usually measuring 1 to 4 µm in an open porous matrix, and ternesite form prisms like in the SD2 clinkers (Figure 66)
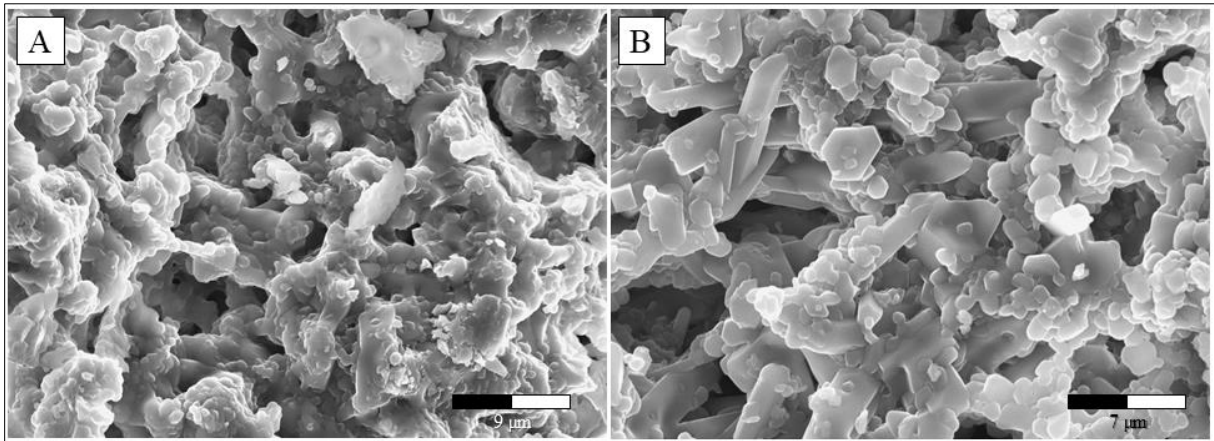
Figure 66 A: Aggregates of ye'elimite in the clinker SD3-11. B: ye'elimite and prisms of ternesite in the clinker SD3-OP. Image acquired at the University of Halle.

4.3 Clinkers produced using Bauxite Washing Clay

Considering the chemical and mineralogical similarities between the bauxite washing clay and the Belterra Clay, and the results from the previous experiments, a narrowed composition range of the raw materials was chosen to produce the clinkers using bauxite washing clay. From the previous experiments, it was observed that the stoichiometric modelling can be used as a good proxy to define the composition of the raw meal.

4.3.1 Phase Composition

Four clinkers using bauxite washing clay were produced (Table 11). The raw composition (bauxite washing clay, $CaCO_3$ and $CaSO_4 \cdot 2H_2O$) of the clinker BWC-SM (clinker made out of bauxite washing clay after stoichiometric modelling). Two other clinkers were produced by slightly varying the raw meal composition defined for BWC-SM. They are named respectively BWC-2, produced with higher amounts of bauxite washing clay and gypsum, and BWC-3 with the same bauxite washing clay amount of BWC-SM but with more gypsum in the raw meal. Finally, the clinker BWC-3[HT] was produced using the same raw mixture composition as BWC-3, but at a higher temperature of 1300 °C.

Table 11 Phase and raw meal composition (in wt.%) of the clinkers produced using the Bauxite Washing Clay at 1250 °C.

		BWC-SM Goal*			BWC-SM	BWC-2	BWC-3	BWC-3[HT]
phase				ort.	24	20	29	25
	ye'elimite	46	ye'elimite	cub.	18	17	17	19
				total	42	37	45	44
	larnite	41	larnite		39	29	40	39
	ferrite (C$_2$F)	12	brownmillerite		9	1	4	3
	perovskite (CT)	2	Fe-perovskite		5	8	9	9
			gehlenite		3	20	1	2
			amorphous		2	6	2	3
Rietveld indicators			GOF		1.24	1.33	1.26	1.22
			Rwp		4.43	4.69	4.48	4.31
raw meal	bauxite washing clay	37.6	-		37.6	40	37.6	37.6
	CaCO$_3$	53.7	-		53.7	50	52.9	52.9
	CaSO$_4$·2H$_2$O	8.7	-		8.7	10	9.5	9.5

Ye'elimite: ort. = orthorhombic, cub. = cubic; R-indicators are the Rietveld refinement indicators, GOF = goodness of fit and Rwp = R weighted profile. Goal*= stoichiometric modelled goal composition calculated for the BWC-SM clinker. BWC-3[HT] = BWC-3 clinker produced at 1300 °C.

The clinkers are composed of ye'elimite, larnite, brownmillerite, Fe-perovskite, gehlenite and amorphous (Table 11). Ye'elimite occurs in the orthorhombic and cubic polymorphs. Ye'elimite and larnite are the most abundant phases of the clinkers. The higher contents of ye'elimite over larnite define the clinkers produced using bauxite washing clay as CSAB clinkers.

The total amounts of ye'elimite (42%) and larnite (39%) in the clinker BWC-SM is under the projected by the stoichiometric computations of 46% and 42%, respectively. That is mainly explained by part of the Al in the brownmillerite and gehlenite (which also has Si). BWC-SM also has higher Fe-perovskite amounts, as similarly observed in the previous clinkers produced with Belterra Clay.

The changes in the raw meal composition to produce BWC-2 resulted in lower ye'elimite and larnite contents, as well as much more gehlenite (20%) and Fe-perovskite (8%), whereas brownmillerite contents decreased sharply.

The highest ye'elimite content (45%) was observed in the clinker BWC-3 (Figure 67), which has a raw meal composition with slightly higher amounts of gypsum compared to the clinker BWC-SM. The amount of larnite in the clinker BWC-3 is almost the same as in the clinker BWC-SM. The main difference is that the BWC-3 has less gehlenite and opposite contents of Fe-perovskite and brownmillerite.
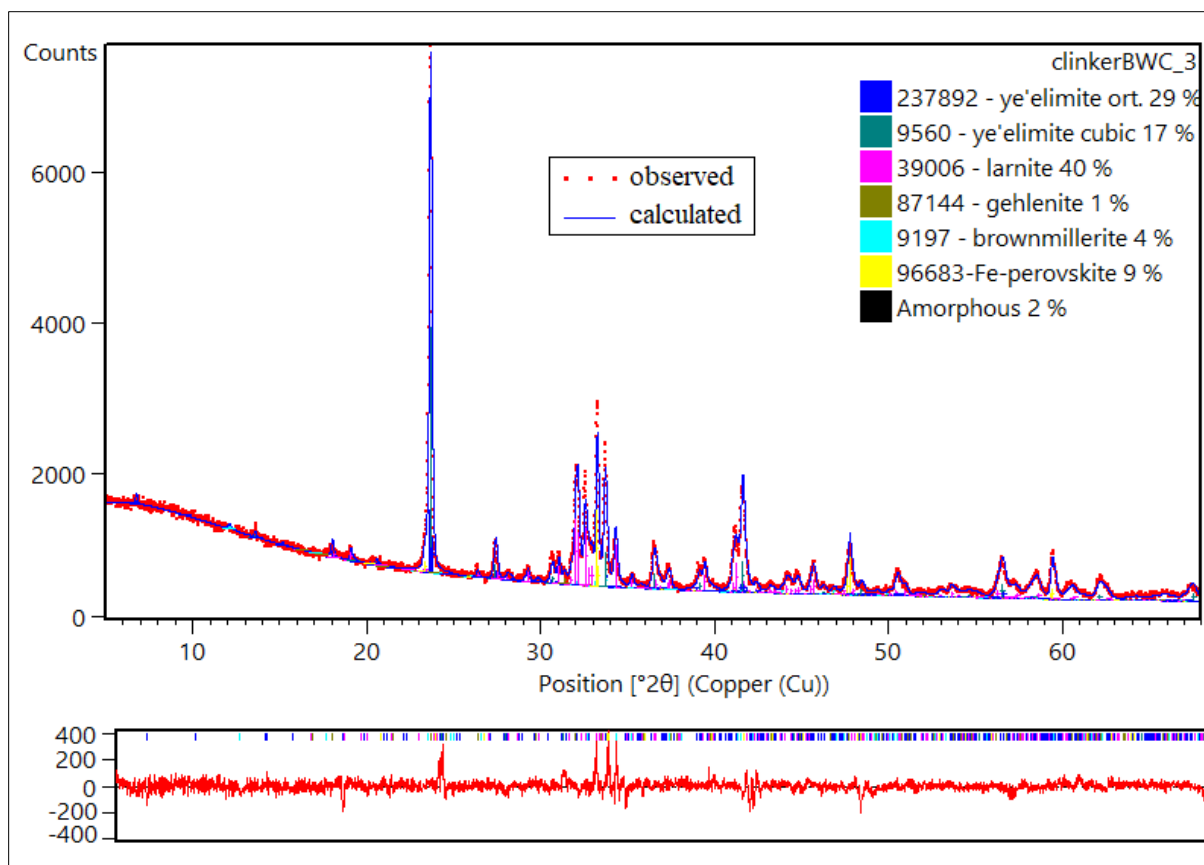
Figure 67 Rietveld-refined XRPD pattern and different plot of the clinker BWC-3 produced at 1250 °C using the bauxite washing clay residue. GOF = 1.26, Rwp = 4.48

The clinker BWC-3^{HT}, produced at 1300 °C, has an almost identical mineralogical composition to BWC-3, but with a slightly lower (1% less) amount of ye'elimite and larnite. Moreover, the proportion of cubic ye'elimite over the orthorhombic form is higher in the clinker produced at 1300 °C.

The SO$_3$ contents of both BWC-3 clinkers produced either at 1250 °C or 1300 °C are lower than the calculated amount (i.e., expected, Table 12) considering the initial gypsum contents in its raw meal. This indicates that some small amount of SO$_3$ was lost during clinkerization, and this loss was higher for the clinker produced at 1300 °C.

Table 12 Expected and measured contents (by XRF) of SO$_3$ in the BWC-3 clinker produced at 1250 °C and at 1300 °C.

	expected in the clinker	clinker produced at 1250 °C	clinker produced at 1300 °C
SO$_3$ (wt.%)	6.55	5.92	5.52

4.3.2   Thermal phenomena during clinker formation

Thermogravimetric analysis coupled with differential scanning calorimetry and mass spectrometry was conducted to identify the thermal events during the heating of the raw mixture to produce the clinker BWC-3 (Figure 68). The total mass loss of the raw mixture from 35 to 1300 °C was 34.80%.

The mass loss of up to 1000 °C was 31.96%, a value very close to the calculated after the total loss on ignition (LOI = 31.91%, Table 13) of the raw mixture, considering the loss of CO_2 (LOI attributed to $CaCO_3$), and H_2O (LOIs of gypsum and of the bauxite washing clay). The subsequent mass loss of 2.84% from 1000 to 1300 °C can be attributed to losses of SO_2 or O_2.

Table 13 Calculated relative proportions and total of loss on ignition (LOI) of the raw meal of the clinker BWC-3.

clinker raw meal component	wt.% in clinker BWC-3	LOI proportion	calculated LOI in the clinker raw meal
$CaCO_3$	53.7	0.433	23.27 %
gypsum	8.7	0.205	1.78 %
bauxite washing clay	37.6	0.187	6.86 %
Total calculated LOI of the raw meal			31.91 %

At least eight different main events were identified in the TGA and DSC curves due to the heating and consequent clinkerization of the raw mixture (Figure 68). The coupled mass spectrometer permitted to identify the ion current curves of H_2O, CO_2, and SO_2, and to associate them to the different events during the dehydration and decarbonisation of the raw material, and the later clinkerization processes. These events are described below and some of the possible chemical reactions involved in this process are suggested according to the literature and the mineralogy of the produced clinkers.

In Event 1, gypsum is destabilised and water is released (Strydom et al., 1995) as seen in the ion current curve of H_2O (m=18). Consequently, anhydrite was formed according to Equation 4.1:

$$CaSO_4 \cdot 2H_2O \xrightarrow{90-160\,°C} CaSO_4 + 2H_2O \text{ (Equation 4.1)}$$
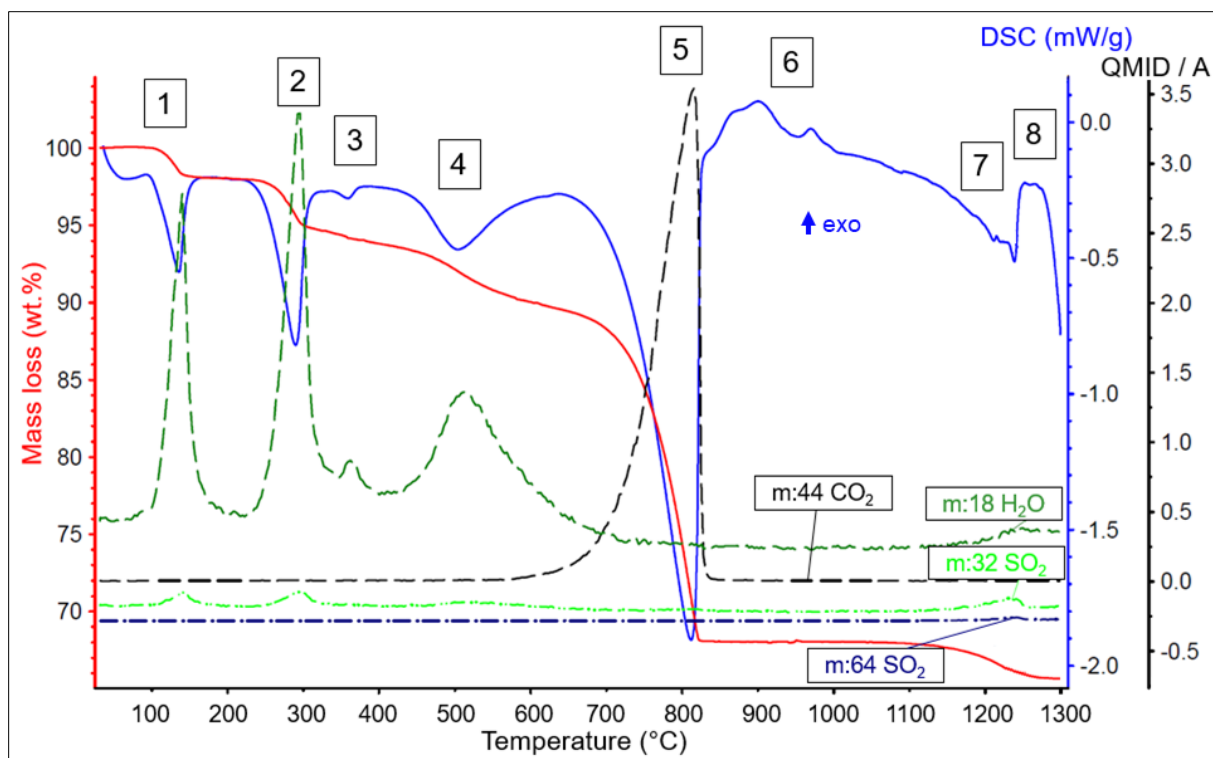
Figure 68 Thermal analysis of the clinkering process of BWC-3 showing the thermogravimetric curve (red), the DSC curve (blue), and the QMID (quasi multiple ion detection) current curves of H_2O (dark green), CO_2 (black), and SO_2 (light green). The sample was measured with a heating rate of 10 K/min. The numbered events 1 to 8 are explained in the text.

Events 2 to 4 are related to the dehydroxylation of the minerals of the bauxite washing clay, as previously shown in section 3.2.3. Gibbsite (Equation 4.2), goethite (Equation 4.3), and kaolinite (Equation 4.4) dehydroxylated to form, respectively, ρ-Al_2O_3 (Colombo and Violante, 1996), hematite (Schulze and Schwertmann, 1984) and metakaolinite (Yeskis et al., 1985), as below:

$$2Al(OH)_3 \xrightarrow{220-320\,°C} Al_2O_3 + 3H_2O + \frac{3}{2}O_2 \text{ (Equation 4.2)}$$

$$2FeO(OH) \xrightarrow{330-380\,°C} Fe_2O_3 + H_2O \text{ (Equation 4.3)}$$

$$Al_2Si_2O_5(OH)_4 \xrightarrow{400-640\,°C} Al_2Si_2O_7 + 2H_2O \text{ (Equation 4.4)}$$
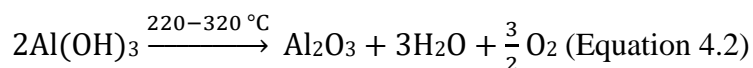
In Event 5, calcite destabilise releasing carbon dioxide (Karunadasa et al., 2019) as seen in the ion current curve of CO_2, and free-lime is formed (Equation 4.5, at 810 °C):

$$CaCO_3 \xrightarrow{550-850\,°C} CaO + CO_2 \text{ (Equation 4.5)}$$

89
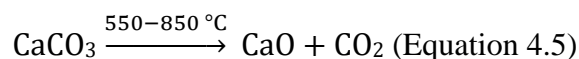
The exothermic peaks from 850 °C on, in Event 6, might be associated with the formation of the first crystalline phases present in the clinker, including gehlenite [$Ca_2Al(AlSiO_7)$] and ye'elimite [$Ca_4Al_6O_{12}(SO_4)$], possibly by the Equation 4.6, Equation 4.7 and Equation 4.8, as suggested by Yao et al. (2020):

$$2CaO + Al_2O_3 + SiO_2 \xrightarrow{900-950\,°C} Ca_2Al(AlSiO_7) \text{ (Equation 4.6)}$$

$$3CaO + 3Al_2O_3 + CaSO_4 \xrightarrow{950-1000\,°C} Ca_4Al_6O_{12}(SO_4) \text{ (Equation 4.7)}$$

$$CaSO_4 \xrightarrow{1170\,°C} SO_2 + CaO + \frac{1}{2}O_2 \text{ (Equation 4.8)}$$
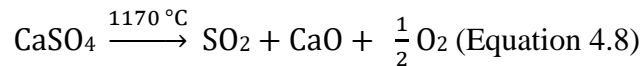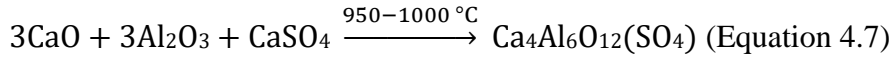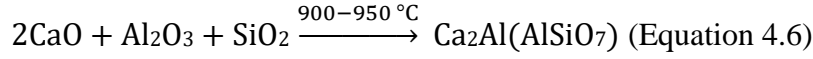
According to Yao et al. (2020), the continuous formation of ye'elimite and belite (Ca_2SiO_4) (Equation 4.9), and the formation of brownmillerite ($Ca_4Al_2Fe_2O_{10}$) (Equation 4.10) can occur in the 1050 °C to 1200 °C temperature range. The slope in the DSC curve close to 1100 °C with endothermic character might indicate the onset of liquid phase formation during clinkerization (Koumpouri et al., 2021). Ternesite, $Ca_5(SiO_4)_2(SO_4)$, probably formed as an intermediary phase from 1000 °C to up to 1250 °C depending on the oven atmosphere and according to Equation 4.11 (Ben Haha et al., 2015; Hanein et al., 2017).

$$3CaO + 3Ca_2Al(AlSiO_7) + CaSO_4 \xrightarrow{1050-1150\,°C} Ca_4Al_6O_{12}(SO_4) + 3Ca_2SiO_4 \text{ (Equation 4.9)}$$

$$2CaO + Ca_2Fe_2O_5 + Al_2O_3 \xrightarrow{1150-1200\,°C} Ca_4Al_2Fe_2O_{10} \text{ (Equation 4.10)}$$

$$2Ca_2SiO_4 + CaSO_4 \xrightarrow{1000-1250\,°C} Ca_5(SiO_4)_2(SO_4) \text{ (Equation 4.11)}$$
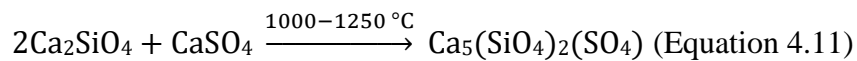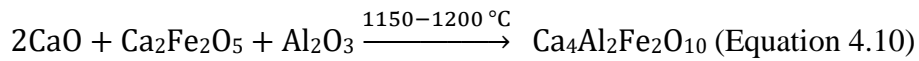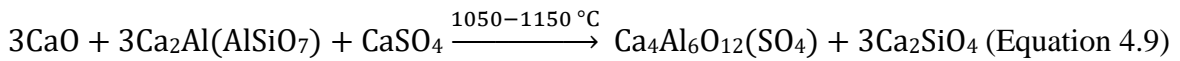
Perovskite ($CaTiO_3$) could have formed directly from the reaction of calcium oxide and titanium oxide (Equation 4.12), whereas these two combined with iron oxide could have formed the Fe-rich perovskites with varying Fe and Ti contents following Equation 4.13, wherein $x=1$ would cause the formation of ferrite ($CaFeO_{2.5}$).

$$CaO + TiO_2 \xrightarrow{1000-1250\,°C} CaTiO_3 \text{ (Equation 4.12)}$$

$$CaO + \frac{x}{2}Fe_2O_3 + (1-x)TiO_2 \xrightarrow{1000-1250\,°C} CaFe_xTi_{1-x}O_{3-x/2} \text{ } (0 \leq x \leq 1) \text{ (Equation 4.13)}$$
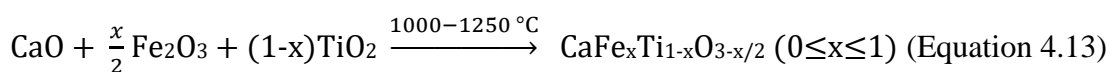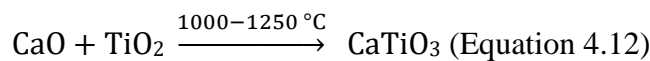
The exothermic peaks in Event 7 indicate that the crystallisation process continued. The mass loss of 0.6% close to 1230 °C is mainly due to a loss in SO_2, as seen in the ion current curve,

and possibly occurred due to the destabilisation of ternesite (Equation 4.14) (Ben Haha et al., 2015). As presented in Table 12, a small amount of sulfate was lost for the same clinker studied here (BWC-3), when produced using the experimental setup of this work in a larger oven (Carbolite RHF 15/3). However, differences in the oven atmosphere used in the experimental setup and of the smaller oven of the Thermo-analyser are expected. Therefore, changes in the oven atmosphere, and consequent O_2 and SO_2 partial pressures, likely affected the stability of ternesite (Hanein et al., 2017).

$$Ca_5(SiO_4)_2(SO_4) \xrightarrow{>1230\,°C} 2Ca_2SiO_4 + CaO + SO_2 + \frac{1}{2}O_2 \text{ (Equation 4.14)}$$
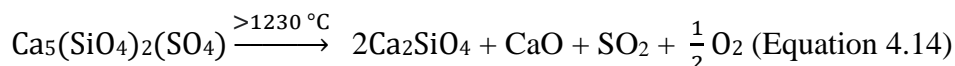
The subsequent Event 8 shows a broad exothermic peak that can be related to the continuous formation of belite and additional ye'elimite by the reaction of gehlenite and some available sulfate and free-lime from the decomposition of ternesite (Equations 4.15):

$$3Ca_2Al(AlSiO_7) + SO_2 + 4CaO + \frac{1}{2}O_2 \xrightarrow{>1230\,°C} Ca_4Al_6O_{12}(SO_4) + 3Ca_2SiO_4 \text{ (Equation 4.15)}$$
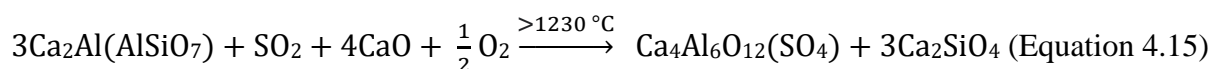
Finally, brownmillerite seems unstable in clinkers produced at 1300 °C and its decomposition (Equation 4.16) can release aluminium to form additional ye'elimite, and iron to form Fe-perovskites, or to be incorporated in the structure of ye'elimite.

$$Ca_4Al_2Fe_2O_{10} \xrightarrow{>1250\,°C} 4CaO + Al_2O_3 + Fe_2O_3 \text{ (Equation 4.16).}$$

4.3.3 Microstructure

The clinker is composed of micrometric crystallites of mainly ye'elimite and larnite occurring in aggregates. Fe-perovskite and brownmillerite could not be distinguished in the BSE analysis, where they have a light-grey colour. However, these phases developed larger crystals within the larnite and ye'elimite crystallites when produced at 1300 °C (Figure 69-B). The clinker BWC-3 produced at this higher temperature developed larger and more edge crystallites when compared to the clinker BWC-3 produced at 1250 °C (Figure 69).
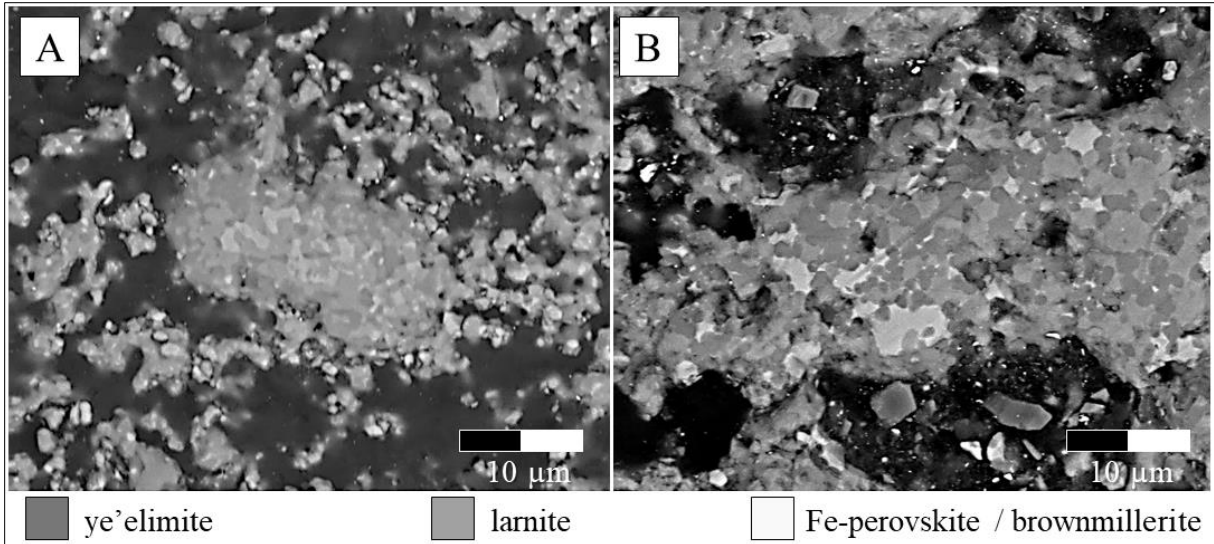
Figure 69 BSE images of the clinker BWC-3 produced at 1250 ℃ (A) and at 1300 ℃ (B). Black portions are filled with epoxy resin. Images acquired at Zentrum für Werkstoffanalytik in Lauf, Germany.

The micromorphology of the clinker BWC-3 is also similar to the other clinkers produced using Belterra Clay. Ye'elimite and larnite have similar size and morphology, with no clear faceting in the crystallites (Figure 70-A). The contrasting whitish crystallites seen in the BSE image (Figure 70-B) are Fe-perovskite and/or brownmillerite.
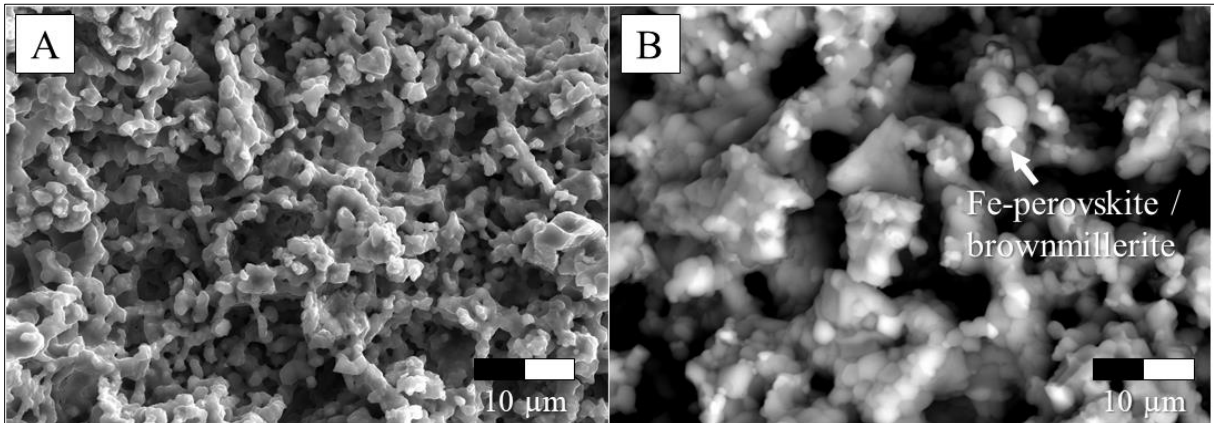
Figure 70 SEM (A) and BSE (B) images of the clinker BWC-3 produced at 1250 ℃. The brighter crystallites in the BSE image are probably Fe-perovskite or brownmillerite. Images acquired at Zentrum für Werkstoffanalytik in Lauf, Germany.

5 Results - Synthesised pure phases

5.1   Ruddlesden-Popper perovskite $3Ca(Ti_{0.67},Fe_{0.33})O_{2.83}\cdot CaO$

The average chemical composition (by EDS) of the clinker phases shows that Fe-perovskites have variable composition. Fe-perovskites have the general formula $CaFe_xTi_{1-x}O_{3-x/2}$ ($0 \leq x \leq 1$), with a quasi-continuous variation of oxygen defect concentrations from zero in $CaTiO_3$, to 0.5 per formula unit, forming a quasi-continuous solid solution with $CaFeO_{2.5}$ (Becerro et al., 2002).

The Fe-perovskite with the average composition $Ca_{1,00}Al_{0,04}Fe_{0,27}Ti_{0,41}Si_{0,13}O_{2,76}$, found in the SD3 clinkers, is not described in the literature. The very low amounts of Al and Si in this phase might come from de surrounding phases in the clinker, whereas the Fe/Ti contents should be closer to the real composition of these perovskites. Therefore, the Fe-perovskite with composition $Ca_4Ti_2FeO_{9.49}$ was synthesised at 1300 ºC and studied in detail (Figure 71).
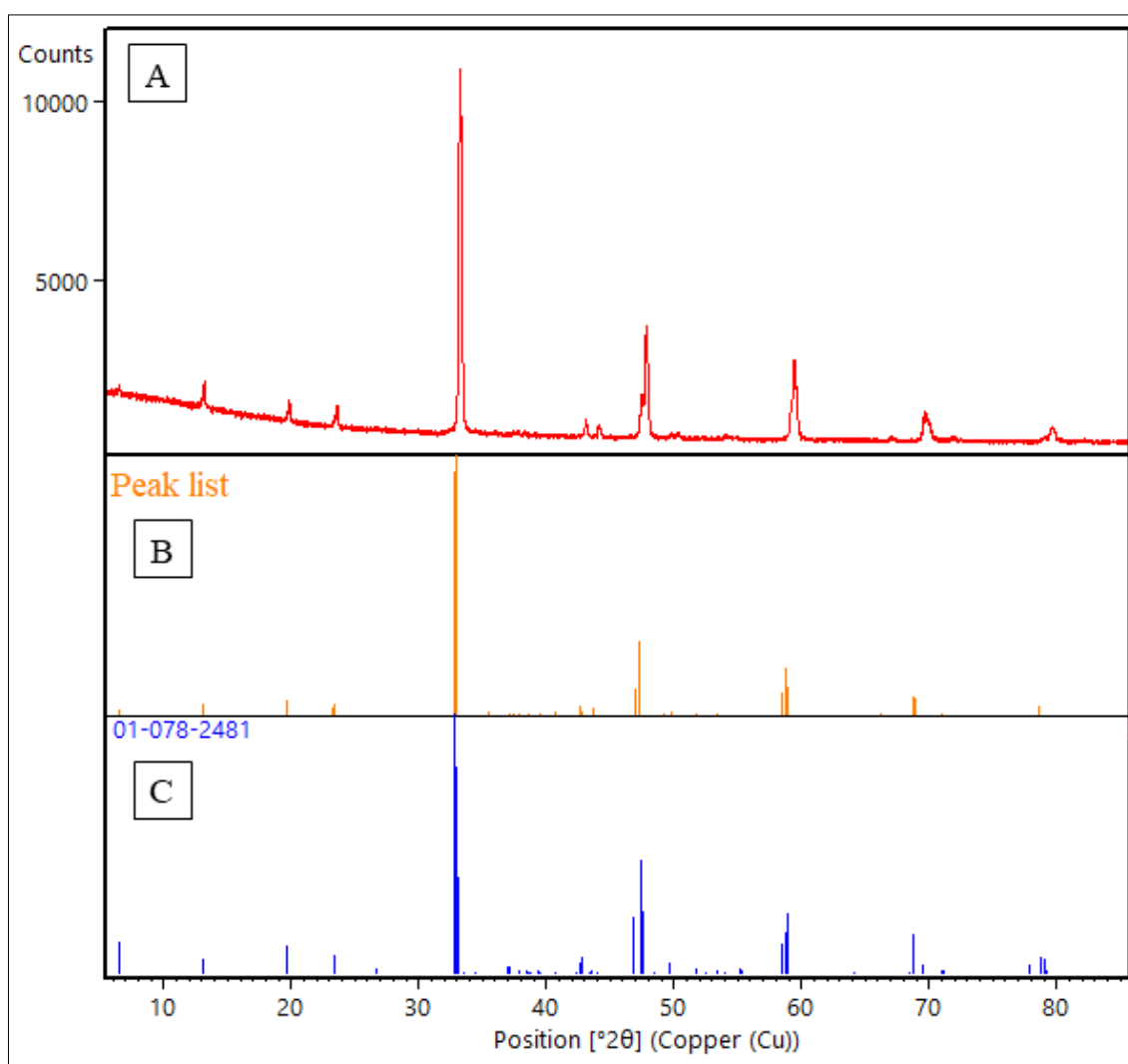
Figure 71 XRPD pattern of the synthesised Fe-perovskite (A), its derived peak positions (B), and the ICDD pattern (code 01-0780-2481) of $3(CaTiO_3)\cdot CaO$ described by Elcombe et al. (1991) (C).

The oxygen-deficient $Ca_4Ti_2FeO_{9.49}$ perovskite has clearly CaO in excess and can be written $3Ca(Ti_{0.67},Fe_{0.33})O_{2.83}\cdot CaO$. The XRPD pattern of the synthesised Fe-perovskite (sample P-AQ, Figure 71) matches the orthorhombic *Pbca* layered perovskite described by (Elcombe et al., 1991), which has the general formula $3(CaTiO_3)\cdot CaO$, and is a layered Ruddlesden-Popper (RP) perovskite with n=3. RP-perovskites have the generic formula $A_{n+1}B_nX_{3n+1}$ [or, $n(ABX_3)\cdot AX$] (Elcombe et al., 1991), and can be described as perovskite-like structures with an excess of A cations (generally alkaline-earth metals) structurally accommodated in regular distorted cubic intergrows with perovskite blocks (ABX_3), where B is usually a transition metal and X an anion (here, oxygen).

The Fe-free perovskite described by Elcombe et al. (1991) (ICSD 86242) was used as a starting model to refine the structure of the synthesised Fe-perovskite. For that, the atomic positions of Ti were shared with Fe in the centre of the octahedra of the modified structure, idealised in Figure 72. The known amounts of Ca permitted fixing the occupancies of this atom in the structure to 1. Likewise, the occupancies of Fe and Ti atoms was respectively fixed to 0.333 and 0.667. Since it was assumed that Fe and Ti share the same positions in the octahedra, their atomic displacement parameters (ADP) were constrained to the same values in the refinements. Because oxygen is the only atom likely to change contents in the structure due to the heating of the sample, only the relative occupancies of the oxygens were refined.
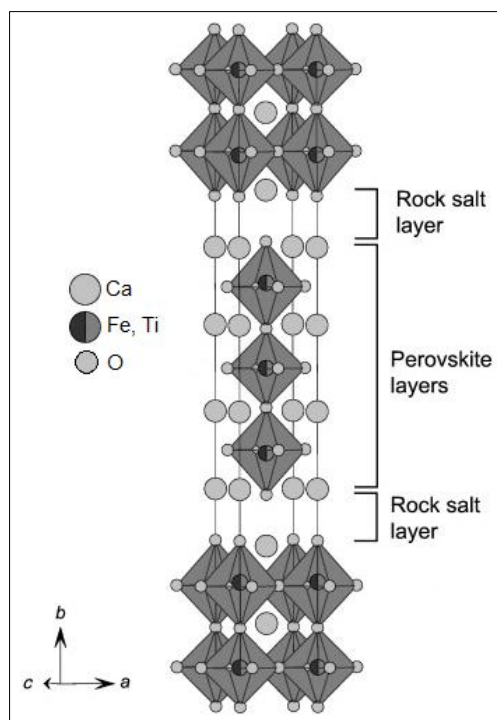
Figure 72 Structure of the Ruddlesden-Popper Fe-perovskite with n=3. In the image of the idealised structure, Fe^{3+} is sharing the octahedra positions with Ti^{4+}, and no vacancies and consequent distortions in the octahedra are considered.

Figure 73 shows the Rietveld-refined XRPD pattern of the adapted structure after the Rietveld-refinement. The obtained unit cell parameters were a = 5.433(1), b = 27.0938(3), and c = 5.434(1). The final atomic position and occupation parameters obtained from the structural refinement of the sample P-AQ are displayed in Table 14.
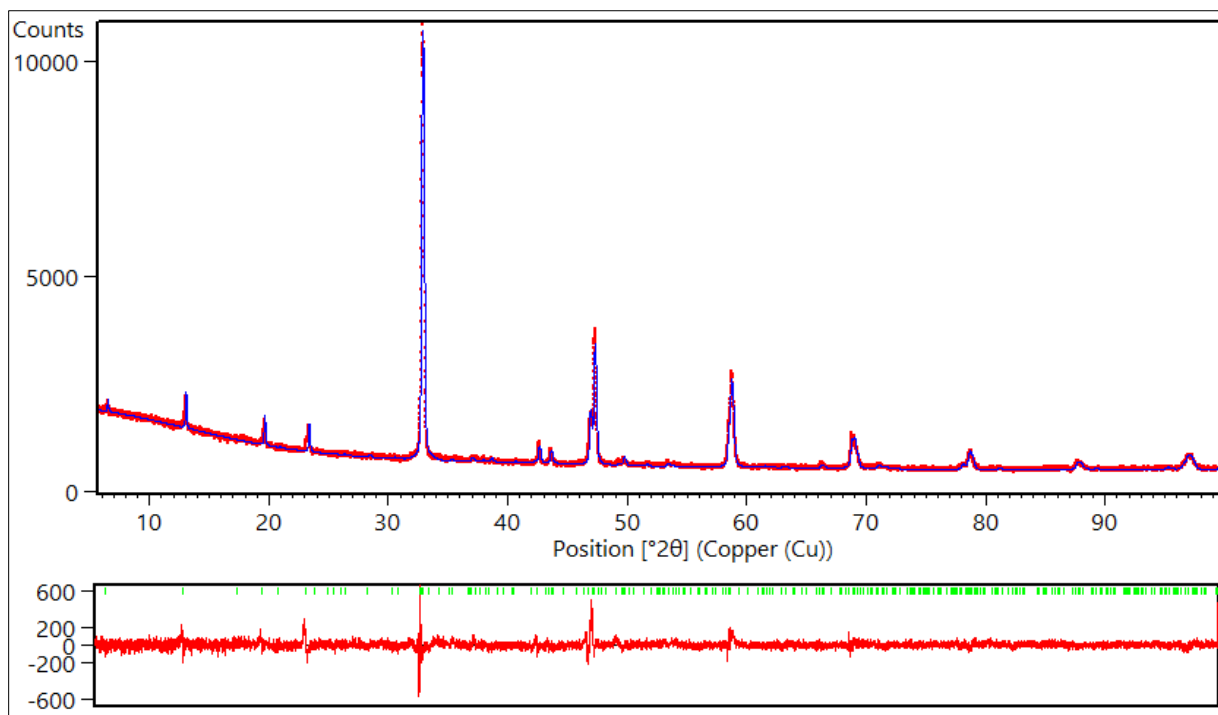
Figure 73 Rietveld-refined XRPD pattern of the synthesised air-cooled Fe-perovskite. GOF = 1.14 and Rwp = 3.96.

Table 14 Atomic positions, Wyckoff symbols, occupation factors and isotropic atomic displacement parameters (ADP) from the Rietveld-refinement of the RP-perovskite air-quenched (sample P-AQ).

atom	symbol	x	y	z	ADP/ Å^2	occupancy
Ca1	8c	0.490(2)	0.0764(1)	0.010(3)	0.007(1)	1
Ca2	8c	-0.002(2)	0.20484(9)	0.498(3)	0.008(1)	1
Ti1	4a	0	0	0	0.007(1)	0.667
Fe1	4a	0	0	0	0.007(1)	0.333
Ti2	8c	0	0.143(9)	0.8(3)	0.025(1)	0.667
Fe2	8c	0	0.14(2)	0.10(1)	0.025(1)	0.33333
O1	8c	0.507(6)	0.4264(5)	0.011(9)	0.067(7)	0.93(2)
O2	8c	0.013(5)	0.2145(3)	-0.010(9)	0.029(4)	1
O3	8c	0.235(6)	0.1320(5)	0.266(5)	0.10(1)	0.81(4)
O4	8c	0.195(5)	0.3519(5)	0.188(6)	0.10(1)	0.82(4)
O5	8c	0.299(6)	-0.0003(9)	0.203(6)	0.009(5)	0.85(1)

High-temperature XRPD was conducted in transmission geometry to observe possible phase transitions in the synthesised Fe-perovskite (sample P-AQ). The sample was heated from 25 ℃ to 905 ℃, and the XRPD patterns were recorded at each 20 ℃. Figure 74 shows the distinguished XRPD patterns measured at the higher temperatures and the changes of the unit cell parameters of the structure at each 50 ℃. At approximately 350 °C a, b and c drastically changed. After that, the a and c cell parameters remained with very close values until approximately 700 ℃, when they slightly diverged.

The sharpened peaks in the XRPD pattern became better individualised by the increasing temperature and shifted to lower 2θ angles as a consequence of the expansion of the unit cell. However, all the reflexes previously observed in the patterns at room temperature remained in the diffractograms obtained at higher temperatures, and no new reflexes were observed. Therefore, no change in the space group *Pbca* was detected.
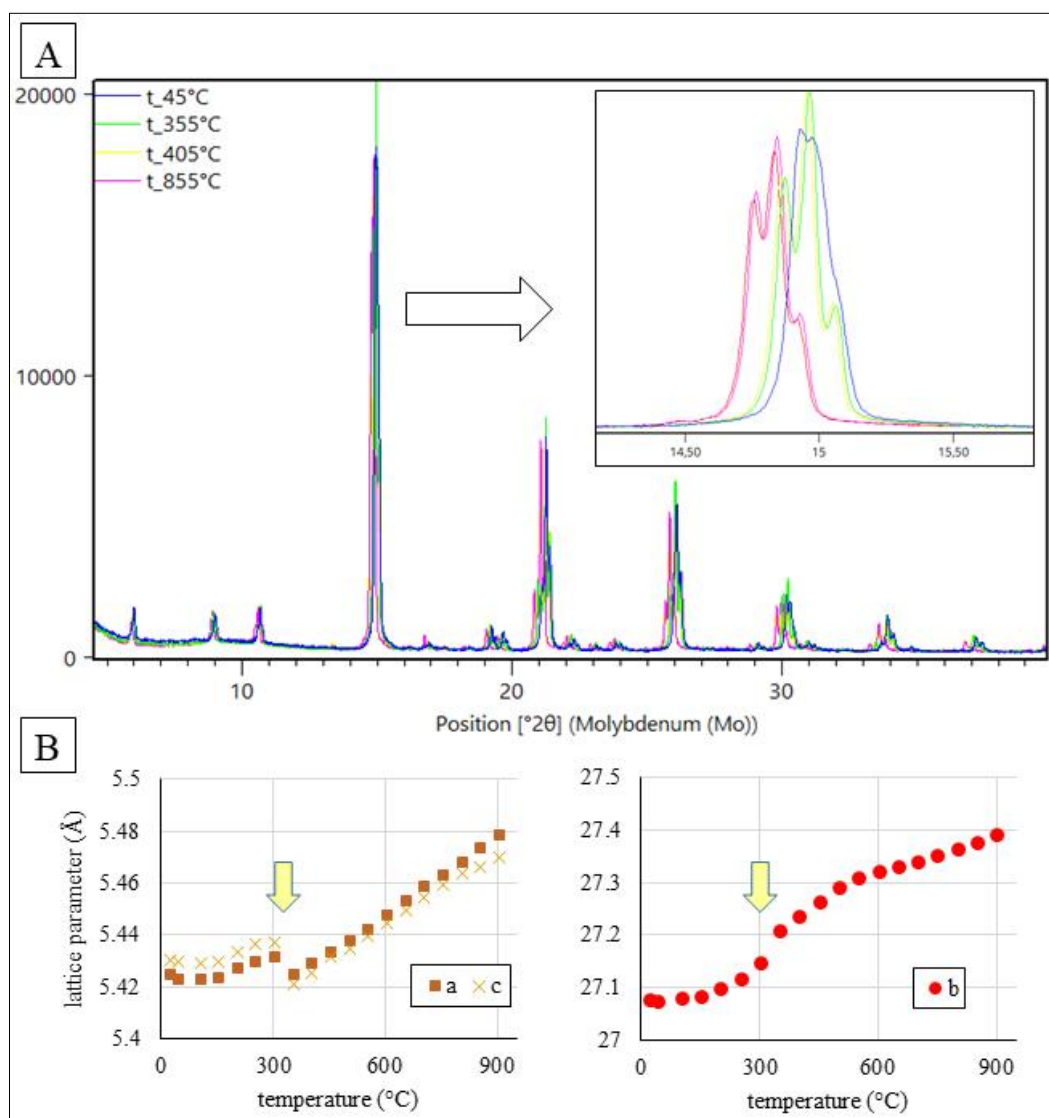
Figure 74 A: XRPD patterns measured with increasing temperature. B: refined unit cell parameters.

To stabilise the structure observed in the 350 – 700 °C range, the sample P-AQ air-cooled at room temperature was heated again to 500 °C and rapidly quenched in water. This new sample, named P-WQ-500, was refined using the adapted structure file with the starting parameters shown in Table 14. The obtained unit cell parameters of the sample P-WQ-500 were $a =$ 5.4312(5), $b =$ 27.115(8), and $c =$ 5.4248(1), and Rietveld-refinements agreements were GOF = 1.25, Rwp = 4.60. The unit cell parameters obtained from the structural refinement of the sample P-WQ-500 are displayed in Table 15. The main difference to the air-cooled sample is the increased oxygen vacancies in the water-quenched sample. Mössbauer analyses were conducted to probe the Fe oxidation state in both the air-cooled sample (P-AQ) and the water quenched sample (P-WQ-500).

Table 15 Atomic positions, Wyckoff symbols, occupation factors and isotropic atomic displacement parameters (ADP) from the Rietveld-refinement of water-quenched RP-perovskite, sample P-WQ-500.

atom	symbol	x	y	z	ADP/$Å^2$	occupancy
Ca1	8c	0.500(2)	0.0747(2)	-0.010(6)	0.012(1)	1
Ca2	8c	0.003(5)	0.20466(9)	0.501(3)	0.005(1)	1
Ti1	4a	0	0	0	0.3(1)	0.66666
Fe1	4a	0	0	0	0.4(2)	0.33332
Ti2	8c	0	0.1497(3)	0.015 (4)	0.008(2)	0.66666
Fe2	8c	0	0.1289(4)	-0.007(6)	0.004(3)	0.33
O1	8c	0.487(6)	0.4296(6)	-0.044(7)	0.057(9)	0.91(2)
O2	8c	0.016(6)	0.215(1)	0.046(6)	0.007(5)	1
O3	8c	0.274(6)	0.135(1)	0.233(5)	0.012(1)	0.76(3)
O4	8c	0.275(5)	0.352(1)	0.271(4)	0.010(8)	0.88(2)
O5	8c	0.329(5)	0.005(1)	0.178(5)	0.009(6)	0.75(1)

5.1.1 ^{57}Fe Mössbauer spectroscopy

The Mössbauer spectra of the air-cooled RP-perovskite (P-AQ) and the water-quenched P-WQ-500 one are clearly different (Figure 75), suggesting that Fe has a different coordination number and oxidation state in the samples, instead of only Fe^{3+} as initially assumed. Diverse models were performed to prove if Fe^{4+} was present in the samples. Mössbauer fits with and without Fe^{4+} are both similar and good for P-WQ-500 (Figure 75 and Table 16). All fits with reasonable hyperfine parameters give an average intensity ratio of 6±6%. The Mössbauer fits of the air-cooled sample (P-AQ) are better with both Fe^{3+} and Fe^{4+}, with the last presenting an average intensity of about 24±4%.
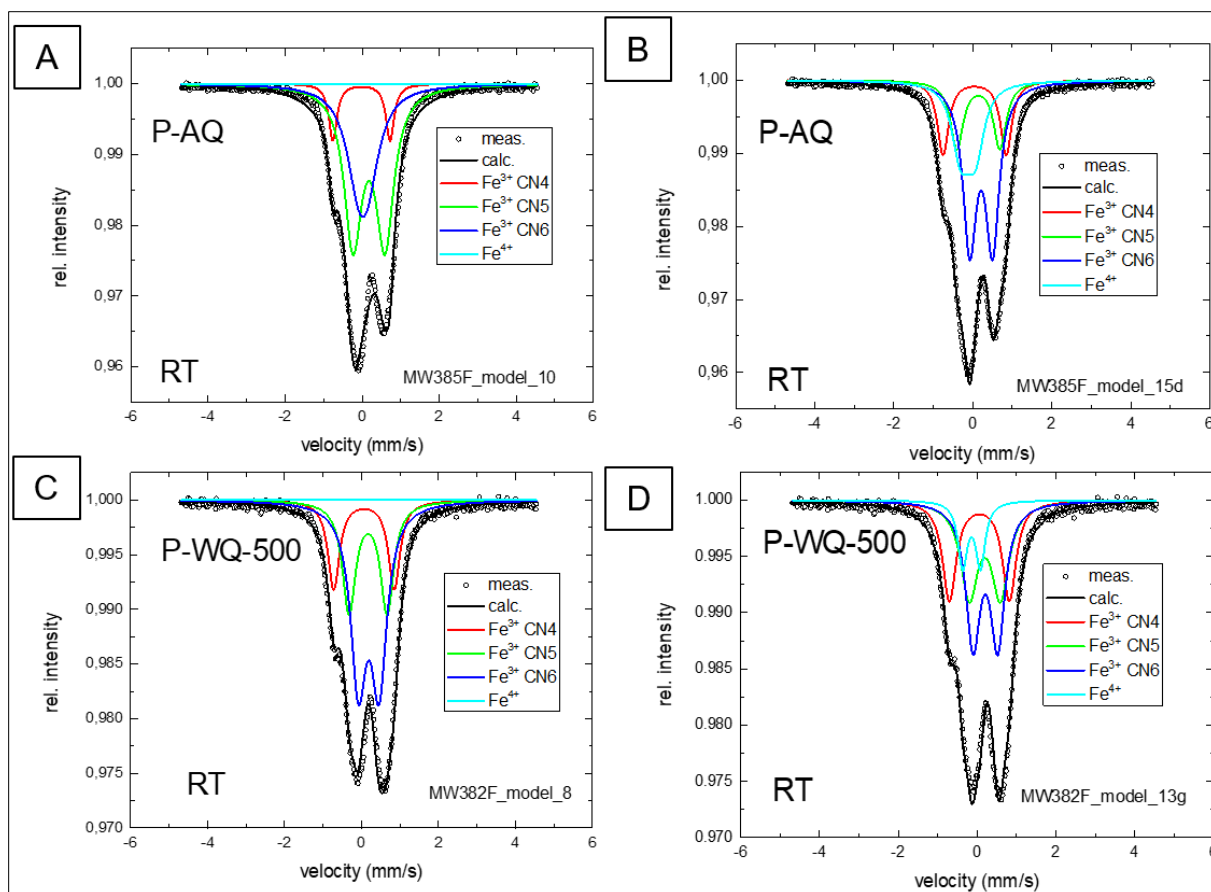
Figure 75 ^{57}Fe Mössbauer fits for the air-cooled (P-AQ) and quenched (P-WQ-500) samples obtained in a fit with three (A and C) and four (B and D) subspectra. The fits parameters are given in Table 16. The measurements were performed in the Technische Universität Wien by Professor Dr. Reissner.

Comparing the air-cooled and the water-quenched samples, the approximately 74% reduction of Fe^{4+} is accompanied by a reduction of ~8% of Fe^{3+} in the CN4 sites, an increase of ~5% Fe^{3+} in the CN5 and ~17% in the CN6 sites. That is, the loss of Fe^{4+} in the sample quenched at 500 °C is mainly compensated by an increase of the Fe^{3+} in octahedral sites, whereas the amount of Fe^{3+} in other sites is more or less constant.

The QS values increase from CN6 to CN5 to CN4 for both samples. The small difference between the two samples indicates that the influence of the next nearest neighbourhood is small. The half-width G/2 is larger for the Fe^{3+} subspectra in the quenched sample probably due to higher disorder. This is not reflected by an increase in QS, indicating that the local symmetry is not much different. For the Fe^{4+} subspectrum, the uncertainty in the obtained parameters is too large to make such straightforward propositions. Fe^{4+} is expected to be mainly in the highly ordered surrounding (CN6). This seems to be confirmed by the above-described change in the intensities, which are strongest for CN6 and by the fact that QS is rather small, which indicates high symmetry.

Table 16: Center shift (CS rel. to Co**Rh**), quadrupole splitting QS=eQV$_{zz}$/4 and half-width G/2 in mm/s for Fe^{3+} in tetrahedral (CN4), pentacoordinate (CN5), and octahedral (CN6) positions and for Fe^{4+} for the air-cooled (P-AQ) and rapidly water-quenched (P-WQ-500) samples; results of different fit models are shown. Parameters slightly outside of the expected values described in Table 4 are marked in red. Quality of fits is determined by the regression coefficient r.

	fit model	CN4 Fe3$^+$				CN5 Fe3$^+$				CN6 Fe3$^+$				Fe4$^+$				r
		CS	QS	G/2	Area	CS	QS	G/2	Area	CS	QS	G/2	Area	CS	QS	G/2	Area	
P-AQ	Model 10*	-0.012	0.74	0.13	9.59	0.18	0.42	0.28	55.88	0.02	0.12	0.37	34.58					0.99686
	Model 14b	0.04	0.80	0.17	15.01	0.13	0.50	0.21	21.40	0.22	0.28	0.23	41.48	-0.13	0.16	0.26	22.12	0.99921
	Model 15d*	0.05	0.80	0.17	16.56	0.14	0.55	0.17	17.18	0.21	0.29	0.21	43.42	-0.12	0.18	0.24	22.84	0.99918
	Model 15	0.05	0.79	0.17	16.59	0.12	0.53	0.19	18.81	0.20	0.31	0.20	34.61	-0.01	0.18	0.26	29.99	0.99902
	Model 22	0.05	0.78	0.16	17.82	0.22	0.43	0.23	27.19	0.20	0.29	0.18	32.93	-0.13	0.26	0.17	22.06	0.99893
	Mean	**0.05**	**0.79**	**0.17**	**16.50**	**0.15**	**0.50**	**0.20**	**21.15**	**0.21**	**0.29**	**0.20**	**38.11**	**-0.10**	**0.19**	**0.23**	**24.25**	
P-WQ-500	Model 3	0.07	0.79	0.20	18.63	0.17	0.51	0.23	29.42	0.19	0.27	0.25	51.95					0.99777
	Model 8*	0.06	0.79	0.18	19.77	0.17	0.49	0.21	28.13	0.19	0.27	0.25	52.10					0.99794
	Model 6	0.06	0.78	0.19	24.10	0.16	0.51	0.20	22.61	0.22	0.28	0.20	38.85	-0.01	0.21	0.20	14.44	0.99902
	Model 7	0.07	0.78	0.19	19.54	0.17	0.50	0.22	27.62	0.20	0.27	0.25	50.10	-0.14	0.04	0.16	2.74	0.99862
	Model 7a	0.07	0.78	0.19	19.17	0.17	0.50	0.22	28.08	0.20	0.27	0.25	50.08	-0.14	0.04	0.16	2.67	0.99859
	Model 13c	0.08	0.78	0.20	23.01	0.17	0.51	0.15	17.25	0.19	0.28	0.25	59.00	-0.17	0.28	0.10	0.74	0.99815
	Model 13g*	0.06	0.76	0.21	24.34	0.20	0.40	0.27	28.56	0.21	0.31	0.22	36.20	-0.14	0.23	0.14	10.90	0.99832
	Mean	**0.07**	**0.78**	**0.20**	**22.03**	**0.17**	**0.52**	**0.21**	**24.82**	**0.20**	**0.28**	**0.23**	**40.05**	**-0.12**	**0.16**	**0.15**	**6.31**	

Mean only for fits with four subspectra * Best fit models shown in Figure 75.

Results – Synthesised pure phases

5.1.2   Thermal Analysis

At least three endothermic peaks in the DSC curve and a fourth one close to 1300 °C are seen from the heating of the P-AQ sample (Figure 76). The first one, within 100 °C, is related to the loss of residual humidity of the sample. The second, close to 400 °C, confirms the transition observed in the HTXRD and has an associated mass loss of 0.55% in the thermogravimetric curve. After stoichiometric calculations and considering that only oxygen was lost, this mass loss represents 0.16 mol of oxygen. The next DSC peak at around 700 °C is related to another mass loss of approximately 0.7%. However, no changes were observed in the unit cell by HTXRPD at this temperature, except for the continuous cell parameters increase with the temperature.
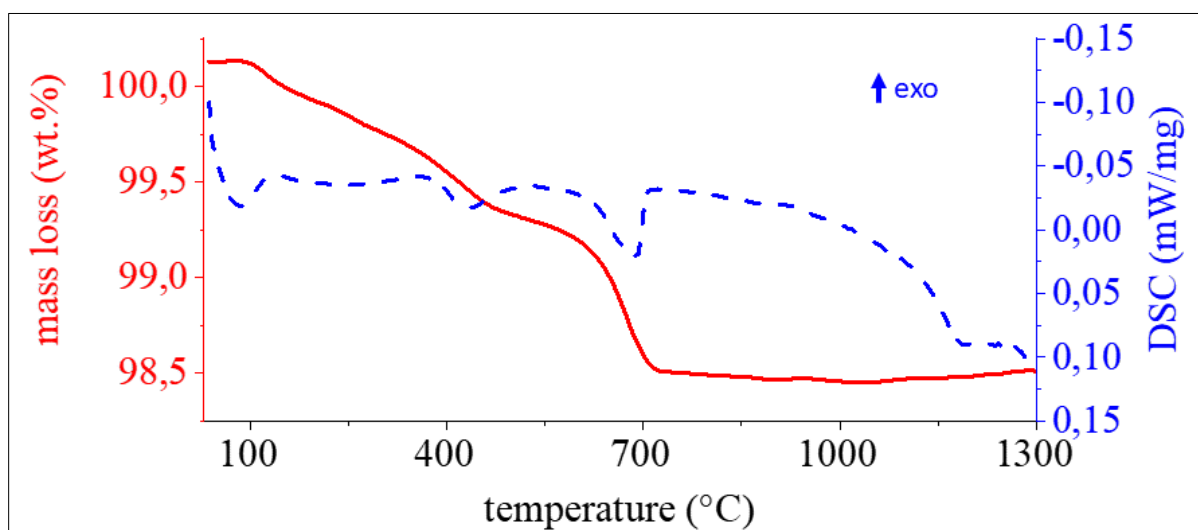
Figure 76 Thermogravimetric and DSC curves of the studied RP-perovskite. Measured with a heating rate of 10 K/min^{-1} in Ar atmosphere.

5.2 **Perovskite CaTiO₃**

The sample of iron-free perovskite synthesised at 1250 ºC, with stoichiometric composition CaTiO₃, resulted in a single-phase characterised by XRPD (Figure 77). The perovskite has the orthorhombic *Pnma* space group and its XRPD pattern was refined using the crystal structure described by Liu and Liebermann (1993). The refined unit cell parameters were $a = 5.4411$, $b = 7.6405$ and $c = 5.3799$.
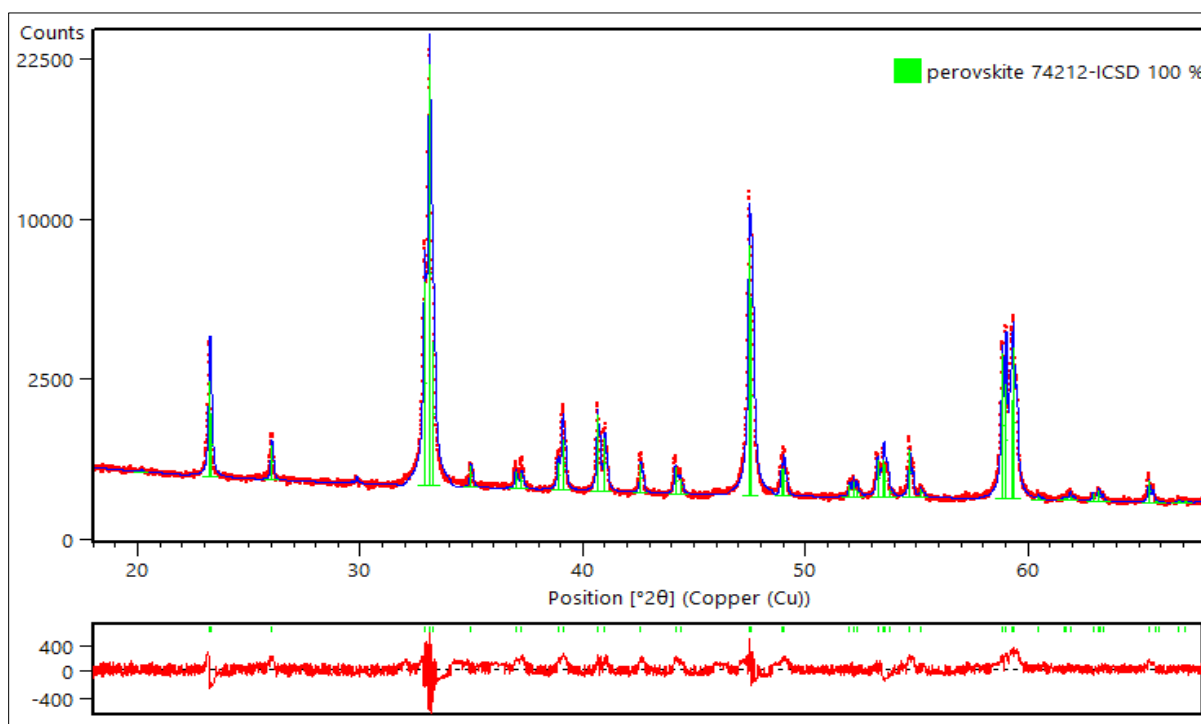
Figure 77 Rietveld-refined XRPD of the synthesised perovskite with composition CaTiO₃. Rietveld indicators *GOF* = 1.71 and *Rwp* = 7.28.

5.3 Brownmillerite Ca₂FeAlO₅

The synthesis of brownmillerite with the stoichiometric composition Ca_2FeAlO_5, at 1250 °C, resulted in brownmillerite and 5% of calcium aluminate $CaO.Al_2O_3$ (Figure 78). The obtained brownmillerite is, therefore, slightly more enriched in Fe than in the goal composition. It has the orthorhombic *Ima2* space group, which was refined using the structure described by (Colville and Geller, 1971). The refined unit cell parameters of brownmillerite were *a* = 14.5248, *b* = 5.5675 and *c* = *5.3515*.
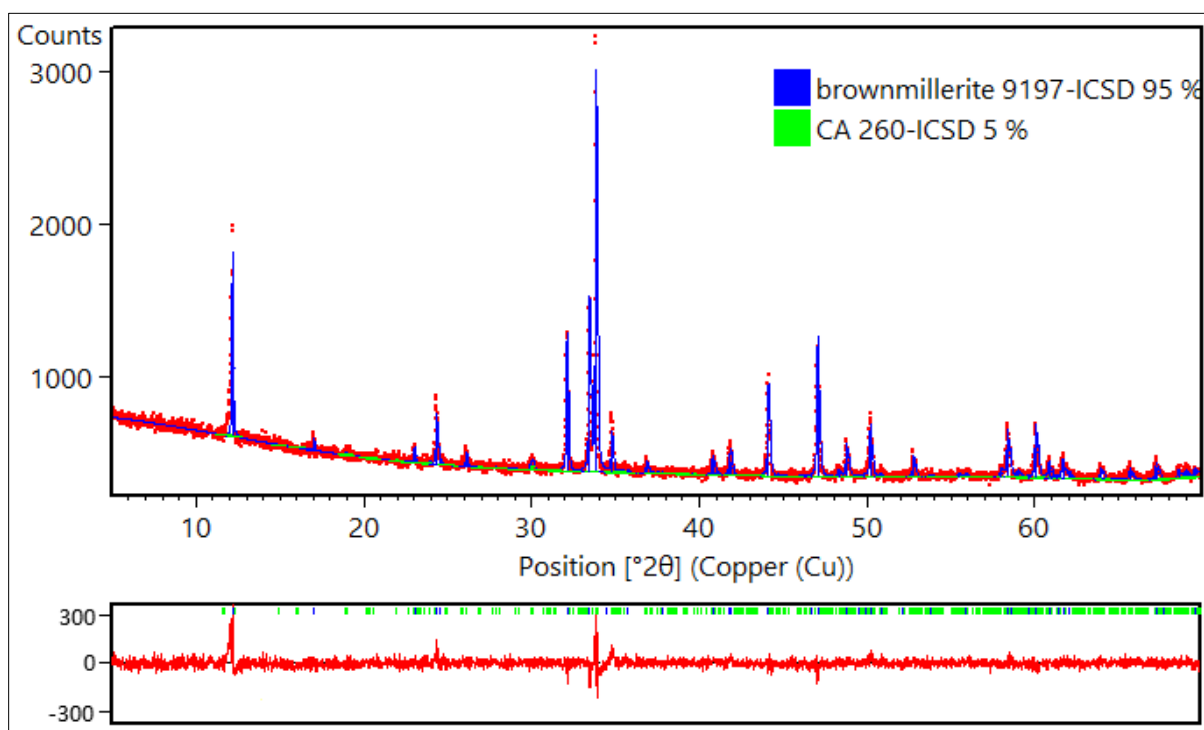
Figure 78 Rietveld-refined XRPD of the synthesised brownmillerite. GOF = 1.04 and Rwp = 4.84.

5.4 Stability of main phases of the CSA clinkers mixed with perovskite and brownmillerite

A binary mixture (1:1 ratio) of brownmillerite and perovskite (PB) and, ternary mixtures (1:1:1 ratios) of ye'elimite-brownmillerite-perovskite (YBP), larnite-brownmillerite-perovskite (LBP), and ternesite-brownmillerite-perovskite (TBP) were studied to investigate the stability of these phases at different clinkering temperatures.

Despite the attempt to mechanically mix the phases as pure, some of the mineral samples had impurities. The brownmillerite sample had calcium aluminate (CA), the ternesite sample had few amounts of larnite, and the larnite sample had also γ-belite as an impurity (Table 17). Therefore, the binary/ternary nomenclature of the mixtures is given here considering the main phases. Table 17 displays the phase contents of each of the mixtures before heating them (room temperature 25 °C), and after firing the samples for 1 h hour at 1250 °C and at 1300 °C.

Table 17 Rietveld-quantified phase contents (in wt.%) of the binary and ternary mixtures after firing at 1250 °C and 1300 °C. BP – binary mixture of brownmillerite and perovskite; YBP – ternary mixture of ye'elimite, brownmillerite and perovskite; TBP – ternary mixture of ternesite, brownmillerite and perovskite; LBP – ternary mixture of larnite, brownmillerite and perovskite.

Mixture		BP			YBP			TBP			LBP	
Temperature (°C)	25	1250	1300	25	1250	1300	25	1250	1300	25	1250	1300
brownmillerite	45	23	-	30	16	-	30	29	12	30	23	-
perovskite	50	34	28	33	23	15	33	32	26	33	31	19
ye'elimite	-	0	-	33	32	30	-	2	4	-	-	-
larnite	-	-	-	-	-	-	2	18	32	28	26	32
ternesite	-	-	-	-	-	-	31	19	-	-	-	-
shulamitite	-	39	67	-	25	49	-	-	24	-	-	-
CA	5	5	5	3	5	6	3	-	-	3	-	-
γ-belite	-	-	-	-	-	-	-	-	-	5	5	2
UCP	-	-	-	-	-	-	-	-	-	-	10	48
gehlenite	-	-	-	-	-	-	-	-	-	-	4	-
anhydrite	-	-	-	-	-	-	-	1	3	-	-	-
GOF	-	1.02	1	-	1.02	1.05	-	1.05	1.09	-	1.01	1.11
Rwp	-	5.84	5.44	-	6.07	5.48	-	6.36	6.55	-	6.24	6.83

(The row label "phases" spans the mineral-phase rows.)

CA: calcium aluminate; UCP: unknown cubic perovskite.

The PB mixture resulted in the formation of $Ca_3TiFe^{(3+)}AlO_8$ (shulamitite) at 1250 °C, whereas after firing the sample to 1300 ºC, only perovskite and shulamitite were stable and brownmillerite was absent. The mineral-related shulamitite was described in the Negev Desert in Israel (Sharygin et al., 2013). It is considered an intermediate phase of the perovskite-

brownmillerite series (Mitchell et al., 2017) and an analogue to the Al-free synthetic $Ca_3TiFe_2^{(3+)}O_8$ already described in clinkers by Rodríguez-Carvajal et al. (1989).

The YBP mixture resulted in the formation of shulamitite at 1250 °C and at 1300 °C, again with the total consumption of brownmillerite at 1300 °C. Ye'elimite contents remained almost the same as before firing at 1250 °C (32%) and 1300 °C (30%). BSE images combined with EDS mappings confirmed the mineral assemblage (Figure 79).
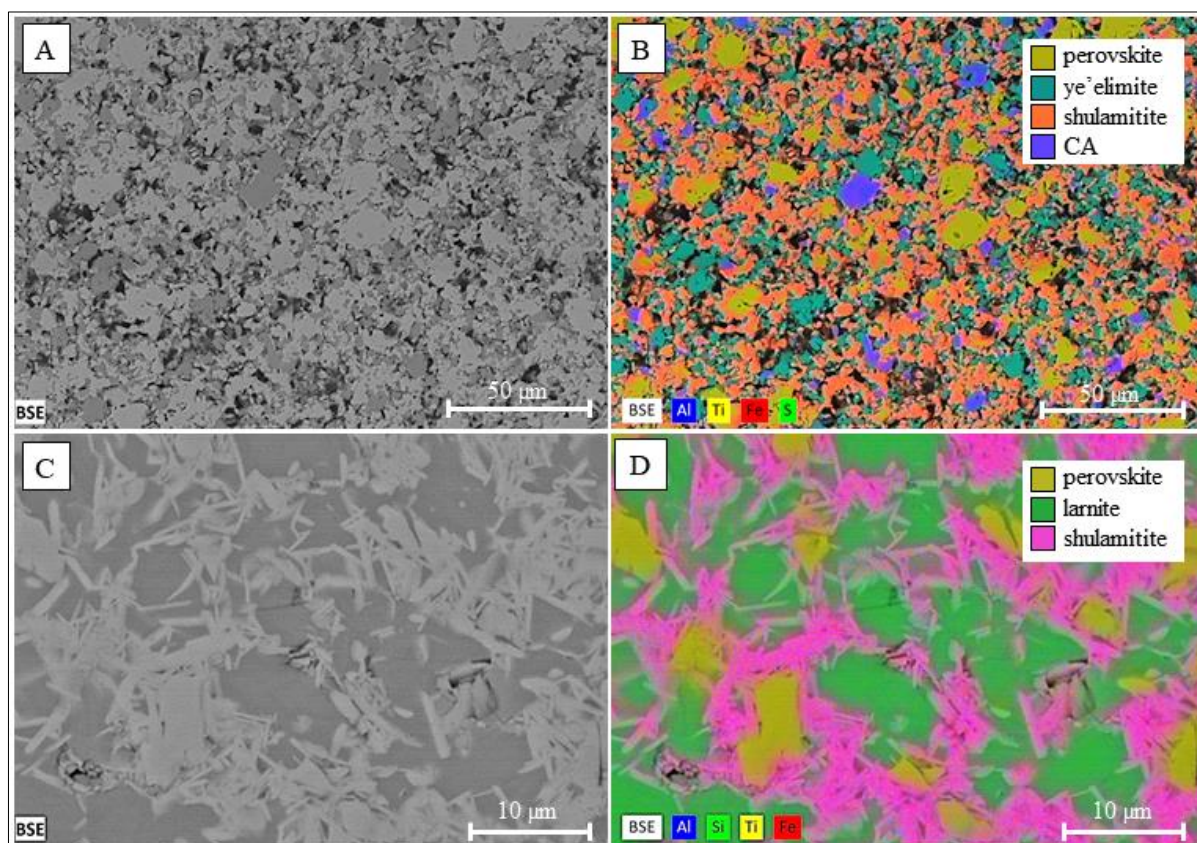
Figure 79 BSE images and combined BSE-EDS-mappings of ternary mixtures after firing at 1300 °C. A and B: ternary mixture YBP (ye'elimite-brownmillerite-perovskite). C and D: ternary mixture TBP (ternesite-brownmillerite-perovskite). To simplify, the EDS mapping of Ca and O are not shown in both mappings because they are present in all identified phases. Black portions are the pores or cracks filled with epoxy resin.

In the TBP mixture, brownmillerite and ternesite decreased respectively to 26% and 19% after firing at 1250 °C. Larnite contents increased to 15%, and anhydrite (1%) was formed, confirming the partial destruction of ternesite. Ye'elimite (2%) was formed probably by the expenses of sulfate from ternesite, and by aluminium from brownmillerite and calcium aluminate. Firing at 1300 °C resulted in the complete decomposition of ternesite, unstable at this temperature. Consequently, larnite (29%), ye'elimite (4%) and anhydrite (2%) contents increased. Brownmillerite sharply decreased to 6.1%. 24% of shulamitite was formed only at

1300 °C. BSE images show that this phase formed thin prismatic crystals (Figure 79 - C and D) differently than the shulamitite observed in the YBT mixture (Figure 79 A and B).

In the LBP mixture fired at 1250 °C, 10% of a cubic unknown phase was formed. The XRPD pattern of this phase fitted in the structure of a cubic perovskite (Barth, 1925), and therefore this phase was here named "unknown cubic perovskite" (UCP). UCP coexisted with orthorhombic perovskite (31%) and brownmillerite (23%). The firing at 1300 °C resulted in the decomposition of brownmillerite, decrease contents of orthorhombic perovskite (from 31 to 19%), and increase of UCP to 48%. Larnite and γ-belite remained almost invariable summing 34%, and gehlenite disappeared. Shulamitite, which has an orthorhombic space group, was not detected in the LBP mixture. However, according to the SEM-EDS analyses of 14 crystals of UCP (Figure 80), its Ca-normalised empirical formula is $Ca_3Ti_{1.08}Fe_{0.93}Al_{0.69}Si_{0.21}O_{9.3}$. This composition, except for Si, is very similar to the composition of shulamitite ($Ca_3TiFeAlO_8$).

B	O	Al	Si	Ca	Ti	Fe	phase
1	37,5			28,2	34,3		perovskite
2	38,1			27,0	34,9		perovskite
3	41,0			26,0	33,0		perovskite
4	37,4			28,9	33,7		perovskite
5	41,8		11,7	46,5			larnite
6	40,3		11,6	48,1			larnite
7	39,8		12,6	47,7			larnite
8	41,0		10,4	48,6			larnite
9	38,3		10,1	51,5			larnite
10	35,7	4,2	1,0	32,3	13,5	13,4	unknown
11	36,2	4,9	1,3	30,2	14,0	13,4	unknown
12	35,4	4,7	1,5	32,0	12,9	13,5	unknown
13	35,9	4,1	1,5	32,6	13,1	12,8	unknown
14	38,5	4,3	1,3	29,4	14,3	12,2	unknown
15	36,7	4,3	1,5	29,8	12,2	15,6	unknown
16	36,2	3,9	1,1	32,0	14,1	12,7	unknown

Figure 80 A: BSE image of the ternary mixture PBL (perovskite-brownmillerite-larnite) after firing the sample at 1300 °C. C: EDS-mapping of the same sample. D: EDS spectra and point analysis (B) of the unknown cubic perovskite (UCP) with composition $CaTi_{0.36}Fe_{0.31}Al_{0.23}Si_{0.07}O_{3.10}$.

6 Results - Properties of selected clinkers and cements

The clinkers SD2-6 and SD2-OP produced with Belterra Clay from the Círiaco pilot-mine, the clinkers SD3-11, SD3-OP and BRA-SM produced with Belterra Clay from the Branco pilot-mine, and the clinker BWC-3 produced with the bauxite washing clay were chosen for further characterisation and performance evaluation, including hydration studies of cement pastes and cement mortars produced with them.

6.1 **Raw material-related CO_2 emissions**

The raw material-related (RM) CO_2 emissions of the selected clinkers vary from 0.312 to 0.383 (Figure 81). For comparison, OPCs have an average RM-CO_2 = 0.507, which means 507 Kg of CO_2 is generated per ton of produced OPC clinker (Gibbs et al., 2002). The saving in CO_2 emissions, compared to the production of OPC, vary from 25% (clinker BRA-SM) to 38% in the clinker SD2-OP (Figure 81).
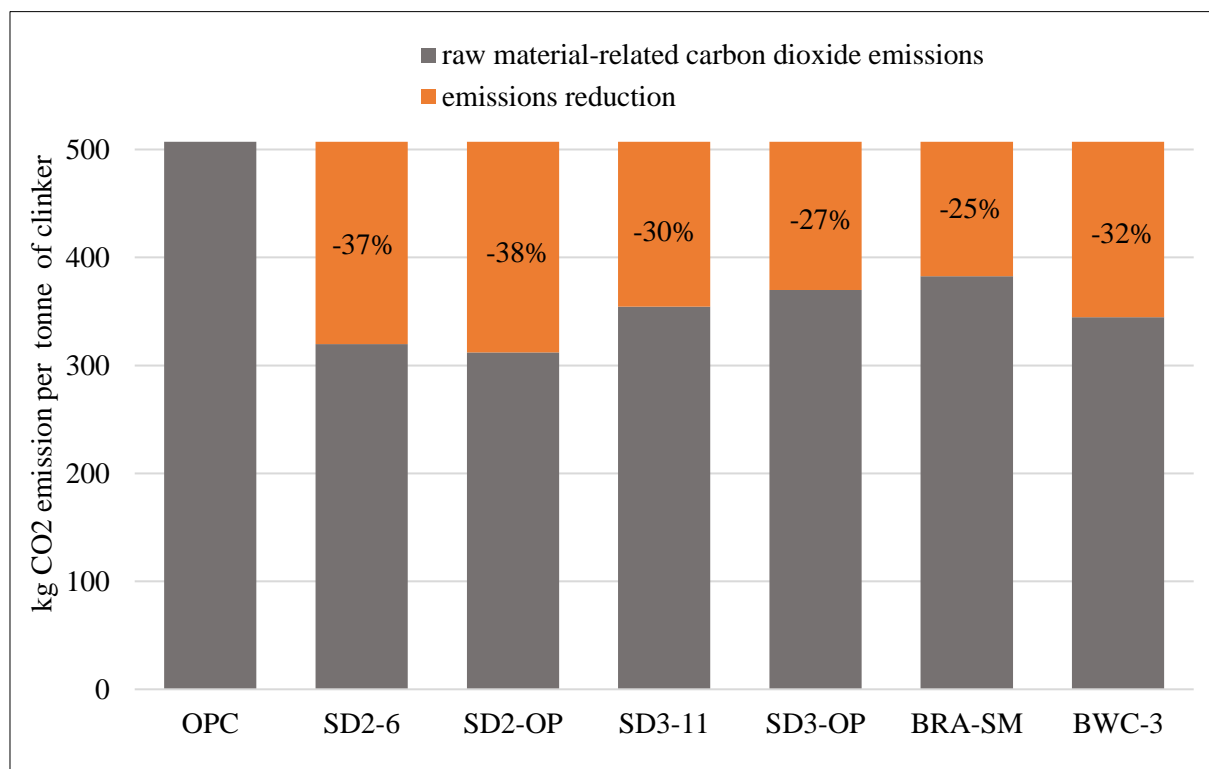
Figure 81 Raw material-related CO_2 emissions of OPC clinker and of the clinkers produced in this work, and their correspondent CO_2 emissions reductions compared to the OPC.

The RM-CO_2 emissions are lower for the clinkers produced with the Al-richer Belterra Clay from the Círiaco pilot-mine (clinkers SD2-) and with the bauxite washing clay (clinker BWC-

3) than those produced using the Belterra Clay from the Branco mine (clinkers SD3- and BRA-SM). Compared to the OPC, the lower CO_2 emissions of the produced clinkers come from the lower $CaCO_3$ amounts used to produce the CSA-based clinkers. For the clinkers produced in this work, the lowering in $CaCO_3$ is related to the use of both bauxite residues (Belterra Clay or bauxite washing clay) and gypsum in the raw meal.

For instance, clinkers with increased ternesite contents required more gypsum in their raw meal and consequently have a higher emission reduction. However, the sulfur source can be other than gypsum in practical applications. Sulfur-rich kiln fuels can be used as sulfate sources (Dienemann et al., 2013), which might change the raw meal composition towards higher amounts of $CaCO_3$ to supply Ca, therefore slightly decreasing emission reductions of the produced ternesite-rich CSA clinkers.

6.2 **Density**

The calculated (after mineralogical composition) and determined (with pycnometer) densities of selected clinkers are very similar and close to 3 g/cm^3 (Table 18). Therefore, the averages of these values were used to calculate the cements specific surfaces (using Blaine) and water demands.

Table 18 Density (in g/cm^3) of selected clinkers, calculated after their mineralogical composition and determined with a pycnometer.

density	SD2-6	SD2-OP	SD3-11	SD3-11 1300	SD3-OP	SD3-OP-B	BRA-SM	BWC-3
calculated	3.06	2.97	3.06	3.10	3.11	3.07	3.13	3.04
determined	3.08	3.02	3.11	3.17	3.16	3.10	3.15	3.16
average	3.07	2.99	3.08	3.14	3.14	3.08	3.14	3.10

6.3 **Fineness**

The Blaine fineness of the clinkers is reported in Table 19. The cement fineness influences the hydration kinetics of the cement phases, as well as the hardening and the strength development of mortars (Zhang, 2011). The produced clinkers were ground for approximately 5 minutes until a similar specific surface close to 3500 cm^2/g was achieved, to produce comparable results of the hydrated cements.

BRA-SM and BWC-3 produced at 1250 °C were ground for a longer time (7 min) and their specific surface were finer, respectively 6619 cm^2/g and 5727 cm^2/g. For comparison purposes, the clinker BRA-SM produced at 1300 °C was ground for the same time but resulted in a coarser powder (4086 cm^2/g).

Table 19 Specific surface area (cm^2/g) of the clinkers determined with the Blaine apparatus.

Clinker	specific surface area 1	specific surface area 2	specific surface area 3	average
SD2-6	3760	3733	3733	3742
SD2-OP	3484	3514	3453	3484
SD3-11	3397	3441	3441	3426
SD3-11 1300 °C	3317	3288	3317	3307
SD3-OP	3346	3346	3375	3356
SD3-OP-B	3337	3411	3411	3386
BRA-SM	6622	6616	6619	6619
BRA-SM 1300 °C	4083	4099	4076	4086
BWC-3	5740	5660	5780	5727

6.4   Hydration of the cement pastes

The hydration of cement pastes using the clinkers SD2-6, SD2-OP, SD3-11, SD3-11 1300°C, SD3-OP, SD3-OP-B, BRA-SM and BWC-3 were studied in detail. Isoperibolic calorimetry was used to probe the heat release of the clinkers in their first 72 hours of hydration. For that, the clinkers were hydrated pure, and mixed with different amounts of gypsum, initially using a w/c=1 to ensure the complete hydration of the pastes. The strength development of mortars (not pastes) is presented later with their quantitative phase evolution.

6.4.1   Gypsum additions

Gypsum was added to the CSA-based clinkers to react with ye'elimite and enhance ettringite formation, the phase responsible for the early strength gain in CSA cements. The heat flow curves from the hydration process of the clinkers are similar. In general, the hydration of the pure clinkers (without gypsum) presented a longer induction period of approximately 30 hours (Figure 82), except for the clinker SD2-OP (9 hours). SD2-OP already had some sulfate (~3% of anhydrite) available left from the clinkering process, resulting in a higher total available sulfate in solution to form ettringite, which explains the shorter induction period of this clinker.
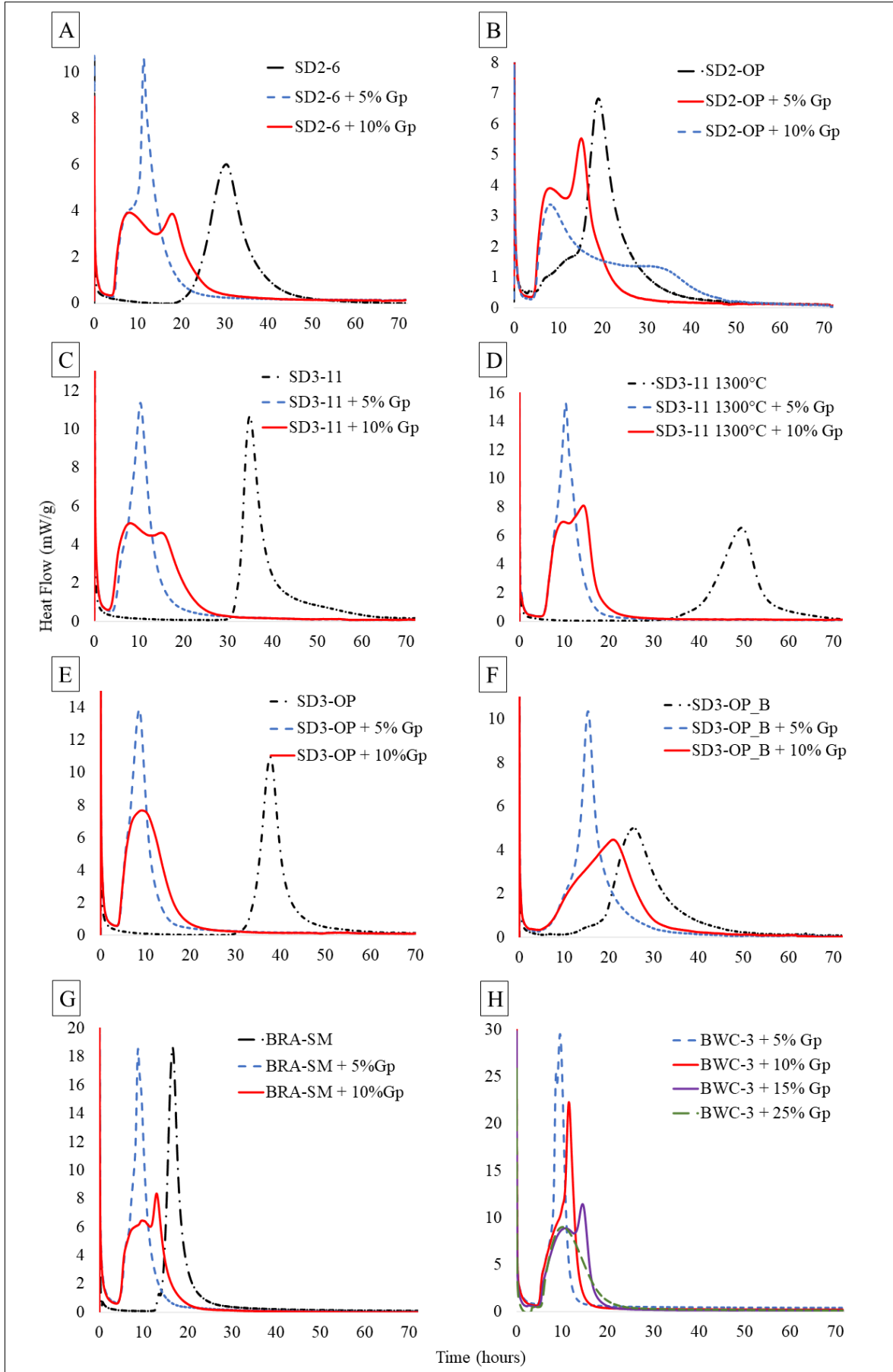
Figure 82 Calorimetric curves clinkers pure and mixed with gypsum (Gp), using w/c=1. A: SD2-6; B: SD2-OP; C: SD3-11; D: SD3-11 1300°C; E: SD3-OP; F: SD3-OP-B; G: BRA-SM; H: BWC-3.

The gypsum additions influenced the hydration of all compositions, shortening the dormant periods to at least 5 hours (Figure 82). The cements with 5% gypsum had the main heat flow maxima anticipated to 8 and 13 hours, which were in most of the cases accompanied by earlier shoulder peaks. The addition of higher gypsum amounts (>10%) to the clinkers resulted in broader peaks, with the heat flow curve reaching its base line after approximately 20, 30 and even 50 hours. Consequently, the overall main hydration times were longer for the clinkers mixed with 10% or more of gypsum.

Ettringite, kuzelite, straetlingite, gibbsite and hemicarboaluminate were the main hydrated phases identified in the cement pastes (Figure 83). Larnite and ternesite were still present after 72 hours of hydration. Other non-reacted phases of the clinker include brownmillerite, Fe-perovskite, gehlenite, and even small amounts of ye'elimite. Some amorphous can also be inferred by the background intensity hump in the 20-2θ (Cu) region (Figure 83 and 84).

A simple qualitative comparison of the characterised XRPD patterns of the hydrated cement pastes shows that the main reflex of ettringite, at 9.1° 2θ (Cu), increased with the increasing gypsum additions (Figure 83), suggesting that the gypsum additions resulted in the formation of ettringite to a greater extent. On the other hand, the monosulfoaluminate kuzelite is present in higher amounts in the cement pastes without gypsum additions, as observed in its peak intensities. That is expected, as calcium sulfate promotes the formation of ettringite by consuming ye'elimite, whereas in the presence of water only, ye'elimite first hydrates to kuzelite before forming ettringite (Allevi et al., 2016; Winnefeld et al., 2017).
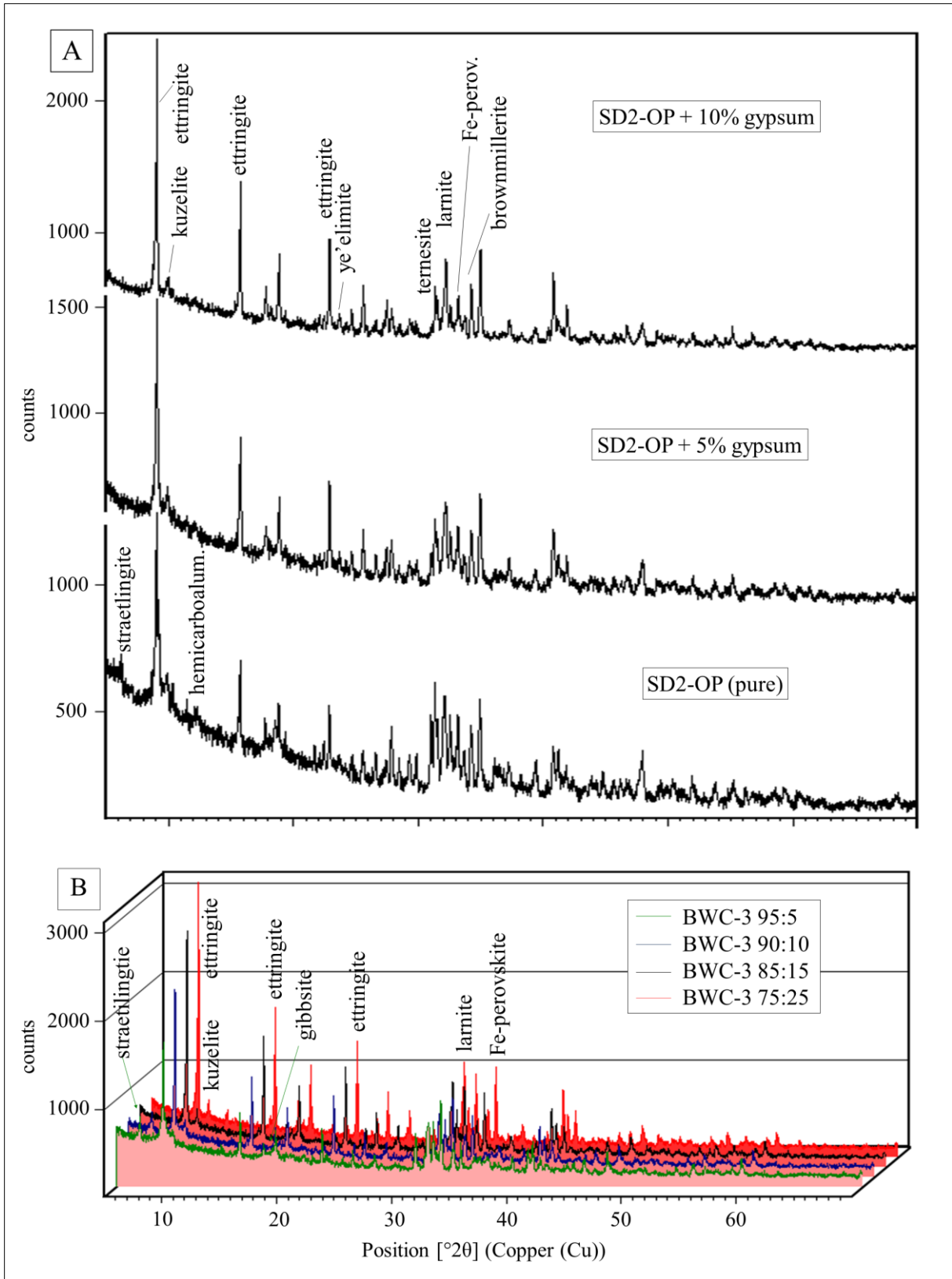
Figure 83 XRPD patterns of the hydrated cements SD2-OP (A) and BWC-3 (B, compared 3D view), after 72 hours and using a w/c = 1.

The calorimetry measurements of SD2-6 and SD2-OP were conducted again using a w/c = 0.5 to verify if the lowering of the w/c ratio would influence the main hydration time and phase composition of the cements. The results show that the hydration behaviours of the cements are very similar when using both a w/c = 1 and w/c = 0.5, at least in the first 72 hours of studied time (Figure 84). The XRPD patterns of the hydrated systems are also similar (Figure 84). Therefore, the presented results of the hydration time and consequent formed phase assemblage using a w/c = 1 or 0.5 are not likely to change much within the first 72 hours.
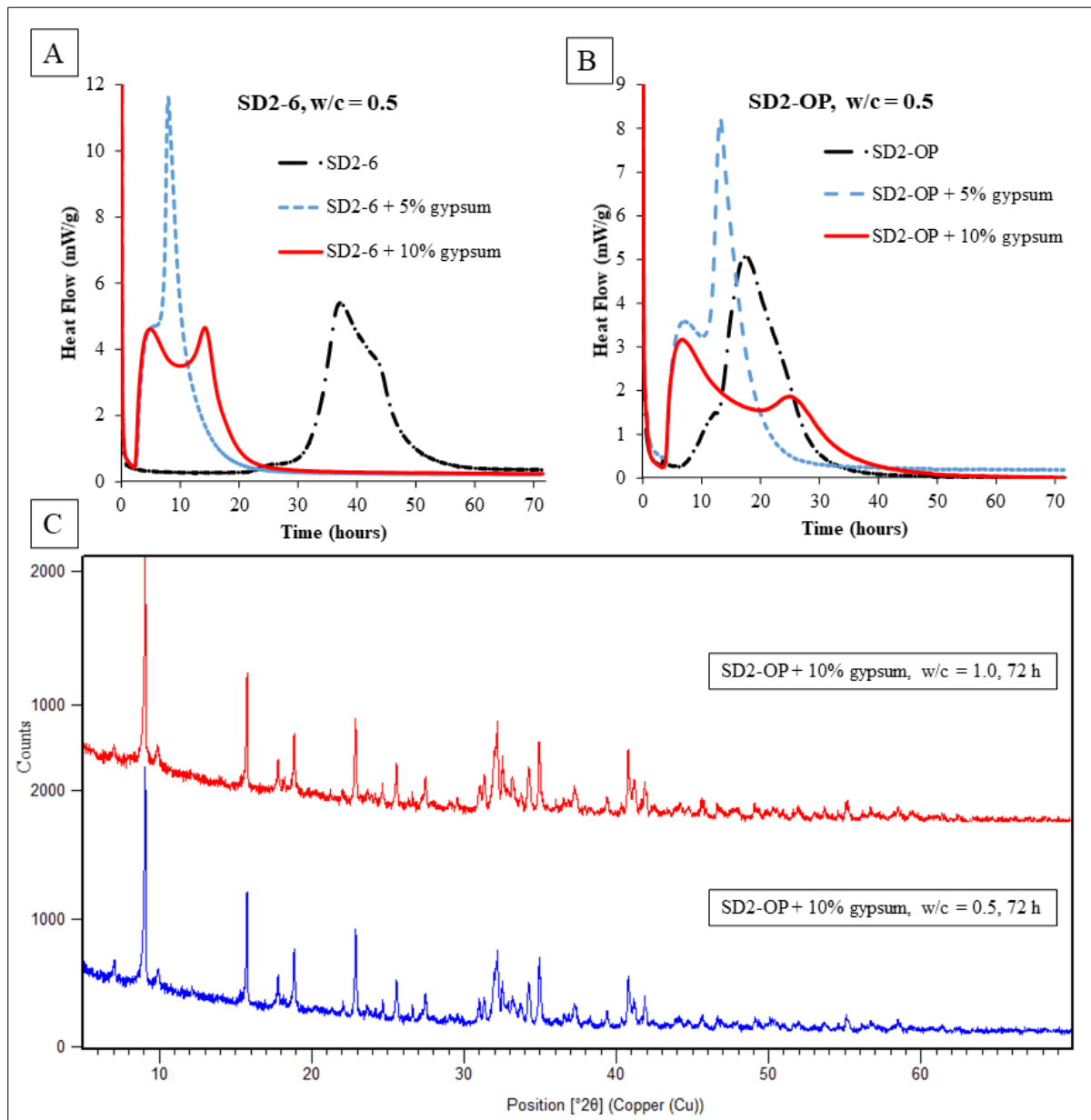
Figure 84 Isoperibolic heat flow curves of the hydrated clinkers SD2-6 (A) and SD2-OP (B), with gypsum additions using w/c = 0.5. C: XRPD pattern of the hydrated SD2-OP with 10% gypsum added and using the different w/c ratios of 0.5 and 1.

6.4.2   Water demand of the cements

The water demand of the cements, which is the necessary amount of water to fill the cement voids and saturate the cement powder, is expressed in Table 20. The values represent w/c ratios close to 0.3.

Table 20 Determined water to cement ratio (w/c) and water demand (g/m^3) of the cements.

Clinker	SD2-6	SD2-OP	SD3-11	SD3-11 1300°C	SD3-OP	SD3-OP-B
w/c ratio	0.350	0.332	0.320	0.302	0.340	0.300
water demand	0.518	0.498	0.496	0.487	0.516	0.480

6.4.3   Micromorphology of the hydrated cements

SEM micrographs of the SD2-6 and SD2-OP cements (pure and added with gypsum) are reported after 72 hours of curing using a w/c = 1 (Figure 85). In all products, ettringite is abundant and formed needle-like and large micrometric prisms reaching close to 10 µm. Large monosulfoaluminate crystals were also observed in the cement matrix and were more abundant in the cements without (or with lower) gypsum additions.

Individual larnite crystals were not recognised in the SEM images of the hydrated cements. Instead, there appear to be fragments of larnite partially or entirely involved by a material similar to calcium silicate hydrates (C-S-H), which are the main hydration product of Portland cements. SEM-EDS point analysis reveals that these sponges are mainly composed of Ca, Si and Al. Therefore, they might represent straetlingite or an amorphous hydrate with C-S-A-H composition (Figure 86).
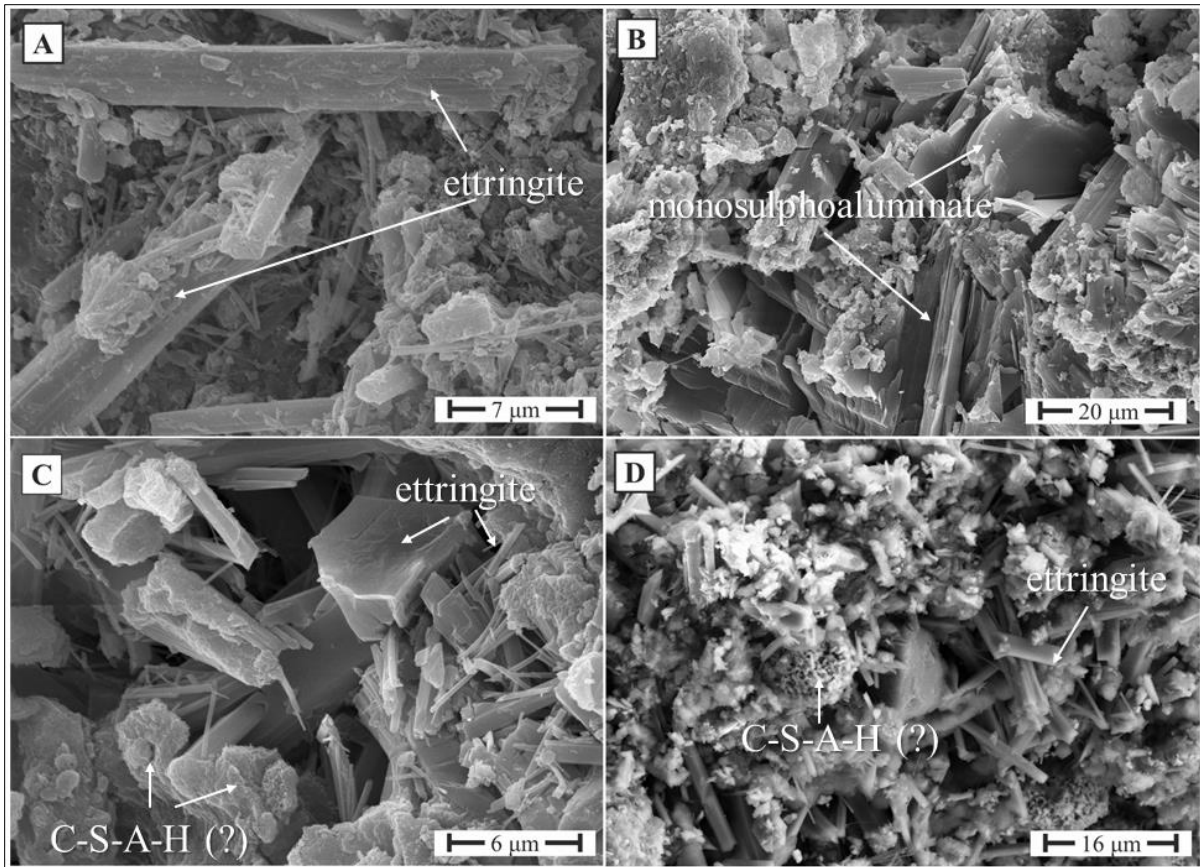
Figure 85 Micromorphology of the hydrated clinkers after 72 hours. A: prismatic and thin needle-shaped and larger ettringite crystals in the cement SD2-OP with 10% of gypsum; B: platy monosulfoaluminate (kuzelite) aggregates, ettringite prisms, and unreacted larnite aggregates in the cement SD2-6; C and D: ettringite needles and prisms and C-S-A-H (or straetlingite) in the cement SD2-6 with 10% of gypsum. Images acquired at Zentrum für Werkstoffanalytik in Lauf, Germany. Source: Negrão et al. (2021c).
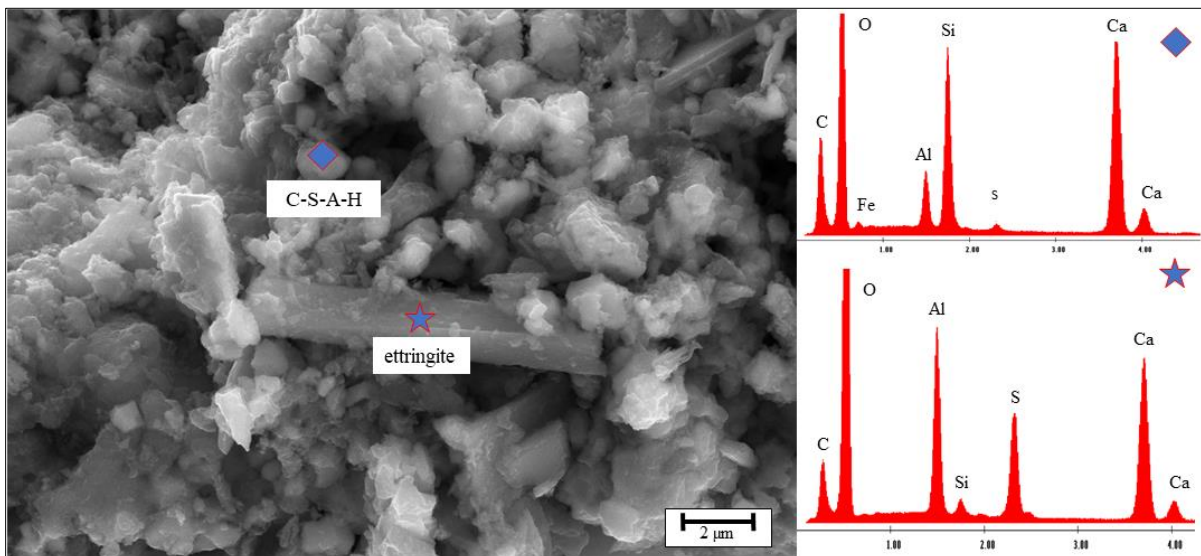
Figure 86 SEM image of the cement SD2-6 and corresponding SEM-EDS spectra showing ettringite prisms and sponge-like aggregates with C-S-A-H composition (possibly straetlingite). Hydration time 72 hours, and w/c = 1. Images acquired at Zentrum für Werkstoffanalytik in Lauf, Germany.

Monosulfoaluminate (kuzelite) was much more abundant in the samples without gypsum additions (Figure 87). This phase builds large and well-formed hexagonal crystals, sometimes larger than 30 μm.
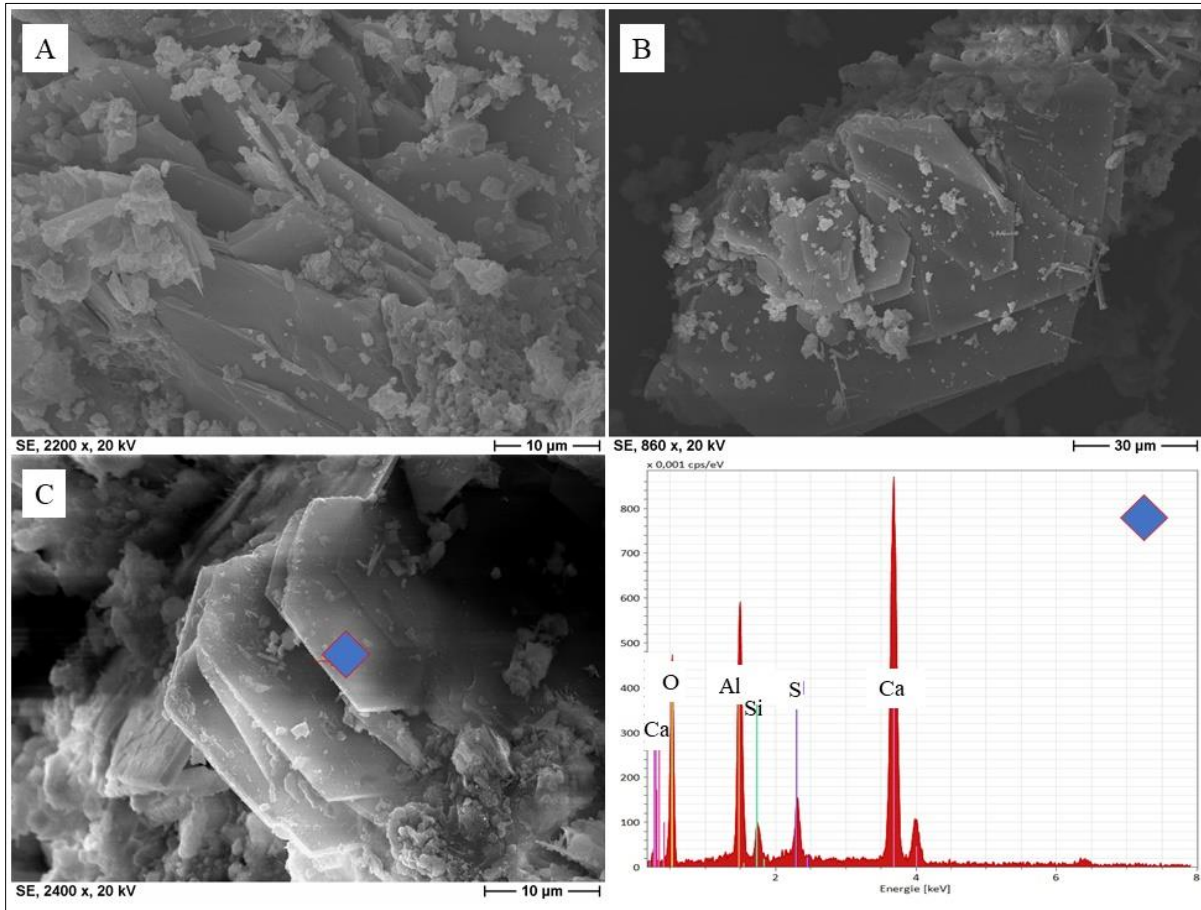
Figure 87 SEM images of crystallites of monosulfoaluminate with pseudo-hexagonal shapes in the hydrated cements SD3-11(A); SD3-11 with 10% gypsum (B), and SD3-OP (C), with corresponding SEM-EDS spectra. Hydration time 72 hours, and w/c = 1. Images acquired at the University of Halle.

6.5 Compressive strength and phase evolution of produced mortars

The compressive strength of the cement mortars produced with the clinkers made with Belterra Clay from the Círiaco pilot-mine (SD2-2 and SD2-OP) and from the Branco pilot-mine (SD3-11, SD3-11 1300 °C, SD3-OP and SD3-OP-B) are reported in the section 6.5.1. These mortars were produced using reduced water to cement ratios of 0.3, as determined by the Puntke method (Puntke, 2002). Five percent of gypsum was add to each clinker to produce the mortars.

The mortars produced with the clinker BWC-3, made with the bauxite washing clay residue, are reported separately in the section 6.5.2 because these mortars were produced using diverse

clinker to gypsum ratios. The different water to cement ratio of 0.45 was used to ensure enough water was present to form the expected larger amounts of ettringite due to the larger amount of sulfate available.

6.5.1   Mortars using a w/c ratio = 0.3

The mortars developed different strengths at the investigated times. A minimum of 24 Mpa (mortar SD3-OP) and a maximum of 37 Mpa (mortar SD2-OP) was achieved within 7 days of curing (Figure 88). The compression strength of the mortars increased to at least 26 Mpa (SD3-OP), reaching a maximum of 46 Mpa (SD3-11 1300°C) after 28 days. The specimens achieved similar strength when compared to the Portland cement (48 Mpa after 28 days) tested with the same mortar size and w/c ratio (Figure 88).
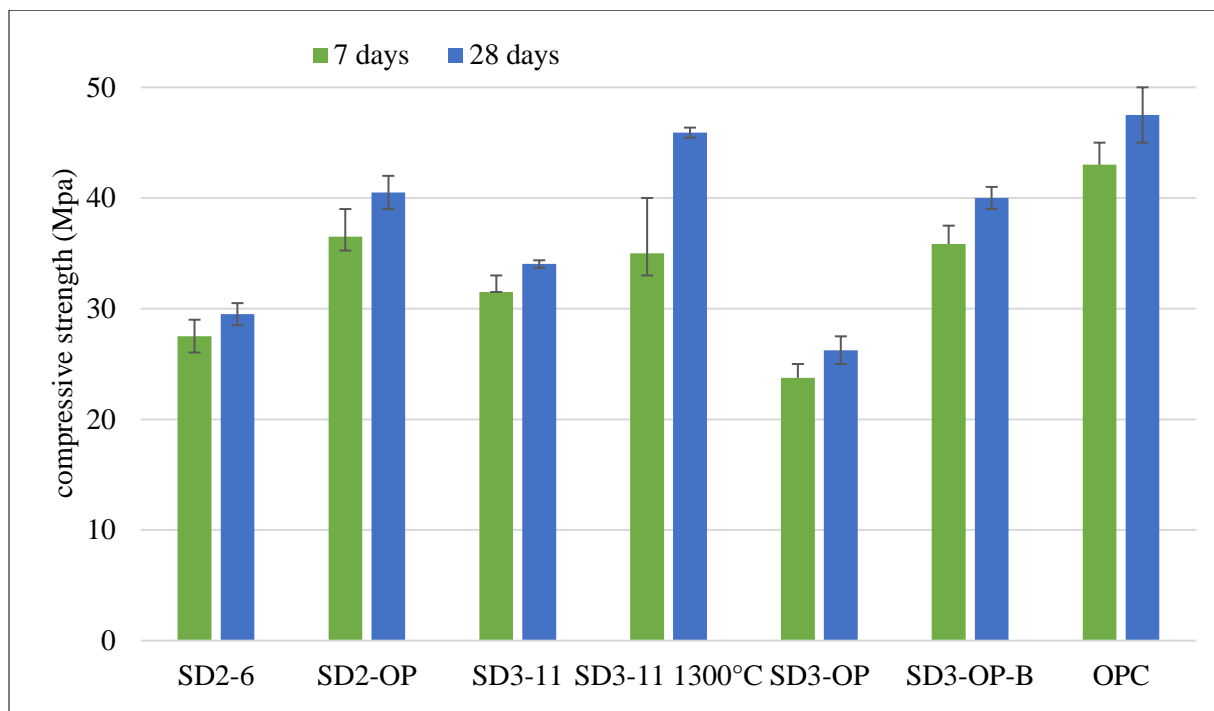
Figure 88 Compressive strength development of the mortars produced with clinkers produced using the Belterra Clay. The clinkers were mixed with 5% of gypsum. The compared OPC is a type CEM I 42.5 R. The testing results are after 7 and 28 days of hydration and using a w/c = 0.3 in all mortars.

The Rietveld-quantified phase and amorphous contents of the cements before and after hydration are expressed in Table 21. The phase contents are normalised to the non-reacted water, to make possible a direct observation of the evolution of the mineral assemblage. In all samples, ye'elimite was completely (or almost) consumed. The very small content of remaining

ye'elimite after hydration in some cements can be due to minor trapped non-hydrated cement grains. The anhydrous phase assemblages of the mortars have large amounts of belite (larnite or flamite) and ternesite, besides lesser amounts of brownmillerite, Fe-perovskite and gehlenite.

Considering the uncertainty of at least ±1% of the XRPD-Rietveld results, it is clear that the amount of belite (as larnite or flamite) decreased in the first 7 days and then was practically constant from 7 to 28 days. Only the mortar SD3-OP had a more expressive decrease in the larnite contents from day 7 to day 28. Similarly, ternesite and brownmillerite remained almost invariable from day 7 to day 28 of hydration. The uncertainty of the Rietveld quantifications and the high amorphous contents prevent an accurate evaluation of if the phases occurring in lower amounts (i.e., Fe-perovskite and gehlenite) reacted to some minor extent.

The mortars have high amounts (up to 19%) of amorphous, which decrease in all samples from day 7 to day 28. The non-reacted water decreased from day 0 to day 7 but remains practically constant after that.
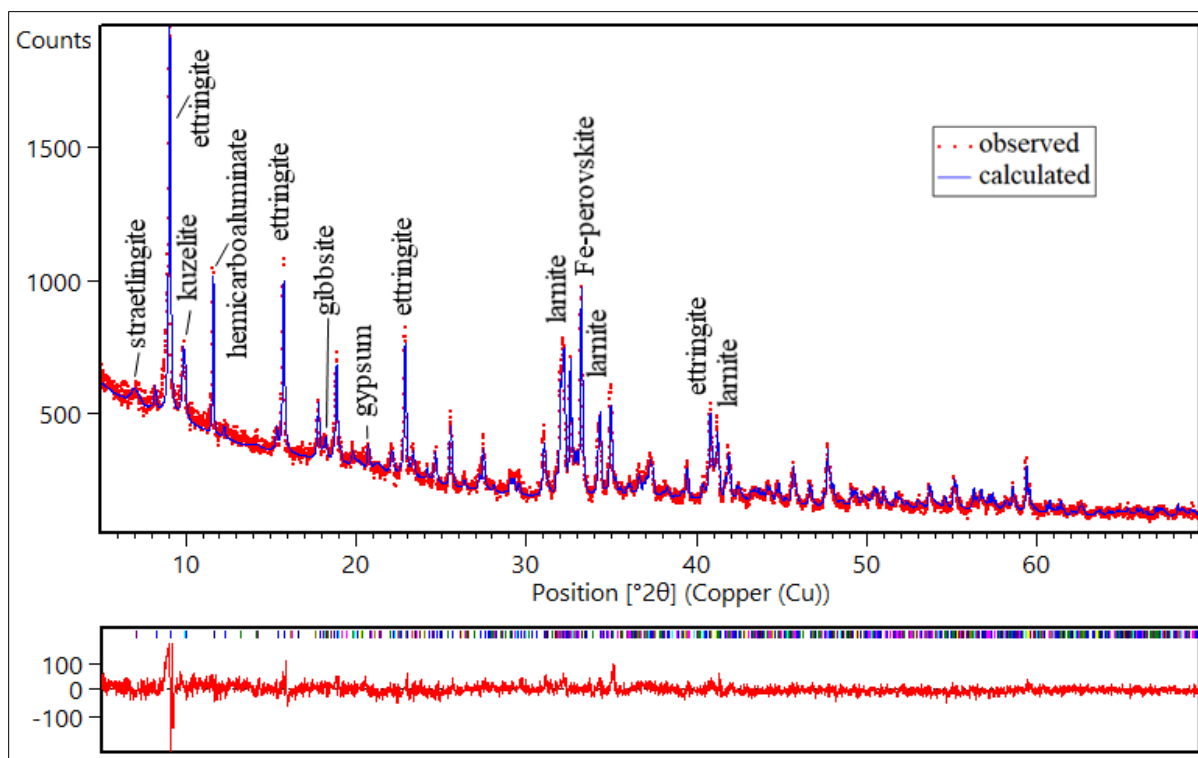
Figure 89 Rietveld-refined XRPD and its difference plot of the mortar SD3-OP-B produced with clinker to gypsum ratio of 95:05. The quantitative results are given in Table 21.

The hydrated assemblage has ettringite as the main hydration product, which is expected as previously commented. According to the XRPD-Rietveld analysis (i.e., Figure 89), the

ettringite contents did not change much from day 7 to day 28, with a possible small increase in the mortars SD3-11 1300 °C and SD3-OP-B. Kuzelite is the second most abundant hydration product in the mortars, with slightly increased contents, but still within the quantification uncertainties of the Rietveld method. Ettringite and kuzelite are further confirmed by their mass losses and DSC curves in the thermal analysis. The first mass loss and associated DSC peak close to 150 °C is mainly attributed to ettringite but is also influenced by kuzelite, which has an additional shoulder peak in the 170 – 200 °C range.

Table 21 Normalised Rietveld-quantified phase and amorphous contents, and non-reacted water of the cement mortars produced with w/c = 0.3. Time = 0 refers to the mixtures before hydration. The used clinker to gypsum ratio to produce all mortars was 95:5. Hemicarb. = hemicarboaluminate.

mortars	SD2-6			SD2-OP			SD3-11			SD3-11 1300°C			SD3-OP			SD3-OP-B		
time (days)	0	7	28	0	7	28	0	7	28	0	7	28	0	7	28	0	7	28
ye'elimite	27	-	1	28	2	2	24	1	1	27	4	4	21	-	-	21	2	3
larnite	25	20	18	13	12	12	24	20	19	33	26	27	34	24	19	-	-	-
flamite	-	-	-	-	-	-	-	-	-	-	-	-	-	-	-	25	22	23
ternesite	4	1	2	19	15	15	14	10	11	-	-	-	4	2	3	-	-	-
brownmillerite	5	1	1	1	-	-	8	6	5	7	4	4	10	5	4	3	3	2
Fe-perovskite	5	6	4	5	4	4	1	1	1	4	2	2	1	1	1	4	2	3
gehlenite	7	8	8	5	6	6	1	2	2	1	3	2	1	1	2	8	9	10
anhydrite	-	-	-	3	-	-	2	-	-	4	-	-	3	-	-	2	-	-
gypsum	4	-	-	4	-	-	4	-	-	4	-	-	4	-	-	4	-	-
ettringite	-	15	14	-	19	21	-	19	20	-	23	25	-	20	19	-	23	26
kuzelite	-	12	13	-	8	9	-	6	7	-	4	6	-	8	11	-	3	2
straetlingite	-	3	7	-	1	2	-	-	3	-	-	1	-	6	12	-	-	-
gibbsite	-	-	5	-	2	4	-	-	-	-	-	-	-	2	2	-	2	-
hemicarb.	-	3	-	-	1	1	-	1	-	-	1	1	-	-	-	-	2	2
amorphous	-	19	13	-	16	14	-	19	16	-	18	14	-	18	16	10	18	17
non-reacted water	22	13	13	22	13	11	22	15	15	22	14	13	22	12	12	22	14	12
GOF	1.3	1.2	1.1	1.3	1.3	1.2	1.1	1.2	3.3	1.4	1.2	1.3	1.2	1.2	1.2	1.1	1.3	1.3
Rwp	4.5	7.4	6.7	4.4	7.5	7.2	4	6.8	5.4	4.9	6.8	7.7	4.4	7.1	6.9	7.0	7.2	7.8

Straetlingite and gibbsite are the only hydrated phases that had a clearer increase from day 7 to day 28 according to the Rietveld quantifications. In the mortar SD3-11 1300 °C, no straetlingite or gibbsite was detected by XRPD. Nevertheless, the discrete mass losses around 220 and 300 °C (Figure 90) can be attributed to small amounts of these phases, which can be partially amorphous, as is often the case of gibbsite. Therefore, the DSC peaks around 220 °C and 300

°C, are attributed respectively to the decomposition of straetlingite and gibbsite. When straetlingite and gibbsite are more abundant, as in SD2-OP, better-individualised peaks are observed.
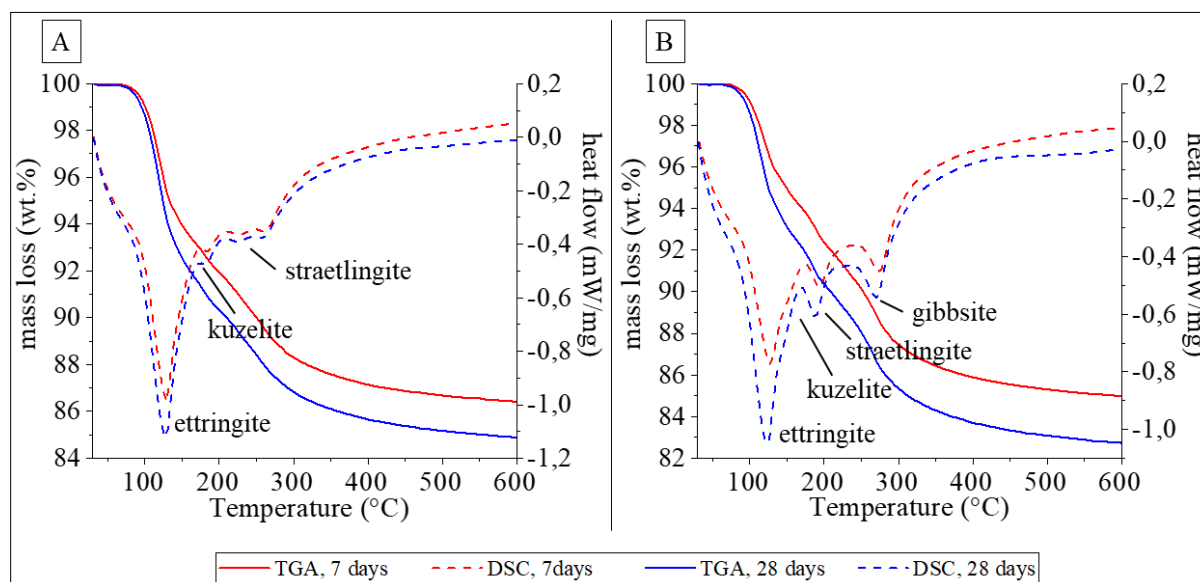
Figure 90 Thermal analyses of the mortars SD3-11 1300 °C (A) and SD2-OP (B).

The stronger strength development of the mortars SD3-11 1300°C and SD3-OP-B, compared to the other mortars, can be attributed to the higher amounts of formed ettringite. The increase in strength from day 7 to day 28 is apparently not related to an increase in ettringite or kuzelite but might be related to a complexation in the amorphous fraction, including some possible C-S-A-H as observed by SEM, but not reached by XRPD.

6.5.2   Mortars using a w/c ratio = 0.45

The mortars made using the clinker BWC-3, produced out of the bauxite washing clay, developed increasing strength in the studied period from 7 to 28 days, and comparable and higher compressive strength than the OPC mortar (Figure 91). However, all of them developed in general lower compressive strength when compared to the other mortars produced using a w/c ratio of 0.3. The comparatively lower strength due to the higher w/c of 0.45 used for the BWC-3 mortars was expected. Higher w/c ratios commonly result in higher porosity and increased pore size in the mortars, which in turn gives lower compressive strengths (García-Maté et al., 2012; Morin et al., 2017).

The increased gypsum amounts used in these mortars resulted in an increase of compressive strength to up to 51 Mpa (mortar BWC-3 85:15, after 28 days), for a maximum of 15% of gypsum added to the clinker. However, the strength development sharply decreased to a maximum of only 33 Mpa when 25% of gypsum was added (mortar BWC-3 75:25).
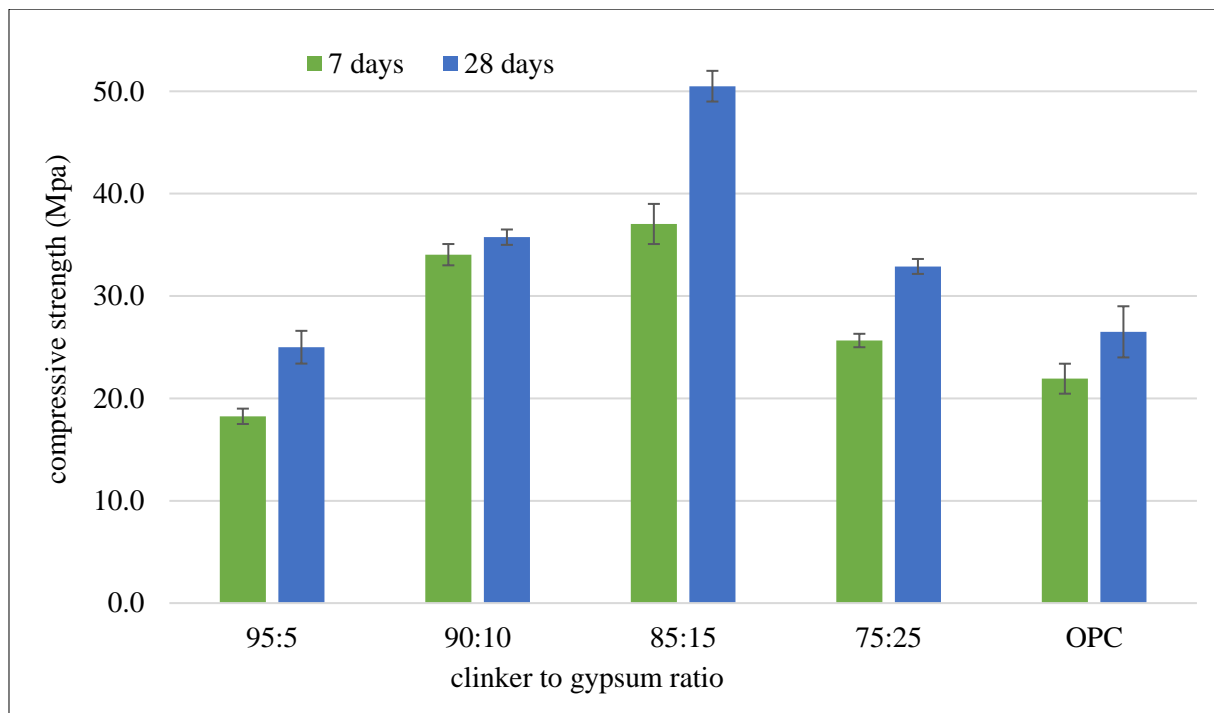
Figure 91 Compressive strength development of the mortars BWC-3, produced with clinker made with the bauxite washing clay sample. The mortars produced with different clinker to gypsum ratios are compared with an Portland cement type CEM I 42.5 R. The tests were performed after 7 and 28 days of hydration and using a w/c = 0.45 in all mortars.

In all mortars, ye'elimite was completely (or almost completely) consumed upon hydration (Table 22). The larnite contents decreased with the course of hydration in all mortars, confirming its participation in the hydration of the cement. However, larnite was consumed to a larger extent in the mortars produced with lower gypsum contents. Up to 32% of larnite was consumed in the mortar BCW-3 95:5 (28 days), whereas 21% of this phase was consumed in the mortar BCW-3 75:25 (28 days).

No brownmillerite was characterised in the hydrated mortars, suggesting that the initial low amount of this phase reacted completely, or that some few left brownmillerite is under the limit of quantification. Perovskite and gehlenite are not believed to have reacted when the Rietveld-quantification uncertainties are considered.

Ettringite was again the main hydration product quantified in the mortars (Table 22), reaching 42% in the mortar BWC-3 75:25 after 28 days of hydration. Ettringite's contents increased with the increasing gypsum addition in the clinkers, confirming its increased formation upon sulfate addition.

Table 22 Normalised Rietveld-quantified phase contents, amorphous, and non-reacted water of the BWC-3 cement mortars produced using w/c=0.45. Time = 0 refers to the mixtures before hydration. Hemicarb. = hemicarboaluminate.

clinker:gypsum ratio	95:5			90:10			85:15			75:25		
time (days)	0	7	28	0	7	28	0	7	28	0	7	28
ye'elimite	29	-	-	28	1	-	26	1	-	23	1	1
larnite	26	21	18	25	21	19	23	19	18	21	16	17
brownmillerite	3	-	-	2	-	-	2	-	-	2	-	-
Fe-perovskite	6	5	5	6	5	4	5	4	4	5	4	4
gehlenite	1	2	1	1	1	1	1	1	1	1	-	-
gypsum	3	-	-	7	-	-	10	3	3	17	5	5
ettringite	-	16	15	-	24	24	-	29	31	-	38	42
kuzelite	-	10	11	-	4	6	-	3	4	-	-	-
straetlingite	-	3	6	-	1	5	-	1	1	-	-	-
gibbsite	-	2	3	-	3	3	-	2	2	-	2	2
hemicarb.	-	-	1	-	2	1	-	1	1	-	1	1
amorphous	-	21	22	-	20	19	-	19	18	-	14	11
non-reacted water	31	19	19	31	19	18	31	18	17	31	18	16
GOF	1.2	1.4	1.3	1.2	1.4	1.2	1.2	1.3	1.3	1.2	1.4	1.4
Rwp	4.3	8.1	7.5	4.3	8.4	7.3	4.3	7.7	7.3	4.3	8.5	8.3

Kuzelite was the second most abundant hydrated phase, showing slightly increasing contents with time for the same cement composition, but decreasing amounts for the mortars produced with higher gypsum contents, and finally absent in the mortar BWC-3 75:25. Straetlingite showed similar behaviour to kuzelite. Gibbsite seems to be more abundant in the mortars produced with less gypsum, and small amounts of hemicarboaluminate were quantified in almost all mortars. Last, the high amorphous contents in the hydrated mortars decreased with the hydration time and were also lower in the mortars produced with more gypsum.
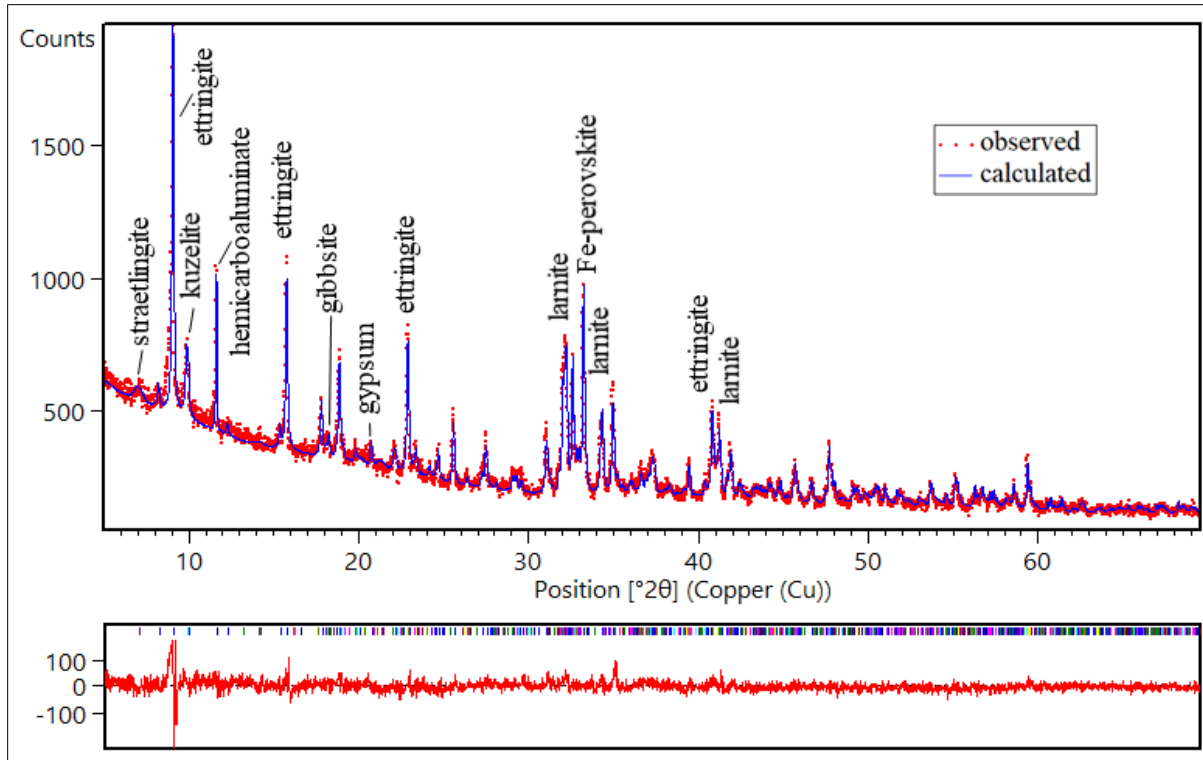
Figure 92 Rietveld-refined XRPD and its difference plot of the mortar BWC-3 85:15. The quantitative results are given in Table 20.

Like the mortars produced with w/c ratios = 0.3, the mortars produced with w/c ratios = 0.45 have the strength development mainly controlled by the formed amount of ettringite. The exception is for the mortar BWC-3 75:25, which achieved a lower compressive strength, besides the highest ettringite contents formed. This situation seems to be related to an excess of added sulfate, as observed by García-Maté et al. (2012) and Morin et al. (2017b).

7 Summary and discussions

7.1   Raw meal compositions and clinkering temperature

The design of experiments helped to find optimal raw meal compositions to produce the CSA-based clinkers using a reduced number of experimental trials. Nevertheless, the software computations do not consider the complex chemical interactions that occur during clinkering (Galluccio et al., 2019), and the changes in the phase assemblage of the clinkers must be carefully considered in the determination of the optimal clinkering conditions.

The optimised clinkers were here defined as those with maximised contents of ye'elimite, produced using as much as possible of the bauxite residues (Belterra Clay or bauxite washing clay), and a minimum of calcium carbonate. To obtain a maximum of ye'elimite, aluminium has preferentially to be in ye'elimite. However, both brownmillerite and gehlenite also capture aluminium. Brownmillerite is a very common phase in clinkers (Stutzman et al., 2014; Isteri et al., 2020) and is expected due to the high iron contents in the bauxite residues, whereas gehlenite could be partially restricted by adjusting the Belterra Clay / $CaCO_3$ ratios in the raw mixtures.

The clinker SD2-OP represents the optimal raw meal composition to produce CSA-based clinkers using Belterra Clay from the Círiaco pilot-mine. Its raw meal composition is formed of 38% of Belterra Clay, 47% of $CaCO_3$ and 15% of gypsum. This amount of gypsum is more than needed to form ye'elimite (considering the Al contents in the raw meal). Consequently, high contents of ternesite were formed in the clinker SD2-OP.

From the clinkers produced out of Belterra Clay from the Branco pilot-mine, the clinker SD3-OP was the optimised one and produced using 33% Belterra Clay, 57% of $CaCO_3$ and 10% of gypsum. Again, the excess of sulfate to that needed for ye'elimite resulted in extra ternesite (6%) in this clinker. Because ternesite and/or belite were not considered response variables in the design of experiments, the software suggested more gypsum in the modelled raw meal compositions to increase ye'elimite in the clinker and this excess of sulfate resulted in the conversion of part of belite into ternesite.

For comparison, the clinker BRA-SM was produced from a stoichiometric calculated raw mixture of 34.4% of Belterra Clay, 58.7% $CaCO_3$%, and 6.9% of gypsum. This amount of gypsum was calculated only to form ye'elimite, therefore no ternesite was formed in this clinker. That is, BRA-SM and SD3-OP were produced using almost the same Belterra Clay / $CaCO_3$ ratio close to 0.58, but with different gypsum contents that resulted, respectively, in a belitic calcium sulfoaluminate clinker (BCSA), and a BCSA rich in ternesite (BCSAT).

The clinker BWC-3 produced using the bauxite washing clay, is considered the optimised one due to its higher ye'elimite contents compared to the clinkers BWC-SM and BWC-2, also produced out of bauxite washing clay. BWC-3 raw meal is composed of 37.6% of bauxite washing clay, 52.9% of $CaCO_3$, and 9.5% of gypsum and was synthesised at 1250 °C.

Saving energy in the clinker production is directly proportional to the firing time in the kilns and inversely related to the chosen firing temperature. To reduce the usually close to 1450 °C temperatures used to produce Portland cements (Habert, 2013), diverse firing temperatures in the 1100 – 1300 °C range were tested. Overall, the clinkering temperature of 1250 °C is considered the ideal one in this work, and the formed mineral assemblage agrees to the found in the C-S-A-s-F system studied by Galan et al. (2017), besides the occurrence of perovskite due to the TiO_2 present in the bauxite residues. Temperatures lower than 1250 °C were not sufficient to maximise the contents of ye'elimite in the clinkers and often resulted in clinkers with excesses of free-lime and gehlenite. On the other hand, the higher temperature of 1300 °C was observed to slightly increase the ye'elimite contents in the clinkers but resulted in harder-to-grind clinkers and the formation of hydraulically inactive Fe-perovskite by the expenses of the hydraulic-reactive brownmillerite (Raab and Pöllmann, 2012). Moreover, 1300 °C is beyond the temperature stability of ternesite and this firing temperature might cause loss of SO_3 (Ben Haha et al., 2015; Liu et al., 2021).

7.2   Clinker compositions after the heterogeneity of the bauxite residues

The higher alumina contents of the Belterra Clay sample from the Círiaco pilot-mine (39.73% of Al_2O_3) resulted in clinkers with higher ye'elimite contents when compared to those produced using Belterra Clay from the Branco pilot-mine (35.58% of Al_2O_3), which had lower ye'elimite and consequently higher belite contents. Likewise, the higher alumina content of the bauxite washing clay (41.12% of Al_2O_3) resulted in clinkers with even higher amounts of ye'elimite.

The maximum amount of Belterra Clay or bauxite washing clay in the clinker raw mixtures also varied according to the composition of the used residue. The SD2-OP clinker required 38% of the Belterra Clay from the Círiaco pilot-mine, whereas the SD3-OP required 34% of Belterra Clay from Branco pilot-mine. The slightly higher alumina amounts in the bauxite washing clay enabled the use of up to 37.6% of this material to produce the clinker BWC-3.

The ye'elimite and belite contents in the clinkers are therefore controlled by the major differences in the chemical composition of the Belterra Clay samples (from the Círiaco or the Branco pilot-mine), and of the bauxite washing clay sample. The changes in the clinkers' phase compositions are majorly controlled by the variable Al_2O_3 and SiO_2 contents of the bauxite residues. Their Fe_2O_3 and TiO_2 contents are very similar and explain the similar amounts of brownmillerite and perovskite in the produced clinkers when using the same clinkering temperature.

The ye'elimite contents in all the clinkers produced at 1250 °C vary from 30 to 45%. The relative abundance of belite (as larnite or flamite) and ternesite resulted in CSAT (SD2-OP), CSAB (SD2-6 and BWC-3), and BCSA (SD3-OP and BRA-SM) clinkers.

7.3 Fe$_2$O$_3$-TiO$_2$ influence in the phase assemblage of the clinkers

7.3.1 Fe-rich perovskites in the produced clinkers

Perovskites are expected phases in CSA cements produced with Ti-containing raw materials (Telesca et al., 2019). Le Saout et al. (2019) reported a CSA-belite cement composed of only 0.76% of TiO$_2$, but with 11% of perovskite having the Ca$_{2.00}$Ti$_{0.40}$Fe$_{1.06}$Mg$_{0.05}$Al$_{0.30}$Si$_{0.22}$O$_{5.31}$ average composition. Koumpouri et al. (2021) used bauxite with a high content of TiO$_2$ (7.8%) to produce BCSA clinkers and also reported the formation of Fe-rich perovskites.

The TiO$_2$ contents of Belterra Clay and in the bauxite washing clay are slightly higher than 2%, and the optimised clinkers produced in this work have approximately 1 to 2% of TiO$_2$. The expected stoichiometric calculated contents of Fe-free perovskite (CaTiO$_3$) in the clinkers should vary from only 2 to 2.9%. However, up to 11% of perovskite was quantified by XRPD-Rietveld analysis in the produced clinkers. The SEM-EDS analyses show that the formed perovskites are Fe-rich and might contain some Si and Al, having the general average composition Ca$_{1.00}$Al$_{0.04}$Fe$_{0.27}$Ti$_{0.41}$Si$_{0.13}$O$_{2.76}$. Nevertheless, this composition is not representative of all Fe-perovskites in the clinkers, as most of the perovskite crystallites were very small and their measured chemical composition was affected by the surrounding phases in the SEM-EDS analyses.

The increased amounts of Fe-perovskite were inversely proportional to the amounts of brownmillerite in clinkers produced using higher CaCO$_3$ amounts, and within clinkers with the same chemical composition produced at the higher 1300 °C temperature. The effect of an excess of Ca resulting in lesser amounts of brownmillerite formed in the clinker was previously observed by Yao et al. (2020). Koumpouri et al. (2021) observed that the increase in temperature from 1270 °C to 1340 °C to produce similar CSA-based clinkers increased Fe-perovskites and decrease brownmillerite contents. Additionally, the authors reported that the decreased contents of perovskite were also related to the uptake of Ti in the structure of belite and consequent stabilisation of higher amounts of α_H'-belite. However, such effect was not observed in the clinkers produced in this work, in which β-belite was the only polymorph stabilised without external doping. This disagreement might be related to the amount of TiO$_2$, in the BCSA clinker produced by Koumpouri et al. (2021), which is twice the amounts in the clinkers produced in this work.

7.3.2 Structure of perovskite-related oxides and clinkering formation

$CaTiO_3$ perovskites comprise a structure of corner-shared octahedral layers formed by the close successive packing of Ca and O, with Ti in the centre of the octahedra surrounded by O (Rao, 2003). Ideally, perovskite has a cubic structure, but it can be distorted to the tetragonal, rhombohedral, or orthorhombic symmetry depending on the present cations and on oxygen vacancies. Whereas the perovskite is tolerant to some oxygen defects accompanied by the wide isomorphic cation substitution in its structure, tetrahedra layers might form depending on the extension of the substitution and oxygen deficit. The periodical alternation of tetrahedral (due to the oxygen vacancies) and octahedral layers results in the formation of brownmillerite-like $[Ca_2(Fe,Al)_2O_5]$ structures (Rao, 2003). That is, brownmillerite can be described as an oxygen-deficient perovskite-related structure, which is also able to accommodate diverse cations forming complex solid solutions (Broekmans and Pöllmann, 2018), including Mg^{2+}, Ti^{4+}, Si^{4+} (Marinho and Glasser, 1984), and Mn^{3+} (Stöber et al., 2013).

The pseudo-binary perovskite-brownmillerite series includes diverse compounds synthesised and described in the systems $CaTiO_3$–$Ca_2Fe_2O_5$ and $CaTiO_3$–Ca_2FeAlO_5 (Grenier et al., 1977; Marinho and Glasser, 1984; González-Calbet and Vallet-Regí, 1987; Hovmöller et al., 1988; Rodríguez-Carvajal et al., 1989; McCammon et al., 2000; Becerro et al., 2002). Some compounds of these systems have been described in nature as natural minerals, such as perovskite, brownmillerite, srebrodolskite $Ca_2Fe_2O_5$, shulamitite $Ca_3TiFeAlO_8$ (Sharygin et al., 2013), and nataliakulikite $Ca_4Ti_2(Fe^{3+}, Fe^{2+})(Si,Fe^{3+},Al)O_{11}$ (Sharygin et al., 2019).

Fe-perovskite is favoured over brownmillerite in the clinkers produced in this work at the high 1300 °C clinkering temperature. Therefore, most of the brownmillerite's Fe, and possibly even some Al, might accommodate in the Ti^{4+} position of perovskite. Due to the different charges of, Ti^{4+}, Fe^{3+} (or Fe^{4+}), and Al^{3+}, oxygen vacancies are formed, resulting in oxygen-deficiency Fe-rich perovskites.

7.3.3 Effect of brownmillerite-perovskite series on the clinker phase assemblage

The brownmillerite-perovskite stability depends on many factors, including the clinkering temperature, the raw meal homogeneity, the clinkering time, and the partial oxygen pressure (Zötzl and Pöllmann, 2006). In the experimental setup used in this work, the investigation on the stability of ternary mixtures of clinkers minerals showed that in all cases brownmillerite

was unstable already at 1250 °C, and most of the time completely decomposed after firing the sample at 1300 °C, with its Fe and Al being captured in the structure of perovskite and forming shulamitite $Ca_3TiFeAlO_8$. Si was also present in shulamitite, which is expected in this structure (Sharygin et al., 2013).

In the perovskite-brownmillerite-ternesite ternary mixture, not only brownmillerite but also ternesite was destabilised at 1300 °C and the contents of ye'elimite increased by the available S, Al, and Ca. The same mechanism can explain the slightly higher ye'elimite contents observed in the clinkers fired at 1300 °C, where ternesite and brownmillerite were also destabilised.

The average chemical composition of ye'elimite ($Ca_{4,64}Al_{5,08}Fe_{0,21}S_{1,00}O_{15,46}$) in the clinkers indicates that the destabilisation of brownmillerite can also contribute to iron intake by ye'elimite. The ~0.2 mol% of Fe present is under the maximum content close to 0.3 mol% of Fe found in Fe-rich ye'elimites (Chen et al., 1993; Idrissi et al., 2010; Touzo et al., 2013; Yao et al., 2020). The increased substitution of Al for Fe in the structure of ye'elimite has been linked to the increasing amounts of the cubic modification of ye'elimite by the expenses of the orthorhombic one at higher temperatures (Álvarez-Pinazo et al., 2012; Bullerjahn et al., 2014). That is, the phenomena observed in this work of the increasing contents of ye'elimite at higher temperatures with increasing contribution of the cubic polymorph is in agreement with an intake of Fe by this phase to a greater extent.

Comparing the produced clinkers with the ternary mixtures, no shulamitite formed in the clinkers. Therefore, it is suggested that in the 1250 °C – 1300 °C temperature range, Al preferably forms ye'elimite if enough sulfate is available.

The Fe-rich perovskite $Ca(Ti_{0.75}Fe_{0.25})O_{2.88}$ used in the Rietveld refinements (Dunyushkina and Gorbunov, 2002) was an approximation of the composition found in the clinkers. However, the perovskites in the clinkers have a heterogeneous chemical composition. Becerro et al. (2002) investigated the stability of Fe-doped perovskites and found tetragonal, cubic, and orthorhombic modifications depending on the Fe content and quenching temperature. Nevertheless, such modifications were not identified in the clinkers produced in this work and, if present, are in minor non-detectable amounts.

The Ruddlesden-Popper (RP) Fe-perovskite synthesised in this work is though more unlikely to occur in the clinkers. The measured average EDS composition of this phase was likely affected by the surrounding phases in the clinker, resulting in an excess of Ca. Instead of

forming an RP-Perovskite, the excess of Ca of this perovskite would probably trigger the formation of brownmillerite and/or form free-lime as observed in the produced clinkers. The characterisation of this synthesised phase is discussed below.

7.3.4 The $3(CaTi_{0.66}Fe_{0.33}O_{2.83}) \cdot CaO$ RP-perovskite

The synthesised RP-perovskite undergoes a transition at around 350 °C, assuming a pseudo-tetragonal unit cell but still with the *Pbca* space group. This transition was observed both by High-Temperature XRPD and in the thermal analysis. In this last, the endothermic peak in the DSC curve and the mass loss attributed to oxygen loss in the TG curve confirm the pseudo-transition.

According to the Mössbauer fits, around 24% of Fe^{4+} is present in the air-cooled sample, whereas the increase in temperature (sample quenched at 500 °C) resulted in few or no Fe^{4+}. The $Fe^{4+} \rightarrow Fe^{3+}$ reduction with the increase of temperature results also in a loss of 0.16 mol of oxygen, and possibly influences the phase transition to a pseudo-tetragonal cell.

The higher amounts of vacancies in the positions of the oxygens in the structure of the water-quenched sample (P-WQ-500) compared to the air-quenched sample (P-AQ) also indicates that oxygen was lost. Nevertheless, no preferable position was found for the oxygen vacancies, as these oxygen vacancies and the consequent defects are most likely randomly distributed in the structure of the studied phase.

The different Fe^{3+} coordination (CN4, CN5 and CN6) and the vacancies obtained by the refinement of the structures suggest that the oxygen deficiencies cause additional different coordination environments for iron, other than the CN6 forming octahedra in ideal perovskite. Such coordination could form pyramids and bipyramids (CN5) and/or tetrahedra (CN4), as observed in RP-perovskites with n=2 (Samain et al., 2015).

7.4   **Hydration of the produced CSA-based cements**

The main hydrated phase of the cements was, as expected, ettringite ($C_3A\cdot3Cs\cdot32H$). Ettringite is formed from the hydraulic reaction of ye'elimite (C_4A_3s) with calcium sulfates, here gypsum. Following the reaction path of ettringite formation (Equation 7.1), 2 moles of calcium sulfate (Cs) are necessary to react with 1 mole of ye'elimite and form 1 mole of ettringite (Winnefeld et al., 2017):

$$C_4A_3s + 2\ Cs + 38\ H \rightarrow C_3A\cdot3Cs\cdot32H + 2AH_3 \text{ (Equation 7.1)}$$
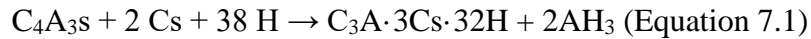
However, if no sulfate is present in solution, the reaction of ye'elimite only with water results in the formation of monosulfoaluminate (i.e. kuzelite), according to Equation 7.2 (Winnefeld et al., 2017):

$$C_4A_3s + 18\ H \rightarrow C_3A\cdot Cs\cdot12H + 2AH_3 \text{ (Equation 7.2)}$$

For a clinker with approximately 30% of ye'elimite, 16% of gypsum would be necessary to convert all ye'elimite into ettringite according to Equation 7.1. Likewise, 33.7% of water is required to balance the equation.
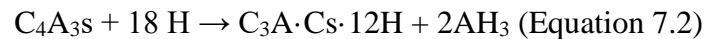
The w/c ratios of 0.3 used to produce the mortars were calculated after the Puntke method to determine the water demand of the cements and are on the limit of the needed water if all ye'elimite is consumed to form ettringite. However, less water is required for the amount of added gypsum (5%) to the clinkers, which is lower than the required in Equation 7.1. Besides lower, most of the CSA-based cement produced in this work using 5% of gypsum completed their main hydration in the first 24 h and developed strength comparable to OPC. Similar BCSA cements produced with the same amount of calcium sulfate also developed high strength (Li et al., 2019).

In fact, the clinker to calcium sulfate ratio is used to adjust the performance of CSA cements. Mehta (1980) proposed Equation 7.3 to calculate the required calcium sulfate to clinker ratio (C_T), to produce CSA cements for different field applications.

$$C_T = 0.13\cdot M\cdot A/s \text{ (Equation 7.3)}$$

C_T is the molar ratio of calcium sulfate over clinker, 0.13 is a stoichiometric factor containing all the conversions between mass and molar units, M is the calcium sulfate/ye'elimite molar ratio, A is the mass content of ye'elimite in the clinker and s is the mass (wt.%) of SO_3 in the

used calcium sulfate (anhydrite, basanite, or gypsum). Values of M from 0 to 1.5 are used for rapid hardening and high strength CSA cements, whereas higher values are for expansive (M = 1.5 to 2.5) or self-stressing cements (M = 2.5 to 6) (Mehta, 1980). The cements produced in this work with clinker to calcium sulfate ratios of 95:5 correspond to an M value varying from 0.5 to 0.6.

The BWC-3 mortars produced with clinker to gypsum ratios higher than 95:5 developed higher compressive strengths than the OPC mortar tested under the same conditions. The amounts of ettringite in the mortars produced with higher gypsum amounts were also higher and resulted in higher compressive strengths, except for the mortar BWC-3 75:25. Following Equation 7.1, the amount of ye'elimite in the clinker BWC-3 (45%) would need 23% of gypsum to convert all its ye'elimite into ettringite, which results in an M = 2.5. The mortar BWC-3 75:25 was produced with 25% of gypsum but had a decrease in the compressive strength when compared to BWC-3 90:10 and BWC-3 85:15.

This amount of gypsum (25%) resulted in a dimensionally unstable mortar and indicates that some expansive behaviour might have changed the mortar's internal framework, as observed in other CSA mortars produced with an excess of sulfate (García-Maté et al., 2012; Morin et al., 2017). That is, the amount of ye'elimite in the clinkers BWC-3 can even be adequate for expansive cements, according to the Mehta (1980) equation.

The second most abundant hydrate phase of the produced cements was monosulfoaluminate (kuzelite). This phase is mainly formed after all calcium sulfate is consumed to produce ettringite, leading to the reaction described in Equation 7.2. The lower amounts of monosulfoaluminate when more ettringite was formed are in agreement with the proposed equations.

Equations 7.1 and 7.2 show that aluminium hydroxide is an important product of the hydration of the CSA-based cements. This phase is usually amorphous (Wang, 2010), but can also crystallise as gibbsite and was identified in the hydrate assemblage of the cements. Aluminium hydroxide was also observed to have a positive influence on the strength gain of CSA cements by filling empty spaces and increasing the compactness of the cement paste (Chang et al., 2017).

The slower dissolution of belite and ternesite releases Ca and Si, which combine with the aluminium hydroxide to form straetlingite (Equation 7.4) and C-S-H gel (Equation 7.5) (Álvarez-Pinazo et al., 2016; Winnefeld and Lothenbach, 2016):

$$C_2S + AH_3 + 5H \rightarrow C_2ASH_8 \text{ (Equation 7.4)}$$

$$C_2S + (2 - x + y) H \rightarrow C_xSH_y + (2 - x) CH \text{ (Equation 7.5)}$$
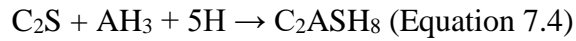
Straetlingite was present in most of the clinkers and was characterised by XRPD and in the thermal analysis of the cements. C-S-H can be amorphous or have a tobermorite-like structure, which was not observed in the XRPD. Instead, sponge-like C-S-H but with C-S-A-H composition was observed by SEM-EDS.

The dissolution of ternesite additionally releases SO_4^{2-}, which in turn might enhance the formation of ettringite or monosulfoaluminate in the systems. In the produced clinkers, ternesite was consumed to a greater extent if compared to larnite or flamite. However, an increase in ettringite formation could not be directly associated with that, as additional anhydrite was present in the clinker (SD2-OP). According to Ben Haha et al. (2015), ternesite's hydraulic reactivity can be further enhanced with $[Al(OH)_4]^-$ in solution.

Fe- and Si-rich hydrogarnets, considered a product of the hydration of ferrites (Wang, 2010; Gartner et al., 2011; Álvarez-Pinazo et al., 2016), were not identified in the XRPD patterns of the mortars.

7.5 Produced CSA-based cements in comparison to Portland cements

7.5.1 Properties and norming of CSA-based cements

As previously demonstrated, depending on the gypsum admixtures to the clinker, the obtained cements are comparable to commercial OPC. Specifically, the strength development of the CSA-based cements produced in this work are comparable to the compressive strength of a commercial OPC classified as CEM I 42R, which is a high initial strength Portland cement with no principal addition, composed of 95 to 100% of Portland clinker according to the European Norm EN 197-1. The closest composition of this cement in the Brazilian Norm (ABNT NBR 16697) is the high initial strength CP V, composed of 90 to 100% of Portland clinker.

CSA cements are known for their applications for rapid setting and high-early strength development (Allevi et al., 2016; Ben Haha et al., 2019; Bescher and Kim, 2019). However, these properties can be adjusted depending on the fineness of the cement and the use of admixtures to the clinker. The most important admixture to the CSA clinker is the type and amount of sulfate that will regulate the formation of ettringite in the hydration products (Mehta, 1980). Moreover, the naturally higher amounts of slow-reactive belite and/or ternesite in BCSA will partially control/delay the early hydration of these cements. In this respect, diverse CSA-based cements have been extensively studied and presented comparable or even better properties than Portland cements (Gartner et al., 2011; García-Maté et al., 2012; Álvarez-Pinazo et al., 2013, 2016; Bullerjahn et al., 2015; Li et al., 2019; Paul et al., 2021).

CSA-based cements are commercialised by diverse cement companies, as the CSAB Alipre® cement (60% C_4A_3s, 18% C_2S, 9% Cs) from Italcementi, the CSA NEXT® from Buzzi Unicem, and the ALPENAT® from Vicat. Additionally, BCSA-ternesite Ternocem® from Heidelberg Cement and BCSA Aether™ from Lafarge are alternative CSA cements with lower ye'elimite amounts. Particularly, the data of performance and durability of the BCSA Aether™ cement obtained in the EU's Aether project attested that the produced BCSA cements have good quality and are comparable to OPC, with even a better sulfate resistance and other improved characteristics such as dimensional stability after several tests (Gartner and Sui, 2018).

Most of the countries do not have specific norms for CSA-based cements. Even so, they are commercialised as rapid strength binders for special applications. In Brazil, at least a CSA cement (Fragumax) is currently commercialised as a rapid strength cement by Maxim Cimentos Especiais. The description of the Fragumax cement states it is composed of 1/3 of ye'elimite

and 2/3 of belite (Especiais, n.d.), and can reach > 25 Mpa after 1.5 days and at least 60 Mpa after 28 days.

7.5.2 Sustainability of the produced CSA-based cements

Compared to OPC, the CSA-based cements produced in this work represent savings of 25 to 38% of CO_2. The higher savings result from the ternesite-rich CSA compositions, which had part of the Ca from gypsum in the raw meal. For the ternesite-free clinkers, these savings are of at least 30%. The expressive CO_2 saving is expected higher for the whole production process of the cements, considering the lower clinkering temperatures used and the softer clinker, which needs a less energy-intensive grinding process.

Decreasing the amount of clinker used in the cement is another way to increase cement sustainability, as less clinker in the cement mixture means reduced CO_2 emission from the clinkering process. That is especially true for OPC, in which several natural or industrial by-products (including slags, fly ash and calcined clays) have had their pozzolanic activity tested for use as supplementary cementitious materials (Lothenbach et al., 2011; IEA, 2018). One of the interesting initiatives is the Calcined Clay Limestone Cement, or LC3 (Scrivener et al., 2019), in which a blend of calcined clay and limestone could replace large amounts of Portland clinker in the Portland cement, and representing a saving of at least 30% of CO_2 emissions by the sector.

Therefore, a fair comparison of the sustainability of Portland cements and the CSA-based cements must consider not only their clinker production but also the clinker to cement ratios. Some studies have shown that CSA-based cements can also be mixed with supplementary cementitious materials (Majling et al., 1999; García-Maté et al., 2013; Allevi et al., 2016; Pedersen et al., 2018), including limestone (Martin et al., 2015). The admixtures had a positive influence on the strength development of the CSA-based mortars and indicate that, as for OPCs, the clinker factor of CSA-based cements can also be reduced, enhancing its sustainability.

The optimal determined clinkering temperature of the CSA-based cements produced in this work is 1250 ºC, around 200 ºC lower than the temperature required to produce OPC clinkers. The lower temperature will certainly be related to lower energy consumption in the kilns, and since fossil fuel is used to heat the kilns, further CO_2 emissions will be comparatively reduced. Based on theoretical thermodynamic data, Ben Haha et al. (2019) estimated energy

consumption of 1426 kJ/g for a BCSA clinker composed of 50% of belite, 30% of ye'elimite and 20% of ferrite, which is approximately 20% less than the consumed to produce a Portland clinker composed of 67% of alite. According to the authors, further advantages in reducing the firing temperature in the cement kilns are the reduced formation of nitrogen oxides in the combustion gas, and the saving on refractory bricks in the clinkering zone of the kiln.

Likewise, the energy consumed in the grinding process is expected to be lower, as CSA-base cements are easier to grind than OPCs (Ben Haha et al., 2019). However, at the stage of this work, a complete and precise energy quantification is unviable to predict, as it depends on cement plant technology, the type of fuel to heat the cement kiln and the grinding equipment.

7.5.3   Industrial production of CSA-based cements

CSA-based cements can be produced in rotary kilns of OPCs, without extensive modifications to the industrial plant (Gartner and Sui, 2018). Just like for OPCs, careful monitoring of the production process, and more specifically in the kiln atmosphere, are necessary. The approach presented by Hanein et al. (2017) to capture elemental sulfur from sulfur-rich fossil fuels used to heat the kiln seems promising. The oxidation of sulfur leads to the formation of gaseous SO_2, which when fed in the kiln reacts with the raw materials to form increased amounts of ye'elimite, ternesite or anhydrite in the clinkers. This strategy is particularly interesting for the Brazilian scenario, as most of the petroleum coke used as fuel in the Brazilian cement industry is classified as High Sulfur Coke, a technical specification for the petroleum coke with S contents above 6% (Wainwright, 2018).

The demand for large amounts of raw materials by the cement industry can be filled on a regional scale by using the Belterra Clay and/or the bauxite washing clay residue. No additional bauxite was needed to produce the CSA-based cements presented in this work. The residues are easily and extensively available on the surface after the mining and beneficiation of the bauxite ore and are relatively homogeneous. Local and small variations in the alumina content, as the example of the lower-alumina Belterra Clay from the Branco pilot-mine, can be corrected with only small amounts of bauxite to achieve goal clinker compositions, which is already used to correct the raw meal compositions in the production of Portland clinker.

7.6   Perspectives considering the cement production in Brazil

Brazil has 100 cement factories, 64 of which have integrated production that covers the entire cycle, from the exploration of the raw materials to the clinker production. The other 36 are grinding plants that purchase the ready-made clinker and therefore do not have kilns (Fornari, 2019). The annual production of 53 million tons of cement ranks the country as the 12th largest cement producer in the world in 2019, but it is much lower than the 71.7 million tons produced in 2014 when Brazil was among the five largest cement producers in the world. This explains the current high idle capacity of 47% of cement production corresponding to 20 inactive factories in the country. The drop in cement production is linked to the economic recession that the country has experienced in recent years.

Brazil has also a relatively low consumption of cement per capita of 260 kg per inhabitant each year, compared to the world average (553 kg). However, the high housing and infrastructure deficit in the country and the expectation of population growth, points to growing production in the medium and long term, with a 60% to 120% increase of cement consumption in 2050 compared to 2014 (Fornari, 2019). These studies are part of the Cement Technological Roadmap project, developed by the cooperation of six cement factories in Brazil, in collaboration with the International Energy Agency, the International Finance Corporation, the World Business Council for Sustainable Development, and by the academic community. According to the study, the strategies for CO_2 reductions by the national cement industry cannot be considered homogeneous given the continental dimensions of Brazil.

In 2020, 55.97 million tons of cement were consumed in the country. The northern region was responsible for 3.40 million, with the State of Pará consuming 1.33 million, while the cement production in the same state was only close to 729 thousand tons (SNIC, 2021). The average price of cement in the State of Pará (Portland cement type 32) is approximately 21% higher than the average price in the country in the last three years (CBIC, 2021). These data show that cement production in the State of Pará was 601 thousand tons lower than consumption in 2020.

As mentioned earlier, CSA-based cements are comparable to OPC and can be produced in the same industrial plant with minor modifications (Gartner and Sui, 2018). The results indicate that at least 33% of Belterra Clay and 37.6% of bauxite washing clay can be used in the cement raw meal to produce CSA-based cements. Such replacements have a direct positive environmental impact, as they mean lesser CO_2 emissions by the cement sector and the use of

mining residues. Furthermore, the lower clinkering temperatures of the produced clinkers result in further energy savings.

Around 11.6 million tons of bauxite are produced per year in Paragominas in the State of Pará, Brazil, which generates close to 4.3 million tons of bauxite washing clay, and the relocation of much more amounts of Belterra Clay in the mining sites. Table 23 gives an estimate of how much of these residues could be used to produce 100 tons of some selected CSA-based clinkers produced in this work. The results are optimistic. From an economic point of view, reducing the use of limestone ($CaCO_3$) means an overall saving of local limestone reserves, and therefore an extension of the lifespan of limestone mines and, consequently in the cement factories.

Table 23 Amounts of raw materials to produce 100 tons of the different CSA-based clinkers produced in this work and relate CO_2 savings to produce the clinker compared to the production of an OPC clinker.

experimental clinker	clinker type	tons of raw material to produce 100 tons of clinker			CO_2 saving* (wt.%)
		bauxite reside	limestone*	gypsum	
SD2-OP	BCSAT	51 (Belterra clay - Círiaco)	64	20	38
SD3-OP	BCSA	46 (Belterra clay - Branco)	79	14	27
BWC-3	CSAB	52 (bauxite washing clay)	73	13	32

limestone* is here considered as $CaCO_3$. CO_2 saving* is the estimated save in CO_2 from the burning of the raw materials.

One of the most obvious barriers for CSA-based cement production has been the availability of alumina rich materials at low prices and which are largely available and relatively homogeneous. Here is shown that Belterra Clay and the bauxite washing clay fulfil these requirements. These materials can be converted from mining residues to an important raw material for CSA-based cements, at least regionally. The produced cements can be used in special applications considering their relatively high amounts of ye'elimite (up 45%), or to applications where OPC is used.

The initiative proves to be ecological and sustainable not only for its CO_2-reduction and reuse of mining residues to promote a circular economy but also due to the current scenario of carbon pricing, as several countries have already implemented carbon taxation policies.

8   Conclusions and perspectives

8.1 Conclusions

The bauxite clay overburden Belterra Clay and the clay residue from the washing of bauxite have similar chemistry and mineral composition. This doctoral thesis shows that both these residues from the mining of bauxite are suitable as raw materials to produce CSA-based cements. The high alumina contents of the residues enabled to define different raw material meals for CSA-based clinkers with aid of the design of experiments and stoichiometric modelling. Up to 38% of the alumina-richer Belterra Clay from the Círiaco pilot-mine, 34.4% of the lower-alumina Belterra Clay from the Branco pilot-mine, or a maximum of 37.6% of bauxite washing clay could be mixed with calcium carbonate and calcium sulfate (as gypsum) to form the raw meal of the clinkers.

The produced CSA-based clinkers have a maximum of 45% of ye'elimite. The clinkers have high amounts of belite (up to 49%), which was partially converted to ternesite depending on the gypsum contents used in the raw meal. The main mineralogical composition comprising ye'elimite, belite and ternesite permitted classifying the produced clinkers as CSAB, BCSA, and CSAT clinkers. Brownmillerite and Fe-perovskite summed together 10 to 15% of the phase assemblage. Minor amounts of gehlenite and anhydrite were also present in the clinkers.

The clinkering temperature of 1250 °C with one hour dwell time was defined optimum after comparing the experimental clinkers. Lower temperatures were not sufficient to maximise the ye'elimite contents in the clinkers, and the higher temperature of 1300 °C resulted in the decomposition of ternesite and brownmillerite, with the formation of higher amounts of non-reactive iron-rich perovskite.

The studies on the phase stability of the main phases present in the clinkers show that brownmillerite is already unstable at 1250 °C, but at a higher temperature, it is almost completely decomposed. Its reaction with perovskite formed Fe-rich perovskites, which can also incorporate some Si and Al. The experiments also showed that the decomposition of ternesite results in more sulfate available in the system, which when combined with Al from brownmillerite's decomposition can form some extra ye'elimite in the clinkers produced at 1300 °C. Besides the increased ye'elimite contents in the clinkers formed at this higher temperature, they have a closer matrix, are harder to grind and therefore consume more energy in both their production and grinding process.

The produced cements developed similar and even higher compressive strength compared to a commercial OPC within 7 and 28 days. The main hydrate phase in the cements was ettringite,

which increased in the clinkers according to their natural available or added amount of calcium sulfate. Higher amounts of ettringite in the produced mortars were directly related to higher strength. Besides ettringite, monosulfoaluminate, straetlingite, aluminium hydroxide (amorphous or as gibbsite), hemicarboaluminate and C-S-A-H were also identified in the hydrate assemblage of the mortars. The produced cements can partially substitute OPCs or be used in special applications. According to the literature, the content of ye'elimite (45%) in the CSAB clinker made with the bauxite washing clay permits its utilisation as expansive cement.

The production of the CSA-based cements using residues of the bauxite mining, and under lower temperatures than the production of OPCs, poses the binders as interesting alternatives to promote a sustainable initiative in both the mining and cement industry in the Amazon region. The production of the clinkers generates at least 30% less CO_2 compared to the CO_2 generated in the production of OPC clinkers. Additional savings in energy consumption in both clinkerization and grinding processes result in additional CO_2 savings.

In the regional scenario of the Brazilian Amazon, the CSA-based cements can rise the competitiveness of the local cement industry, turn mining residues into mining by-products, extend the lifespan of limestone reserves by producing less $CaCO_3$-intensive clinkers, and reduce the environmental impacts of the cement industry related to CO_2 emissions.

8.2 Perspectives

Besides promising, CSA-based cements still need to be regulated by national agencies before larger-scale commercialisation. In the meantime, deeper studies of the obtained cements might contribute to understanding their clinkering conditions and hydration. Specifically, more studies in the system C-S-A-s-F-T under a controlled atmosphere is suggested to understand their phase assemblage under different clinkering temperatures.

Provided an up-scaling to produce larger amounts of clinkers, more and longer-term testing of the mortars can contribute to the understanding of the development and stability of the hydrate assemblage. Finally, the production of mortars using the CSA-based cements produced in this work and additional supplementary cementitious materials might enhance even more the sustainability of CSA-based cements.

9   References

Abouchami, W., Näthe, K., Kumar, A., Galer, S.J.G., Jochum, K.P., Williams, E., Horbe, A.M.C., Rosa, J.W.C., Balsam, W., Adams, D., Mezger, K., Andreae, M.O., 2013. Geochemical and isotopic characterization of the bodélé depression dust source and implications for transatlantic dust transport to the Amazon basin. Earth Planet. Sci. Lett. https://doi.org/10.1016/j.epsl.2013.08.028

Adolfsson, D., Menad, N., Viggh, E., Bjo, B., 2007. Steelmaking slags as raw material for sulphoaluminate belite cement. Adv. Cem. Res. 7605, 147–156. https://doi.org/10.1680/adcr.2007.19.4.147

Allevi, S., Marchi, M., Scotti, F., Bertini, S., Cosentino, C., 2016. Hydration of calcium sulphoaluminate clinker with additions of different calcium sulphate sources. Mater. Struct. Constr. https://doi.org/10.1617/s11527-014-0510-5

Allmann, R., 1977. Refinement of the hybrid layer structure hexahydroxoaluminodicalcium hemisulfate trihydrate $[Ca_2Al(OH)_6]^+.[1/2SO_4.3H_2O]^-$. Neues Jahrb. fuer Mineral. Monatshefte 136–144.

Álvarez-Pinazo, G., Cuesta, A., García-Maté, M., Santacruz, I., Losilla, E.R.R., la Torre, A.G.D.G. De, León-Reina, L., Aranda, M.A.G.A.G., 2012. Rietveld quantitative phase analysis of Yeelimite-containing cements. Cem. Concr. Res. 42, 960–971. https://doi.org/https://doi.org/10.1016/j.cemconres.2012.03.018

Álvarez-Pinazo, G., Santacruz, I., Aranda, M.A.G., De La Torre, Á.G., 2016. Hydration of belite-ye'elimite-ferrite cements with different calcium sulfate sources. Adv. Cem. Res. https://doi.org/10.1680/jadcr.16.00030

Álvarez-Pinazo, G., Santacruz, I., León-Reina, L., Aranda, M.A.G., De La Torre, A.G., 2013. Hydration reactions and mechanical strength developments of iron-rich sulfobelite eco-cements. Ind. Eng. Chem. Res. https://doi.org/10.1021/ie402484e

Andrew, R.M., 2019. Global CO_2 emissions from cement production, 1928–2018. Earth Syst. Sci. Data 11, 1675–1710. https://doi.org/10.5194/essd-11-1675-2019

Antony, J., 2003. Design of Experiments for Engineers and Scientists, Design of Experiments for Engineers and Scientists. https://doi.org/10.1016/B978-0-7506-4709-0.X5000-5

Archambo, M., Kawatra, S.K., 2020. Red Mud: Fundamentals and New Avenues for

References

Utilization. Miner. Process. Extr. Metall. Rev. 1–24. https://doi.org/10.1080/08827508.2020.1781109

Arjunan, P., Silsbee, M.R., Della M. Roy, 1999. Sulfoaluminate-belite cement from low-calcium fly ash and sulfur-rich and other industrial by-products. Cem. Concr. Res. 29, 1305–1311. https://doi.org/10.1016/S0008-8846(99)00072-1

Balan, E., Lazzeri, M., Morin, G., Mauri, F., 2006. First-principles study of the OH-stretching modes of gibbsite. Am. Mineral. https://doi.org/10.2138/am.2006.1922

Balan, E., Saitta, A.M., Mauri, F., Calas, G., 2001. First-principles modeling of the infrared spectrum of kaolinite. Am. Mineral. https://doi.org/10.2138/am-2001-11-1201

Barreto, I.A.R., Costa, M.L. da, 2018a. Viability of Belterra clay, a widespread bauxite cover in the Amazon, as a low-cost raw material for the production of red ceramics. Appl. Clay Sci. https://doi.org/10.1016/j.clay.2018.06.010

Barreto, I.A.R., Costa, M.L. da, 2018b. Sintering of red ceramics from yellow Amazonian latosols incorporated with illitic and gibbsitic clay. Appl. Clay Sci. https://doi.org/10.1016/j.clay.2017.11.003

Barreto, I.A.R., da Costa, M.L., 2021. Use of the clayey cover of bauxite deposits of the Amazon region for geopolymer synthesis and its application in red ceramics. Constr. Build. Mater. 300, 124318. https://doi.org/https://doi.org/10.1016/j.conbuildmat.2021.124318

Barth, T., 1925. Die Kristallstruktur von Perowskit und verwandter Verbindungen. Nor. Geol. Tidsskr. 8, 201–219.

Batchelder, D.N., Simmons, R.O., 1964. Lattice constants and thermal expansivities of silicon and of calcium fluoride between 6° and 322°K. J. Chem. Phys. https://doi.org/10.1063/1.1726266

Becerro, A.I., Redfern, S.A.T., Carpenter, M.A., Knight, K.S., Seifert, F., 2002. Displacive phase transitions in and strain analysis of Fe-doped $CaTiO_3$ perovskites at high temperatures by neutron diffraction. J. Solid State Chem. https://doi.org/10.1016/S0022-4596(02)99663-5

Ben Haha, M., Bullerjahn, F., Zajac, M., 2015. On the reactivity of ternesite, in: Proceedings of the 14th International Congress on the Chemistry of Cement, Beijing, China.

References

https://doi.org/10.1248/cpb.6.638

Ben Haha, M., Winnefeld, F., Pisch, A., 2019. Advances in understanding ye'elimite-rich cements. Cem. Concr. Res. https://doi.org/10.1016/j.cemconres.2019.105778

Beretka, J., Cioffi, R., Marroccoli, M., Valenti, G.L., 1996. Energy-saving cements obtained from chemical gypsum and other industrial wastes. Waste Manag. 16, 231–235. https://doi.org/10.1016/S0956-053X(96)00046-3

Bergmann, J., Kleeberg, R., 1998. Rietveld Analysis of Disordered Layer Silicates. Mater. Sci. Forum 278–281, 300–305. https://doi.org/10.4028/www.scientific.net/MSF.278-281.300

Berrio, A., Rodriguez, C., Tobón, J.I., 2018. Effect of Al_2O_3/SiO_2 ratio on ye'elimite production on CSA cement. Constr. Build. Mater. 168, 512–521. https://doi.org/10.1016/j.conbuildmat.2018.02.153

Bescher, E., Kim, J., 2019. Belitic Calcium Sulfoaluminate Cement: History, Chemistry, Performance, and Use in the United States, in: 1st International Conference on Innovation in Low-Carbon Cement & Concrete Technology. London, p. 4.

Bish, D.L., Howard, S.A., 1988. Quantitative phase analysis using the Rietveld method. J. Appl. Crystallogr. 21, 86–91. https://doi.org/10.1107/S0021889887009415

Bish, D.L., Von Dreele, R.B., 1989. Rietveld refinement of non-hydrogen atomic positions in kaolinite. Clays Clay Miner. https://doi.org/10.1346/CCMN.1989.0370401

Black, D.R., Mendenhall, M.H., Windover, D., Henins, A., Filliben, J., Cline, J.P., 2016. Certification of standard reference material 1878b respirable α-quartz. Powder Diffr. https://doi.org/10.1017/S0885715616000336

Brindley, G.W., Kao, C.C., Harrison, J.L., Lipsicas, M., Raythatha, R., 1986. Relation between structural disorder and other characteristics of kaolinites and dickites. Clays Clay Miner. https://doi.org/10.1346/CCMN.1986.0340303

Broekmans, M.A.T.M., Pöllmann, H., 2018. Applied Mineralogy of Cement & Concrete. De Gruyter. https://doi.org/doi:10.1515/9781501508356

Bullerjahn, F., Schmitt, D., Ben Haha, M., 2014. Effect of raw mix design and of clinkering process on the formation and mineralogical composition of (ternesite) belite calcium sulphoaluminate ferrite clinker. Cem. Concr. Res. 59, 87–95. https://doi.org/10.1016/j.cemconres.2014.02.004

References

Bullerjahn, F., Zajac, M., Ben Haha, M., 2015. CSA raw mix design: effect on clinker formation and reactivity. Mater. Struct. Constr. https://doi.org/10.1617/s11527-014-0451-z

Buntenbach, S., 2008. Mineral Processing technologies in the Bauxite and Alumina Industry, in: Conference: 8th International Alumina Quality Workshop 2008. Darwin, Australia, Australia.

CBIC, 2021. Cimento - Consumo, Produção e Valores de Materiais de Construção - Câmara Brasileira da Indústria da Construção [WWW Document]. URL http://www.cbicdados.com.br/menu/materiais-de-construcao/cimento (accessed 7.22.21).

Chang, J., Zhang, Y., Shang, X., Zhao, J., Yu, X., 2017. Effects of amorphous AH_3 phase on mechanical properties and hydration process of $C_4A_3\bar{S}$-$C\bar{S}H_2$-CH-H_2O system. Constr. Build. Mater. 133, 314–322. https://doi.org/https://doi.org/10.1016/j.conbuildmat.2016.11.111

Chen, D., Feng, X., Long, S., 1993. The influence of ferric oxide on the properties of $3CaO \cdot 3Al_2O_3 \cdot CaSO_4$. Thermochim. Acta 215, 157–169. https://doi.org/https://doi.org/10.1016/0040-6031(93)80089-S

Chen, Y.F., Wang, M.C., Hon, M.H., 2004. Phase transformation and growth of mullite in kaolin ceramics. J. Eur. Ceram. Soc. https://doi.org/10.1016/S0955-2219(03)00631-9

Chukanov, N. V., Chervonnyi, A.D., 2016. IR Spectra of Minerals and Related Compounds, and Reference Samples' Data. https://doi.org/10.1007/978-3-319-25349-7_2

Colombo, C., Violante, A., 1996. Effect of time and temperature on the chemical composition and crystallization of mixed iron and aluminum species. Clays Clay Miner. https://doi.org/10.1346/CCMN.1996.0440110

Colville, A.A., Geller, S., 1971. The crystal structure of brownmillerite, Ca_2FeAlO_5. Acta Crystallogr. Sect. B Struct. Crystallogr. Cryst. Chem. 27, 2311–2315. https://doi.org/10.1107/s056774087100579x

Commission, E., 2006. Mining Waste [WWW Document]. URL https://ec.europa.eu/environment/topics/waste-and-recycling/mining-waste_en (accessed 8.20.21).

Costa, M.L. da, Cruz, G. da S., Almeida, H.D.F. de, Poellmann, H., 2014. On the geology, mineralogy and geochemistry of the bauxite-bearing regolith in the lower Amazon basin:

References

Evidence of genetic relationships. J. Geochemical Explor. 146, 58–74. https://doi.org/https://doi.org/10.1016/j.gexplo.2014.07.021

Cuesta, A., De La Torre, A.G., Losilla, E.R., Peterson, V.K., Rejmak, P., Ayuela, A., Frontera, C., Aranda, M.A.G., 2013. Structure, atomistic simulations, and phase transition of stoichiometric yeelimite. Chem. Mater. 25, 1680–1687. https://doi.org/10.1021/cm400129z

d'Amour, H., Denner, W., Schulz, H., 1979. Structure determination of α-quartz up to 68 x 10 8 Pa . Acta Crystallogr. Sect. B Struct. Crystallogr. Cryst. Chem. https://doi.org/10.1107/s056774087900412x

De Oliveira, S.B., Costa, M.L. da, Dos Prazeres Filho, H.J., 2016. The lateritic bauxite deposit of Rondon do Pará: A new giant deposit in the Amazon Region, Northern Brazil. Econ. Geol. 111, 1277–1290. https://doi.org/10.2113/econgeo.111.5.1277

Dienemann, W., Schmitt, D., Bullerjahn, F., Ben Haha, M., 2013. Belite-Calciumsulfoaluminate-Ternesite (BCT) - A new low-carbon clinker Technology. Cem. Int. 11, 100–109.

Doebelin, N., Kleeberg, R., 2015. Profex: A graphical user interface for the Rietveld refinement program BGMN. J. Appl. Crystallogr. https://doi.org/10.1107/S1600576715014685

Dunyushkina, L.A., Gorbunov, V.A., 2002. Crystal structure and electrical conductivity correlation in $CaTi_{1-x}Fe_xO_{3-\delta}$ system. Ionics (Kiel). 8, 256–261. https://doi.org/10.1007/BF02376076

El Hayek, R., Ferey, F., Florian, P., Pisch, A., Neuville, D.R., 2017. Structure and properties of lime alumino-borate glasses. Chem. Geol. 461, 75–81. https://doi.org/https://doi.org/10.1016/j.chemgeo.2016.11.025

Elcombe, M.M., Kisi, E.H., Hawkins, K.D., White, T.J., Goodman, P., Matheson, S., 1991. Structure determinations for $Ca_3Ti_2O_7$, $Ca_4Ti_3O_{10}$, $Ca_{3.6}Sr_{0.4}Ti_3O_{10}$ and a refinement of $Sr_3Ti_2O_7$. Acta Crystallogr. Sect. B. https://doi.org/10.1107/S0108768190013416

Especiais, M.C., n.d. FRAGUA-MIX. Concreto ensacado de pega rápida! [WWW Document]. URL http://www.maximcimentosespeciais.com.br/fraguamix.html

Figueiredo, F.M., Waerenborgh, J., Kharton, V. V, Näfe, H., Frade, J.R., 2003. On the relationships between structure, oxygen stoichiometry and ionic conductivity of

References

$CaTi_{1-x}Fe_xO_{3-\delta}$ (x=0.05, 0.20, 0.40, 0.60). Solid State Ionics 156, 371–381. https://doi.org/https://doi.org/10.1016/S0167-2738(02)00762-2

Fornari, M., 2019. Saneamento Ambiental. O esforço da indústria Bras. do Cim. para reduzir as Emiss. CO_2 6–10. https://doi.org/ISSN 0103-7056

Galan, I., Hanein, T., Elhoweris, A., Bannerman, M.N., Glasser, F.P., 2017. Phase compatibility in the system $CaO-SiO_2-Al_2O_3-SO_3-Fe_2O_3$ and the effect of partial pressure on the phase stability. Ind. Eng. Chem. Res. https://doi.org/10.1021/acs.iecr.6b03470

Galluccio, S., Beirau, T., Pöllmann, H., 2019. Maximization of the reuse of industrial residues for the production of eco-friendly CSA-belite clinker. Constr. Build. Mater. 208, 250–257. https://doi.org/10.1016/j.conbuildmat.2019.02.148

García-Maté, M., De la Torre, A.G., León-Reina, L., Aranda, M.A.G., Santacruz, I., 2013. Hydration studies of calcium sulfoaluminate cements blended with fly ash. Cem. Concr. Res. 54, 12–20. https://doi.org/https://doi.org/10.1016/j.cemconres.2013.07.010

García-Maté, M., Santacruz, I., De La Torre, Á.G., León-Reina, L., Aranda, M.A.G., 2012. Rheological and hydration characterization of calcium sulfoaluminate cement pastes. Cem. Concr. Compos. https://doi.org/10.1016/j.cemconcomp.2012.01.008

Gartner, E., Sui, T., 2018. Alternative cement clinkers. Cem. Concr. Res. 114, 27–39. https://doi.org/10.1016/j.cemconres.2017.02.002

Gartner, E., Walenta, G., Morin, V., Termkhajornkit, P., Baco, I., Casabonne, J.-M., 2011. Hydration of a Belite-CalciumSulfoaluminate-Ferrite cement: AetherTM, in: 13th International Congress on the Chemistry of Cement, Madrid, Spain.

Gatti, C., 2016. The Allumina Issue and the Bauxite Project in Rondon, Pará [WWW Document]. VII Brazilian Symp. Miner. Explor. URL http://www.adimb.com.br/simexmin2016/palestra/auditorio_sao_joao_delrey_16/15h00 Carlos Gatti.pdf (accessed 10.4.20).

Gesenhues, U., Rentschler, T., 1999. Crystal Growth and Defect Structure of Al^{3+}-Doped Rutile. J. Solid State Chem. 143, 210–218. https://doi.org/10.1006/jssc.1998.8088

Gibbs, M.J., Soyka, P., Conneely, D., 2002. Background Papers IPCC Expert Meetings on Good Practice Guidance and Uncertainty Management in National Greenhouse Gas Inventories - CO_2 Emissions from Cement Production.

References

González-Calbet, J.M., Vallet-Regí, M., 1987. A new perovskite-type compound: $Ca_4Fe_2Ti_2O_{11}$. J. Solid State Chem. 68, 266–272. https://doi.org/https://doi.org/10.1016/0022-4596(87)90312-4

Grenier, J., Schiffmacher, G., Caro, P., Pouchard, M., Hagenmuller, P., 1977. Etude par diffraction X et microscopie electronique du système $CaTiO_3$-$Ca_2Fe_2O_5$. J. Solid State Chem. 20, 365–379.

Grubb, P.L.C., 1979. Genesis of bauxite deposits in the lower Amazon Basin and Guianas coastal plain. Econ. Geol. 74, 735–750. https://doi.org/10.2113/gsecongeo.74.4.735

Habert, G., 2013. Assessing the environmental impact of conventional and "green" cement production, in: Eco-Efficient Construction and Building Materials: Life Cycle Assessment (LCA), Eco-Labelling and Case Studies. https://doi.org/10.1533/9780857097729.2.199

Hanein, T., Galan, I., Glasser, F.P., Skalamprinos, S., Elhoweris, A., Imbabi, M.S., Bannerman, M.N., 2017. Stability of ternesite and the production at scale of ternesite-based clinkers. Cem. Concr. Res. 98, 91–100. https://doi.org/10.1016/j.cemconres.2017.04.010

Horbe, A.M.C., Costa, M.L. da, 2005. Lateritic crusts and related soils in eastern Brazilian Amazonia. Geoderma 126, 225–239. https://doi.org/10.1016/j.geoderma.2004.09.011

Hörkner, W., Müller-Buschbaum, H., 1976. Zur kristallstruktur von $CaAl_2O_4$. J. Inorg. Nucl. Chem. 38, 983–984. https://doi.org/https://doi.org/10.1016/0022-1902(76)80011-5

Hovmöller, S., Zou, X., Wang, D.N., González-Calbet, J.M., Vallet-Regí, M., 1988. Structure determination of $Ca_4Fe_2Ti_2O_{11}$ by electron microscopy and crystallographic image processing. J. Solid State Chem. https://doi.org/10.1016/0022-4596(88)90254-X

Hydro, 2021. Hydro [WWW Document]. Nov. bauxite tailings concept a success full Oper. URL https://www.hydro.com/en/about-hydro/stories-by-hydro/novel-bauxite-tailings-concept-a-success-in-full-operation/ (accessed 11.11.21).

Idrissi, M., Diouri, A., Damidot, D., Greneche, J.M., Talbi, M.A., Taibi, M., 2010. Characterisation of iron inclusion during the formation of calcium sulfoaluminate phase. Cem. Concr. Res. 40, 1314–1319. https://doi.org/https://doi.org/10.1016/j.cemconres.2010.02.009

IEA, 2018. Technology Roadmap Low-Carbon transition in the Cement Industry, International Energy Agency. https://doi.org/10.1007/1-4020-0612-8_961

References

Irran, E., Tillmanns, E., Hentschel, G., 1997. Ternesite, $Ca_5(SiO_4)_2SO_4$, a new mineral from the Ettringer Bellerberg/Eifel, Germany. Mineral. Petrol. 60, 121–132. https://doi.org/10.1007/BF01163138

Isteri, V., Ohenoja, K., Hanein, T., Kinoshita, H., Tanskanen, P., Illikainen, M., Fabritius, T., 2020. Production and properties of ferrite-rich CSAB cement from metallurgical industry residues. Sci. Total Environ. 712, 136208. https://doi.org/10.1016/j.scitotenv.2019.136208

Jay, A.H., Andrews, K.W., 1946. Note on Oxide Systems Pertaining to Steel-making Furnace Slags. J. Iron Steel Inst., London 152, 15–18.

Karunadasa, K.S.P., Manoratne, C.H., Pitawala, H.M.T.G.A., Rajapakse, R.M.G., 2019. Thermal decomposition of calcium carbonate (calcite polymorph) as examined by in-situ high-temperature X-ray powder diffraction. J. Phys. Chem. Solids 134, 21–28. https://doi.org/https://doi.org/10.1016/j.jpcs.2019.05.023

Kelly, T.D., Matos, G.R., 2014. Historical Statistics for Mineral and Material Commodities in the United States. U.S. Geol. Surv. Data Ser. 140.

Kirfel, A., Will, G., 1980. Charge density in anhydrite, $CaSO_4$, from X-ray and neutron diffraction measurements. Acta Crystallogr. Sect. B Struct. Crystallogr. Cryst. Chem. 36, 2881–2890. https://doi.org/10.1107/S0567740880010461

Klein, A., 1963. Calcium aluminosulfate and expansive cement containing same. United States Pat. Off.

Kobilsek, B., Lucas, Y., 1988. Morphologic and petrographic study of a bauxitic formation in Amazonia, district of Juruti, State of Para, Brazil. Sci. Geol. - Bull. 41, 71–84.

Kotschoubey, B., Truckenbrodt, W., Calaf, J.M.C., 2005. Evolução geológica da porção meridional da Província Bauxitífera de Paragominas durante o Neógeno/Pleistoceno (noroeste da Bacia do Grajaú, nordeste do Pará e extremo oeste do Maranhão). Rev. Bras. Geociências 35, 263–272. https://doi.org/10.25249/0375-7536.2005352263272

Koumpouri, D., Karatasios, I., Psycharis, V., Giannakopoulos, I.G., Katsiotis, M.S., Kilikoglou, V., 2021. Effect of clinkering conditions on phase evolution and microstructure of Belite Calcium-Sulpho-Aluminate cement clinker. Cem. Concr. Res. 147, 106529. https://doi.org/https://doi.org/10.1016/j.cemconres.2021.106529

References

Kronberg, B.I.I., Fyfe, W.S.S., McKinnon, B.J.J., Couston, J.F.F., Filho, B.S.S., Nash, R.A.A., 1982. Model for bauxite formation: Paragominas (Brazil). Chem. Geol. 35, 311–320. https://doi.org/10.1016/0009-2541(82)90008-0

Kuzel, H.J., Pöllmann, H., 1989. Einsatz von Wärmeleitkalorimetrie bei der Untersuchung chemischer Reaktionen. Fortschritte der Mineral. 67.

Kvande, H., Drabløs, P.A., 2014. The Aluminum Smelting Process and Innovative Alternative Technologies. J. Occup. Environ. Med. 56.

Le Saout, G., Idir, R., Roux, J.-C., 2019. Characterisation of Perovskites in a Calcium Sulfo Aluminate Cement, in: Glagolev, S. (Ed.), 14th International Congress for Applied Mineralogy (ICAM2019). Springer International Publishing, Cham, pp. 339–343.

Leonardi, A., Bish, D.L., 2020. Understanding Powder X-ray Diffraction Profiles from Layered Minerals: The Case of Kaolinite Nanocrystals. Inorg. Chem. https://doi.org/10.1021/acs.inorgchem.9b03464

Li, C., Wu, M., Yao, W., 2019. Effect of coupled B/Na and B/Ba doping on hydraulic properties of belite-ye'elimite-ferrite cement. Constr. Build. Mater. 208, 23–35. https://doi.org/10.1016/j.conbuildmat.2019.02.163

Li, D., O'Connor, B.H., Low, I.-M., Riessen, A. van, Toby, B.H., 2006. Mineralogy of Al-substituted goethites. Powder Diffr. https://doi.org/10.1154/1.2358358

Liu, L., Zhang, W., Ren, X., Ye, J., Zhang, J., Qian, J., 2021. Formation, structure, and thermal stability evolution of ternesite based on a single-stage sintering process. Cem. Concr. Res. 147, 106519. https://doi.org/https://doi.org/10.1016/j.cemconres.2021.106519

Liu, X., Liebermann, R.C., 1993. X-ray powder diffraction study of $CaTiO_3$ perovskite at high temperatures. Phys. Chem. Miner. https://doi.org/10.1007/BF00200119

Lothenbach, B., Scrivener, K., Hooton, R.D., 2011. Supplementary cementitious materials. Cem. Concr. Res. https://doi.org/10.1016/j.cemconres.2010.12.001

Louisnathan, S.J., 1971. Refinement of the crystal structure of a natural gehlenite, $Ca_2Al(Al,Si)_2O_7$. Can. Mineral. 10, 822–837.

Majling, J., Strigáč, J., Roy, D.M., 1999. Generalized Bogue computations to forecast the mineralogical composition of sulfoaluminate cements based on fly ashes. Adv. Cem. Res. https://doi.org/10.1680/adcr.1999.11.1.27

References

Marinho, M.B., Glasser, F.P., 1984. Polymorphism and phase changes in the ferrite phase of cements induced by titanium substitution. Cem. Concr. Res. 14, 360–368. https://doi.org/https://doi.org/10.1016/0008-8846(84)90054-1

Martín-Sedeño, M.C., Cuberos, A.J.M., De la Torre, Á.G., Álvarez-Pinazo, G., Ordónez, L.M., Gateshki, M., Aranda, M.A.G., 2010. Aluminum-rich belite sulfoaluminate cements: Clinkering and early age hydration. Cem. Concr. Res. 40, 359–369. https://doi.org/10.1016/J.CEMCONRES.2009.11.003

Martin, L.H.J., Winnefeld, F., Müller, C.J., Lothenbach, B., 2015. Contribution of limestone to the hydration of calcium sulfoaluminate cement. Cem. Concr. Compos. https://doi.org/10.1016/j.cemconcomp.2015.07.005

McCammon, C.A., Becerro, A.I., Langenhorst, F., Angel, R.J., Marion, S., Seifert, F., 2000. Short-range ordering of oxygen vacancies in $CaFe_xTi_{1-x}O_{3-x/2}$ perovskites (0 $<x<$ 0.4). J. Phys. Condens. Matter 12, 2969–2984. https://doi.org/10.1088/0953-8984/12/13/308

Mehta, P., 1980. Investigations on energy-saving cements. World Cem. Technol. 11, 166–177.

Mitchell, R.H., Welch, M.D., Chakhmouradian, A.R., 2017. Nomenclature of the perovskite supergroup: A hierarchical system of classification based on crystal structure and composition. Mineral. Mag. https://doi.org/10.1180/minmag.2016.080.156

Moore, A.E., Taylor, H.F.W., 1970. Crystal structure of ettringite. Acta Crystallogr. Sect. B 26, 386–393. https://doi.org/10.1107/S0567740870002443

Morin, V., Termkhajornkit, P., Huet, B., Pham, G., 2017. Impact of quantity of anhydrite, water to binder ratio, fineness on kinetics and phase assemblage of belite-ye'elimite-ferrite cement. Cem. Concr. Res. 99, 8–17. https://doi.org/https://doi.org/10.1016/j.cemconres.2017.04.014

Mørup, S., Both, E., 1975. Interpretation of Mössbauer spectra with broadened lines. Nucl. Instruments Methods 124, 445–448. https://doi.org/https://doi.org/10.1016/0029-554X(75)90595-9

Mumme, W.G., Hill, R.J., Bushnell-Wye, G., Segnit, E.R., 1995. Rietveld crystal structure refinements, crystal chemistry and calculated powder diffraction data for the polymorphs of dicalcium silicate and related phases. Neues Jahrb. fuer Mineral.

Naqi, A., Jang, J.G., 2019. Recent progress in green cement technology utilizing low-carbon

References

emission fuels and raw materials: A review. Sustain. https://doi.org/10.3390/su11020537

Negrão, L.B.A., Costa, M.L. da, Pöllmann, H., 2018a. The Belterra Clay on the bauxite deposits of Rondon do Pará, Eastern Amazon. Brazilian J. Geol. 48, 473–484. https://doi.org/10.1590/2317-4889201820180128

Negrão, L.B.A., Costa, M.L. da, Pöllmann, H., Horn, A., 2018b. An application of the Rietveld refinement method to the mineralogy of a bauxite-bearing regolith in the Lower Amazon. Mineral. Mag. 82, 413–431. https://doi.org/10.1180/minmag.2017.081.056

Negrão, L.B.A., Pöllmann, H., 2020. The Phase Addition method to evaluate Rietveld mineral quantitative analysis of hydrated cements. Bol. DO Mus. GEOCIÊNCIAS DA Amaz. 7, 7. https://doi.org/10.31419/issn.2594-942x.v72020i2a3lban

Negrão, L.B.A., Pöllmann, H., Cortinhas Alves, T.K., 2021a. Mineralogical Appraisal of Bauxite Overburdens from Brazil. Minerals 11, 1–14. https://doi.org/10.3390/min11070677

Negrão, L.B.A., Pöllmann, H., Costa, M.L. da, 2021b. Chapter 18 Eco-cements out of Belterra Clay: An extensive Brazilian bauxite overburden to produce low-CO_2 eco-friendly calcium sulphoaluminate based cements, in: Pöllmann, H. (Ed.), Industrial Waste. De Gruyter, pp. 553–580. https://doi.org/doi:10.1515/9783110674941-018

Negrão, L.B.A., Pöllmann, H., da Costa, M.L., 2022. Clinkering design of sulfobelite cements using clay overburden residue from bauxite mining. Adv. Cem. Res. 0, 1–15. https://doi.org/10.1680/jadcr.21.00118

Negrão, L.B.A., Pöllmann, H., da Costa, M.L., 2021c. Production of low-CO_2 cements using abundant bauxite overburden "Belterra Clay." Sustain. Mater. Technol. 29, e00299. https://doi.org/https://doi.org/10.1016/j.susmat.2021.e00299

Pace, M.L., Telesca, A., Marroccoli, M., Valenti, G.L., 2011. Use of industrial byproducts as alumina sources for the synthesis of calcium sulfoaluminate cements. Environ. Sci. Technol. 45, 6124–6128. https://doi.org/10.1021/es2005144

Paul, G., Boccaleri, E., Marchese, L., Buzzi, L., Canonico, F., Gastaldi, D., 2021. Low temperature sulfoaluminate clinkers: The role of sulfates and silicates on the different hydration behavior. Constr. Build. Mater. https://doi.org/10.1016/j.conbuildmat.2020.121111

References

Paz, S.P.A., Angélica, R.S., Kahn, H., 2017. Optimization of the reactive silica quantification method applied to Paragominas-type gibbsitic bauxites. Int. J. Miner. Process. 162, 48–57. https://doi.org/10.1016/j.minpro.2017.03.003

Pedersen, M., Lothenbac, B., Winnefeld, F., Skibsted, J., 2018. Hydrate phase assemblages in calcium sulfoaluminate – Metakaolin – Limestone blends, in: RILEM Bookseries. https://doi.org/10.1007/978-94-024-1207-9_57

Péra, J., Ambroise, J., 2004. New applications of calcium sulfoaluminate cement. Cem. Concr. Res. 34, 671–676. https://doi.org/10.1016/j.cemconres.2003.10.019

Pöllmann, H., Costa, M.L. da, Angélica, R.S., 2015. Sustainable Secondary Resources from Brazilian Kaolin Deposits for the Production of Calcined Clays, in: Scrivener, K., Favier, A. (Eds.), Calcined Clays for Sustainable Concrete. Springer Netherlands, Dordrecht, pp. 21–26.

Pöllmann, H., Stöber, S., 2014. Investigations on commercial and synthetic calciumsulfoaluminate cements, in: 36th International Conference on Cement Microscopy 2014.

Popovics, S., 1980. Calculation of the water requirement of mortar and concrete. Matériaux Constr. 13, 343–352. https://doi.org/10.1007/BF02476531

Prazeres Filho, H., Oliveira, S., Molinari, L., Belther, J., 2015. The rediscovery of Rondon do Para, the last giant world-class bauxite deposit in an attractive geography. 33th ICSOBA - International Committee for Study of Bauxite, Alumina & AluminiumAt: Dubai, United Arab Emirates.

Puntke, W., 2002. Wasseranspruch von feinen Kornhaufwerken. Beton 52, 242-248.

Raab, B., Pöllmann, H., 2012. Synthesis and Hydration of High Reactive Brownmillerites $Ca_2(Fe_{2-x}Al_x)O_5$, in: Broekmans, M.A.T.M. (Ed.), Proceedings of the 10th International Congress for Applied Mineralogy (ICAM). Springer Berlin Heidelberg, Berlin, Heidelberg, pp. 559–566.

Racanelli, L. de A., Oliveira, R.C. de, Brito, W. da S., Souza, J.A. da S., 2020. Uso de Rejeito de Lavagem de Bauxita para a Fabricação de Ligantes Geopoliméricos. Matéria (Rio Janeiro) 25. https://doi.org/10.1590/s1517-707620200001.0921

Rao, C.N.R., 2003. Perovskites, in: Meyers, R.A.B.T.-E. of P.S. and T. (Third E. (Ed.), .

References

Academic Press, New York, pp. 707–714. https://doi.org/https://doi.org/10.1016/B0-12-227410-5/00554-8

Rietveld, H.M., 1969. A profile refinement method for nuclear and magnetic structures. J. Appl. Crystallogr. 2, 65–71. https://doi.org/10.1107/S0021889869006558

Rodríguez-Carvajal, J., Vallet-Regí, M., Calbet, J.M.G., 1989. Perovskite threefold superlattices: A structure determination of the A3M3O8 phase. Mater. Res. Bull. https://doi.org/10.1016/0025-5408(89)90023-8

Ruan, H.D., Frost, R.L., Kloprogge, J.T., Duong, L., 2002. Infrared spectroscopy of goethite dehydroxylation. II. Effect of aluminium substitution on the behaviour of hydroxyl units. Spectrochim. Acta - Part A Mol. Biomol. Spectrosc. https://doi.org/10.1016/S1386-1425(01)00556-X

Runčevski, T., Dinnebier, R.E., Magdysyuk, O. V., Pöllmann, H., 2012. Crystal structures of calcium hemicarboaluminate and carbonated calcium hemicarboaluminate from synchrotron powder diffraction data. Acta Crystallogr. Sect. B Struct. Sci. 68, 493–500. https://doi.org/10.1107/S010876811203042X

Saalfeld, H., Depmeier, W., 1972. Silicon-Free Compounds with Sodalite Structure. Krist. und Tech. 7, 229–233. https://doi.org/https://doi.org/10.1002/crat.19720070125

Saalfeld, H., Wedde, M., 1974. Refinement of the crystal structure of gibbsite, A1(OH)$_3$. Zeitschrift fur Krist. - New Cryst. Struct. 139, 129–135. https://doi.org/10.1524/zkri.1974.139.1-2.129

Sadykov, V.A., Isupova, L.A., Tsybulya, S. V., Cherepanova, S. V., Litvak, G.S., Burgina, E.B., Kustova, G.N., Kolomiichuk, V.N., Ivanov, V.P., Paukshtis, E.A., Golovin, A. V., Avvakumov, E.G., 1996. Effect of mechanical activation on the real structure and reactivity of iron (III) oxide with corundum-type structure. J. Solid State Chem. https://doi.org/10.1006/jssc.1996.0168

Samain, L., Amshoff, P., Biendicho, J.J., Tietz, F., Mahmoud, A., Hermann, R.P., Istomin, S.Y., Grins, J., Svensson, G., 2015. Crystal structure and high-temperature properties of the Ruddlesden–Popper phases $Sr_{3-x}Y_x(Fe_{1.25}Ni_{0.75})O_{7-\delta}$ ($0 \leq x \leq 0.75$). J. Solid State Chem. 227, 45–54. https://doi.org/https://doi.org/10.1016/j.jssc.2015.03.018

Santacruz, I., De La Torre, Á.G., Álvarez-Pinazo, G., Cabeza, A., Cuesta, A., Sanz, J., Aranda, M.A.G., 2016. Structure of stratlingite and effect of hydration methodology on

microstructure. Adv. Cem. Res. https://doi.org/10.1680/adcr.14.00104

Santiago, E.N., Fernandez, O.J.C., Figureira, B.A.M., Gomes, L.G., 2018. Rejeitos de bauxita e sua aplicação em materiais de construção. BOMGEAM - Bol. Geociências da Amaz. 1. https://doi.org/10.31419/ISSN.2594-942X.v52018i1a6ENS

Santos, D.H. dos, Souza, J.A. da S., Gonçalves, S.G., Azevedo, C.M., Macêdo, A.N., 2013. Características do resíduo de lavagem de bauxita para utilização na indústria de cerâmica vermelha, in: 57º Congresso Brasileiro de Cerâmica, 5º Congresso Iberoamericano de Cerâmica. pp. 1434–1441.

Schmidt, R., Pöllmann, H., 2000. Quantification of calcium sulpho-aluminate cement by Rietveld analysis. Mater. Sci. Forum.

Schulze, D.G., Schwertmann, U., 1984. The influence of aluminium on iron oxides: X. properties of Al-substituted goethites. Clay Miner. https://doi.org/10.1180/claymin.1984.019.4.02

Scrivener, K., Avet, F., Maraghechi, H., Zunino, F., Ston, J., Hanpongpun, W., Favier, A., 2019. Impacting factors and properties of limestone calcined clay cements (LC3). Green Mater. 7, 3–14. https://doi.org/10.1680/jgrma.18.00029

Seewald, W., Grize, Y.L., 1997. Stavex: A sophisticated but user-friendly expert system for the design and analysis of experiments. Ther. Innov. Regul. Sci. https://doi.org/10.1177/009286159703100227

Sharygin, V. V., Lazic, B., Armbruster, T.M., Murashko, M.N., Wirth, R., Galuskina, I.O., Galuskin, E. V., Vapnik, Y., Britvin, S.N., Logvinova, A.M., 2013. Shulamitite $Ca_3TiFe^{3+}AlO_8$ - a new perovskite-related mineral from Hatrurim Basin, Israel. Eur. J. Mineral. https://doi.org/10.1127/0935-1221/2013/0025-2259

Sharygin, V. V, Yakovlev, G.A., Wirth, R., Seryotkin, Y. V, Sokol, E. V, Nigmatulina, E.N., Karmanov, N.S., Pautov, L.A., 2019. Nataliakulikite, $Ca_4Ti_2(Fe^{3+},Fe^{2+})(Si,Fe^{3+},Al)O_{11}$, a New Perovskite-Supergroup Mineral from Hatrurim Basin, Negev Desert, Israel. Minerals 9. https://doi.org/10.3390/min9110700

Shen, L., Gao, T., Zhao, J., Wang, Limao, Wang, Lan, Liu, L., Chen, F., Xue, J., 2014. Factory-level measurements on CO_2 emission factors of cement production in China. Renew. Sustain. Energy Rev. 34, 337–349. https://doi.org/https://doi.org/10.1016/j.rser.2014.03.025

References

Snellings, R., Bazzoni, A., Scrivener, K., 2014. The existence of amorphous phase in Portland cements: Physical factors affecting Rietveld quantitative phase analysis. Cem. Concr. Res. 59, 139–146. https://doi.org/10.1016/j.cemconres.2014.03.002

SNIC, 2021. Sindicato Nacional da Indústria do Cimento - Números da Indústria [WWW Document]. URL http://snic.org.br/numeros-industria.php (accessed 7.22.21).

Sombroek, W.G., 1966. Amazon soils. A reconnaissance of the soils Region, the Brazilian Amazonitle. Wageningen University.

Stöber, S., Redhammer, G., Schorr, S., Prokhnenko, O., Pöllmann, H., 2013. Structure refinements of members in the brownmillerite solid solution series $Ca_2Al_x(Fe_{0.5}Mn_{0.5})_{2-x}O_{5+\delta}$ with $1/2 \leq x \leq 4/3$. J. Solid State Chem. 197, 420–428. https://doi.org/https://doi.org/10.1016/j.jssc.2012.08.032

Strydom, C.A., Hudson-Lamb, D.L., Potgieter, J.H., Dagg, E., 1995. The thermal dehydration of synthetic gypsum. Thermochim. Acta 269–270, 631–638. https://doi.org/https://doi.org/10.1016/0040-6031(95)02521-9

Stutzman, P., Heckert, A., Tebbe, A., Leigh, S., 2014. Uncertainty in Bogue-calculated phase composition of hydraulic cements. Cem. Concr. Res. https://doi.org/10.1016/j.cemconres.2014.03.007

Tardy, Y., 1997. Petrology of laterites and tropical soils, Petrology of laterites and tropical soils.

Tardy, Y., 1993. étrologie des latérites et des sols tropicaux. Masson.

Taylor, H.F.W., 1989. Modification of the Bogue calculation. Adv. Cem. Res. https://doi.org/10.1680/adcr.1989.2.6.73

Telesca, A., Marroccoli, M., Winnefeld, F., 2019. Synthesis and characterisation of calcium sulfoaluminate cements produced by different chemical gypsums. Adv. Cem. Res. 31, 113–123. https://doi.org/10.1680/jadcr.18.00122

Touzo, B., Scrivener, K.L., Glasser, F.P., 2013. Phase compositions and equilibria in the CaO–Al_2O_3–Fe_2O_3–SO_3 system, for assemblages containing ye'elimite and ferrite $Ca_2(Al,Fe)O_5$. Cem. Concr. Res. 54, 77–86. https://doi.org/https://doi.org/10.1016/j.cemconres.2013.08.005

Truckenbrodt, W., Kotschoubey, B., 1981. Argila da Belterra - Cobertura Terciária das bauxitas amazônicas. Rev. Bras. Geociências 11, 203–208. https://doi.org/10.25249/0375-

<center>References</center>

7536.1981203208

Truckenbrodt, W., Kotschoubey, B., Schellmann, W., 1991. Composition and origin of the clay cover on North Brazilian laterites. Geol. Rundschau 80, 591–610. https://doi.org/10.1007/BF01803688

U.S Geological Survey, 2020. Mineral Commodity Summaries 2020, U.S Departtment of The Interior,.

Udagawa, S., Urabe, K., 1978. Crystal Structure of modifications of calcium silicate Ca_2SiO_4 and their phase transformation. Semento Gijutsu Nenpo 32, 35–38.

Ufer, K., Kleeberg, R., Monecke, T., 2015. Quantification of stacking disordered Si-Al layer silicates by the Rietveld method: Application to exploration for high-sulphidation epithermal gold deposits, in: Powder Diffraction. https://doi.org/10.1017/S0885715615000111

Ukrainczyk, N., Franković Mihelj, N., Šipušić, J., 2013. Calcium sulfoaluminate eco-cement from industrial waste, in: Chemical and Biochemical Engineering Quarterly.

Waerenborgh, J.C., Figueiredo, F.M., Frade, J.R., Colomer, M.T., Jurado, J.R., 2001. Fe^{4+} content and ordering of anion vacancies in partially reduced $AFe_xTi_{1-x}O_{3-y}$ (A=Ca, Sr;x$\leqslant$0.6) perovskites. An ^{57}Fe Mössbauer spectroscopy study. J. Phys. Condens. Matter 13, 8171–8187. https://doi.org/10.1088/0953-8984/13/35/322

Wainwright, R., 2018. Optimising Brazil's Petcoke Supply Chain. World Cem.

Wang, J., 2010. Hydration mechanism of cements based on low-CO_2 clinkers containing belite, ye'elimite and calcium alumino-ferrite. 7th Int. Symp. Cem. Concr.

Weirich, T.E., Winterer, M., Seifried, S., Hahn, H., Fuess, H., 2000. Rietveld analysis of electron powder diffraction data from nanocrystalline anatase, TiO_2. Ultramicroscopy. https://doi.org/10.1016/S0304-3991(99)00189-8

Westphal, T., Füllmann, T., Pöllmann, H., 2009. Rietveld quantification of amorphous portions with an internal standard—Mathematical consequences of the experimental approach. Powder Diffr. https://doi.org/10.1154/1.3187828

Winnefeld, F., Lothenbach, B., 2016. Phase equilibria in the system $Ca_4Al_6O_{12}SO_4$ – Ca_2SiO_4 – $CaSO_4$ – H_2O referring to the hydration of calcium sulfoaluminate cements. RILEM Tech. Lett. 1, 6. https://doi.org/10.21809/rilemtechlett.2016.5

References

Winnefeld, F., Martin, L.H.J., Müller, C.J., Lothenbach, B., 2017. Using gypsum to control hydration kinetics of CSA cements. Constr. Build. Mater. 155, 154–163. https://doi.org/10.1016/j.conbuildmat.2017.07.217

Yao, X., Yang, S., Dong, H., Wu, S., Liang, X., Wang, W., 2020. Effect of CaO content in raw material on the mineral composition of ferric-rich sulfoaluminate clinker. Constr. Build. Mater. 263, 120431. https://doi.org/https://doi.org/10.1016/j.conbuildmat.2020.120431

Yeskis, D., Van Groos, A.F.K., Guggenheim, S., 1985. The dehydroxylation of kaolinite. Am. Mineral.

Zhang, H., 2011. 4 - Cement, in: Zhang, H.B.T.-B.M. in C.E. (Ed.), Woodhead Publishing Series in Civil and Structural Engineering. Woodhead Publishing, pp. 46–423. https://doi.org/https://doi.org/10.1533/9781845699567.46

Zhang, L., Su, M., Wang, Y., 1999. Development of the use of sulfo- and ferroaluminate cements in China. Adv. Cem. Res. https://doi.org/10.1680/adcr.1999.11.1.15

Zötzl, M., Pöllmann, H., 2006. Stability and Properties of Brownmillerites $Ca_2(Al, Mn, Fe)_2O_5$ and Perovskites $Ca(Mn, Fe)O_{3-x}$ in the System $Ca_2Fe_2O_5$–"$Ca_2Mn_2O_5$"–"$Ca_2Al_2O_5$." J. Am. Ceram. Soc. 89, 3491–3497. https://doi.org/https://doi.org/10.1111/j.1551-2916.2006.01242.x

10   Appendix

10.1 **Disclaimer**

The results presented in this doctoral thesis are from the doctoral research carried by its author Leonardo Boiadeiro Ayres Negrão. Parts of these results are published and discussed elsewhere, as described below, and are accordingly referenced in this thesis.

Research papers:

Negrão, L.B.A., Alves, T.K.C., Pöllmann, H., 2021. Mineralogical Appraisal of Bauxite Overburdens from Brazil. **Minerals**, 11(7):677. – Mineralogical monitoring and characterization of the Belterra Clay raw material.

Negrão, L.B.A., Pöllmann, H., da Costa, M.L., 2021. Production of low-CO_2 cements using abundant bauxite overburden "Belterra Clay." **Sustainable Materials and Technologies,** Volume 29, e00299, ISSN 2214-9937. – Results, production of CSA-based cements using the Al-richer Belterra Clay from Círiaco pilot-mine.

Negrão, L.B.A., Pöllmann, H., da Costa, M.L., 2022. Clinkering design of sulfobelite cements using clay overburden residue from bauxite mining. **Advances in Cement Research**, 1-15, DOI: 10.1680/jadcr.21.00118, Published Online on February 16, 2022 – Results, production of CSA-based cements using the Al-poorer Belterra Clay from Branco pilot-mine.

Book chapter:

Negrão, L.B.A., Pöllmann, H., Costa, M.L. da, 2021b. Chapter 18 Eco-cements out of Belterra Clay: An extensive Brazilian bauxite overburden to produce low-CO_2 eco-friendly calcium sulfoaluminate based cements, in: Pöllmann, H. (Ed.), **Industrial Waste.** De Gruyter, *pp. 553– 580* – Main goals of the project and preliminary results

Others:

Negrão, L.B.A., Pöllmann, H., 2020. The Phase Addition method to evaluate Rietveld mineral quantitative analysis of hydrated cements. **Boletim do Museu de Geociências da Amazônia**, 7 – Part of the used methodology.

10.2 **Eidesstattliche Erklärung / Declaration under Oath**

Ich erkläre an Eides statt, dass ich die Arbeit selbstständig und ohne fremde Hilfe verfasst, keine anderen als die von mir angegebenen Quellen und Hilfsmittel benutzt und die den benutzten Werken wörtlich oder inhaltlich entnommenen Stellen als solche kenntlich gemacht habe.

I declare under penalty of perjury that this thesis is my own work entirely and has been written without any help from other people. I used only the sources mentioned and included all the citations correctly both in word or content.

_____   _____

Datum / date   Leonardo Boiadeiro Ayres Negrão

Unterschrift des Antragstellers / Signature

10.3 Curriculum Vitae

Personal Information

Full name	Leonardo Boiadeiro Ayres Negrão
Birth	04.02.1992 - Campinas/SP - Brazil
Nationality	Brazilian

Formal Education

2015 - 2017   **Master's degree in Science** – Geochemistry and Petrology
Universidade Federal do Pará, UFPA, Belém, Brazil
Advisor: Prof. Dr. Marcondes Lima da Costa
With a scholarship from the Brazilian National Council for Scientific and Technological Development – CNPq

2010 - 2015   **Graduation – Bachelor's degree in Geology**.
Universidade Federal do Pará, UFPA, Belém, Brazil. With Exchange program in the Martin-Luther-Universität Halle-Wittenberg (Advisor: Prof. Dr. Dr. Herbert Pöllmann)

Experience

Apr. 2011 – Jan. 2013 - Undergraduate research projects. Mineralogical and geochemical studies on rocks, ores, laterites, and related soils of Amazonia. Scholarship holder of the Coordination for the Improvement of Higher Education Personnel – CAPES Foundation, Brazil

Mar. 2013 – July 2014 - Exchange program in the Martin-Luther-Universität Halle-Wittenberg.

First Semester 2017 - Developed and implemented lessons of General Geology in the Universidade Federal Rural da Amazônia UFRA. As a collaborator of Prof. Dr. Maria do Socorro Progene Vilhena.

Feb. 2018 – Jan. 2019 - Teaching assistant / Senior Intern – German University of Technology in Oman – GUtech – Department of Applied Geosciences

Jun. 2020 – 2021 - Research assistant / PhD Student – Martin-Luther-Universität Halle-Wittenberg

Winter Semester 2021 - Developed and implemented lessons for the course Quantitative Mineral Analysis by XRD (Rietveld-Method), in cooperation with Prof. Dr. Dr. Pöllmann and PD Dr. Stöber – Martin-Luther-Universität Halle-Wittenberg

---

10.4   List of publications of the author

Research Papers

Negrão, L.B.A., Pöllmann, H., da Costa, M.L. 2022. Clinkering design of sulfobelite cements using clay overburden residue from bauxite mining. Advances in Cement Research, 1-15, DOI: 10.1680/jadcr.21.00118, Published Online on February 16, 2022 – Results, production of CSA-based cements using the Al-poorer Belterra Clay from Branco pilot-mine.

Alves de Moraes, C.; Costa, M.L.; Guida, A.N.; Nunes, M.E.S.N; **Negrão, L.B.A.**; Pöllmann, H.; Behling, Hermann. **2021**. Holocene coastal environmental changes inferred by multi-proxy analysis from Lago Formoso sediments in Maranhão State, northeastern Brazil. *Quaternary Science Reviews*, v.273, 107234. DOI: 10.1016/j.quascirev.2021.107234

Negrão, L.B.A.; Pöllmann, H.; Cortinhas Alves, T.K. **2021**. Mineralogical Appraisal of Bauxite Overburdens from Brazil. *Minerals*, v.11, 677. DOI: 10.3390/min11070677

Negrão, L.B.A.; Costa, M.L. **2021**. Mineralogy and geochemistry of a bauxite-bearing lateritic profile supporting the identification of its parent rocks in the domain of the huge Carajás iron deposits, Brazil. *Journal of South American Earth Sciences*, v.108, 103164. DOI: 10.1016/j.jsames.2021.103164

Negrão, L.B.A.; Pöllmann, H.; Costa, M.L.. **2021**. Production of low-CO_2 cements using abundant bauxite overburden Belterra Clay. *Sustainable Materials and Technologies*, v.29, e00299. DOI: 10.1016/j.susmat.2021.e00299

Negrão, L.B.A.; Pöllmann, H. **2020**. The phase addition method to evaluate Rietveld mineral quantitative analysis of hydrated cements. *Boletim do Museu de Geociências da Amazônia*, v.7, 1-7. DOI: 10.31419/issn.2594-942x.v72020i2a3lban

Negrão, L.B.A.; Costa, M.L.; Pöllmann, H.; Horn, A. **2018**. An application of the Rietveld refinement method to the mineralogy of a bauxite-bearing regolith in the Lower Amazon. *Mineralogical Magazine*, v.82, 413-431. DOI: 10.1180/minmag.2017.081.056

Negrão, L.B.A.; Costa, M.L.; Pöllmann, H. **2018**. The Belterra Clay on the bauxite deposits of Rondon do Pará, Eastern Amazon. *Brazilian Journal of Geology*, v.48, 473-484. DOI: 10.1590/2317-4889201820180128

Book Chapters

Negrão, L.B.A., Pöllmann, H., Costa, M.L., **2021**. Chapter 18 Eco-cements out of Belterra Clay: An extensive Brazilian bauxite overburden to produce low-CO_2 eco-friendly calcium sulphoaluminate based cements. In: *Industrial Waste*. Edited by Herbert Pöllmann. De Gruyter, pp. 553–580. DOI: 10.1515/9783110674941-018

Negrão, L.B.A.; Costa, M.L.; Pöllmann, H.; Abreu, D.S.S.; Silva, A.C.S.; Santos, P.H.C. **2017**. Quantification of Al in goethites and hematites of Salinópolis-PA and lateritic profiles in Carajás, Juruti and Rondon do Pará (Eastern Amazon). In: *Contribuições à geologia da amazônia Vol. 10*, Edited by Aline Maria Meiguns de Lima & Paulo Sergio de Sousa Gorayeb. Vol. 10, 1-400: SBG/NO. ISBN: 9788588692121

Conference Abstracts

Negrão, L.B.A.; Pöllmann, H.; Costa, M.L. **2021**. Belterra Clay: a promissory raw material for the production of low CO_2 binders in the Brazilian Amazon. In: *3ʳᵈ International Conference on the Chemistry of Construction*, GDCh - Gesellschaft Deutscher Chemiker, Online

Negrão, L.B.A.; Pöllmann, H.; Costa, M.L. **2021**. Eco-Cements based on residues of bauxite mining. 2021. *In: 3ʳᵈ European Mineralogical Conference*, Online

Negrão, L.B.A.; Reissner, M.; Stöber, S.; Cortinhas Alves, T.K.; Pöllmann, H. **2021**. High temperature phase transition of $3(CaTi_{0.66}Fe_{0.33}O_{2.83})\cdot CaO$ perovskite of the Ruddlesden-Popper series. In: *3ʳᵈ European Mineralogical Conference*, Online

Negrão, L.B.A. 2021. Monitoramento mineralógico da cobertura bauxítica do Brasil. 2021. In: *29º Workshop de Análises de Minérios e Minerais (OMA)*, Malvern Panalytical, Online

Negrão, L.B.A.; Costa, M.L.; Pöllmann, H. 2016. The Belterra Clay on the bauxite deposits of Rondon do Pará, Brazil. In: *48º Congresso Brasileiro de Geologia*, Porto Alegre-RS, Brazil

Negrão, L.B.A.; Costa, M.L.; Pöllmann, H. **2014**. The Rietveld refinement applied to the bauxite and its clay cover of Juruti, Pará, Brazil. In: *47º Congresso Brasileiro de Geologia*, Salvador-BA, Brazil

Negrão, L.B.A.; Costa, M.L.; Pöllmann, H. **2014**. The Lateritic-Bauxite Profile in Carajás, Pará, Brazil. In: GAEA heidelbergensis - *The 23ʳᵈ Colloquium on Latin American Earth Sciences*, Heidelberg, Germany

Negrão, L.B.A.; Costa, M.L.; Pöllmann, H. **2014**. The Rietveld refinement applied to the bauxite and its clayey cover at Juruti, Pará, Brazil. In: *Deutsche Mineralogische Gesellschaft 92ⁿᵈ Annual Meeting DMG - Minerals at Focal Point*, Jena, Germanzy